

AD-767 241

MODELING A HIGH-PRESSURE-RATION
CENTRIFUGAL COMPRESSOR USING A LOW-
SPEED-OF-SOUND GAS

James A. Block, et al

Creare, Incorporated

Prepared for:

Army Mobility Research and Development
Laboratory

May 1973

DISTRIBUTED BY:

NTIS

National Technical Information Service
U. S. DEPARTMENT OF COMMERCE
5285 Port Royal Road, Springfield Va. 22151

AD

USAAMRDL TECHNICAL REPORT 73-18

MODELING A HIGH-PRESSURE-RATIO CENTRIFUGAL COMPRESSOR USING A LOW-SPEED-OF-SOUND GAS

By

James A. Block
Peter W. Runstadler, Jr.

May 1973

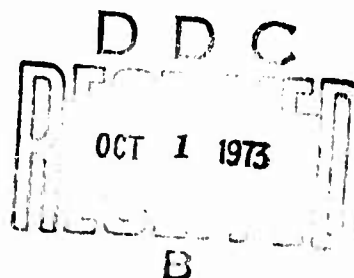
EUSTIS DIRECTORATE
U. S. ARMY AIR MOBILITY RESEARCH AND DEVELOPMENT LABORATORY
FORT EUSTIS, VIRGINIA

CONTRACT DAAJ02-70-C-0022
CREARE INCORPORATED
HANOVER, NEW HAMPSHIRE

Approved for public release;
distribution unlimited.



Reproduced by
NATIONAL TECHNICAL
INFORMATION SERVICE
U.S. Department of Commerce
Springfield, VA. 22151



245

DISCLAIMERS

The findings in this report are not to be construed as an official Department of the Army position unless so designated by other authorized documents.

When Government drawings, specifications, or other data are used for any purpose other than in connection with a definitely related Government procurement operation, the U. S. Government thereby incurs no responsibility nor any obligation whatsoever; and the fact that the Government may have formulated, furnished, or in any way supplied the said drawings, specifications, or other data is not to be regarded by implication or otherwise as in any manner licensing the holder or any other person or corporation, or conveying any rights or permission, to manufacture, use, or sell any patented invention that may in any way be related thereto.

Trade names cited in this report do not constitute an official endorsement or approval of the use of such commercial hardware or software.

DISPOSITION INSTRUCTIONS

Destroy this report when no longer needed. Do not return it to the originator.

ACCESSION for

NYIS

BBC

RECORDED

INDEXED

1964

1965

1966

1967

1968

1969

1970

1971

1972

1973

1974

1975

1976

1977

1978

1979

1980

1981

1982

1983

1984

1985

1986

1987

1988

1989

1990

1991

1992

1993

1994

1995

1996

1997

1998

1999

2000

2001

2002

2003

2004

2005

2006

2007

2008

2009

2010

2011

2012

2013

2014

2015

2016

2017

2018

2019

2020

2021

2022

2023

2024

2025

2026

2027

2028

2029

2030

2031

2032

2033

2034

2035

2036

2037

2038

2039

2040

2041

2042

2043

2044

2045

2046

2047

2048

2049

2050

2051

2052

2053

2054

2055

2056

2057

2058

2059

2060

2061

2062

2063

2064

2065

2066

2067

2068

2069

2070

2071

2072

2073

2074

2075

2076

2077

2078

2079

2080

2081

2082

2083

2084

2085

2086

2087

2088

2089

2090

2091

2092

2093

2094

2095

2096

2097

2098

2099

2100

2101

2102

2103

2104

2105

2106

2107

2108

2109

2110

2111

2112

2113

2114

2115

2116

2117

2118

2119

2120

2121

2122

2123

2124

2125

2126

2127

2128

2129

2130

2131

2132

2133

2134

2135

2136

2137

2138

2139

2140

2141

2142

2143

2144

2145

2146

2147

2148

2149

2150

2151

2152

2153

2154

2155

2156

2157

2158

2159

2160

2161

2162

2163

2164

2165

2166

2167

2168

2169

2170

2171

2172

2173

2174

2175

2176

2177

2178

2179

2180

2181

2182

2183

2184

2185

2186

2187

2188

2189

2190

2191

2192

2193

2194

2195

2196

2197

2198

2199

2200

2201

2202

2203

2204

2205

2206

2207

2208

2209

2210

2211

2212

2213

2214

2215

2216

2217

2218

2219

2220

2221

2222

2223

2224

2225

2226

2227

2228

2229

2230

2231

2232

2233

2234

2235

2236

2237

2238

2239

2240

2241

2242

2243

2244

2245

2246

2247

2248

2249

2250

2251

2252

2253

2254

2255

2256

2257

2258

2259

2260

2261

2262

2263

2264

2265

2266

2267

2268

2269

2270

2271

2272

2273

2274

2275

2276

2277

2278

2279

2280

2281

2282

2283

2284

2285

2286

2287

2288

2289

2290

2291

2292

2293

2294

2295

2296

2297

2298

2299

2300

2301

2302

2303

2304

2305

2306

2307

2308

2309

2310

2311

2312

2313

2314

2315

2316

2317

2318

2319

2320

2321

2322

2323

2324

2325

2326

2327

2328

2329

2330

2331

2332

2333

2334

2335

2336

2337

2338

2339

2340

2341

2342

2343

2344

2345

2346

2347

2348

2349

2350

2351

2352

2353

2354

2355

2356

2357

2358

2359

2360

2361

2362

2363

2364

2365

2366

2367

2368

2369

2370

2371

2372

2373

2374

2375

2376

2377

2378

2379

2380

2381

2382

2383

2384

2385

2386

2387

2388

2389

2390

2391

2392

2393

2394

2395

2396

2397

2398

2399

2400

2401

2402

2403

2404

2405

2406

2407

2408

2409

2410

2411

2412

2413

2414

<



DEPARTMENT OF THE ARMY
U. S. ARMY AIR MOBILITY RESEARCH & DEVELOPMENT LABORATORY
EUSTIS DIRECTORATE
FORT EUSTIS, VIRGINIA 23604

The objective of this contractual effort was to provide a new and useful research and development tool for those involved in the advancement of high-pressure-ratio centrifugal compressor technology. This particular program was to demonstrate the validity of using data acquired in a test gas other than air to represent compressor air performance. For the low-speed-of-sound test gas used, full design speed air data were replicated while operating the compressor at a nominal 64% of that speed. Certainly there are many other test gas possibilities that will provide even greater benefits. It is also certain that this R&D tool will be found useful in other fields of endeavor.

This report was prepared by Creare, Incorporated, under the terms of Contract DAAJ02-70-C-0022. It describes the analytical procedures, test rigs, and testing techniques used in meeting the program objectives. In addition, the data acquired in the low-speed-of-sound test gas are compared with data previously acquired on the same hardware in air. The utility of this tool was demonstrated by acquiring high-response-rate pressure data using instrumentation that could not function in the usual corresponding air environment.

This report has been reviewed by technical personnel of this Directorate. The conclusions contained herein are concurred in by this Directorate and will be considered in any future compressor research programs. The U.S. Army project engineer for this effort was Mr. Robert A. Langworthy, Technology Applications Division.

Task 1G162207AA7101
Contract DAAJ02-70-C-0022
USAAMRDL Technical Report 73-18
May 1973

MODELING A HIGH-PRESSURE-RATIO
CENTRIFUGAL COMPRESSOR USING A LOW-SPEED-OF-SOUND GAS

Final Report

By

James A. Block
Peter W. Runstadler, Jr.

Prepared by

Creare Incorporated
Hanover, New Hampshire

for

EUSTIS DIRECTORATE
U. S. ARMY AIR MOBILITY RESEARCH AND DEVELOPMENT LABORATORY
FORT EUSTIS, VIRGINIA

Approved for public release;
distribution unlimited.

Unclassified
Security Classification

| 14. | KEY WORDS | LINK A | | LINK B | | LINK C | |
|-----|--|--------|----|--------|----|--------|----|
| | | ROLE | WT | ROLE | WT | ROLE | WT |
| | Centrifugal Compressor Modeling of Compressors Low-Speed-of-Sound Modeling Aerodynamic Modeling High-Pressure-Ratio Compressor Fluid Mechanics Small Gas Turbine | | | | | | |

ii
1/a

Unclassified
Security Classification

Unclassified

Security Classification

DOCUMENT CONTROL DATA - R & D

(Security classification of title, body of abstract and indexing annotation must be entered when the overall report is classified)

| | | | |
|---|--|---|-----------------------|
| 1. ORIGINATING ACTIVITY (Corporate author) Creare Incorporated Hanover, New Hampshire | | 2a. REPORT SECURITY CLASSIFICATION Unclassified | |
| | | 2b. GROUP | |
| 3. REPORT TITLE MODELING A HIGH-PRESSURE-RATIO CENTRIFUGAL COMPRESSOR USING A LOW-SPEED-OF-SOUND GAS | | | |
| 4. DESCRIPTIVE NOTES (Type of report and inclusive dates) Final Report | | | |
| 5. AUTHOR(S) (First name, middle initial, last name) James A. Block Peter W. Runstadler, Jr. | | | |
| 6. REPORT DATE May 1973 | | 7a. TOTAL NO. OF PAGES 240 | 7b. NO. OF REFS 30 |
| 8a. CONTRACT OR GRANT NO. DAAJ02-70-C-0022 | | 9a. ORIGINATOR'S REPORT NUMBER(S) USAAMRDL Technical Report 73-18 | |
| b. PROJECT NO. Task 1G162207AA7101 | | | |
| c. | | 9b. OTHER REPORT NO(S) (Any other numbers that may be assigned this report) | |
| d. | | | |
| 10. DISTRIBUTION STATEMENT Approved for public release; distribution unlimited. | | | |
| 11. SUPPLEMENTARY NOTES | | 12. SPONSORING MILITARY ACTIVITY Eustis Directorate, U.S. Army Mobility Research and Development Laboratory Fort Eustis, Virginia | |
| 13. ABSTRACT <p>The results of a program are presented which demonstrate that low-speed-of-sound modeling is a practical tool for the research and development of high-pressure-ratio, high-speed centrifugal compressors.</p> <p>The compressor air performance and the details of its internal fluid dynamics were replicated at reduced rotational speed when a low-speed-of-sound gas was used, providing inlet Mach number, Reynolds number, and gas specific heat ratio were duplicated.</p> <p>Duplication of inlet specific heat ratio was essential to accurate modeling of the air-equivalent flow rate. Stage pressure ratio and stage efficiency were found to be less sensitive to the accurate replication of air-equivalent inlet specific heat ratio.</p> <p>This work has shown that in order to replicate stage efficiency, similarity in stage hardware geometry must be maintained. (It was held 1:1 in this program.) Stage isentropic efficiency increased as impeller-to-shroud running clearance was reduced from 15% to 5% of impeller tip depth. (This has been demonstrated for LSM and is expected to be true also for air.) In addition, the measured stage efficiency was shown to depend strongly on the heat transfer between the compressor and surroundings.</p> <p>The LSM modeling technique has been used to obtain detailed aerodynamic data of time-varying characteristics of the compressor.</p> <p>Data and results of this program are presented and discussed.</p> | | | |

DD FORM 1473

REPLACES DD FORM 1473, 1 JAN 64, WHICH IS OBSOLETE FOR ARMY USE.

Unclassified

Security Classification

SUMMARY

The results of a program are presented which demonstrate that low-speed-of-sound modeling is a practical tool for the research and development of high-pressure-ratio, high-speed centrifugal compressors.

The compressor air performance and the details of its internal fluid dynamics were replicated at reduced rotational speed when a low-speed-of-sound gas was used, providing inlet Mach number, Reynolds number, and gas specific heat ratio were duplicated.

Duplication of inlet specific heat ratio was essential to accurate modeling of the air-equivalent flow rate. Stage pressure ratio and stage efficiency were found to be less sensitive to the accurate replication of air-equivalent inlet specific heat ratio.

This work has shown that in order to replicate stage efficiency, similarity in stage hardware geometry must be maintained. (It was held 1:1 in this program.) Stage isentropic efficiency increased as impeller-to-shroud running clearance was reduced from 15% to 5% of impeller tip depth. (This has been demonstrated for LSM and is expected to be true also for air.) In addition, the measured stage efficiency was shown to depend strongly on the heat transfer between the compressor and surroundings.

The LSM modeling technique has been used to obtain detailed aerodynamic data of time-varying characteristics of the compressor.

Data and results of this program are presented and discussed.

FOREWORD

This work is part of a continuing effort to unravel and better understand the complicated fluid dynamics of the centrifugal compressor. The emphasis for this work arose from the desirability of establishing the efficacy and practicality of facilities and techniques more amenable to the research and development of the high-pressure-ratio centrifugal compressor.

We wish to acknowledge the support, the contributions, and the active criticism of people who have aided this work. Particularly we recognize the support of Robert Langworthy, Henry Morrow, and LeRoy Burrows of the U.S. Army Air Mobility Research and Development Laboratory, Eustis Directorate, in seeing this work through to its successful completion. Their appreciation of the importance of this work to future advances in centrifugal compressor technology was in large part responsible for the results achieved.

The program reported herein was authorized by Contract DAAJ02-70-C-0022, DA Task 1G162207AA7101.

TABLE OF CONTENTS

| | <u>Page</u> |
|---|-------------|
| SUMMARY. | iii |
| FOREWORD | v |
| LIST OF ILLUSTRATIONS. | x |
| LIST OF TABLES | xvi |
| LIST OF SYMBOLS. | xvii |
| 1.0 INTRODUCTION | 1 |
| 2.0 SUMMARY OF PROJECT RESULTS | 4 |
| 3.0 BACKGROUND | 5 |
| 3.1 Boeing/USAAVLABS Program | 5 |
| 3.2 Boeing's Hardware and Instrumentation. | 6 |
| 3.3 Air Data Available | 6 |
| 3.4 Estimate of the Uncertainty in the Air Data | 6 |
| 4.0 LSM SCALING -- THEORY AND DISCUSSION | 9 |
| 4.1 Philosophy of LSM Scaling. | 9 |
| 4.2 General LSM Scaling Relationships. | 10 |
| 4.3 Special Case | 15 |
| 5.0 LSM GAS SELECTION AND COMPRESSOR MODELING. | 18 |
| 5.1 Gas Selection. | 18 |
| 5.2 Determination of the Required LSM Mixture Fractions. | 19 |
| 5.3 Other Modeling Considerations. | 20 |
| 6.0 LSM TEST FACILITIES AND OPERATING PROCEDURES | 23 |
| 6.1 Test Compressor. | 23 |
| 6.2 LSM Test Facility. | 31 |
| 6.3 Auxiliary Equipment. | 34 |

TABLE OF CONTENTS - Continued

| | <u>Page</u> |
|---|-------------|
| 6.4 Test Loop Operation and Control. | 36 |
| 7.0 INSTRUMENTATION AND EXPERIMENTAL TECHNIQUES . | 39 |
| 7.1 Instrumentation. | 39 |
| 7.2 Data Reduction Procedures. | 60 |
| 7.3 Uncertainty Analysis | 63 |
| 8.0 MODELING CORRELATION - TEST RESULTS. | 66 |
| 8.1 Test Scheme. | 66 |
| 8.2 Summary of the Modeling Correlation Results. | 70 |
| 8.3 Test Results | 71 |
| 9.0 DYNAMICS MEASUREMENTS - TEST RESULTS | 118 |
| 9.1 Test Scheme. | 118 |
| 9.2 Dynamic Pressure Data. | 122 |
| 10.0 FLUID DYNAMIC INTERPRETATION OF LSM DATA . . . | 143 |
| 10.1 Summary of Results | 143 |
| 10.2 Time-Average Measurements. | 145 |
| 10.3 Dynamic Pressure Measurements. | 145 |
| 11.0 SUMMARY AND CONCLUSIONS. | 162 |
| 11.1 Summary of Program Results | 162 |
| 11.2 Recommendations for Future Work. | 164 |
| 11.3 LSM Testing - A Practical Tool?. | 167 |
| LITERATURE CITED | 170 |
| APPENDIX I - LSM GAS PROPERTY EQUATIONS. | 174 |
| Equations for the Individual Components. | 174 |
| Equations for the LSM Gas Mixture. | 180 |
| APPENDIX II - UNCERTAINTY ANALYSIS | 190 |
| Definition of Uncertainty. | 190 |

TABLE OF CONTENTS - Continued

| | <u>Page</u> |
|---|-------------|
| LSM Uncertainty Analysis. | 191 |
| APPENDIX III - EFFECT OF HEAT TRANSFER ON MEASURED EFFICIENCY | 210 |
| APPENDIX IV - CALCULATION OF JET/WAKE FRACTIONAL PRESSURE RISE | 217 |
| DISTRIBUTION. | 222 |

LIST OF ILLUSTRATIONS

| <u>Figure</u> | | <u>Page</u> |
|---------------|--|-------------|
| 1 | Specific Heat Ratio Variation With Temperature for Various CBrF_3 /Argon LSM Gas Mixtures | 21 |
| 2 | Test Compressor as Set Up in the LSM Test Loop | 24 |
| 3 | RF-2 Impeller. | 25 |
| 4 | RF-2 Impeller Geometry at Zero RPM | 26 |
| 5 | V2-2 Diffuser Geometry | 27 |
| 6 | Time-Average Static Pressure Taps in Region Beyond Impeller Exit | 29 |
| 7 | Low-Speed-of-Sound Modeling Test Facility. . . | 32 |
| 8 | Compressor Speed to Model 50,000 RPM for "1.4" LSM Gas. | 37 |
| 9 | Compressor Speed to Model 50,000 RPM for "k=1.3" LSM Gas. | 38 |
| 10 | Cover Static Pressure Taps With RF-2 Impeller. | 42 |
| 11 | Diffuser Static Pressure Taps. | 44 |
| 12 | Locations of Pressure Taps for Dynamic Pressure Measurements. | 49 |
| 13 | Location of Impeller Cover Dynamic Static Pressure Taps. | 51 |
| 14 | Dynamic Static Pressure Taps | 53 |
| 15 | Dynamic Total-Pressure Probe and Plugs | 54 |
| 16 | Schematic of the Speed-of-Sound Measuring Instrument | 55 |

LIST OF ILLUSTRATIONS - Continued

| <u>Figure</u> | | <u>Page</u> |
|---------------|--|-------------|
| 17 | Calibration of the Impeller Angular Position Indicating System. | 58 |
| 18 | Typical LSM Compression From Plenum (State 1) to Collector (State 2) Conditions. | 61 |
| 19 | Compressor Map - Boeing's Air Data With RF-2 Impeller and V2-2 Diffuser | 68 |
| 20 | Compressor Map - LSM Test 71-1 With "k=1.4" Inlet Gas. | 72 |
| 21 | Compressor Map - LSM Test 72-1 With "k=1.4" Inlet Gas and Small Clearance. | 73 |
| 22 | Compressor Map - LSM Test 72-4 With "k=1.4" Inlet Gas and Large Clearance. | 74 |
| 23 | Compressor Map - LSM Test 72-2 With Insulated Compressor and Small Clearance . . . | 75 |
| 24 | Compressor Map - LSM Test 71-2 With "k=1.32" Inlet Gas. | 76 |
| 25 | Compressor Map - LSM Test 71-2 With "k=1.32" Inlet Gas and With Flow Rate Scaled by the Air Choked Flow Rate | 77 |
| 26 | Compressor Map - LSM Test 72-3 With "k=1.45" Inlet Gas. | 78 |
| 27 | Stage Pressure Ratio for LSM Data Between "Knee" and Surge | 81 |
| 28 | Stage Pressure Ratio for LSM Data Between "Knee" and Surge | 82 |
| 29 | Mass Flow Rate at Choke. | 84 |
| 30 | Mass Flow Rate at Choke. | 85 |

LIST OF ILLUSTRATIONS - Continued

| <u>Figure</u> | | <u>Page</u> |
|---------------|---|-------------|
| 31 | Measured Efficiency With Uninsulated Compressor and 0.005" to 0.010" Impeller Running Clearance. | 87 |
| 32 | Measured Efficiency With Uninsulated Compressor and 0.020" to 0.025" Impeller Running Clearance. | 89 |
| 33 | Measured Efficiency With Uninsulated Compressor, "k=1.45" LSM, and 0.005" to 0.010" Impeller Running Clearance. | 90 |
| 34 | Isentropic Efficiency With Insulated Compressor and 0.005" to 0.010" Impeller Running Clearance. | 91 |
| 35 | Inducer Shroud Static Pressure Distribution for Air. | 94 |
| 36 | Inducer Shroud Static Pressure Distribution for LSM. | 95 |
| 37 | Inducer Shroud Static Pressure Distribution for LSM and Air. | 96 |
| 38 | Impeller Shroud Static Pressure Distribution for LSM. | 98 |
| 39 | Impeller Shroud Static Pressure Distribution for LSM. | 99 |
| 40 | Impeller Shroud Static Pressure Distribution for LSM. | 100 |
| 41 | Impeller Shroud Static Pressure Distribution for LSM. | 101 |
| 42 | Circumferential Variation of Impeller Exit Static Pressure for Air. | 102 |

LIST OF ILLUSTRATIONS - Continued

| <u>Figure</u> | | <u>Page</u> |
|---------------|--|-------------|
| 43 | Circumferential Variation of Impeller Exit Static Pressure for Air | 103 |
| 44 | Circumferential Variation of Impeller Exit Static Pressure for Air. | 105 |
| 45 | Circumferential Variation of Impeller Exit Static Pressure for LSM. | 106 |
| 46 | Circumferential Variation of Impeller Exit Static Pressure for LSM. | 107 |
| 47 | Circumferential Variation of Impeller Exit Static Pressure for LSM. | 108 |
| 48 | Circumferential Variation of Impeller Exit Static Pressure for LSM. | 109 |
| 49 | Circumferential Variation of Impeller Exit Static Pressure for LSM and Air. | 110 |
| 50 | Circumferential Variation of Impeller Exit Static Pressure for LSM and Air. | 111 |
| 51 | Static Pressure Variation Through the Diffuser | 112 |
| 52 | Static Pressure Variation Through the Diffuser | 113 |
| 53 | Static Pressure Variation Through the Diffuser | 114 |
| 54 | Static Pressure Variation Through the Diffuser | 115 |
| 55 | Static Pressure Variation Through the Diffuser | 116 |

LIST OF ILLUSTRATIONS - Continued

| <u>Figure</u> | | <u>Page</u> |
|---------------|--|-------------|
| 56 | Static Pressure Variation Through the Diffuser | 117 |
| 57 | State Point Regions for the Dynamic Pressure Data | 123 |
| 58 | Examples of Data Photos. | 124 |
| 59 | Impeller Shroud Pressure Fluctuations. | 127 |
| 60 | Impeller Shroud Pressure Fluctuations. | 128 |
| 61 | Impeller Shroud Pressure Fluctuations. | 129 |
| 62 | Impeller Exit Shroud Pressure Fluctuations | 130 |
| 63 | Impeller Exit Hub Pressure Fluctuations. | 131 |
| 64 | Impeller Exit Hub Pressure Fluctuations. | 132 |
| 65 | Semivaneless Hub Pressure Fluctuations | 133 |
| 66 | Diffuser Hub Pressure Fluctuations | 134 |
| 67 | Effect of the Total-Pressure Probe at Tap 301 on the Compressor Map. | 137 |
| 68 | Effect of the Total-Pressure Probe at Tap 302 on the Compressor Map. | 138 |
| 69 | Effect of Total-Pressure Probe on Time-Average Static Pressures. | 139 |
| 70 | Effect of Total-Pressure Probe on Time-Average Static Pressures. | 140 |
| 71 | Effect of Total-Pressure Probe on Time-Average Static Pressures. | 141 |

LIST OF ILLUSTRATIONS - Continued

| <u>Figure</u> | | <u>Page</u> |
|---------------|---|-------------|
| 72 | RF-2 Blade Loading at Cover From the Potential Solution and From Cover Dynamic Pressure Measurements. | 148 |
| 73 | Model for Jet Pressure Variation | 153 |
| 74 | Vortex Pattern at Impeller Exit in Relative Flow | 157 |
| 75 | Relation Between Mole and Mass Fractions of CBrF ₃ in a CBrF ₃ /Argon Mixture | 183 |
| 76 | Mixture Molecular Weight and Gas Constant for CBrF ₃ /Argon Mixture. | 184 |
| 77 | Viscosity of Various CBrF ₃ /Argon Gas Mixtures. | 186 |
| 78 | Speed-of-Sound Variation With Temperature for Various CBrF ₃ Argon LSM Gas Mixtures. | 189 |
| 79 | Influence of Wake Mass Flow Fraction Distribution on Wake and Jet Tangential Pressure Rise. | 221 |

LIST OF TABLES

| <u>Table</u> | | <u>Page</u> |
|--------------|---|-------------|
| I | Estimated Uncertainties in the Original Boeing Air Data. | 8 |
| II | Typical Air and LSM Actual Modeling Values . . | 22 |
| III | RF-2 Impeller Geometry at Zero RPM | 30 |
| IV | Circumferential Cover Static Pressure Tap Locations. | 43 |
| V | Locations of Pressure Taps for Dynamic Pressure Measurements (Reference Figures 12 and 13). | 52 |
| VI | Uncertainties in the Primary Measurements. . . | 59 |
| VII | Uncertainty in the Derived Quantities. | 64 |
| VIII | Summary of LSM Test Conditions | 69 |
| IX | Vertical Scales of the Dynamic Pressure Data Photos | 135 |
| X | Angular Sizes of Impeller Blades and Pressure Transducers. | 146 |
| XI | Overall Uncertainties for a Typical LSM Gas Mixture as it Exists in the Test Loop. | 193 |
| XII | Summary of the Flow Rate Uncertainty Analysis. | 207 |
| XIII | Values Used for Heat Transfer Calculation. . . | 214 |
| XIV | Heat Transfer - Four Cases | 215 |
| XV | Effect of Heat Transfer on Efficiency. | 215 |

LIST OF SYMBOLS

| | |
|-----------|---|
| A | area |
| A | general dependent variable |
| a | speed of sound |
| b | impeller passage depth |
| C | a constant |
| c | absolute velocity (relative to a Newtonian frame, e.g., compressor casing) |
| c_p | specific heat at constant pressure |
| c_v | specific heat at constant volume |
| d | flowmeter orifice diameter |
| f | a function defined in Appendix II |
| g | a function defined in Appendix II |
| g_o | proportionality constant in Newton's Second Law |
| H | enthalpy per unit mass |
| h | a function defined in Appendix II |
| h_i | heat transfer coefficient to the inside wall of the collector |
| h_o | heat transfer coefficient from the outside wall of the collector |
| K | flow coefficient in the flowmeter equation |
| k | ratio of specific heats |
| k | thermal conductivity |
| L | path length along flow "centerline" |
| L | volume fraction of air in the LSM gas mixture |
| M | gas molecular weight |
| M | Mach number |
| m | distance along specified meridional trajectory |
| \dot{m} | mass flow rate |

| | |
|-------------|--|
| m_{eq} | air-equivalent mass flow rate |
| N | compressor shaft rotational speed |
| PR | compressor pressure ratio |
| p | pressure |
| R | radius ratio, r/r_2 |
| R | gas constant |
| \tilde{R} | universal gas constant |
| Re | Reynolds number |
| r | radius from impeller centerline |
| r_2 | impeller tip radius |
| r_h | inducer hub radius |
| r_t | inducer tip radius |
| S | entropy per unit mass |
| S | streamline distance |
| s | circumferential distance from diffuser vane tip |
| s_o | circumferential distance between adjacent diffuser vane tips |
| T | temperature |
| T_w | collector wall temperature |
| T_∞ | ambient air temperature |
| TR | compressor temperature ratio |
| t | blade thickness (in direction specified) |
| t_h | blade thickness at hub |
| t_t | blade thickness at tip |
| U | overall heat transfer coefficient |
| u | impeller (metal) velocity |
| v | specific volume |
| x | general independent variable or parameter |

| | |
|------------|--|
| x | axial coordinate (as specified) |
| x | mass fraction of a component in the LSM gas mixture |
| Y | expansion factor in the flowmeter equation |
| Y | volume fraction of a component in the LSM gas mixture |
| Z | mass fraction of air in the LSM gas mixture |
| Z | number of impeller blades |
| α | blade angle (as specified) |
| δ | $\frac{\text{actual inlet pressure}}{\text{reference pressure}}$ |
| ϵ | emissivity |
| ϵ | ratio of wake/passage widths |
| η | efficiency |
| θ | $\frac{\text{actual inlet temperature}}{\text{reference temperature}}$ |
| μ | viscosity |
| ρ | density |
| σ | Stefan-Boltzmann constant |
| σ | slip factor |
| ϕ | transducer position reference angle |
| Ω | angular rotational speed |

Subscripts

| | |
|-----|--|
| 1 | plenum stagnation conditions with LSM |
| 1 | proper value of Freon-13B1 |
| 2 | collector stagnation conditions with LSM |
| 2 | property value of argon |
| 3 | flowmeter conditions with LSM |
| 3 | property value of air |
| a | air value or "air-equivalent" LSM value |
| col | collector stagnation conditions with LSM |
| i | index, referring to any component in the LSM gas |

j jet
 m actual LSM value
 o stagnation
 pln plenum stagnation conditions with LSM
 s isentropic
 s standard or reference conditions in air (519.7°R
 and 29.92"Hg)
 sos LSM value at the speed-of-sound measuring instrument
 w wake
 θ L tangential leakage

Miscellaneous

ln natural logarithm
 log base 10 logarithm
 f() function of ()
 Δ incremental (but finite) change
 d incremental (but infinitesimal) change, total
 derivative
 ∂ incremental (but infinitesimal) change, partial
 derivative
 comp a general set of variables defining the gas composition

1.0 INTRODUCTION

The testing of small, high-pressure-ratio, high-speed centrifugal turbomachinery presents difficult experimental conditions. For instance, the high shaft speeds, ranging today to 100,000 rpm, engender high blade-passing frequencies. These frequencies strain the capability of even the best dynamic instrumentation to resolve the unsteady flow patterns. In addition, the high material stresses developed are a serious impediment to expedient development. When full-scale prototype machines are run on air, the final stress, vibration, and bearing design must be carried out to make a successful test run. The aerodynamic test impeller must be built nearly as ruggedly as the final production hardware and cannot be freely altered on the test stand. It would be highly desirable if the aerodynamics of the machine could be studied and developed first, using readily modified blading, without critical concern for stressing or vibrations.

For these reasons, modeling compressor aerodynamics with a gas possessing a low speed of sound is attractive. By using an appropriate gas, Mach number, Reynolds number, and gas specific heat ratio can be duplicated but at lower speeds than in air. Since the rotational stresses vary as the square of the speed, a 50% reduction in the speed of sound results in rotational stresses only 25% of those in air. Low-speed-of-sound modeling can thus be used to provide dynamic flow similarity with an air machine but at a reduced rotative speed within the capabilities of existing instrumentation and at reduced research and development model costs. Flow measurements obtained in low-speed-of-sound modeling should more easily provide data from which empirical relationships and theory may be developed to aid the designer of small advanced-technology turbomachinery.

There are, however, several apparent problems with attempting to test turbomachinery using a gas with a low speed of sound. One of the principal reasons previous attempts have failed is the continual changing of the gas composition due to air intrusion. Previous data obtained with low-speed-of-sound gases in wind tunnels is often suspected of large errors due to uncertain composition and continual air intrusion into the test system.

Another difficulty is the problem of complete similarity modeling. No realistic modeling scheme can ever successfully duplicate all of the dimensionless parameters. However, successful modeling is achieved when those dimensionless parameters which significantly influence the results are correctly modeled. Many previous workers (see for example References 1 - 4) have attempted to use a low-speed-of-sound gas for aerodynamic modeling. However, those studies did not attempt to achieve similarity of the specific heat ratio. The work reported here has utilized a gas mixture with both a low speed of sound and a specific heat ratio very close to that of air.

The principal objective of this research was to demonstrate the feasibility of low-speed-of-sound modeling as a practical tool in the research and development of advanced high-pressure-ratio, high-speed centrifugal compressors. Both the practicality of this procedure and the correctness of the modeling had to be established. The research had to demonstrate that filling a closed test loop with an appropriate low-speed-of-sound gas and maintaining its composition known and constant throughout a test sequence were both practical and reasonably inexpensive. Furthermore, the correctness of the modeling scheme chosen had to be firmly and conclusively established so that researchers could utilize this technique without nagging doubts as to the validity of the modeling procedure.

In order to verify this latter goal, low-speed-of-sound gas modeling was done on a compressor stage that was representative of small, high-speed, high-pressure-ratio centrifugal compressors and one that had been extensively tested in air and for which the test data and hardware were readily available. This test hardware consisted of a high-pressure-ratio, high-speed centrifugal compressor stage developed earlier under U. S. Army support by the Boeing Company 5,6. The original Boeing hardware was operated in the low-speed modeling gas (LSM gas), and the test results were then compared with the original Boeing air performance data.

This report describes the equipment and facilities, the rig operation, the experimental studies and the test results of this program to obtain a correlation of low-speed-of-

sound modeling performance data with known air performance data. After LSM modeling was successfully demonstrated, its application for research was demonstrated by securing data with high-response pressure instrumentation. This work is also reported.

2.0 SUMMARY OF PROJECT RESULTS

This program has demonstrated that low-speed-of-sound modeling is a practical tool for the research and development of high-pressure-ratio, high-speed centrifugal compressors.

The compressor air performance and the details of its internal fluid dynamics were replicated at reduced rotational speed when a low-speed-of-sound gas was used, providing inlet Mach number, Reynolds number, and gas specific heat ratio were duplicated.

Duplication of inlet specific heat ratio was essential to accurate modeling of the air-equivalent flow rate. Stage pressure ratio and stage efficiency were found to be less sensitive to the accurate replication of air-equivalent inlet specific heat ratio.

This work has shown that in order to replicate stage efficiency, similarity in stage hardware geometry must be maintained. (It was held 1:1 in this program.) Stage isentropic efficiency increased as impeller-to-shroud running clearance was reduced from 15% to 5% of impeller tip depth. (This has been demonstrated for LSM and is expected to be true also for air.) In addition, the measured stage efficiency was shown to depend strongly on the heat transfer between the compressor and surroundings.

The LSM modeling technique has been used to obtain detailed aerodynamic data of time-varying characteristics of the compressor.

Data and results of this program are presented and discussed in Sections 8, 9, and 10.

3.0 BACKGROUND

One important goal of this program was the clear demonstration that LSM testing accurately reproduces the compressor performance that would be obtained in air using identical hardware. To achieve this goal it was desirable to use compressor hardware that had been extensively tested on air, that was representative of high-speed, high-pressure-ratio centrifugal stages, and for which overall stage performance data as well as detailed impeller and diffuser performance measurements were available.

3.1 BOEING/USA AVLABS PROGRAM

An exploratory development of high-pressure-ratio, centrifugal stages was carried out by the Turbine Division of the Boeing Company under U. S. Army Aviation Materiel Laboratories (USAAVLABS)* sponsorship (Contract DA 44-177-AMC-173 (T)) during the years 1964 to 1967. The results of this program are reported in References 5 and 6. Creare, under USAAVLABS sponsorship, performed a fluid dynamic analysis of the data generated during that program.⁷

Boeing designed and tested three radial and two mixed flow compressors. In addition, various diffuser systems were tested with some of the impellers. Of the configurations tested during that program, all but the "Workhorse" and "RF-2" impellers produced limited and uncertain data, as reported in References 5 and 6. Extensive data were generated with the RF-2 impeller. The last configuration tested, and hence the hardware readily available for LSM testing, was the RF-2 impeller in combination with the V2-2 diffuser. For this reason, this combination was selected for the Creare LSM modeling program to demonstrate the feasibility and correctness of low-speed-of-sound compressor modeling. Specifically, the Creare LSM program sought to duplicate the Boeing 50,000 rpm air data from Boeing test numbers 3369, 3369A, 3369B, and 3370A but at a reduced compressor speed using a gas with a lower-than-air speed of sound.

* Now the Eustis Directorate, U.S. Army Air Mobility Research and Development Laboratory (USAAMRDL).

3.2 BOEING'S HARDWARE AND INSTRUMENTATION

The compressor test rigs constructed by Boeing were very extensively instrumented. The pressure instrumentation included about 150 static pressure taps located on the front shroud and rear cover, a yaw probe in the semivaneless region, and five total pressure rakes with three total pressure probes per rake. The temperature instrumentation included a miniature stagnation temperature probe as well as thermocouples for inlet and collector temperature measurements. [Other instrumentation, not of direct interest to the present LSM program, included a traversing stagnation pressure probe ("railroad track" probe), schlieren photography in the diffuser entry region for one channel, and oil-slick wall traces.]

A more complete discussion of the particular Boeing hardware and instrumentation used on Boeing test numbers 3369, 3369A, 3369B, and 3370A and thus relevant to the current LSM program is given in Section 6.0.

3.3 AIR DATA AVAILABLE

The published air data from the Boeing program is presented in Reference 6. This data was collected, summarized, and analyzed in Reference 7. In addition to this, USAAVLABS made available to Creare several notebooks containing raw data from Boeing's automatic data recording system print-outs, as well as intermediate plots of some of the static pressure data.

3.4 ESTIMATE OF THE UNCERTAINTY IN THE AIR DATA

Although an uncertainty analysis of the experimental data was not performed by Boeing, Dean et al (Reference 7) performed an uncertainty analysis of the Boeing data using uncertainty estimates supplied by personnel of the original Boeing project for the primary measurements. This analysis (contained in Reference 7) estimated that, for Boeing's air tests of interest, the collector pressure was accurate to $\pm 0.4\%$, the mass flow rate measurement was accurate to $\pm 1\%$ (or more), and the temperature measurements taken with thermocouples were accurate to $\pm 5^\circ\text{R}$. These figures imply an uncertainty band on the stage pressure ratio of

0.57%, an uncertainty band on the stage isentropic total-to-static efficiency of 1.14%, and an uncertainty band on the referred mass flow somewhat greater than 1%. No indication of the estimated uncertainty in the shaft speed is available.

Table I summarizes the estimated uncertainties in the original Boeing air data. If the LSM data were precisely accurate, and if the modeling was precisely correct, the LSM data would agree with the Boeing data within these uncertainty bands with a probability of 20:1 (i.e., within two standard deviations).

The uncertainties in the LSM data are discussed in Section 7. The LSM uncertainty analysis is contained in Appendix II.

| TABLE I. ESTIMATED UNCERTAINTIES IN THE ORIGINAL BOEING AIR DATA* | |
|--|--------------|
| Parameter, X | $\Delta X/X$ |
| Stage pressure ratio | $\pm 0.57\%$ |
| Actual mass flow rate | $\pm 1.0\%$ |
| Referred mass flow rate | $>1.0\%$ |
| Stage isentropic efficiency | $\pm 1.1\%$ |
| Actual compressor speed | unknown |
| Referred compressor speed | unknown |
| * Boeing Tests 3369, 3369A, 3369B, 3370A (References 6 and 7) | |

Numerous authors (see for example References 1-4 and 8-10) have derived compressor scaling relations for various gases at different inlet conditions. These relations turn out to be somewhat cumbersome to use experimentally in LSM testing and are made even more cumbersome when the test gas has a specific heat ratio different from that of air. Only the simplest modeling scheme is discussed here. This scheme has been shown to be valid if the specific heat ratio (as well as the geometry, Mach number, and Reynolds number) is duplicated.

4.2 GENERAL LSM SCALING RELATIONSHIPS

The important independent dimensionless parameters which have been duplicated in the LSM tests to reproduce air compressor stage performance are geometry, Mach number, Reynolds number, and ratio of specific heats based on inlet conditions. In this discussion, we will differentiate between specified parameters and derived parameters. The specified parameters are those dimensionless numbers which must be held identical to their corresponding air values to perform a given modeling experiment. These include Mach number, Reynolds number, specific heat ratio, and dimensionless geometric variables. The derived parameters are those "air-equivalent" values which are calculated from the measured LSM parameters by means of scaling relationships which depend upon the scaling scheme chosen. The derived parameters include pressure ratio, efficiency, and flow rate. Of these derived parameters, the pressure ratio and the isentropic efficiency are scaled 1:1. The dimensional air-equivalent mass flow rate is related to the measured LSM flow rate by the scaling equation which is derived in the analysis below.

Specified Parameters

Geometry

Practically all major aspects of the geometry were modeled by using the same hardware for the LSM tests as was employed by Boeing to obtain the original air data. Small dimensional changes due to rotational or different thermal expansion effects were not exactly duplicated; however, the experimental results proved that these factors are of secondary importance.

4.0 LSM SCALING -- THEORY AND DISCUSSION

The modeling philosophy and how it is applied to the low-speed-of-sound compressor modeling program is discussed in this section. Although other scaling systems could be used, the one used in this LSM program combines the important virtues of simplicity and accuracy in predicting (modeling) full-speed air performance parameters.

The scaling scheme used is also shown to be the one most widely used to "refer" air data to standard inlet conditions.

4.1 PHILOSOPHY OF LSM SCALING

The theory of dimensionless scaling for complete modeling of physical processes is well established. However, in practice, complete similarity modeling is never achieved; one must be content with partial modeling. Success in partial modeling is achieved when the important dimensionless parameters influencing the system behavior of interest are correctly modeled. However, correct modeling is not the only criterion for a practical--not just theoretical--success. Also required is an experimental modeling technique which, while correctly modeling all of the parameters of interest, is also simple enough to be easily used.

The inlet scaling system chosen for this program did correctly model the important dimensionless parameters, and in addition contained an inherent simplicity not found in other schemes. Experimentally it has been found that this inlet scaling method works exceptionally well when an LSM gas is chosen that has an inlet specific heat ratio reasonably close to that of air. Inlet scaling, however, does break down when the inlet specific heat ratio deviates significantly from that of air (as was shown by the " $k = 1.3$ " tests of this program). Under these conditions, a more complex scaling scheme could be developed to attempt to correlate (i.e., predict) air data with LSM data. However, there is no guarantee (and it is perhaps unlikely) that such a scheme, if developed, would be capable of "correcting" high-pressure-ratio, centrifugal compressor LSM data obtained with a gas which has a specific heat ratio significantly different from that of air.

Thus, all important geometric parameters were specified to be in the ratio 1:1 by the choice of the test hardware.

Mach Number

The Mach number M chosen for modeling was the impeller tip Mach number referenced to the inlet stagnation speed of sound a_o :

$$M = u/a_o$$

where u = the impeller tip linear speed.

Since the geometry is identical, u is proportional to N , the impeller rotational speed. Therefore, Mach number scaling was achieved by setting the actual speed of the compressor with LSM gas N_m to satisfy the equation

$$N_m = N_a \frac{a_{om}}{a_{oa}} \quad (1)$$

where N_a = actual air compressor speed to be modeled

a_{om} = LSM inlet speed of sound

a_{oa} = air inlet speed of sound (at Boeing's reference conditions of 519.7°R and 29.92" Hg).

The only variable in this equation, a_{om} , is a function of the LSM gas composition and inlet temperature only. These parameters were continuously monitored to determine the inlet speed of sound and hence the required compressor speed. The airspeed to be duplicated, N_a , was 50,000 rpm for this LSM program.

Reynolds Number

The Reynolds number Re was based on inlet density ρ_o , impeller tip speed u , impeller tip diameter D , and inlet viscosity μ_o :

$$Re = \rho_o uD/\mu_o \quad (2)$$

Since Mach number is duplicated, we have

$$\frac{u_a}{a_{oa}} = \frac{u_m}{a_{om}} \quad (3)$$

Using this and the perfect gas law,* the Reynolds number scaling relation results in the following expression for the inlet stagnation pressure:

$$p_{om} = p_{oa} \frac{a_{oa} R_{om} T_{om} \mu_{om}}{a_{om} R_{oa} T_{oa} \mu_{oa}} \quad (4)$$

where p_{om} , p_{oa} = inlet stagnation pressure for LSM, air
 R_{om} , R_{oa} = gas constant for LSM, air
 T_{om} , T_{oa} = inlet stagnation temperature for LSM, air
 μ_{om} , μ_{oa} = inlet viscosity for LSM, air

All "modeling" parameters on the right-hand side of this equation are functions of the LSM gas composition and inlet temperature only. These parameters were continuously monitored and used to set the proper inlet stagnation (plenum) pressure p_{om} to assure continual Reynolds number similarity during a test. The values of the air properties R_{oa} and μ_{oa} , which are constants in this equation for a given air test condition to be modeled, were evaluated at Boeing's air reference conditions of 519.7°R and 29.92" Hg.

Specific Heat Ratio

For the bulk of the testing, the inlet specific heat ratio of the LSM test gas was chosen to duplicate the inlet

* The perfect gas law is applicable to describe the behavior of the LSM gas mixture. However, properties of individual components of the mixture, as well as the mixture properties which resulted, were calculated by using the best available actual equation of state for each gas component. This is discussed in Appendix I.

specific heat ratio of air. However, since testing with a gas that has a lower specific heat ratio than air is attractive (because a higher molecular weight and hence lower-speed-of-sound gas and lower rotational speed can be used), the effect of specific heat ratio on the aerodynamic modeling was investigated using different specific heat ratio gas mixtures. The selection of a gas mixture to achieve the desired specific heat ratios is discussed in Section 5.

Derived Parameters

Pressure Ratio

The stage pressure ratio with LSM gas was compared directly (1:1 scaling) with the air stage pressure ratio. Absolute pressures measured throughout the compressor were ratioed to the inlet pressure and then compared directly with the similarly-formed air pressure ratios at identical measurement locations.

Efficiency

The inlet plenum total to collector static isentropic stage efficiency was calculated from the measured LSM plenum and collector temperatures and pressures and was compared directly (1:1 scaling) with the air efficiency. The isentropic compressor efficiency with LSM gas was calculated using the definition of isentropic efficiency:

$$\eta = \frac{\text{isentropic enthalpy rise}}{\text{actual enthalpy rise}} \quad (5)$$

The data reduction computer program, which was used to calculate the efficiencies reported in this work, calculated the actual and isentropic enthalpy rises of the LSM gas based on the best available expressions for the enthalpy and entropy as a function of pressure, temperature, and composition (see Section 7.2). The efficiency was not calculated from an expression of the form

$$\frac{\frac{k-1}{k} \text{PR} - 1}{\text{TR} - 1}$$

where k would have been some "average" specific heat ratio. Calculation of the efficiency by this method would have been at best only an approximation.

Mass Flow Rate

The mass flow rate, being a dimensional quantity, does not scale directly. The "air-equivalent" mass flow rate m_{eq} was calculated from the actual flow rate of the LSM gas as follows.

From one-dimensional, isentropic mass flow relations for compressible flow, we can write

$$m_{eq} = m_m \left[\frac{R_{om} k_{oa} T_{om}}{R_{oa} k_{om} T_{oa}} \right]^{1/2} \left[\frac{p_{oa}}{p_{om}} \right] \left\{ \frac{\left[1 + \frac{k_{om}-1}{2} M_m^2 \right]^{\frac{k_{om}+1}{2(k_{om}-1)}}}{\left[1 + \frac{k_{oa}-1}{2} M_a^2 \right]^{\frac{k_{oa}+1}{2(k_{oa}-1)}}} \right\} \quad (6)$$

where m_m = the actual mass flow rate of LSM gas
 k_o = the inlet specific heat ratio.

Note that this relation is general for any specific heat ratio test gas used. The specific heat ratio (and the other parameters) was evaluated based on the exact composition and inlet stagnation temperature for each particular test.

Since the LSM tests were conducted with Mach number duplication, we can write

$$M_a = M_m \quad (7)$$

If the LSM and air inlet specific heat ratios are also equal, the bracketed term in the above mass flow rate equation is unity independent of the Mach number. However, even if the LSM inlet specific heat ratio is not equal to the air inlet specific heat ratio, the bracketed term is very nearly independent of the Mach number used in this expression for all Mach numbers between 0 and, say, 1.5 or so. For example, with $k_{oa} = 1.4$ and k_{om} between 1.3 and 1.5, the value of the

bracketed term varies by less than 1% for all Mach numbers between 0 and 1.5 as long as the same Mach number is used in the numerator and the denominator of the bracketed term. Thus, the simplifying assumption $M_a = M_m = 1$ is a very good approximation. The resulting expression,

$$m_{eq} = m_m \left[\frac{R_{om} k_{oa} T_{om}}{R_{oa} k_{om} T_{oa}} \right]^{1/2} \left[\frac{p_{oa}}{p_{om}} \right] \left\{ \frac{\left[\frac{k_{om} + 1}{2} \right]^{\frac{k_{om} + 1}{2(k_{om} - 1)}}}{\left[\frac{k_{oa} + 1}{2} \right]^{\frac{k_{oa} + 1}{2(k_{oa} - 1)}}} \right\} \quad (8)$$

was used for calculating the air-equivalent mass flow.

4.3 SPECIAL CASE

The above scaling relationships were used throughout this program to reduce all data. Below, we consider a special case where the scaling equations can be simplified. These were not used in reducing the data. They are presented to demonstrate that, in the appropriate limits, this scaling scheme reduces to the schemes generally used in compressor testing.

Consider the situation where air performance data is to be obtained by modeling with air. This is actually done every time a compressor is tested and the results are "referred" to a standard reference condition. Boeing used for their work the reference conditions of 519.7°R and 29.92" Hg.

If the modeling gas is air, we have

$$k_m = k_a \quad \text{and}$$

$$R_m = R_a$$

Equation (1) for Mach number scaling then becomes

$$N_m = N_a \sqrt{\frac{T_{om}}{T_{oa}}} \quad (9)$$

where we have used $a = \sqrt{kRT}$. Defining

$$\theta = T_{om}/T_{oa} \quad (10)$$

Equation (9) becomes

$$N_a = N_m / \sqrt{\theta} \quad (11)$$

where T_{oa} is the reference temperature (519.7°R for Boeing), T_{om} is the actual inlet temperature during a given test, N_m is the actual speed for a given test point, and N_a is the "referred" speed.

Equation (8) for mass flow rate becomes (when $k_{om} = k_{oa}$ and $R_{om} = R_{oa}$)

$$m_{eq} = m_m \frac{p_{oa}}{p_{om}} \sqrt{\frac{T_{om}}{T_{oa}}} \quad (12)$$

Defining

$$\delta = p_{om}/p_{oa} \quad (13)$$

Equation (12) becomes

$$m_{eq} = m_m \sqrt{\theta} / \delta \quad (14)$$

where p_{oa} is the reference pressure (29.92"Hg for Boeing), p_{om} is the actual inlet pressure during a given test, m_m is the actual mass flow rate for a given test point, and m_{eq} is the "referred" flow rate.

Equation (4) for the Reynolds number scaling becomes

$$P_{om} = P_{oa} \sqrt{\frac{T_{om}}{T_{oa}}} \frac{\mu_{om}}{\mu_{oa}} \quad (15)$$

or

$$\delta = \sqrt{\theta} \frac{\mu_{om}}{\mu_{oa}} \quad (16)$$

The reader will undoubtedly recognize Equation (11) and Equation (14) as the conventional compressor scaling equations used to "refer" test data to selected standard conditions. However, the reader may not readily recognize Equation (16). This reflects the general lack of care in correctly modeling Reynolds number during air testing. The typical procedure is to measure θ and δ and use these to correct the measured speed and flow rate via Equations (11) and (14). However, if Reynolds number is to be held fixed, Equation (16) states that θ and δ must be set during the experiment in a definite relation to each other. This is not normally done since most compressor designers and testers feel that variations in Reynolds number will not exhibit a strong influence on the compressor performance. Although this is probably true for most "low altitude" testing, one should recognize that testing without regard to satisfying Equation (16) implies testing with an uncontrolled parameter -- the Reynolds number.

Since this program used the same hardware for LSM testing as was used to generate the original air data, the discussion above considered only 1:1 geometry scaling. Real gains can be obtained by using larger-scale LSM hardware. In this case the modeling equations must be appropriately modified in a straightforward manner. See for example, Reference 4.

5.0 LSM GAS SELECTION AND COMPRESSOR MODELING

Proper modeling of the Mach number, Reynolds number, and specific heat ratio with the chosen LSM gas was achieved by mixing the correct proportions of Freon-13B1 with argon. The rationale behind this selection of gas components and how the gas proportions were selected is discussed in this section.

5.1 GAS SELECTION

The overriding goal in the evaluation and selection of the LSM gas mixture was to provide for the modeling of air data at the lowest possible compressor speed yet stay within reasonable cost and maintain relative simplicity of operation.

The duplication of the air inlet Mach number is achieved by satisfying Equation (1). A low compressor speed is achieved by using a gas mixture with a low inlet speed of sound. A low inlet speed of sound implies a gas with a high molecular weight and/or low inlet temperature. The techniques used in this program to achieve a low inlet temperature are discussed in Section 6; in the present section, temperature is discussed only as it affects the properties of the candidate gases.

The requirement of a high molecular weight leads to the consideration of polyatomic gases. Chapman¹¹ performed an excellent evaluation and tabulation of numerous candidate high-molecular-weight gases. His listing contains many fluoro-chemicals (Freons). However, Freons, as well as all polyatomic gases, have a very low specific heat ratio (typically between 1.1 and 1.2). Thus, to match the inlet specific heat ratio of air (1.4), proper amounts of a monatomic gas (with high inlet specific heat ratio -- typically about 1.67) must be mixed with the selected polyatomic gas.

Other considerations entered into the gas mixture selection beyond the obvious factors of high molecular weight and proper specific heat ratio. These included low cost, ready availability, low toxicity, low flammability, good thermal stability, availability of property data, and a saturation line reasonably removed from the "operating" states of the mixture.

Octafluoropropane C_3F_8 was originally considered as the candidate polyatomic gas component. However, since this gas was not readily available in a pure form and since its properties were not well established, bromotrifluoromethane $CBrF_3$ (Freon-13B1) was chosen instead. Freon-13B1 is readily available in sufficiently pure form and its properties have been well established (e.g., Reference 12). In addition, Freon-13B1 is moderately inexpensive (about \$5/lb), has low toxicity, is not flammable (in fact, it is an excellent fire extinguisher), and has excellent thermal stability. When mixed with a suitable monatomic gas, Freon-13B1 is also sufficiently far from its saturation line under normal storage and all test conditions. Thermodynamic properties of Freon-13B1 are found in References 11-15. General characteristics of Freon-13B1 are found in Reference 16.

Candidate monatomic gases included argon, krypton, and xenon. Xenon was immediately removed from consideration due to its extremely high cost and poor availability. Since krypton has a higher molecular weight than argon, its use in an LSM mixture would result in approximately 25% lower compressor speed than a similar mixture with argon. However, krypton costs about 200 times as much as argon. The selection of krypton would have required a special gas recovery and purification system. In addition, the use of krypton would involve a serious cost penalty should the LSM gas mixture become grossly contaminated or should a major leak develop. Therefore, for reasons of cost and simplicity of operation, argon was finally selected as the monatomic component for the LSM gas mixture.

The interested reader is referred to References 4 and 11 for additional discussion on gas selection for low-speed-of-sound modeling.

5.2 DETERMINATION OF THE REQUIRED LSM MIXTURE FRACTIONS

The property equations used to calculate the properties of the individual LSM gas components and mixture are presented and discussed in Appendix I.

The exact fractions of each component of the LSM gas mixture were fixed by the desired inlet specific heat ratio. The LSM program called for utilizing three different gas mixtures:

- 1) Inlet specific heat ratio ≈ 1.4 (used for the bulk of the testing)
- 2) Inlet specific heat ratio ≈ 1.3
- 3) Stage-averaged specific heat ratio of LSM equal to the stage-averaged specific heat ratio of air.

The variation in specific heat ratio of LSM gas with temperature and mass fraction of Freon-13B1 mixed with argon is shown in Figure 1. A mass fraction of CBrF_3 of 0.476 was chosen to duplicate the specific heat ratio of air at the nominal LSM inlet temperature (-5°F). A mass fraction of CBrF_3 of 0.637 was chosen as the " $k = 1.3$ " inlet LSM gas. A mass fraction of CBrF_3 of about 0.38 was chosen to simulate the average specific ratio in the compressor which resulted in an inlet specific heat ratio of 1.45 for this mixture.

Since the fraction of air during any test was always small, its effect on the nominal specific heat ratio was negligible. Of course, the amount of air was continuously monitored during each test, and the actual LSM gas mixture properties were always evaluated using the actual fractions of Freon, argon, and air present during each test.

5.3 OTHER MODELING CONSIDERATIONS

Once the gas composition is known, the molecular weight and gas constant of the mixture are known. (See Appendix I.) These, together with the inlet temperature, determine the inlet speed of sound of the LSM gas mixture which dictates the compressor speed to be set to model any particular air condition. (The details of how this is done are discussed in Section 4.)

The dimensional parameters which affect the duplication of the Reynolds number are inlet speed of sound, inlet viscosity, and inlet pressure (see Equation (4)). The speed of sound and viscosity are uniquely determined by the gas composition and inlet (plenum) temperature. Therefore, for any plenum temperature and gas composition, the plenum pressure is continually maintained at the proper value to assure close similarity between the LSM and the air inlet Reynolds numbers. Typical values of inlet plenum pressure for LSM testing were between 8 and 10 psia.

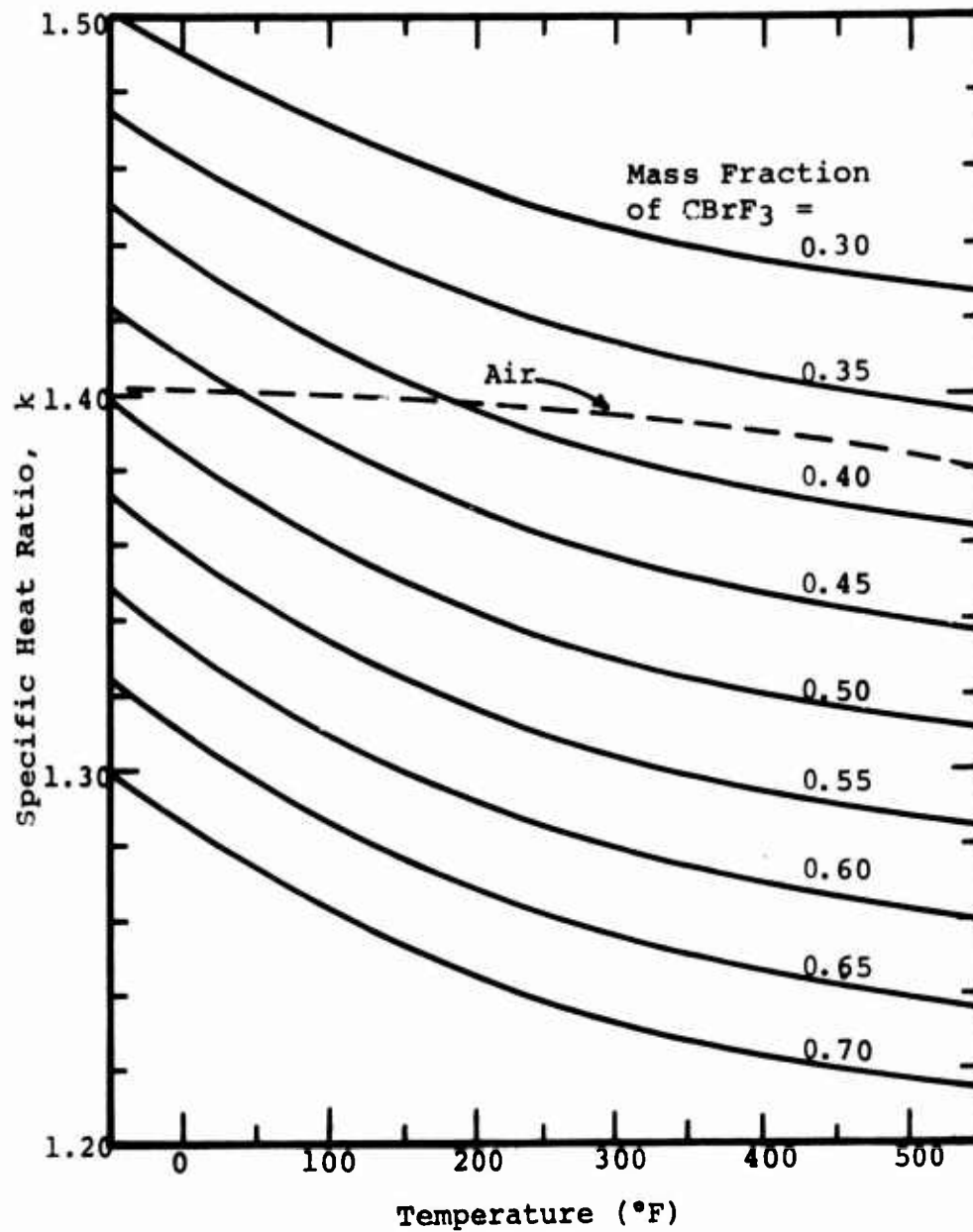


Figure 1. Specific Heat Ratio Variation With Temperature for Various CBrF_3 /Argon LSM Gas Mixtures.

Typical air and LSM conditions are shown in Table II.

| TABLE II. TYPICAL AIR AND LSM ACTUAL MODELING VALUES | | | |
|--|-----------------------------------|-----------------------------------|------------------|
| Parameter | Typical Boeing Air Value | Typical Creare LSM Value | Ratio LSM/Air |
| Actual speed (rpm) | 50,000 | 32,000 | 0.64 |
| Air-equivalent speed (rpm) | 50,000 | 50,000 | 1.0 |
| Actual flow rate (lb/sec) | 1.9 | 1.7 | - |
| Air-equivalent flow rate (lb/sec) | 1.9 | 1.9 | 1.0 |
| Stage pressure ratio | 9.0 | 9.0 | 1.0 |
| Stage efficiency (%) | 72.2 | 71.9 | - |
| Actual power (HP) | 400 | 145 | 0.36 |
| Plenum pressure (psia) | 14.7 | 9.0 | - |
| Collector pressure (psia) | 132 | 81 | - |
| Plenum temperature (°F) | 60 | -5 | - |
| Collector temperature (°F) | 675 | 500 | - |
| Temperature ratio | 2.18 | 2.11 | - |
| Inlet speed of sound (ft/sec) | 1120 | 768 | 0.64 |
| Inlet specific heat ratio | 1.4 | 1.4 | 1.0 |
| Discharge specific heat ratio | 1.37 | 1.33 | - |
| Mach number (inlet) | - | - | 1.0 |
| Reynolds number (inlet) | - | - | 1.0 |
| Mass fraction Freon-13B1 | - | 0.475 | - |
| Mass fraction argon | - | 0.522 | - |
| Mass fraction air | 1.0 | 0.003 | - |

6.0 LSM TEST FACILITIES AND OPERATING PROCEDURES

In this section we describe the Boeing compressor hardware used in this program, discuss the LSM flow loop constructed around this equipment, and relate how the LSM tests were conducted. This LSM test facility is versatile for both fundamental research and practical performance evaluation of compressors. Throughout the course of this program, the operating procedures (and data reduction techniques) have been continually refined to a point where LSM testing is a simple and routine procedure.

6.1 TEST COMPRESSOR

The test compressor used for this program was designed and constructed by the Boeing Company under contract to the U. S. Army Aviation Materiel Laboratories. The development, construction, and air performance testing of this hardware by Boeing are described in References 5, 6 and 7.

During the Boeing/USA AVLABS hardware development and testing program, Boeing constructed two test rigs. These were designated by Boeing as the "diffuser rig" and the "impeller rig". Of the impellers and diffusers developed and tested by Boeing, the RF-2 impeller with the V2-2 diffuser configuration in the "diffuser rig" was chosen for use in the LSM program for the reasons discussed in Section 3.

Figure 2 shows this test compressor (diffuser rig) as set up in the LSM loop. The inlet plenum can be seen on the right side of this photo; the high-speed gearbox is seen on the left.

Photos of the RF-2 impeller are shown in Figure 3. A meridional layout of the RF-2 impeller is sketched in Figure 4, and the geometric parameters for this impeller are listed in Table III.

The V2-2 diffuser geometry is shown in Figure 5. Also displayed in this figure are several of the numerous pressure tap locations in the vaneless and semivaneless space and in the diffuser channel. Figure 6 is a photograph of this region. Although the diffuser vanes have been removed, their locations are clearly visible.

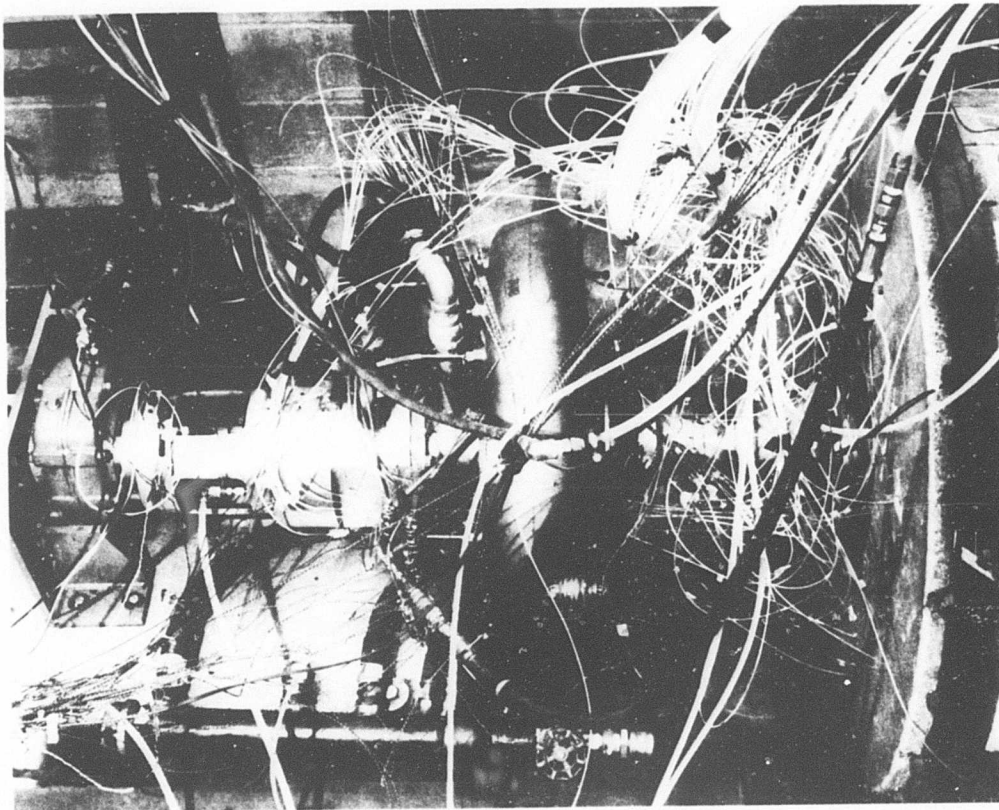
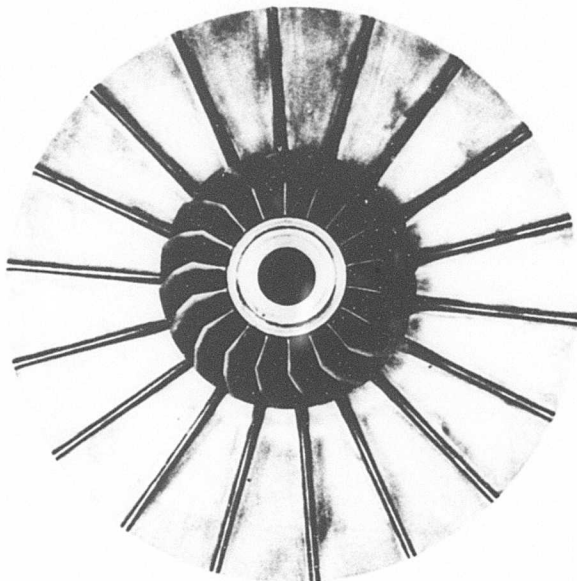
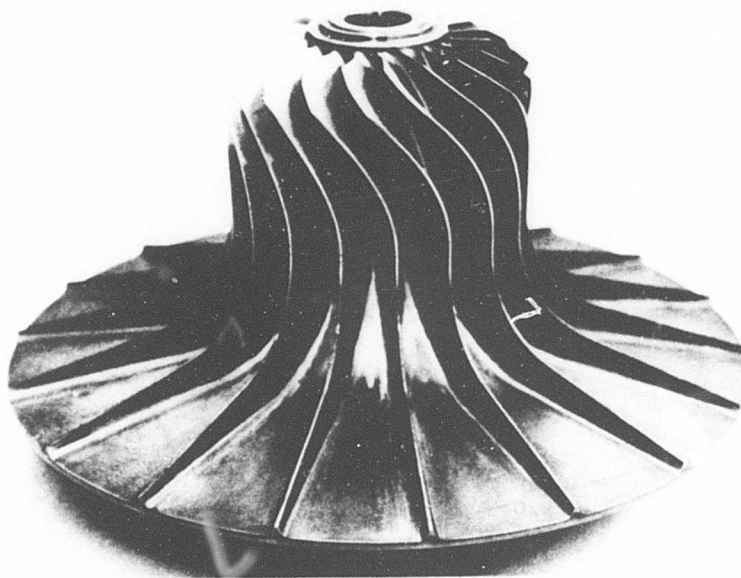


Figure 2. Test Compressor as Set Up
in the LSM Test Loop.

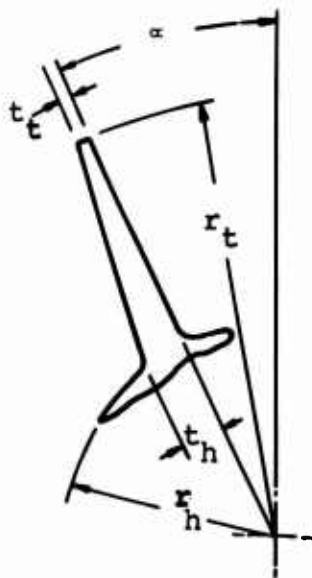
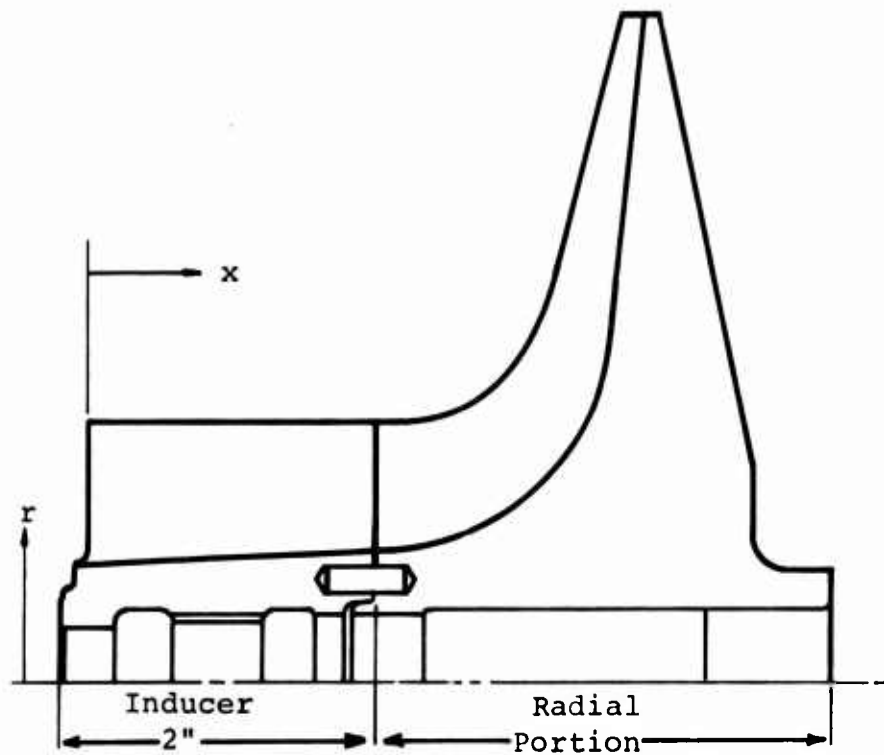


a. View From Inlet.

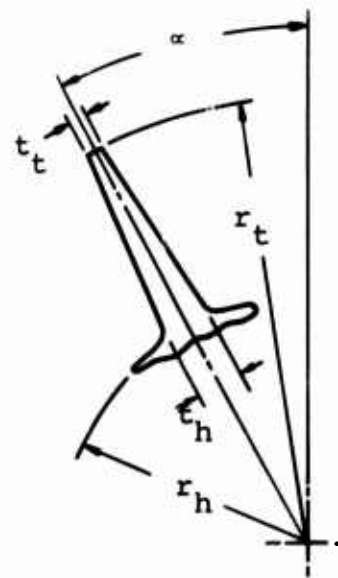


b. Side View.

Figure 3. RF-2 Impeller.



Inducer Blading
(Not Symmetrical)



Impeller Blading
(Symmetrical)

Figure 4. RF-2 Impeller Geometry at Zero RPM.

A

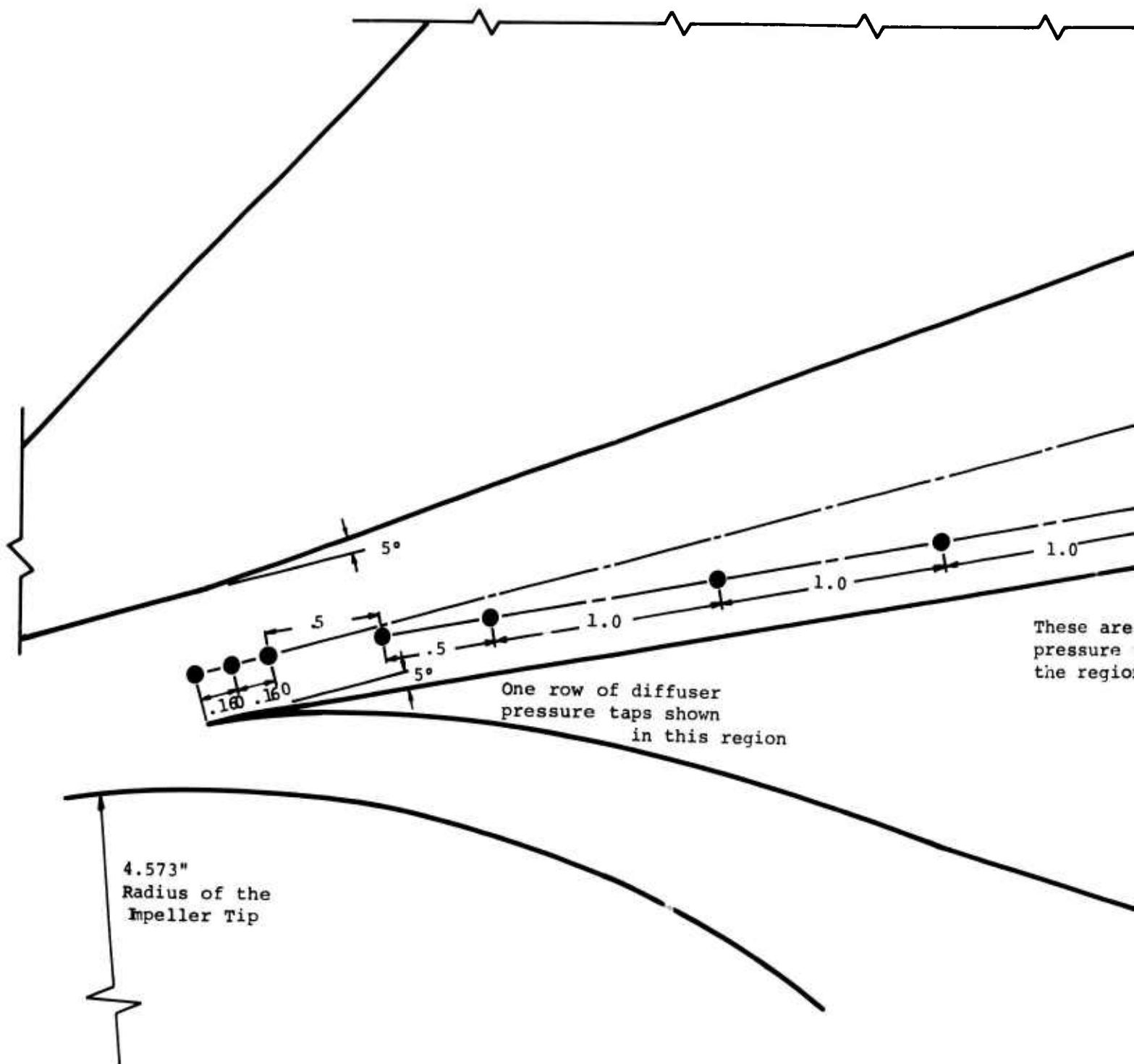
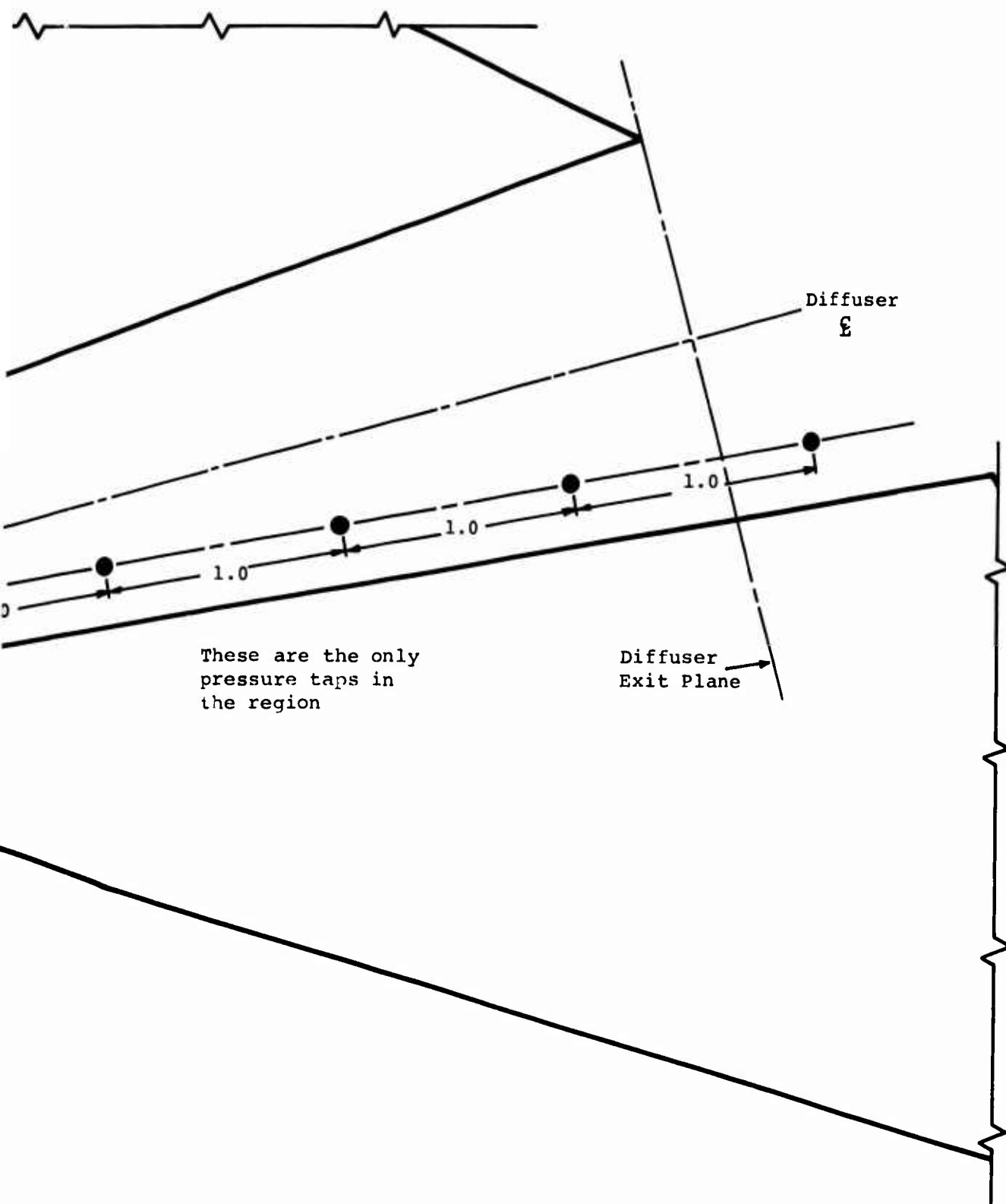


Figure 5. V2-2 Diffuser Geometry.

B



These are the only pressure taps in the region

Diffuser Exit Plane

Diffuser E

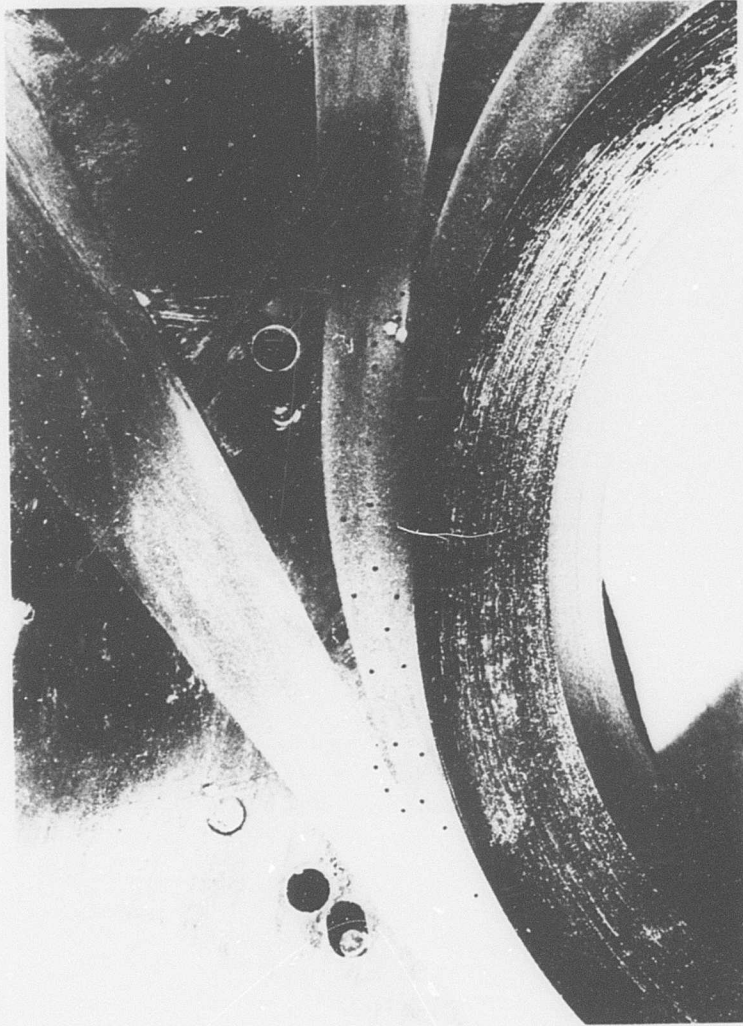


Figure 6. Time-Average Static Pressure Taps
in Region Beyond Impeller Exit.

TABLE III. RF-2 IMPELLER GEOMETRY AT ZERO RPM

| Axial Distance x (in.) | Blade Turning Angle (deg) | Hub Radius r_h (in.) | Tip Radius r_t (in.) | Hub* Thickness t_h (in.) | Tip* Thickness t_t (in.) |
|------------------------------|---------------------------------|------------------------------|------------------------------|----------------------------------|----------------------------------|
| 0 | 0 | 0.813 | 1.80 | 0 | 0 |
| 0.01 | - | 0.813 | 1.80 | 0.023 | 0.032 |
| 0.02 | - | 0.814 | 1.80 | 0.027 | 0.026 |
| 0.03 | - | 0.814 | 1.80 | 0.031 | 0.038 |
| 0.04 | - | 0.815 | 1.80 | 0.034 | 0.04 |
| 0.06 | - | 0.815 | 1.80 | 0.040 | 0.043 |
| 0.08 | - | 0.817 | 1.80 | 0.046 | 0.044 |
| 0.10 | - | 0.818 | 1.80 | 0.050 | 0.044 |
| 0.12 | 4.78*** | 0.819 | 1.80 | 0.054 | 0.044 |
| 0.15 | - | 0.821 | 1.80 | 0.057 | 0.043 |
| 0.3 | 11.60 | 0.829 | 1.80 | 0.062 | 0.042 |
| 0.500 | 18.59 | 0.839 | 1.80 | 0.061 | 0.041 |
| 0.700 | 24.87 | 0.850 | 1.80 | 0.060 | 0.039 |
| 0.900 | 30.32 | 0.860 | 1.80 | 0.059 | 0.037 |
| 1.100 | 34.88 | 0.871 | 1.80 | 0.058 | 0.035 |
| 1.300 | 38.53 | 0.881 | 1.80 | 0.057 | 0.033 |
| 1.500 | 41.27 | 0.892 | 1.80 | 0.056 | 0.032 |
| 1.700 | 43.10 | 0.902 | 1.80 | 0.055 | 0.031 |
| 1.900 | 44.03 | 0.913 | 1.80 | 0.055 | 0.030 |
| 2.000 | 44.15 | 0.918 | 1.80 | 0.055 | 0.030 |
| 2.430 | 44.80 | 0.958 | 1.839 | 0.055 | 0.030 |
| 2.860 | 44.80 | 1.108 | 2.051 | 0.055 | 0.030 |
| 3.290 | 44.80 | 1.431 | 2.711 | 0.055 | 0.030 |
| 3.720 | 44.80 | 2.313 | 4.316 | 0.055 | 0.030 |
| 3.785** | 44.80 | - | 4.573 | 0.055 | 0.030 |
| 3.965** | 44.80 | 4.573 | - | 0.055 | 0.030 |

* Blade thicknesses measured normal to x -- after handworking of the blades

** Estimated graphically (tip of impeller)

*** Not corrected for handworking

All of the aerodynamic instrumentation used is discussed in Section 7.0.

6.2 LSM TEST FACILITY

The low-speed-of-sound modeling test facility was constructed around the test compressor. This facility is shown in Figure 7.

The low-temperature LSM gas flows from the plenum through the test compressor and then through two heat exchangers. These reduce the gas temperature from the collector temperature of about 500°F (PR \approx 9) to about 50°F. These heat exchangers are followed by a flow rate metering section and a valve. From the downstream side of the valve, the flow is expanded through a turbine to return to the inlet plenum at about -5°F. The flow is distributed and turbulence is damped in the inlet plenum through a series of flow distributors, honeycomb sections and screens. The total volume of the test loop is about 30 cubic feet; about half of this volume is in the plenum.

LSM Loop Controls

A small amount of LSM gas is continuously sampled from the loop and its speed of sound measured. This measurement, coupled with a measurement of the plenum temperature, dictates the compressor speed and plenum pressure to be set in order to model any given air Reynolds number and Mach number (compressor speed). The test compressor speed is maintained by an auxiliary drive unit. The plenum pressure is adjusted by controlling the amount of LSM gas in the system. The compressor back pressure (and hence stage pressure ratio) is controlled by the back pressure valve located just upstream of the expansion turbine.

The LSM loop is stable in operation, comes to thermal equilibrium fairly quickly (on the order of 15 minutes), and is easily adjusted to model any air-equivalent speed and compressor pressure ratio. Complete compressor performance stage maps can be easily and quickly produced. In addition, this loop provides easy adjustment of the inlet Reynolds number (through control of the plenum pressure), which could be used, if desired, to study the effect of Reynolds number on compressor stage performance or to simulate altitude effects.

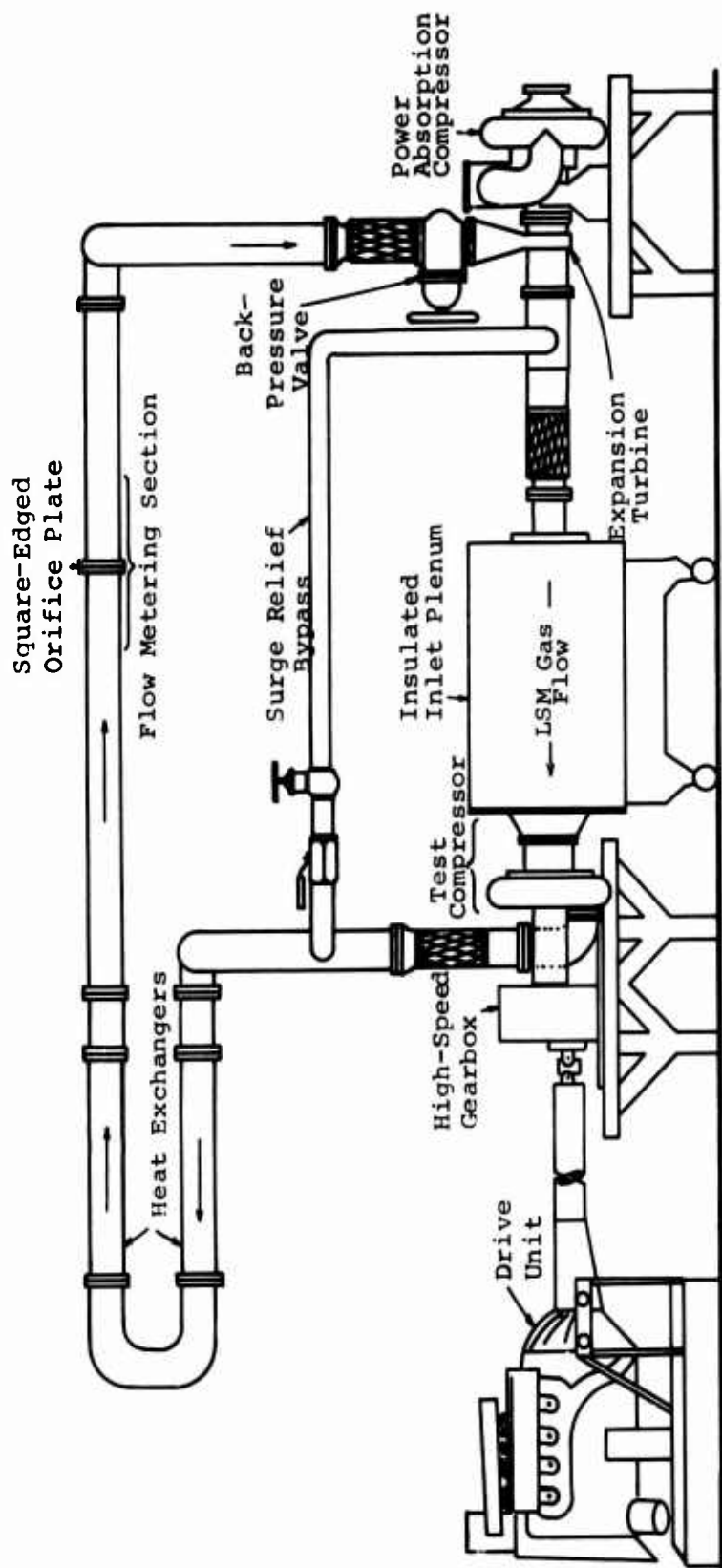


Figure 7. Low-Speed-of-Sound Modeling Test Facility.

LSM Gas Temperature Control

With a typical LSM test gas, the temperature rise through the test compressor at 50,000 rpm was about 500°F. In order to achieve a low inlet speed of sound, it was desired to cool the compressor exit LSM gas to a low temperature at a reasonable cost. In addition, a low plenum temperature was required to keep the temperature of the LSM gas through the impeller and diffuser regions below the temperature limits of available dynamic pressure instrumentation. Since this instrumentation typically has a 500°F maximum temperature, this implies that an inlet temperature of about 0°F had to be achieved.

The temperature reduction was performed using two heat exchangers in series followed by a temperature reducing, expansion turbine. The gas flowing through the water-cooled heat exchangers was cooled to about 50°F. Consideration was given to using a liquid refrigerant in the second heat exchanger, but this was not done for cost reasons. However, future programs might do this to realize an even lower compressor inlet temperature for even lower shaft speeds.

Boeing's "impeller rig" turbine was used as the expansion turbine. Since this turbine was designed for a somewhat higher flow rate than was used in the LSM testing, the turbine was converted to a partial admission design by blocking off five of the sixteen inlet channels. This helped to maintain a high turbine efficiency. The turbine was left connected to the "impeller rig" compressor which operated in a free-wheeling mode on lab air to "absorb" the power extracted by the turbine. The ducting between the expansion turbine and the plenum, as well as the plenum and compressor inlet bellmouth, was insulated to keep heat transfer to a minimum.

Flow Meter

The flow metering section was constructed with flow straighteners according to ASME specifications (Reference 17). A square-edge orifice plate was used with flanged taps located 1" upstream and downstream of the orifice plate. The measurement of the LSM gas flow rate is discussed further in Section 7.0.

Surge Relief

In order to quickly bring the test compressor out of surge, a surge relief bypass loop was provided. This bypass could be quickly opened with a ball valve when the compressor went into surge. Surge was sensed by the onset of large fluctuations at the water manometer used to measure the pressure drop across the flowmeter orifice.

6.3 AUXILIARY EQUIPMENT

Compressor Drive Units

Throughout the first half of this program, the test compressor was driven using the air turbine built by Boeing to drive the diffuser rig. The air supply for this turbine was obtained from compressor bleed ports of a Westinghouse J-46 jet engine located exterior to the main test facility. The test compressor speed was controlled by throttling the turbine drive air supply. No additional heat input to this air supply was required to power the test compressor. However, local noise pollution considerations required that this power supply be abandoned.

The second half of this test program was performed using an internal combustion engine coupled to a high-speed gearbox (15:1 gear ratio) to power the test compressor.

Loop Sealing

To minimize air intrusion into the LSM loop or LSM gas leakage out, careful attention was paid to sealing all joints and regions where leaks could occur. Special O-ring seals were designed for the test compressor and expansion turbine. An LSM gas recirculating system was constructed to deliver an oil/LSM lubrication mist to the carbon-faced seals of the expansion turbine. The carbon-faced shaft seals of the test compressor were lubricated with an LSM gas/oil mist combination using LSM gas from a premixed supply cylinder.

These precautions resulted in a system where the test gas composition would remain unchanged during and after testing. Thus, uncertainties in the data due to a continually changing gas composition were minimized. In addition, the same LSM gas could be stored in the test loop and reused indefinitely,

provided the loop was not disassembled. In any event, the cost of LSM gas was small (less than \$25/hr) compared to the operating costs of typical high-pressure-ratio, high-speed compressor test facilities.

System Evacuation and Filling

Evacuation and filling of the LSM test loop was accomplished in several stages. A pair of vacuum pumps extracted air from the loop to a pressure within several inches of mercury absolute vacuum. At this stage, the system was quickly filled from a premixed, high-pressure LSM gas supply bottle. Complete filling was achieved using about half of a 600-psi bottle and could be accomplished in about ten seconds. The system was filled to slightly greater than atmospheric pressure. Under this condition no further air intrusion is possible while the system is static (no-flow) since any leak is out of the system. (During storage of the LSM gas in the test loop between test runs, the loop was maintained at slightly above atmospheric pressure.)

This initial evacuation and filling step resulted in several percent air remaining in the test loop. The amount of air in the gas mixture in the loop was reduced to a low value by the following procedure. The back pressure valve of Figure 7 was completely closed. Evacuation was then resumed at a point just upstream of this valve. At the same time, pure LSM from a supply cylinder was inserted into the loop just downstream of this closed valve. The loop pressure was maintained slightly above ambient. This caused the "contaminated" LSM gas to flow through the loop and out through the vacuum pumps while at the same time being replaced by pure LSM gas. This procedure was the most efficient way (in terms of gas cost and time) to minimize the final air fraction remaining in the gas mixture.

This process could be continued until the fraction of air remaining in the loop was reduced to a very low value. Typically, this procedure was stopped when the air fraction was 1% or less. The amount of air in the loop could be determined at any time by measuring the speed of sound. However, since the mass fraction of the gas in the loop varied with position in the loop during this procedure, the amount of air in the loop could be accurately determined only during the test run. Once a test began, the composition

of gas in the loop was uniform and remained constant.

Rig Lubrication

An oil lubrication and cooling system was constructed to provide cooling oil to the bearings and thrust disk regions of the drive engine, the test compressor, and the expansion turbine. The return oil from the loop was cooled through a series of heat exchangers.

Rig Control Instrumentation

Both compressor rigs were instrumented with stationary, preset rub sensors. These were wired to provide for immediate, automatic shutdown of the drive engine should a near rub be indicated.

Compressor vibrations were monitored with an accelerometer mounted on the compressor housing.

Oil, bearings, and seal "air" temperatures were continuously monitored with thermocouples.

6.4 TEST LOOP OPERATION AND CONTROL

As described in Section 5.4, all independent test variables associated with each operating point and modeling condition can be expressed as functions of the gas composition and inlet temperature only. The gas composition and inlet plenum temperature were continuously monitored. These inputs were used in conjunction with a series of operating charts. Samples of the operating charts for speed control are shown in Figures 8 and 9. Using charts of this type, the compressor speed to achieve duplication of the air Mach number could be set and maintained. Similar charts for the plenum pressure were used to set inlet Reynolds number.

The compressor speed was controlled by the drive unit. The plenum pressure was controlled by controlling the amount of LSM gas in the test loop. The compressor pressure ratio or back pressure was adjusted using a pair of back pressure valves (a coarse, control in parallel with a fine control) located just upstream of the expansion turbine as shown in Figure 7.

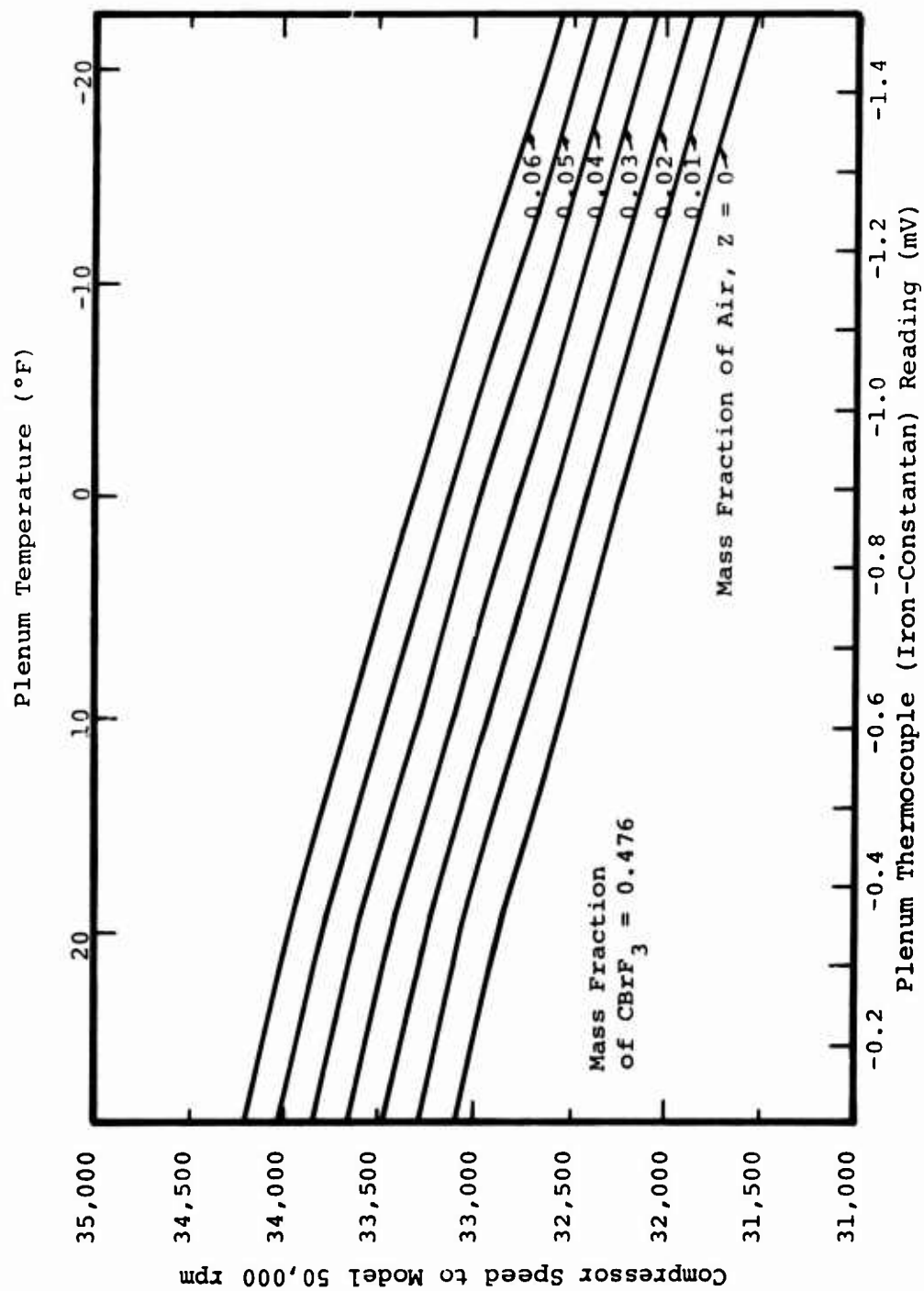


Figure 8. Compressor Speed to Model 50,000 RPM for "1.4" LSM Gas.

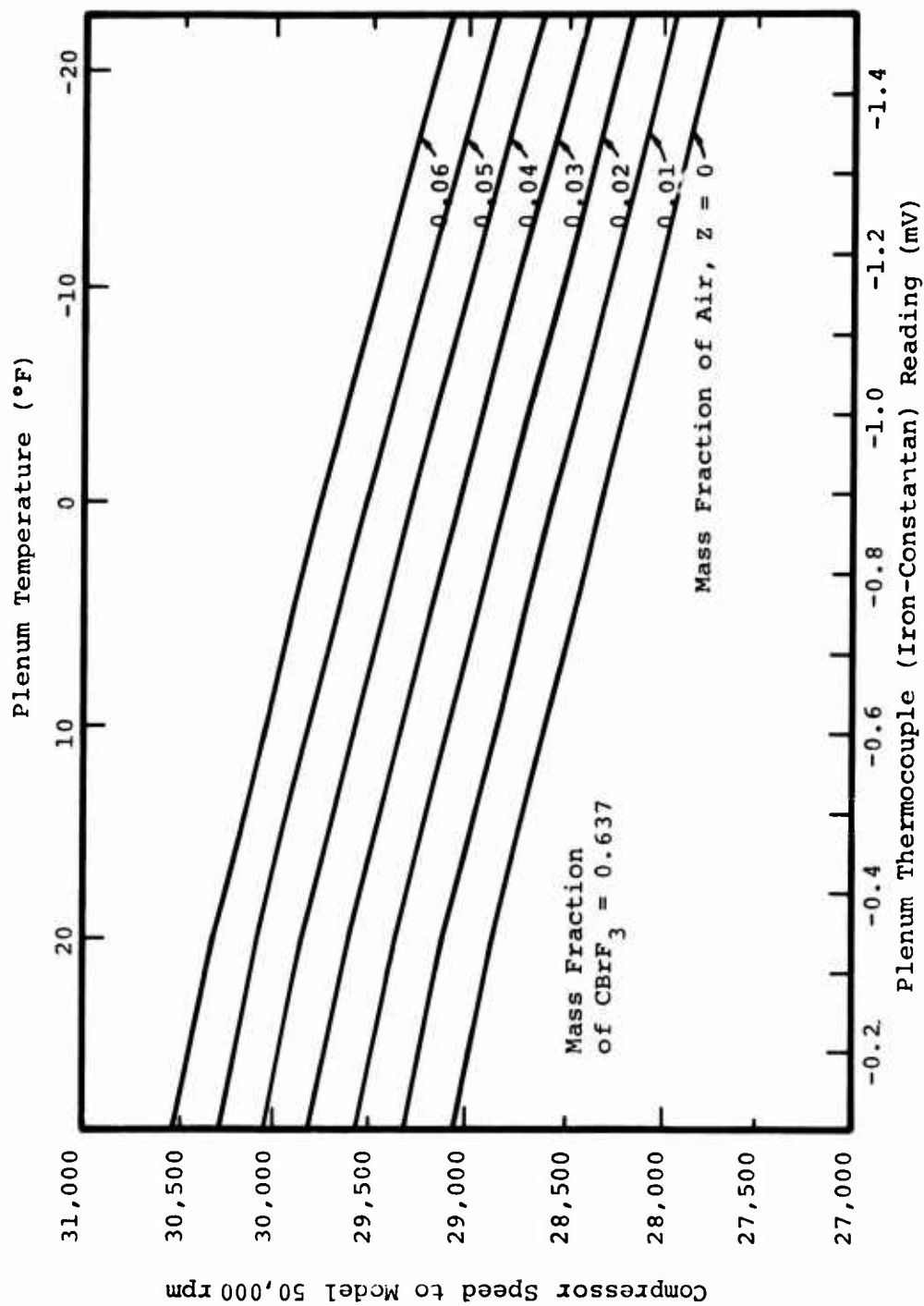


Figure 9. Compressor Speed to Model 50,000 RPM for "k=1.3" LSM Gas.

7.0 INSTRUMENTATION AND EXPERIMENTAL TECHNIQUES

The basic instrumentation used during this program is described in this section. Also presented is an estimate of the uncertainties in the basic measurements, and a summary of the data reduction techniques used during this program. An uncertainty estimate for the derived or calculated quantities is given in Appendix II and is summarized in Section 7.3.

7.1 INSTRUMENTATION

The design, location, calibration, and estimated accuracy of the instruments and their output signals used to measure the "primary" experimental variables are discussed in this section. "Derived" quantities such as pressure ratio, flow rate, and efficiency are discussed in Section 7.3.

Voltage

A four-place, digital millivolt meter was used for the read-out of the thermocouples, the compressor speed indicator, and the time-average signal from the pressure transducers. This instrument was calibrated regularly to 0.01% traceable to National Bureau of Standards. The estimated absolute uncertainty in this instrument is 0.01 millivolt.

Temperature

All temperature measurements were made with premium-grade, iron-constantan (type J) thermocouples with an ice bath reference. The thermocouples were calibrated as-wired against a mercury thermometer standard. The estimated uncertainty for any thermocouple when used in conjunction with the four-place voltmeter is less than $\pm 1^\circ\text{F}$.

Two thermocouples were mounted in the inlet plenum; five were mounted at various locations in the collector. The plenum and collector temperatures used in the data reduction and analysis were averages of the individual readings of the appropriate thermocouples. The individual thermocouple readings were always within 2°F of the average temperature. Assigning an uncertainty of $\pm 2^\circ\text{F}$ to the plenum and collector temperatures implies an uncertainty in plenum temperature ($\Delta T/T$) of 0.44% (using a typical plenum temperature 460°R)

and an uncertainty in the collector temperature of 0.21% (using a typical collector temperature 960°R).

A thermocouple was also placed at a specified location (ASME standards) upstream of the orifice plate in the flowmeter. The estimated uncertainty in this temperature measurement is $\pm 0.30\%$.

Various thermocouples were embedded in the compressor cover and the collector. These surface temperature measurements along the flow path through the compressor were used to:

- 1) Correct the dynamic pressure transducers for temperature effects
- 2) Obtain an estimate of the error in calculating efficiency when conducting tests with an uninsulated compressor (as discussed in Appendix III)

The output signals from the dynamic pressure transducers and the heat transfer calculations are both quite insensitive to small errors in cover surface temperature measurement; thus the accuracy of these measurements was not critical.

Pressure

Numerous kinds and types of pressure measurements were performed throughout this program. These will be discussed in turn.

Barometer

The local barometric pressure was measured using a calibrated mercury barometer. This instrument was checked monthly against a barometer located at Dartmouth College. The estimated uncertainty in the measurement of the local barometric pressure is 0.03%.

Water Manometer

A 4-foot vertical water manometer was used to measure the pressure drop across the flowmeter orifice plate. The estimated uncertainty of this pressure drop measurement is $0.1''\text{H}_2\text{O}$ or 1% of the minimum pressure drop experienced during testing.

Mercury Manometer

A specially constructed 16-foot mercury manometer was used for the calibration of the time-average and dynamic pressure transducers. The estimated uncertainty in this instrument, taking into consideration thermal expansion effects, is 0.06" Hg.

Static (Time-Average) Pressures

A pneumatic switching pressure readout system, similar to that described in Reference 18, was used for selecting the numerous time-average static pressures. This system had the capability of switching to any one of 117 static pressure locations and reading any of these static pressure tap signals on one of two differential pressure transducers: a ± 25 psid or a 0-100 psid pressure transducer. These transducers were referenced to ambient pressure and were used to read all time-average static pressures.

These transducers were calibrated several times during this program against the 16-foot mercury manometer. Taking into consideration the uncertainties in the transducer output voltage reading, the mercury manometer calibration, mercury manometer reading, and the measurement of the local barometric pressure, the ± 25 psid transducer was accurate to 0.05 psia and the 0-100 psid transducer was accurate to 0.08 psia. At a nominal plenum pressure of 10 psia and a nominal collector pressure of 90 psia, this implies uncertainties in plenum and collector pressure measurements of 0.5% and 0.1% respectively.

The static pressure measurements along the compressor cover and in the impeller exit and diffuser passage regions were taken using the same pressure taps as used for the original Boeing data. A full description of these pressure tap locations is found in References 6 and 7. Figure 10 and Table IV show the location of the static pressure measuring stations along the cover of the test compressor rig. At each of these stations there were three static pressure taps located circumferentially around the cover. Figure 11 shows the location of the static pressure taps in the impeller exit and diffuser passage regions. There were static pressure taps on both the front and back covers at each of the indicated locations. Figure 6 is a photo of the

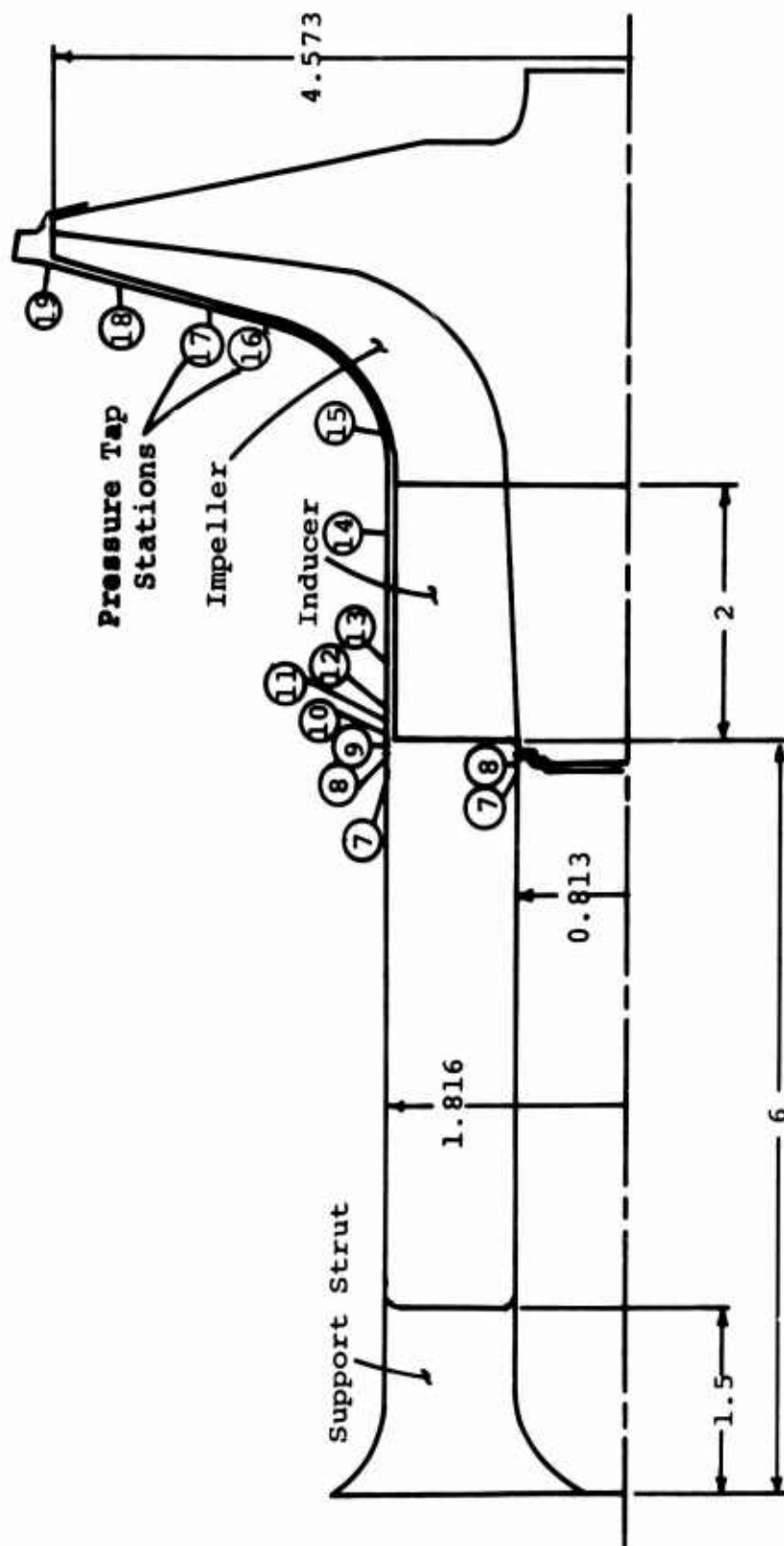


Figure 10. Cover Static Pressure Taps With RF-2 Impeller.

TABLE IV. CIRCUMFERENTIAL COVER STATIC PRESSURE
TAP LOCATIONS

| Station Number | r (in.) | x (in.) | m (in.) |
|-------------------|-------------|------------|------------|
| 7 | 1.816,0.813 | -0.35 | -0.35 |
| 8 | 1.816,0.813 | -0.20 | -0.20 |
| 9 | 1.816 | -0.10 | -0.10 |
| 10 | 1.816 | 0 | 0 |
| 11 | 1.816 | 0.10 | 0.10 |
| 12 | 1.816 | 0.20 | 0.20 |
| 13 | 1.816 | 0.45 | 0.45 |
| 14 | 1.816 | 1.50 | 1.50 |
| 15 | 1.816 | 2.32 | 2.35 |
| 16 | 2.25 | 3.02 | 3.0 |
| 17 | 3.00 | - | 4.0 |
| 18 | 3.80 | - | 4.8 |
| 19 | 4.54 | - | 5.7 |

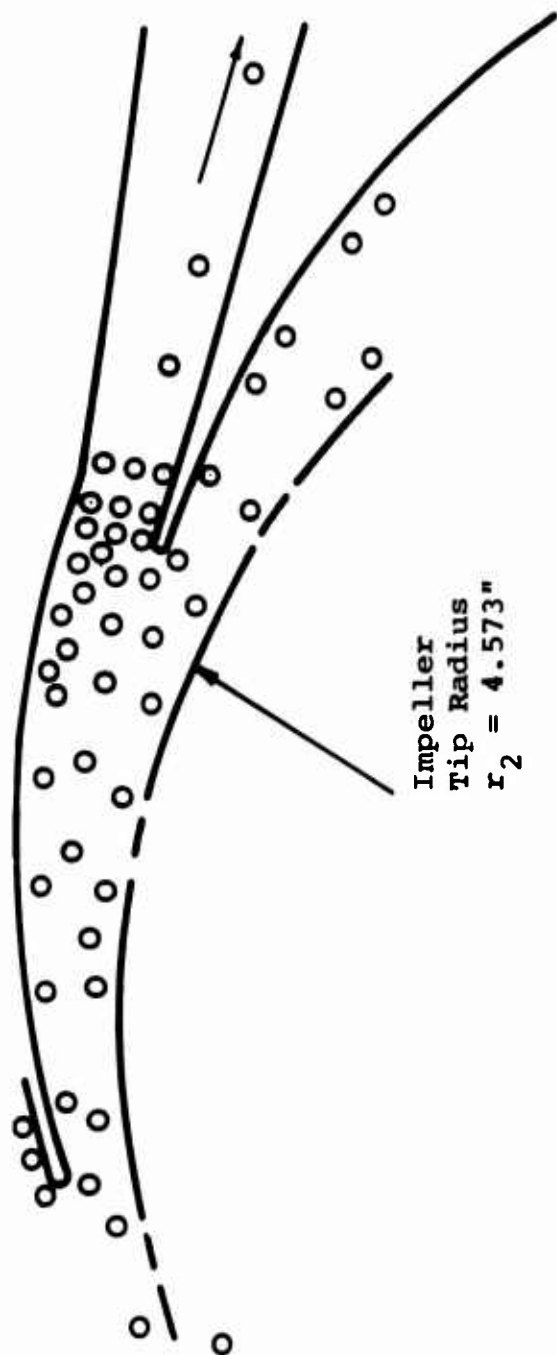


Figure 11. Diffuser Static Pressure Taps.

pressure taps in this region.

Dynamic Pressure Instrumentation

Measurements of the dynamic (unsteady) characteristics of the static and total pressures in the RF-2 compressor were made using miniature high-response-rate transducers. Two general classes of sensors were evaluated prior to the final selection:

- 1) Piezoelectric types, utilizing pressure-sensitive quartz elements
- 2) Strain gauge types with semiconductor sensing elements.

Specific models of each of these types have nominal specifications which satisfy the general requirements for size, frequency response, sensitivity, operating temperature and acceleration compensation.

The final selection of the sensor for use in the dynamic measurement phase of the program was based primarily on the relative sizes of the two transducer types. This size differential becomes important when studying pressures which vary rapidly with position and time, because the transducer senses only the "average" pressure acting on its sensing surface. The larger the sensing surface, the greater the possibility of "losing" important information. The smallest piezoelectric transducer considered for this program has a pressure diaphragm 0.22" in diameter, while the semiconductor strain gauge type eventually selected has a pressure-sensitive surface of 0.085" diameter. This means that the strain gauge transducer can effectively "see" pressure signals with characteristic frequencies about three times higher than those seen by the piezoelectric device. The semiconductor strain gauge transducer was chosen for use in this program.

Secondary considerations which also weighed in favor of the semiconductor strain gauge types were:

- 1) Simpler signal conditioning requirements
- 2) Potentially a dc pressure measurement capability.

The strain gauge transducers were statically calibrated against the reference mercury manometer from 0 to 100 psig. Each transducer was powered by a separate dc supply, and the excitation voltages were adjusted such that each transducer would have approximately the same nominal sensitivity at 70°F. Since the transducers were to be used at temperatures ranging from 70°F to about 500°F, they were calibrated at a number of temperatures in this range.

The result of this calibration yielded curves of transducer sensitivity as a function of temperature for each of the four transducers used. The transducers were linear at each temperature; their sensitivities varied by about 3% over the temperature range of interest (70°F to 500°F). The uncertainty in the sensitivities was about 1%. This uncertainty is composed almost entirely of the scatter in the calibration data. The nominal sensitivity of these transducers is about 0.75 mV/psi.

These four transducers were used to measure the time-varying pressure levels in the compressor at various locations and operating conditions. For these measurements, the transducer outputs were displayed on an oscilloscope, along with an impeller angular-position indicating signal. Photographic records were made of these traces, and all of the dynamic pressure information was extracted from them.

Thermocouples were embedded in the compressor cover to measure the operating temperature of the transducers at each test condition. These temperatures were then used to determine the output sensitivity of the transducers for each data point.

Some preconditioning of the pressure signal was needed to eliminate a very high frequency component in the signals (250 kHz) caused by "ringing" of the transducer diaphragms. This was accomplished by filtering the output with a variable-frequency electronic filter. The upper limit on the pass band was set at 200 kHz, well above the fundamental blade passing frequency of 10 kHz. The filter proved to be satisfactory in minimizing this 250 kHz "noise" with no measurable effect on either phase or amplitude response of the transducer.

The outputs from all four transducers were recorded simultaneously by utilizing a dual-beam oscilloscope, with each beam (operating in a "chopped" mode) displaying the signal from two transducers. By triggering the sweep of each beam with the same source, the outputs from the four transducers were presented in their true time relationship. In addition, the pressure signal from each transducer was separately and individually recorded on another photograph at two sweep rates and two amplifications simultaneously with the impeller position indicating signal. The overall uncertainty in the dynamic pressure measurements was limited by the accuracy and reading precision of the oscilloscope. The overall uncertainty in the dynamic pressure measurements is estimated to be about 3-4% of the amplitude sensitivity measured in psi/division.

The static and total dynamic pressure transducer locations are shown in Figures 12 and 13. The locations of these pressure taps were chosen wherever possible to correspond to the same position (relative to the diffuser vanes) as the Boeing time-average static pressure taps. The exact locations are tabulated in Table V. The 200 series taps were for dynamic static pressure measurements; the 300 series locations were for dynamic total pressure probes. Figure 14 shows the dynamic static pressure tap locations in the region beyond the impeller tip. Seven of the original Boeing time-average static pressure taps can also be seen in one corner of this photo.

The dynamic total pressure probe and two of the plugs used to seal the wall are shown in Figure 15. O-rings, such as shown in this photo, fit in the plug grooves and seal the casing against gas leakage.

The inside diameter of the total pressure tube is 0.023", the outside diameter of the tube is 0.032", and the diameter of the total pressure hole in the tube is 0.013". A transducer was threaded inside the total pressure probe with the pressure sensing surface of the transducer located 0.002" from the end of the tube.

Speed of Sound

An accurate knowledge of the composition of the test gas is essential in any LSM-type modeling study. For this present

program, the required knowledge of the gas properties could have been obtained by either continual component chemical, spectrographic, etc., analysis of the gas composition or by continual measurement of the LSM gas speed of sound. Because the speed of sound of the LSM gas is the more fundamental measurement to make (since it is the parameter that enters the Mach number scaling directly), a device was constructed to measure the speed of sound of the LSM gas mixture.

This device, modeled after the work of El-Hakeem and others^{19,20,21}, is shown schematically in Figure 16. To make measurements, a batch of LSM gas was withdrawn from the LSM loop at various times during a test. This gas flowed through the speed-of-sound instrument driven by the pressure difference established during the test run between the entrance station (just upstream of the back pressure valve) and the exit station (the inlet plenum). When a fresh sample was desired, a sufficient quantity of gas was allowed to flow through the speed-of-sound instrument to assure a complete change of gas in the device. The flow through the instrument was stopped before a speed-of-sound measurement was made.

The driver mike was driven by a signal generator; the frequency of this signal was measured with a digital frequency counter. A movable terminator (piston) was located to set up a standing wave in the inner tube. The output of the pick-up mike was displayed on the vertical axis of an oscilloscope; the input to the driver mike was displayed on the horizontal axis of the oscilloscope. This resulted in a Lissajous pattern. The closing of this Lissajous pattern was used to determine the distance (as measured on the vernier) between half wavelength phase crossings as the terminator was translated.

The speed-of-sound instrument was checked (calibrated) with air, nitrogen, argon, and a certified analysis batch of LSM gas. The uncertainty in measurement of the speed of sound of the LSM gas is estimated to be 0.5%. This uncertainty includes the uncertainty in the position readout on the vernier as well as the uncertainty in the measurement of the driving frequency.

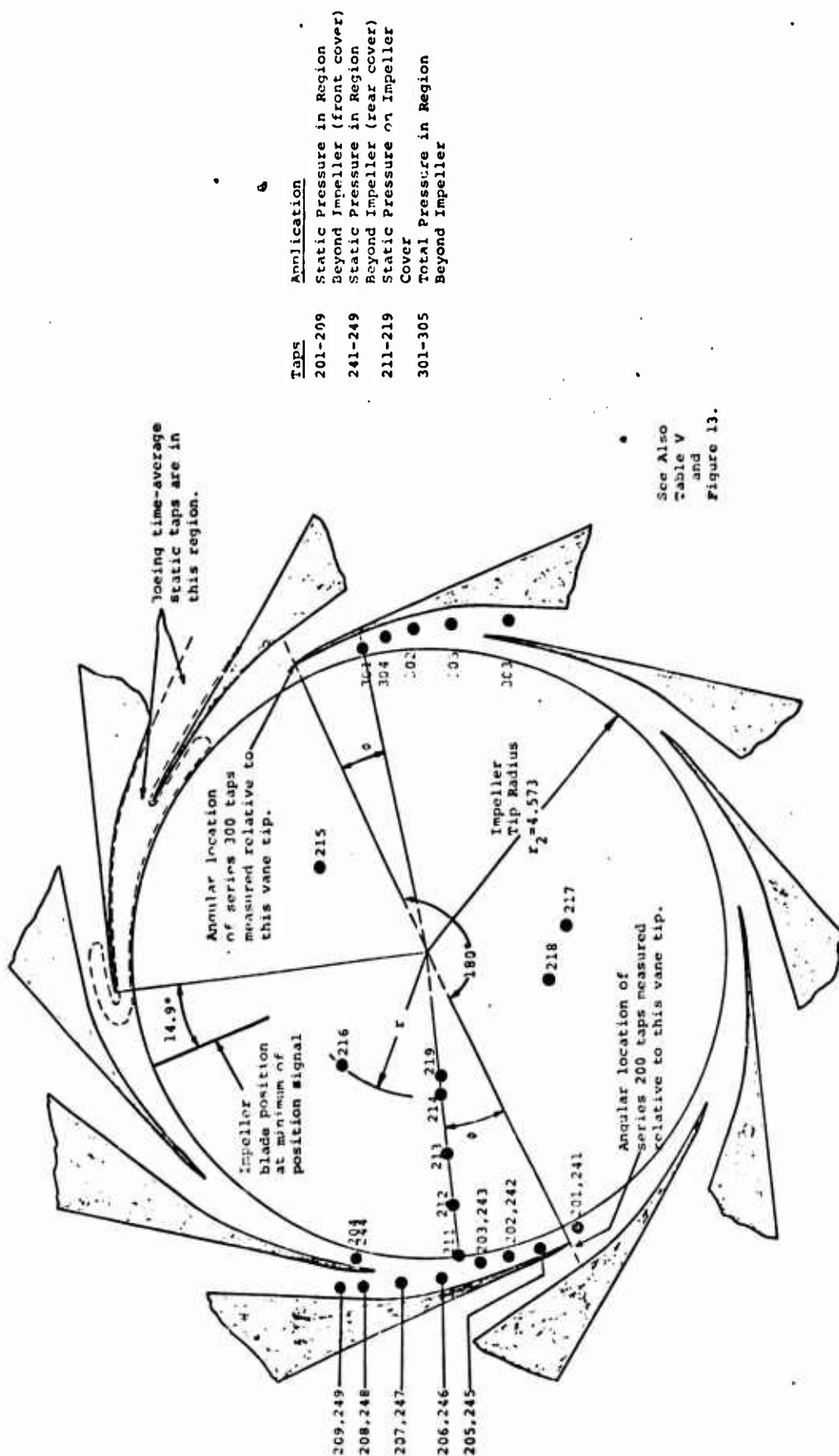


Figure 12. Locations of Pressure Taps for Dynamic Pressure Measurements.

A

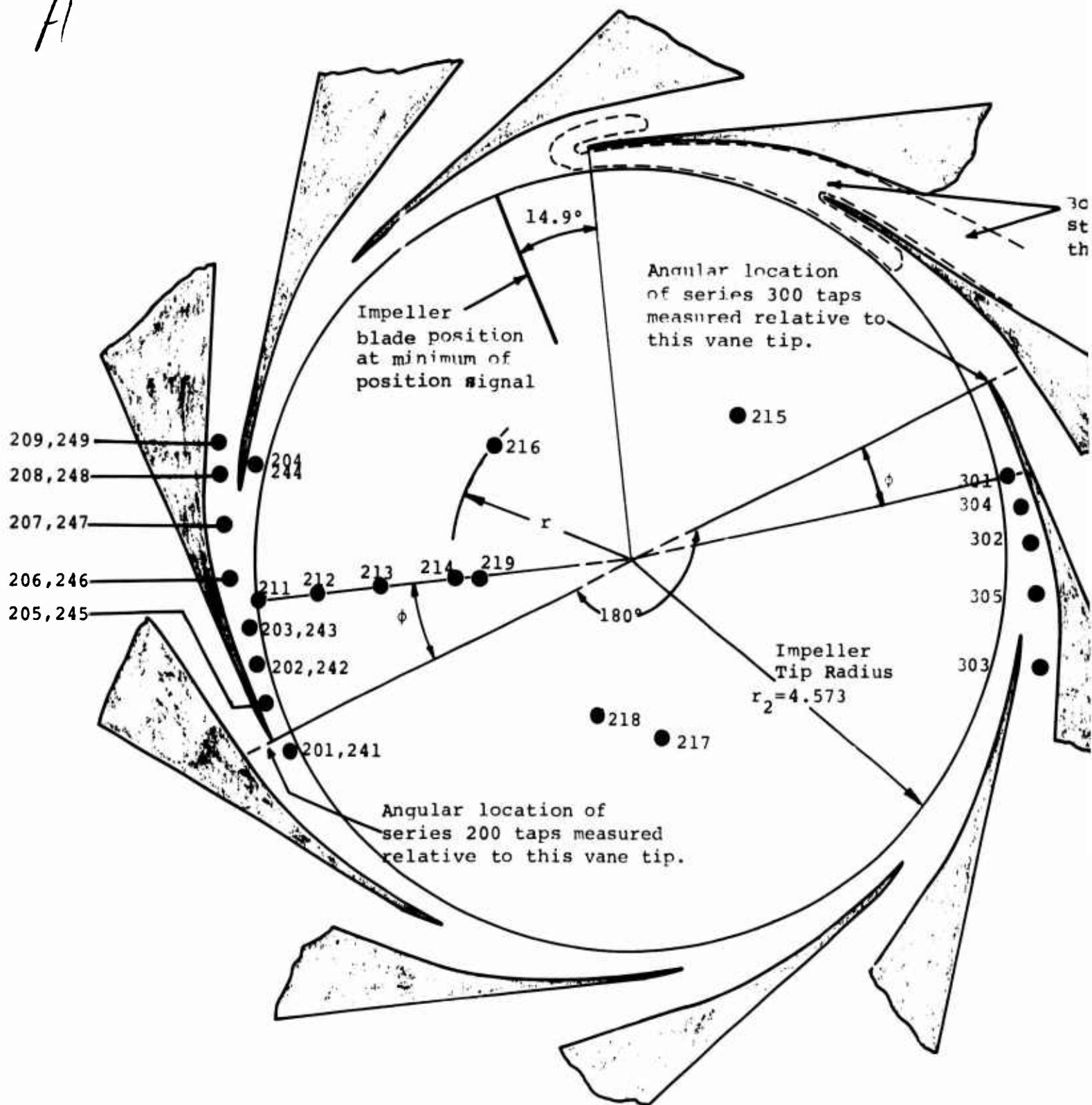
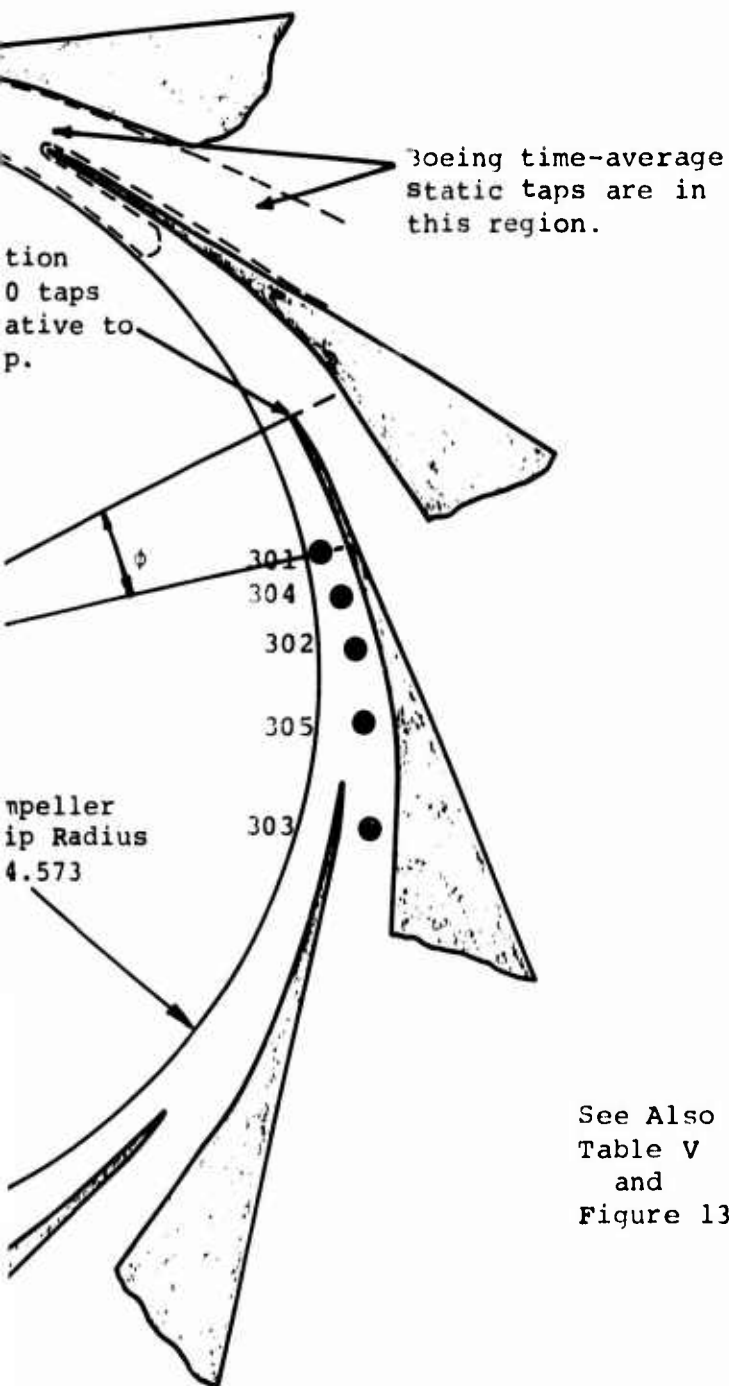


Figure 12. Locations of Pressure Taps for Dynamic Pressure Measurements.

B



| <u>Taps</u> | <u>Application</u> |
|-------------|---|
| 201-209 | Static Pressure in Region Beyond Impeller (front cover) |
| 241-249 | Static Pressure in Region Beyond Impeller (rear cover) |
| 211-219 | Static Pressure on Impeller Cover |
| 301-305 | Total Pressure in Region Beyond Impeller |

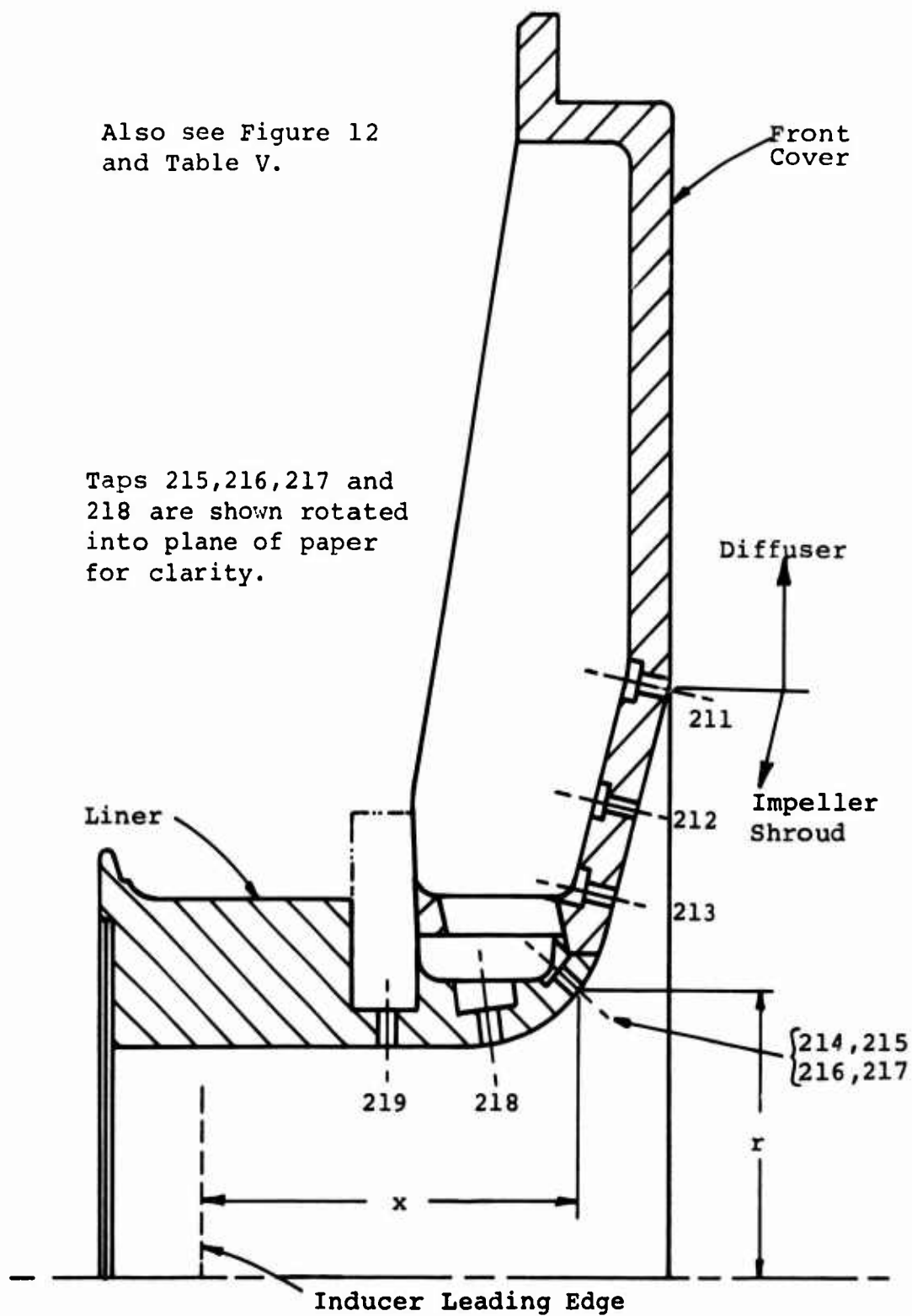


Figure 13. Location of Impeller Cover
Dynamic Static Pressure Taps.

TABLE V. LOCATIONS OF PRESSURE TAPS FOR DYNAMIC
PRESSURE MEASUREMENTS (REFERENCE FIGURES
12 AND 13)

| Tap Number | | ϕ (deg) | r/r_2 | x (in.) |
|------------|------|-----------------|---------|--------------|
| Front | Rear | | | |
| 201 | 241 | -2.72 | 1.028 | - |
| 202 | 242 | 10.6 | 1.028 | - |
| 203 | 243 | 16.07 | 1.028 | - |
| 204 | 244 | 39.4 | 1.028 | - |
| 205 | 245 | 4.72 | 1.061 | - |
| 206 | 246 | 23.2 | 1.069 | - |
| 207 | 247 | 30.5 | 1.089 | - |
| 208 | 248 | 37.0 | 1.115 | - |
| 209 | 249 | 40.75 | 1.137 | - |
| 211 | - | 19.5 | 0.997 | 3.78 |
| 212 | - | 19.5 | 0.831 | 3.58 |
| 213 | - | 19.5 | 0.658 | 3.37 |
| 214 | - | 19.5 | 0.464 | 2.92 |
| 215 | - | 153.67 | 0.464 | 2.92 |
| 216 | - | 63.75 | 0.464 | 2.92 |
| 217 | - | -75.82 | 0.464 | 2.92 |
| 218 | - | -52.0 | 0.402 | 2.32 |
| 219 | - | 19.5 | 0.40 | 1.51 |
| 301 | - | 13.5 | 1.028 | - |
| 302 | - | 23.2 | 1.069 | - |
| 303 | - | 40.0 | 1.135 | - |
| 304 | - | 18.37 | 1.058 | - |
| 305 | - | 30.5 | 1.089 | - |

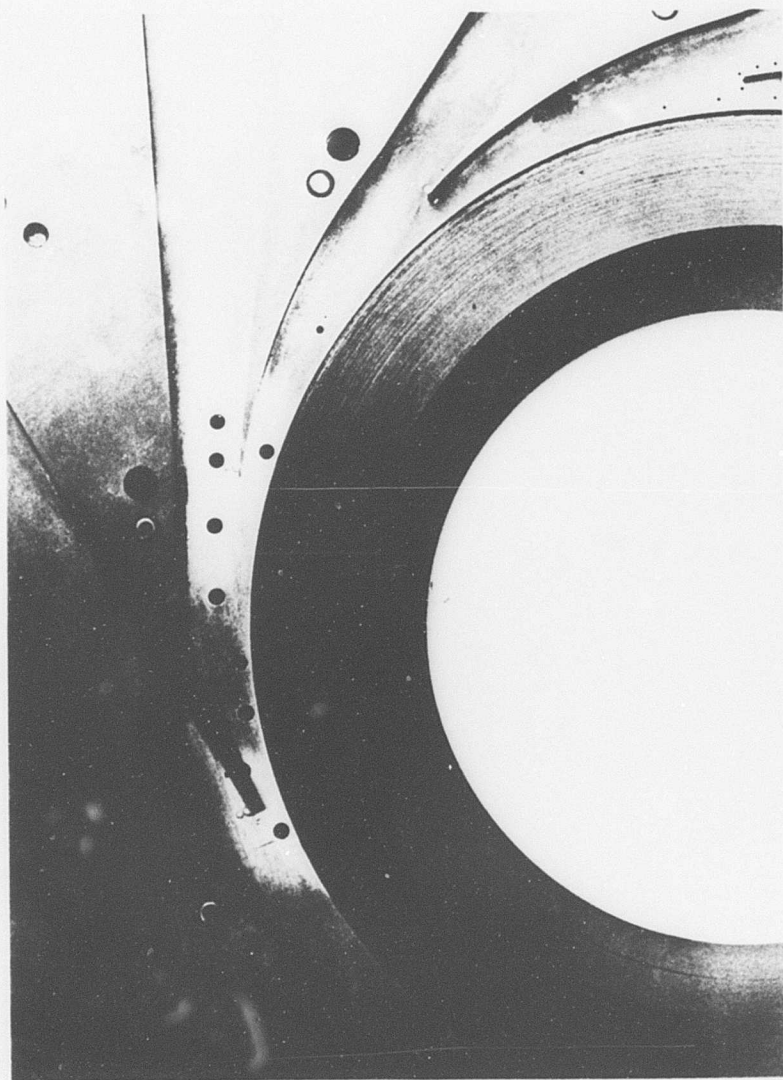


Figure 14. Dynamic Static Pressure Taps.

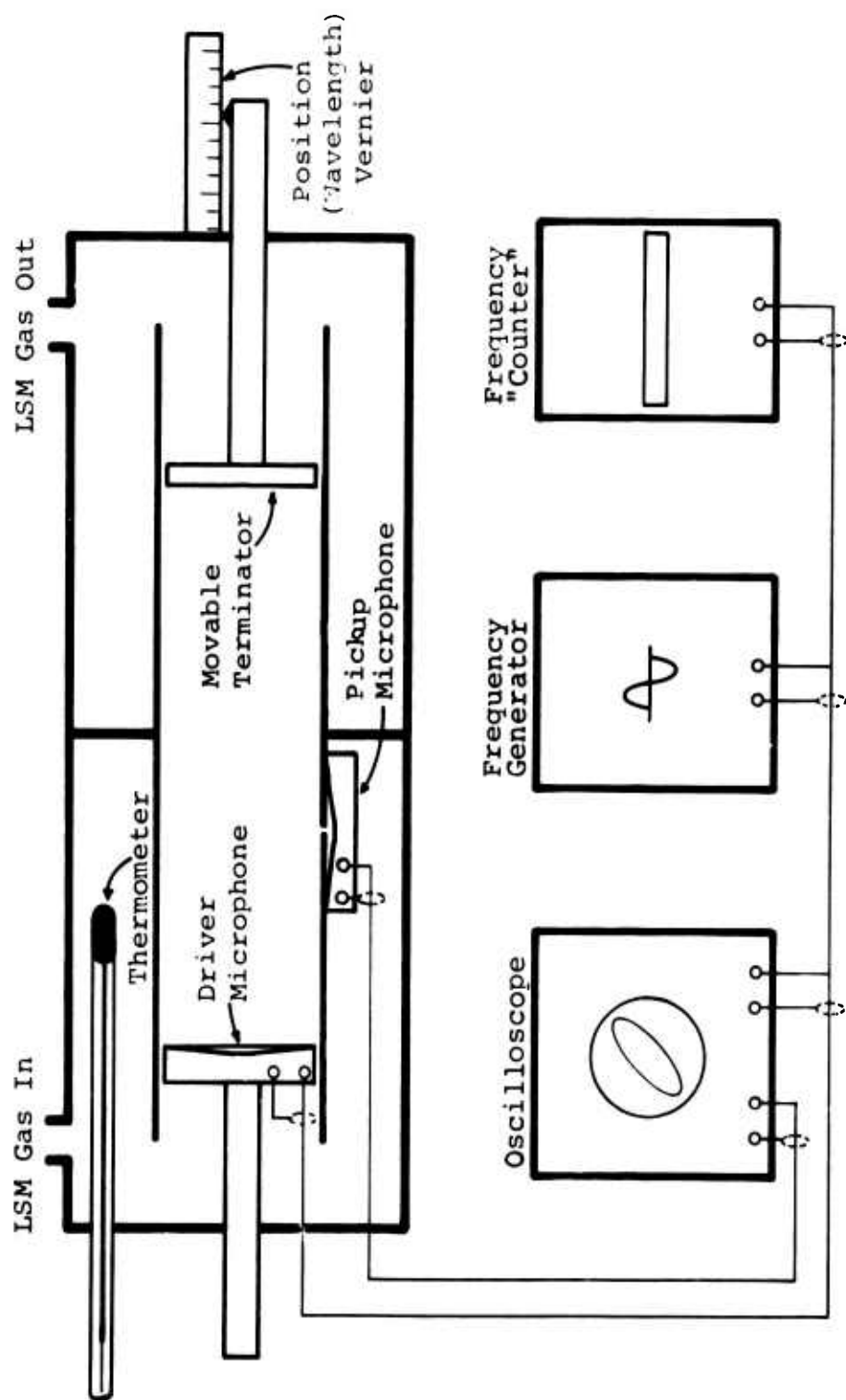


Figure 16. Schematic of the Speed-of-Sound Measuring Instrument.

In order to relate the speed of sound of the gas in the speed-of-sound instrument to the speed of sound of the gas at the plenum temperature, the temperature of the gas in the speed-of-sound instrument had to be measured. The uncertainty in this temperature measurement is estimated to be 0.2%.

Actual Compressor Speed

The compressor speed was sensed using a magnetic pickup which indicated the passage of six magnetic nuts located on the compressor "quill" shaft. This signal was fed into a frequency to voltage converter, and the output of this device was read on a millivolt meter. This system was calibrated with a frequency generator and calibrated frequency counter. It has also been checked using optical strobing of the compressor shaft. The uncertainty in this compressor speed measurement is estimated to be 0.2% in the speed range of interest.

Angular Position of the Impeller Blades

In order to analyze the dynamic pressure signals made with the miniature pressure transducers, it was important to know the relation between the instantaneous impeller blade position and transducer location. To this end, a system was devised whereby the angular position of the impeller is known at any instant in time relative to a reference point on the compressor rear cover. The position of each of the transducers is also known relative to this same fixed reference point. Thus the blade/pressure signal relationship could be determined for any time of interest.

The apparatus used to measure the blade position incorporated a special tapered magnetic pickup which was mounted to sense the presence of six steel bolts on the main drive shaft. One of the bolts was replaced by a stainless steel bolt (nonmagnetic) to which was fixed a 0.005" carbon steel slug. This odd bolt influenced the magnetic sensor differently than the others and produced an oscilloscope trace which was used to monitor the position of the impeller.

However, since the signal from the magnetic pickup was not a pure spike, this system required calibration to determine the precise relationship between a characteristic part of the magnetic pickup's signal and the instantaneous shaft

(and hence impeller) position.

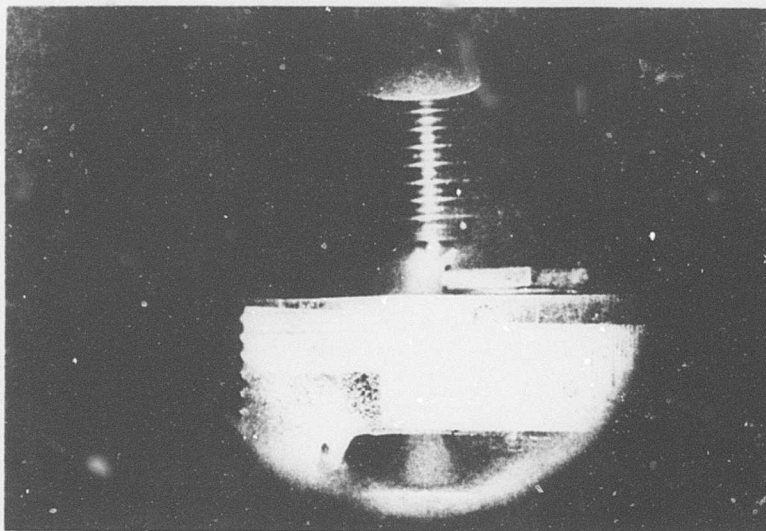
This calibration was performed by simultaneously photographing the bolt/pickup combination and an oscilloscope trace of the pickup signal which was triggered by the stroboscope flash. The stroboscope illuminated and "froze" the rotating shaft in the photograph. Thus the start of the oscilloscope trace corresponded to the instantaneous relative location of pickup and the shaft. Figure 17a shows the pickup and bolt head at the instant the trace of Figure 17b was initiated.

A series of 21 sets of these photographs was taken and used to obtain a precise correlation of the magnetic pickup output signal with the instantaneous position of the impeller blades. Based on this calibration data, the instantaneous angular position of any impeller blade with respect to the dynamic pressure transducer locations is known to within about $\pm 0.5^\circ$ of arc. This corresponds to an uncertainty of 0.043 inch at the impeller tip. This distance is a factor of 2 smaller than the diameter of the pressure transducers and about one and a half blade thicknesses.

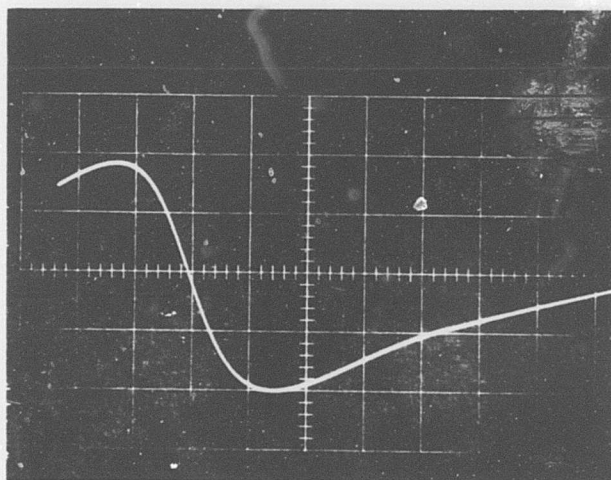
As shown on Figure 12, the minimum of the impeller angular position signal corresponds to an impeller blade instantaneous location 14.9° ahead of the top diffuser vane leading edge. The location of a blade relative to a transducer at any instant can be obtained using this reference location, the actual shaft speed, and the data of Table V when coupled with the trace contained in the oscilloscope data photograph of interest.

Impeller-to-Shroud Running Clearance

A portion of this program was devoted to determining the changes in compressor performance (principally efficiency) with varying running clearances between the impeller blades and the impeller shroud. An abradable sensor was constructed to determine the running clearance during each test. The length of this sensor was accurately measured prior to each test run. This sensor was then inserted so that the tip of the sensor just contacted the tip of the impeller blades when the impeller was stationary and at room temperature. Because of the design of the drive unit used, the axial position of the aft end of the compressor shaft



a. Position of bolt head relative to magnetic sensor at start of trace in photo below.



b. Signal from magnetic pickup induced by small slug on head of bolt shown in a.

Figure 17. Calibration of the Impeller Angular Position Indicating System.

TABLE VI. UNCERTAINTIES IN THE PRIMARY MEASUREMENTS

| Parameter, X | ΔX | $\Delta X/X$ |
|------------------------------|----------------------|--------------|
| Voltage | 0.01 mv | 0.03% |
| Plenum temperature | 2 °F | 0.44% |
| Collector temperature | 2 °F | 0.21% |
| Flowmeter temperature | 2 °F | 0.30% |
| Barometric pressure | 0.01"Hg | 0.03% |
| Mercury Manometer (16') | 0.06"Hg | - |
| Water Manometer (4') | 0.1"H ₂ O | - |
| Flowmeter pressure drop | 0.1"H ₂ O | 1.0% |
| + 25 psid transducer | 0.05 psia | - |
| 0-100 psid transducer | 0.08 psia | - |
| Plenum pressure | 0.05 psia | 0.5% |
| Collector pressure | 0.08 psia | 0.1% |
| Flowmeter pressure | 0.08 psia | 0.1% |
| Speed of sound | - | 0.5% |
| Speed-of-sound temperature | - | 0.2% |
| Actual compressor speed | - | 0.2% |
| Dynamic pressure fluctuation | - | 3.5% |

was predetermined and fixed relative to the shroud. The change in impeller position from stationary to running conditions was always in the direction of reducing the stationary clearance by rotational impeller deflection and (principally) by thermal growth of the compressor shaft. The length of the clearance probe after a test run, coupled with the measured static separation distance between the impeller and the shroud, allowed determination of the minimum running clearance. The uncertainty in this measurement was about 0.003".

Summary of the Uncertainties in the Primary Measurements

A summary of the uncertainties in the primary LSM measurements is presented in Table VI. The resulting uncertainties in the derived quantities are calculated in Appendix II and are summarized in Section 7.3.

7.2 DATA REDUCTION PROCEDURES

In this section we will briefly outline the data reduction procedures used and give a specific example of a typical LSM performance calculation.

The raw data taken during a run are fed into the data reduction program, and the primary conversions are performed. For example, thermocouple voltages and pressure transducer voltages are converted to temperature and pressure respectively. Next, the measured speed of sound of the LSM gas is used to calculate the percentage of air present during the test. This, when combined with the known pure fractions of Freon and argon, completely specifies the gas composition during any one test. From this, the thermodynamic and transport properties of the gas can be calculated at any desired temperature and pressure condition using the equations presented in Appendix I. The equations of Section 4.2 are then used to calculate and display the important compressor performance variables for each data set.

As an example of the type of manipulation that is performed in the data reduction program, consider the calculation of the stage isentropic efficiency. Referring to Figure 18, which shows an entropy/enthalpy diagram for a typical LSM compression from state 1 (plenum) to state 2 (collector),

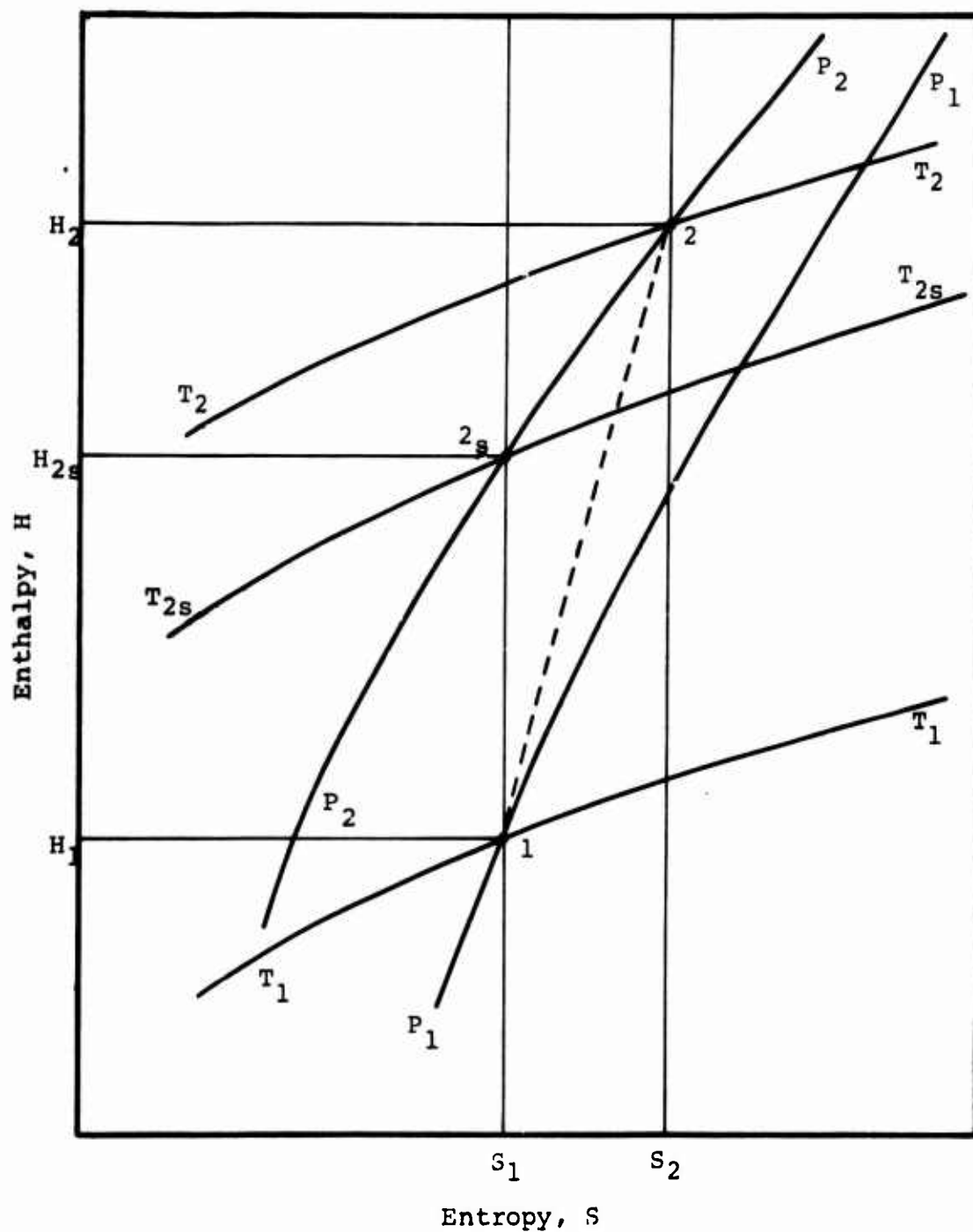


Figure 18. Typical LSM Compression From Plenum (State 1) to Collector (State 2) Conditions.

the following steps are performed by the data reduction program:

Step 1 - The measured speed of sound of the LSM gas is used to determine the precise composition of the mixture.

Step 2 - The collector and plenum pressure transducer readings, combined with the barometric pressure, are used to calculate the absolute pressure in the collector and plenum via the transducer calibration equation.

Step 3 - The collector and plenum thermocouple readings are converted to temperature via the voltage to temperature conversion formula. The collector and plenum temperatures are determined by averaging a number of readings at different positions in the collector and plenum.

Step 4 - The gas composition from Step 1, the pressures from Step 2, and the temperatures from Step 3 are used to calculate the plenum and collector LSM gas specific volume (the reciprocal of the density) via iteration of the state equations (contained in Appendix I).

Step 5 - The composition from Step 1, the temperatures from Step 3, and the specific volumes from Step 4 are used to determine the actual plenum and collector enthalpy and entropies via equations presented in Appendix I; i.e., state points 1 and 2 of Figure 18 are determined.

Step 6 - The actual enthalpy rise ($H_2 - H_1$) is then calculated by subtracting H_1 from H_2 as obtained in Step 5.

Step 7 - Using the composition from Step 1 and the collector pressure from Step 2, an iterative procedure is performed by "marching" down the collector pressure (P_2) line toward point 2S to be determined by this procedure. Point 2S is located when the entropy, calculated using T_2 (the iteration value of this procedure) and P_2 , equals the plenum entropy calculated in Step 5.

Step 8 - The value of T_{2S} (the isentropic collector temperature) is determined when $S_1 = S_2$. T_{2S} is then used

with the collector specific volume to calculate the isentropic collector enthalpy.

Step 9 - The isentropic collector enthalpy (H_{2S}) from Step 8 and the plenum enthalpy (H_1) from Step 5 are used to calculate the isentropic enthalpy rise ($H_{2S} - H_1$).

Step 10 - The ratio of the isentropic enthalpy rise ($H_{2S} - H_1$) from Step 9 and the actual enthalpy rise ($H_2 - H_1$) from Step 6 then gives the isentropic efficiency of this test point.

7.3 UNCERTAINTY ANALYSIS

The uncertainties in the primary quantities were estimated and discussed in Section 7.1 and summarized in Table VI. The level of uncertainty in the derived quantities is calculated by the analysis procedures contained in Appendix II. In this section, we present a brief summary of the analysis and results of Appendix II.

Following Kline and McClintock²², all estimated uncertainties are quoted at a 20:1 odds interval. If these errors are randomly distributed, this uncertainty interval is equal to twice the standard deviation.*

The estimated level of uncertainty in the derived quantities** (calculated and discussed in Appendix II) is summarized in the second column of Table VII. The third column of Table VII shows, for comparison, the uncertainties that would have resulted if the same instrumentation (as was used for LSM) was used with air. These are not Boeing's air uncertainty levels; they are calculated levels, tabulated to show how LSM testing affects the data uncertainties.

* Kline and McClintock have shown that this same criterion is applicable when the form of the distribution of errors is not known.

** The LSM gas property uncertainties are found in Appendix I based on References 11-16 and 23-28.

TABLE VII. UNCERTAINTY IN THE DERIVED QUANTITIES

| Parameter, X | $\Delta X/X$ With LSM | $\Delta X/X$ With Air and Identical Instrumentation |
|--|--------------------------|--|
| Speed of sound at measurement location | 0.5% | - |
| Speed of sound in plenum | 0.55% | - |
| Actual compressor speed | 0.2% | 0.2% |
| Air-equivalent compressor speed | 0.6% | 0.3% |
| Stage pressure ratio | 0.5% | 0.5% |
| Actual mass flow rate | 0.85% | 0.80% |
| Air-equivalent mass flow rate | 1.0% | 1.0% |
| Stage isentropic efficiency | 1.2% | 0.95% |

Perhaps the most important result of the uncertainty analysis of Appendix II is this comparison of the LSM uncertainty with the uncertainties that would have resulted had the test been performed in air with precisely the same instrumentation as used for the LSM testing. As shown in Table VII, the use of LSM gas results in an uncertainty level in the pressure ratio and air-equivalent mass flow rate no larger than would have resulted from an air test with identical instrumentation. Furthermore, had the Creare tests been performed with air using the same instrumentation as used for LSM, the uncertainties in the air-equivalent compressor speed and the stage isentropic efficiency for air would have been only slightly smaller than were experienced with LSM (0.3% vs. 0.6% and 0.95% vs. 1.2% respectively).

In analyzing the modeling correlation data to be presented in Section 8.0, the reader should recognize that the comparison between the Boeing-obtained air data and Creare-obtained LSM data must be made with a full appreciation that uncertainties in the LSM parameters as contained in Table VII, together with uncertainties in the basic air data contained in Table I, must be considered.

Comparing Tables I and VII reveals that the level of uncertainty in the Boeing air results was about the same as the uncertainty in the Creare LSM results.

8.0 MODELING CORRELATION - TEST RESULTS

8.1 TEST SCHEME

The objective of the modeling correlation/feasibility demonstration portion of this program was to "obtain a correlation of low-speed-of-sound modeling performance data with known air performance data of the RF-2 compressor stage". The original project work statement called for using an LSM gas that had "a specific heat ratio k at the inducer inlet conditions equivalent to RF-2 inlet conditions in air". Tests were also to be conducted with a gas which had an inlet specific heat ratio of about 1.3 (compared with 1.4 of air) in order to determine the effect of specific heat ratio on the modeling.

In addition to the obvious measurements required to obtain the compressor map, the contract called for measurements of the static pressure distribution along the inducer and impeller cover and in the vaneless, semivaneless, and channel diffuser regions on the front and rear covers. These were to be taken at the same locations as the Boeing air data. The purpose of these measurements was to demonstrate that testing with a low-speed-of-sound gas accurately replicated the fluid dynamics of the compressor as reflected by static pressure distributions.

When the first sets of LSM data showed replication of the Boeing air results except for a 1 to 2% deficiency in efficiency, several additional tests were added to the work statement to explore the effect of certain variables on the compressor map data principally on the stage efficiency. These variables were:

- 1) Impeller blade to impeller shroud running clearance
- 2) Inlet specific heat ratio (to be set at the stage average value)
- 3) Compressor insulation to reduce heat transfer from the compressor.

In addition, the statement of work specified that "if correlation is obtained between testing in the low-speed-of-sound modeling fluid and the original RF-2 aerodynamic

data as reported in USAAVLABS Technical Report 67-47, the model shall then be probed, utilizing high response, dynamic instrumentation to obtain detailed aerodynamic data and thus substantiate practicality of utilizing low-speed-of-sound modeling as a tool for the research and development of advanced high pressure ratio, high-speed, centrifugal compressors." The details of this dynamic instrumentation program and the results obtained are discussed in Section 9.

Four of the Boeing tests (as reported in Reference 6) were selected as the air test conditions to be duplicated in the LSM test program. The contract called for demonstrating the feasibility of LSM testing by showing duplication of Boeing's air results obtained at a referred speed of around 50,000 rpm. Figure 19, taken from Reference 6, shows a portion of the air data obtained by Boeing with the RF-2 impeller and the V2-2 diffuser combination. It was the goal of the LSM modeling program to replicate the 50,000-rpm Boeing air data shown. The upper right-hand portion of Figure 19 (as indicated) will be expanded and utilized for plotting all LSM data.

All LSM results presented in this section are "air-equivalent" results, i.e., LSM data scaled according to the scheme presented in Section 4.0.

Table VIII summarizes the test conditions used during the LSM modeling program. Test "BOE" shows the conditions for the original Boeing air data. Test 71-1 was the original LSM test condition to verify the correctness of LSM modeling. Test 71-2 was performed to investigate the effect of significantly decreased inlet specific heat ratio on the modeling. (Testing with a low inlet specific heat ratio would be quite attractive if the results could be easily scaled since the lower the inlet specific heat ratio, the higher the gas molecular weight and hence the lower the required rotational speed and impeller stresses.)

Tests 72-1 and 72-4 were performed to investigate the effect of impeller-to-shroud running separation distance. The purpose of Test 72-2 was to investigate the effect of compressor insulation. Test 72-3 was conducted to investigate the effect of using an LSM gas whose stage-average specific heat ratio duplicated the stage-average specific heat ratio of air. Test 72-5 shows the conditions for all of the

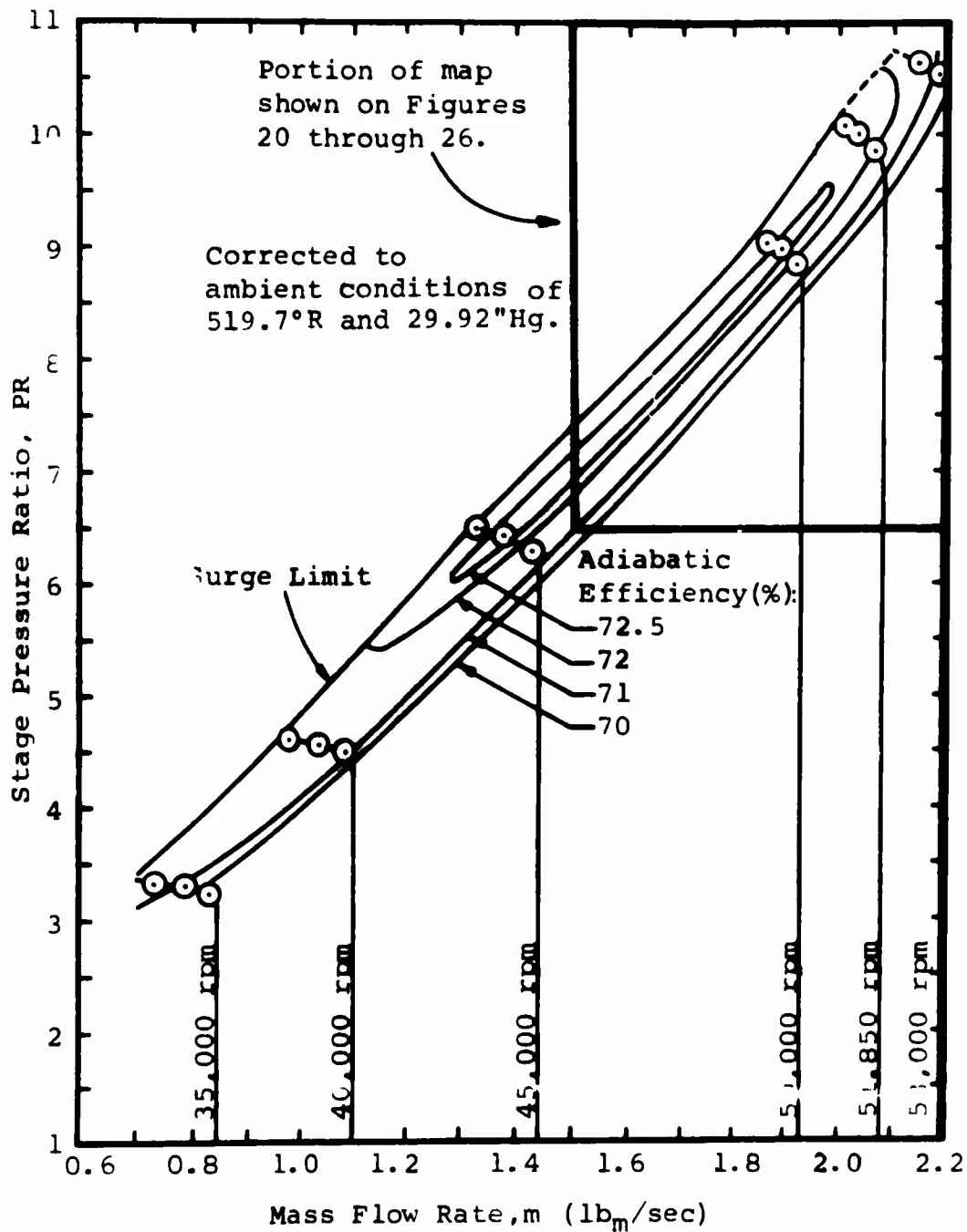


Figure 19. Compressor Map - Boeing's Air Data With RF-2 Impeller and V2-2 Diffuser.

TABLE VIII. SUMMARY OF LSM TEST CONDITIONS

| Test | Volume Fraction of CBrF_3 in Argon | Inlet Specific Heat Ratio | Impeller-to- Shroud Running Separation | Compressor Insulation |
|--|--|------------------------------------|---|--------------------------|
| BOE* | Air | 1.4 | 0.009" | No |
| 71-1 | 0.196 | 1.4 | ** | No |
| 71-2 | 0.32 | 1.32 | ** | No |
| 72-1 | 0.196 | 1.4 | 0.005-0.010" | No |
| 72-2 | 0.196 | 1.4 | 0.005-0.010" | Yes |
| 72-3 | 0.13 | 1.45 | 0.005-0.010" | No |
| 72-4 | 0.196 | 1.4 | 0.020-0.025" | No |
| 72-5 | 0.196 | 1.4 | 0.020-0.025" | No |
| <p>*"BOE" refers to original Boeing air data from Boeing tests 3369, 3369A, 3369B, and 3370A (Reference 19)</p> <p>**The running impeller clearance was not measured for these tests; however, it is believed to be 0.020" - 0.030".</p> | | | | |

dynamic pressure measurements reported in Section 9.

Time-averaged static pressure measurements throughout the compressor were obtained at various test conditions as specified in the contract work statement.

8.2 SUMMARY OF THE MODELING CORRELATION RESULTS

The principal results of the modeling correlation portion of this program are listed below. Additional discussion is provided in Section 8.3 where the data are presented.

1) Modeling air data at a reduced shaft speed using a low-speed-of-sound gas reproduces very well the air compressor map (including efficiency) and the air static pressure distributions through the compressor when all of the important dimensionless variables are accurately modeled.

2) The inlet specific heat ratio of air must be matched to obtain readily scaled results based on the simple inlet scaling scheme developed and used here.

3) Using the inlet scaling scheme, a gas mixture of lower-than-air inlet specific heat ratio results in a higher-than-air referred mass flow rate and a smaller-than-air range from choke to surge, a mixture of higher-than-air inlet specific heat ratio gas results in a lower-than-air referred mass flow rate, and a larger-than-air flow range from choke to surge. Furthermore, it is not obvious that any more complex scaling scheme will be able to correlate LSM data well when the inlet specific heat ratio is not correctly modeled.

4) The air mass flow rate at choke is modeled well with a " $k = 1.4$ " LSM gas mixture but not with an LSM gas mixture that does not replicate the inlet ratio of specific heats of air.

5) The stage pressure ratio data of air are very well replicated with LSM independent of the inlet specific heat ratio of the LSM gas mixture in the range tested ($k = 1.32 - 1.45$).

6) The air stage efficiency is well replicated with LSM when the air conditions of impeller running clearance and compressor insulation (or lack of it) are replicated.

7) The stage efficiency is independent of the inlet specific heat ratio over the range tested (but gas composition must be accurately known to accurately calculate efficiency).

8) The stage efficiency decreased with an increase in running clearance between the impeller and the shroud in the range of clearance tested.

9) The measured stage efficiency decreased significantly when heat losses from the test gas to the environment were reduced. Only when the compressor is well insulated does the measured efficiency approach the true adiabatic (or isentropic) efficiency.

10) The internal fluid dynamics of the compressor, as reflected by the static pressure distribution throughout the stage, are well replicated with proper LSM testing.

This program has demonstrated both the feasibility and correctness of low-speed modeling of high-pressure-ratio centrifugal compressors.

8.3 TEST RESULTS

Compressor Map

LSM test results are shown superimposed over the Boeing air data on Figures 20 through 26. On these figures the pressure ratio is the ratio of the collector static to the plenum total pressure for LSM or air. The mass flow rate for air is the mass flow referred to inlet conditions of 519.7°R and 29.92"Hg using Equation 14. The mass flow rate for LSM was scaled based on inlet conditions as discussed in Section 4.2 according to Equation 8. The lines of constant adiabatic efficiency are those of Boeing, as is the surge limit line. The compressor speed indicated for air is the compressor speed referred to 519.7°R inlet conditions by Equation 11; the compressor speed for LSM is the scaled speed based on Equation 1.

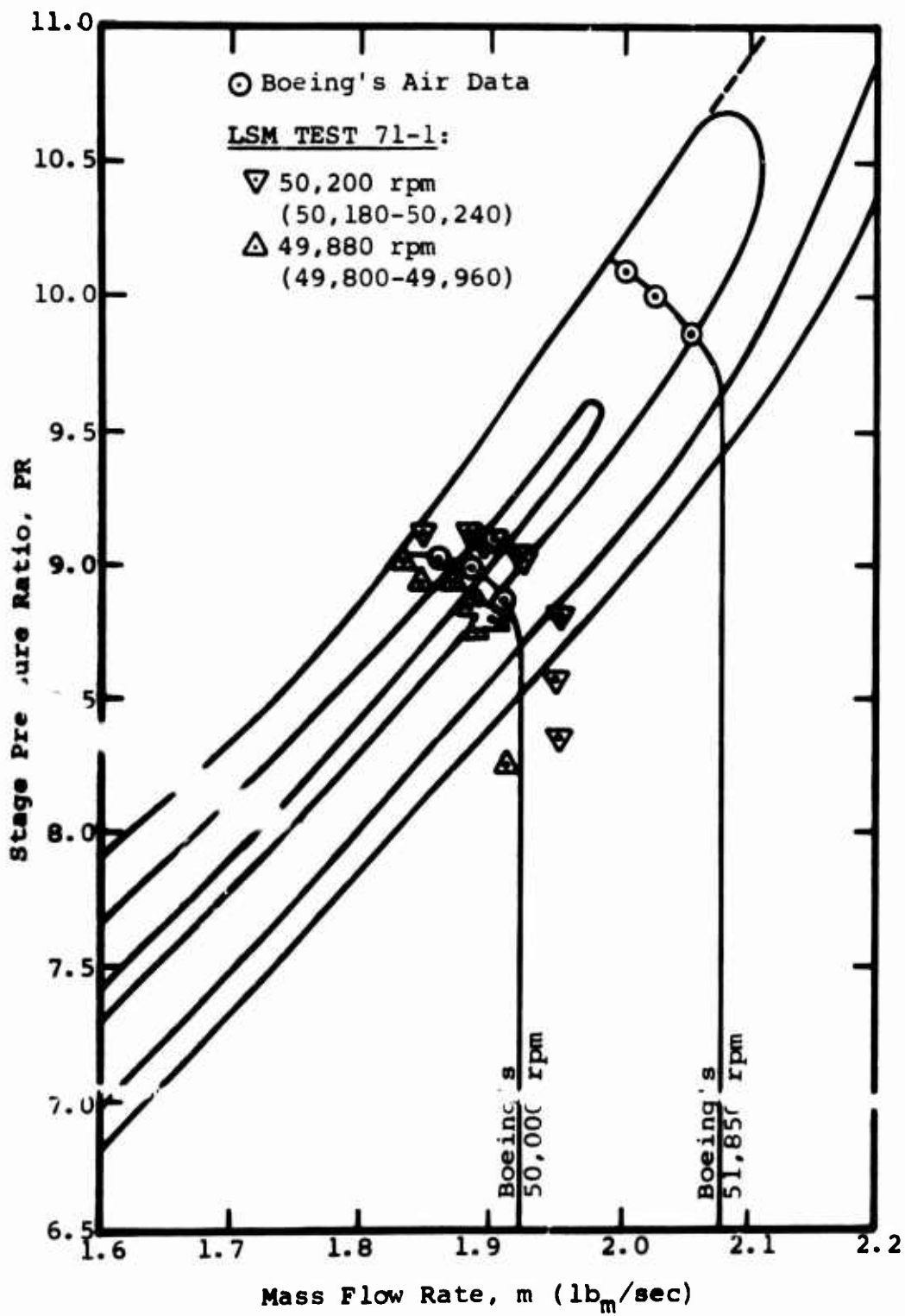


Figure 20. Compressor Map - LSM Test 71-1
 With " $k=1.4$ " Inlet Gas.

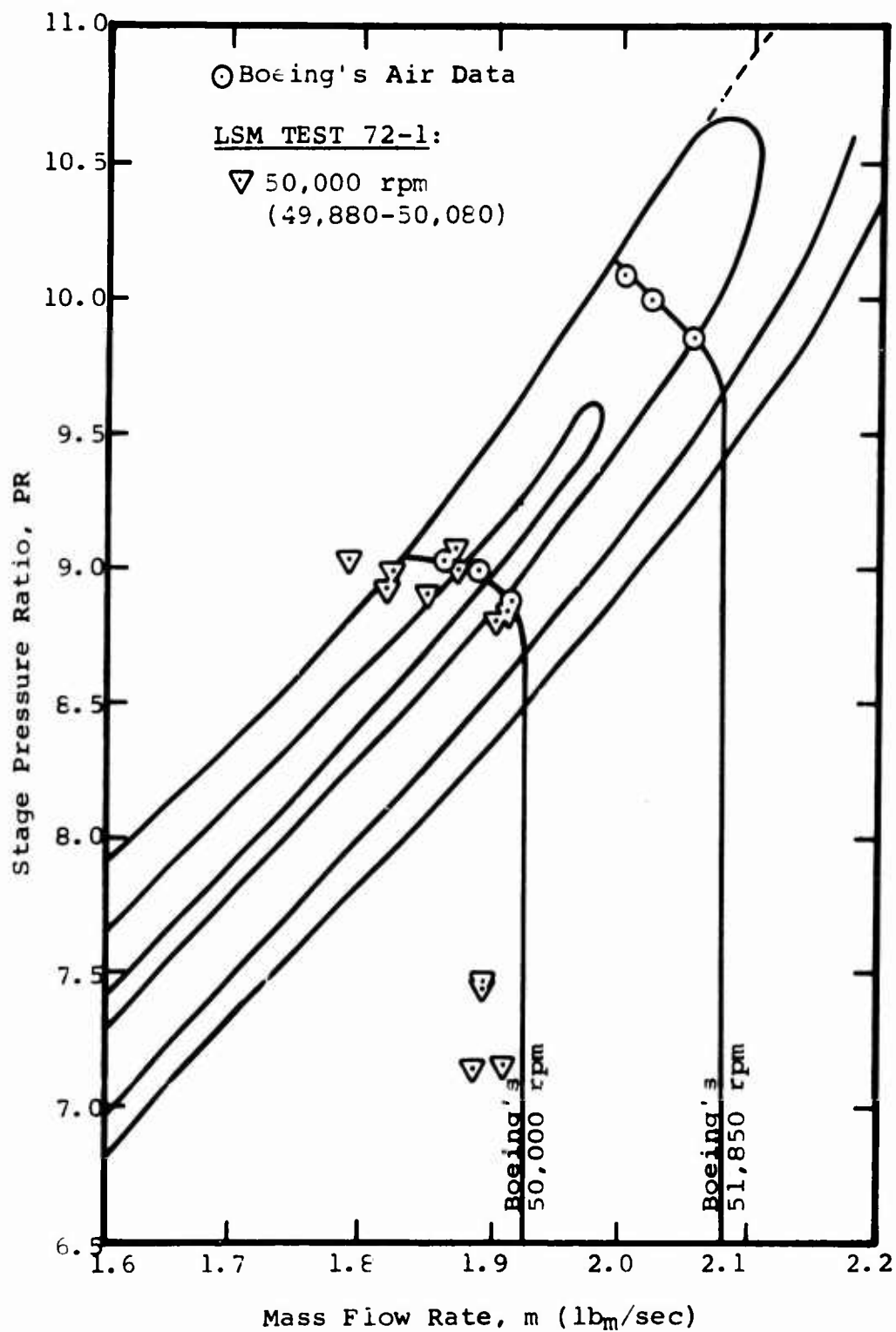


Figure 21. Compressor Map - LSM Test 72-1 With "k=1.4" Inlet Gas and Small Clearance.

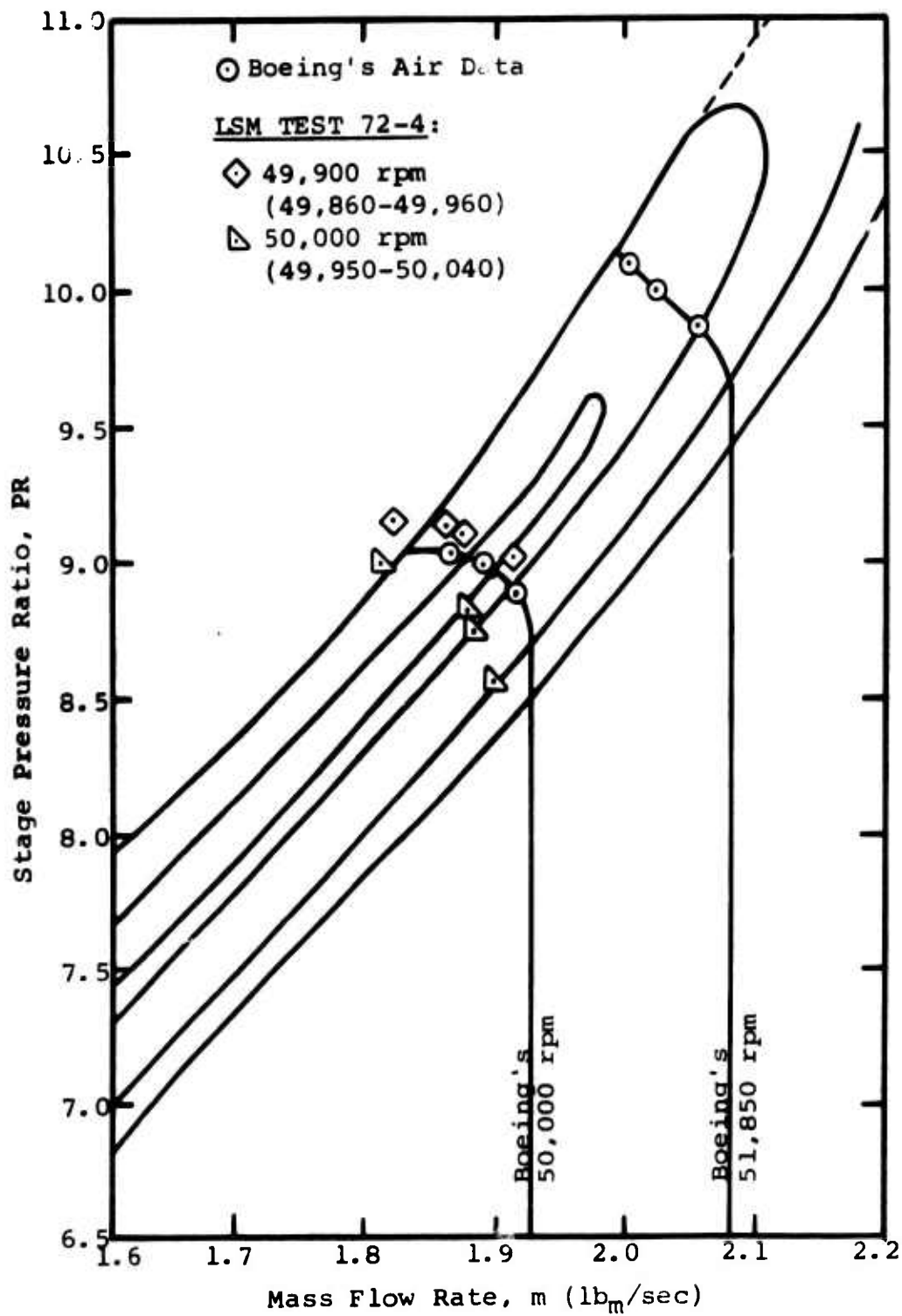


Figure 22. Compressor Map - LSM Test 72-4 With " $\lambda=1.4$ " Inlet Gas and Large Clearance.

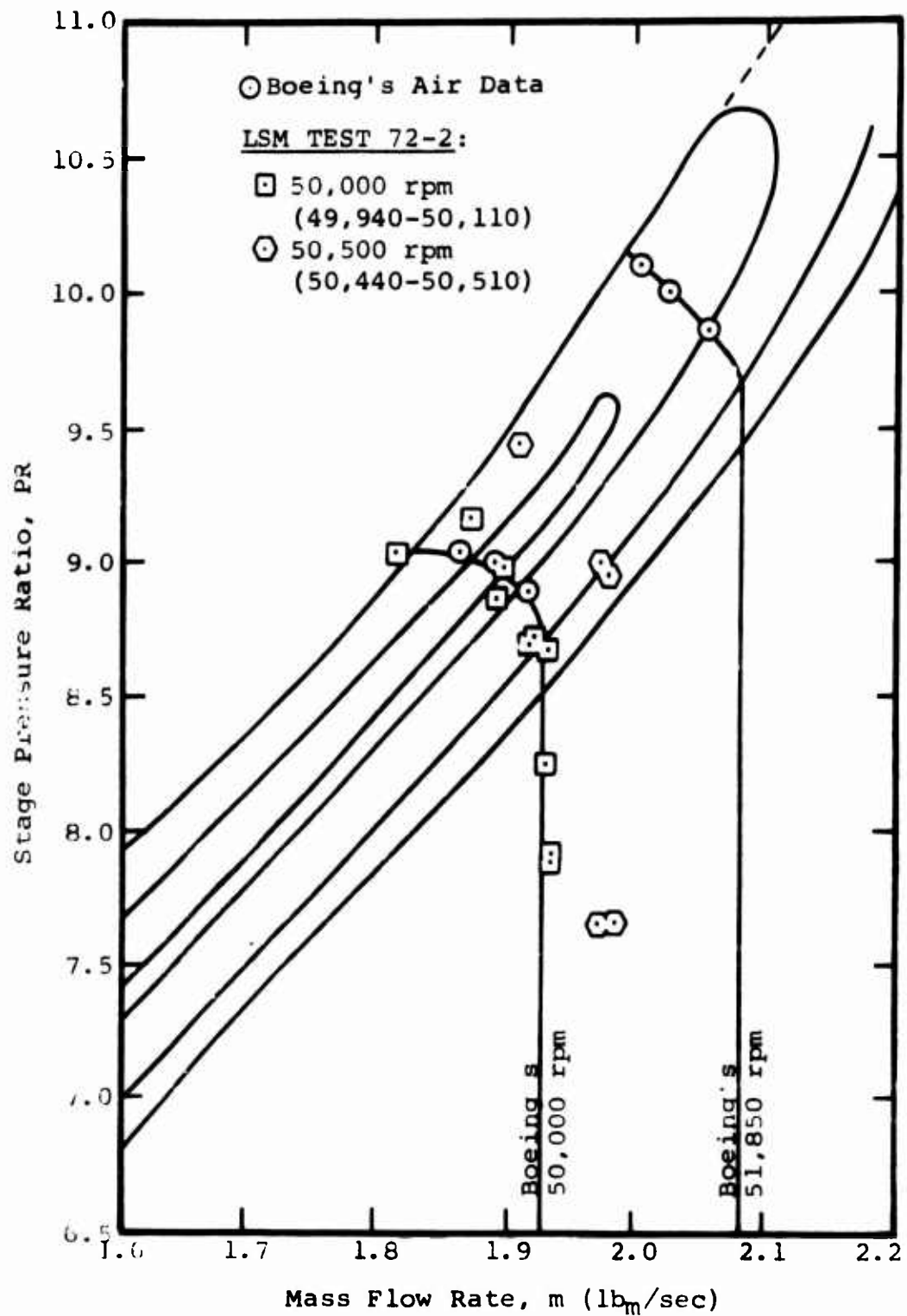


Figure 23. Compressor Map - LSM Test 72-2 With Insulated Compressor and Small Clearance.

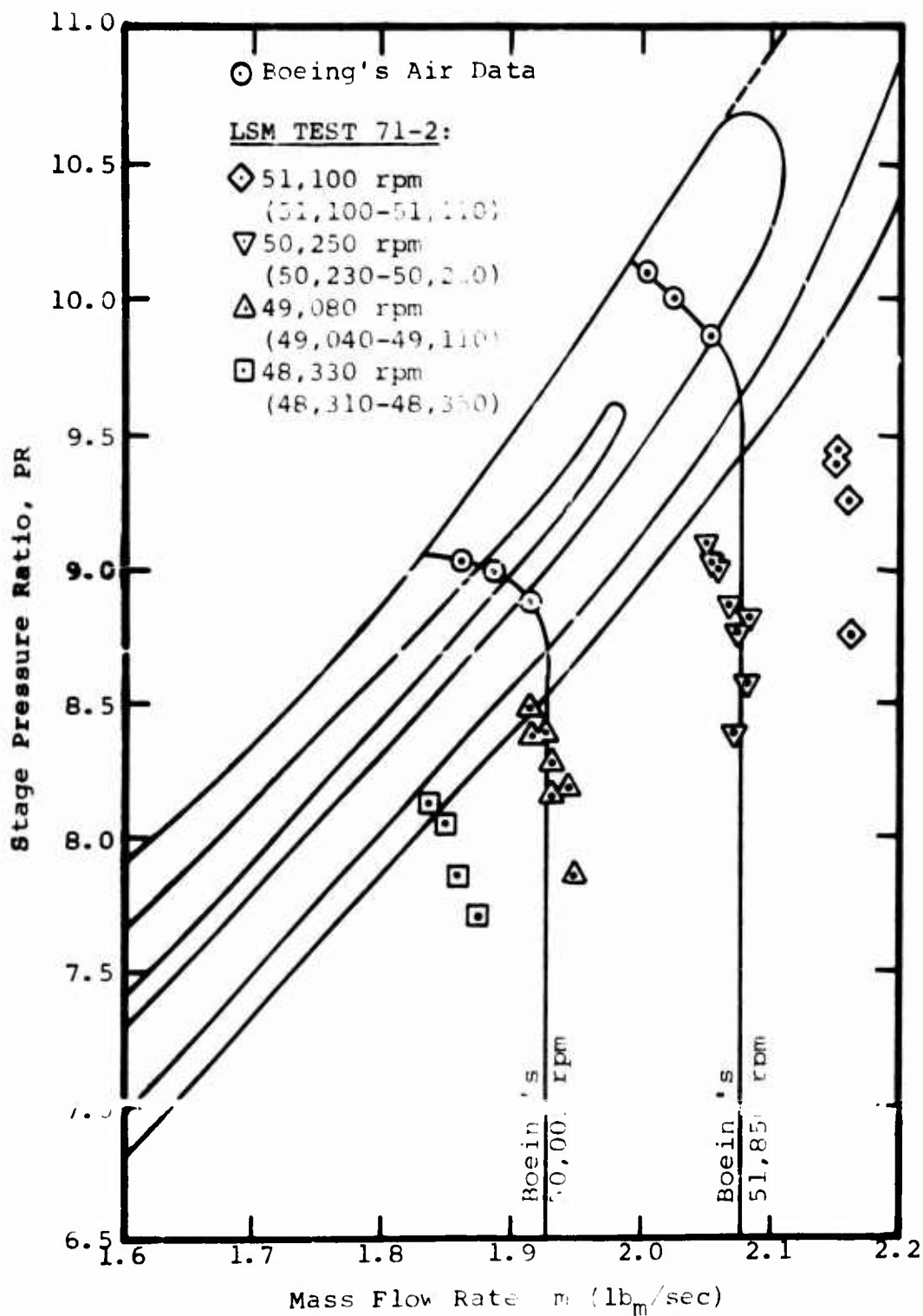


Figure 24. Compressor Map - LSM Test 71-2
With "k=1.32" Inlet Gas.

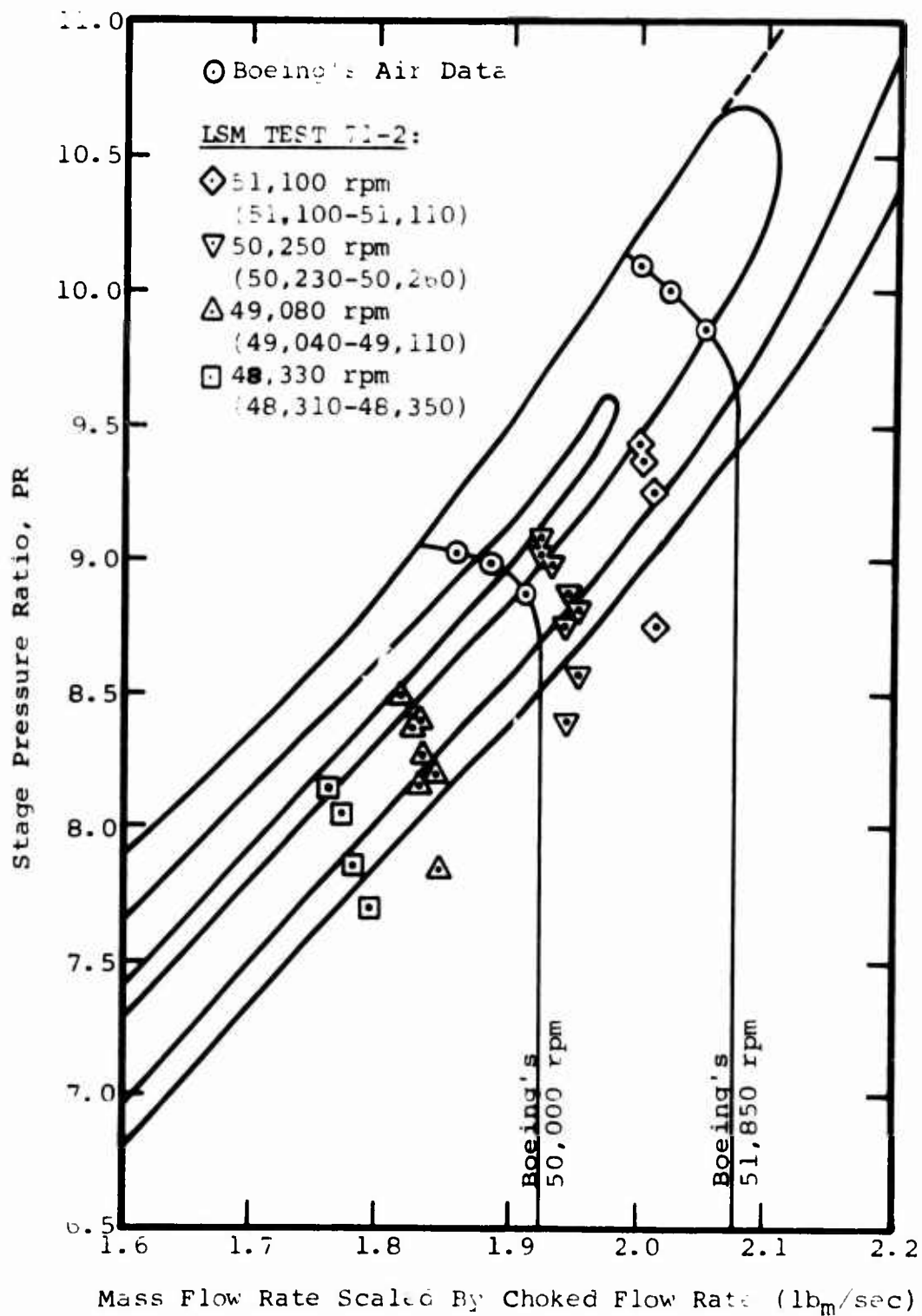


Figure 25. Compressor Map - LSM Test 71-2 With "k=1.32" Inlet Gas and With Flow Rate Scaled by the Air Choked Flow Rate.

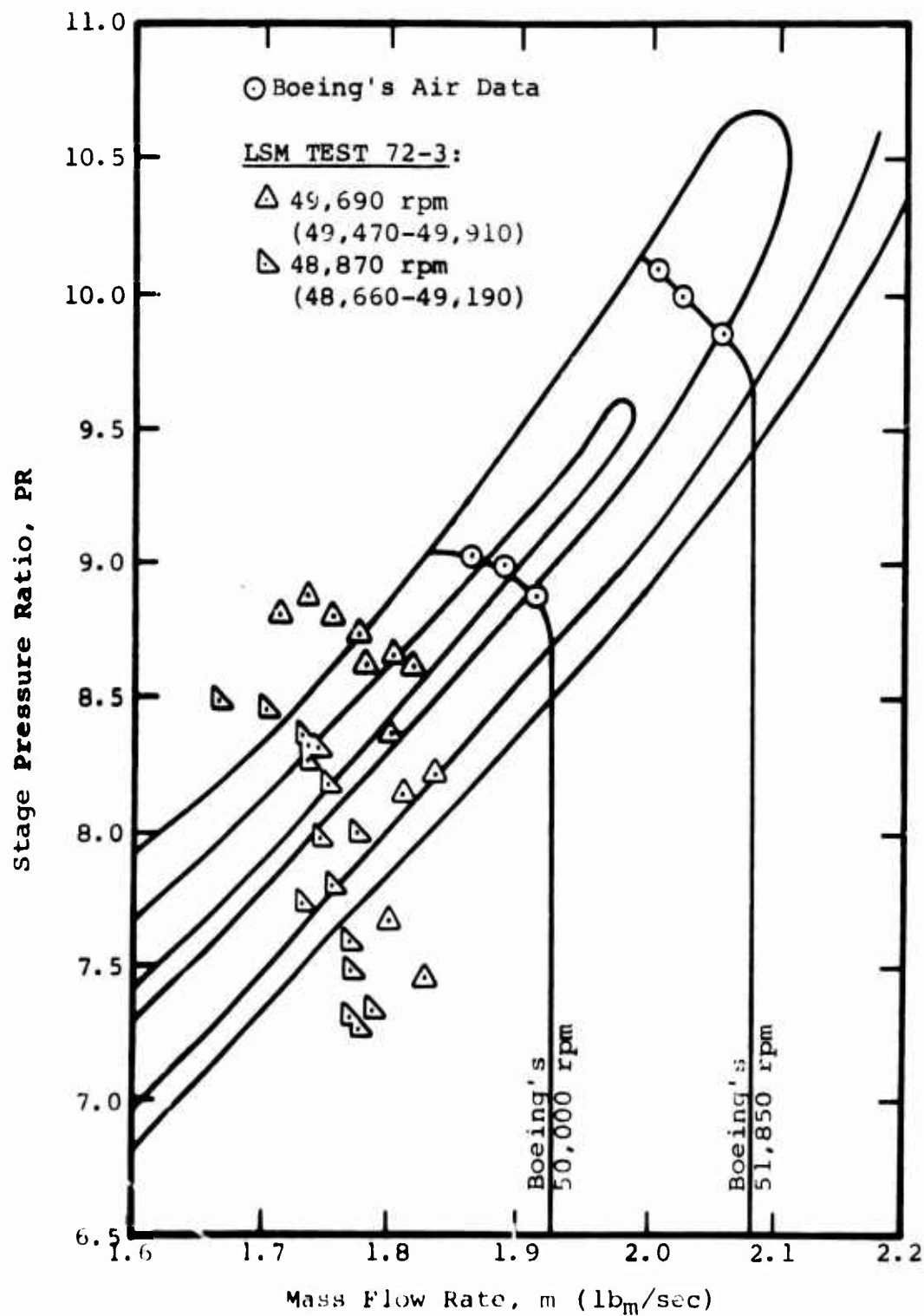


Figure 26. Compressor Map - LSM Test 72-3
 With " $k=1.45$ " Inlet Gas.

Figures 20 through 26 are expanded-scale plots. Analysis of the data on these figures must be done with full appreciation of the combined uncertainty bands for the LSM and the air data. These uncertainty bands are summarized in Tables I and VII. The principal air uncertainties affecting the compressor map data are flow rate ($> 1\%$) and the "label" of the speed lines (estimated at 0.2%); the principal LSM uncertainties affecting the compressor map data are the flow rate (1.0%) and the "label" of the speed lines (0.6%).

Figure 20 shows the results of LSM test 71-1 at two speeds close to 50,000 rpm. Notice that the LSM data fall in the correct location for their respective "air-equivalent" speed. These data, obtained with an LSM gas mixture with an inlet specific heat ratio equal to that of air, demonstrate the physical correctness and feasibility of low-speed-of-sound modeling when the inlet specific heat ratio of air is duplicated.

Figures 21, 22, and 23 show that the compressor map pressure ratio/flow rate data are unaffected by changes in the impeller-to-shroud running clearance or by insulating the compressor. (As will be discussed below, this statement does not apply to the stage efficiency.) Figure 21, showing the results from test condition 72-1 at a small impeller-to-shroud running clearance, should be compared with Figure 22 showing test condition 72-4 at a large impeller-to-shroud running clearance. The data of Figure 23 show the results from test condition 72-2 and demonstrate that insulating the compressor does not affect the basic compressor map. (Again we exclude efficiency from this statement.)

Figure 24 (test condition 71-2) shows that when an LSM gas which has an inlet specific heat ratio of about 1.3 is used, the results do not accurately model the air data. The data shown in Figure 24 is replotted in Figure 25, where the mass flow rate is somewhat arbitrarily corrected by the choked mass flow rate for air at each speed. Examination of Figures 24 and 25 leads one to conclude that testing with an LSM gas mixture which possesses a lower-than-air inlet specific heat ratio:

- 1) Results in an inlet-scaled mass flow rate which is too high compared to the air mass flow rate,

- 2) Results in a reduced range between choke and surge, but
- 3) Does result in approximately the right stage pressure ratio at each speed.

Figure 26 shows the data obtained with an LSM gas mixture which had a higher-than-air inlet specific heat ratio. This gas (test condition 72-3) very closely matches the air stage-averaged specific heat ratio with the LSM stage-averaged specific heat ratio. Although these results are at a slightly lower than 50,000 rpm equivalent speed, it is clear that testing with an inlet specific heat ratio higher than air ($k_{inlet} = 1.45$) results in an inlet scaled mass flow rate which is slightly too low. These conclusions are displayed more clearly on plots to be presented shortly.

In summary, these data demonstrate the physical correctness and feasibility of low-speed-of-sound modeling when the inlet specific heat ratio of air is duplicated. Furthermore, they show that duplication of the inlet specific heat ratio is important in obtaining accurate modeling of high-pressure-ratio centrifugal compressors.

Pressure Ratio Between Surge and "Knee" Vs. Speed

During one " $k = 1.4$ " LSM test (72-1), data were obtained over a wide speed range. These test data, plotted in Figure 27, show that the test results with LSM gas replicate very well the air pressure ratio between the "knee" of a speed line and surge for that speed line. The solid lines of Figure 27 represent the variation with speed in surge pressure ratio and pressure ratio at the "knee" of the air compressor maps of Boeing. The data points of this figure are the LSM pressure ratio vs. speed data points for all LSM data of this test which fall between the surge line and the "knee" of the compressor map with LSM. Agreement is excellent.

A similar plot was constructed using LSM data from various test conditions over a smaller speed range around 50,000 rpm. Figure 28 shows these data. The replication of the air pressure ratio between the "knee" point of a speed

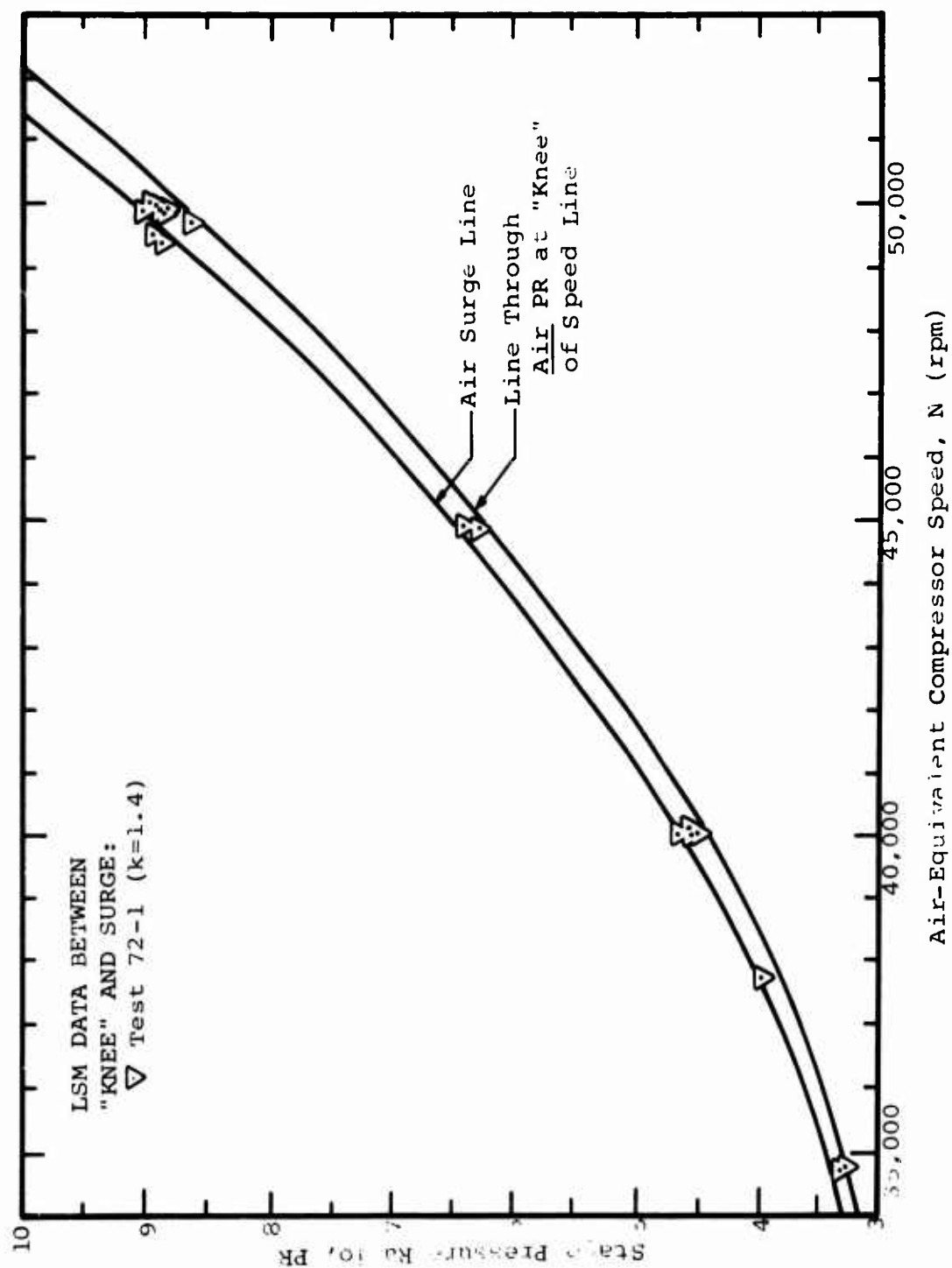


Figure 27. Stage Pressure Ratio for LSM Data Between "Knee" and Surge.

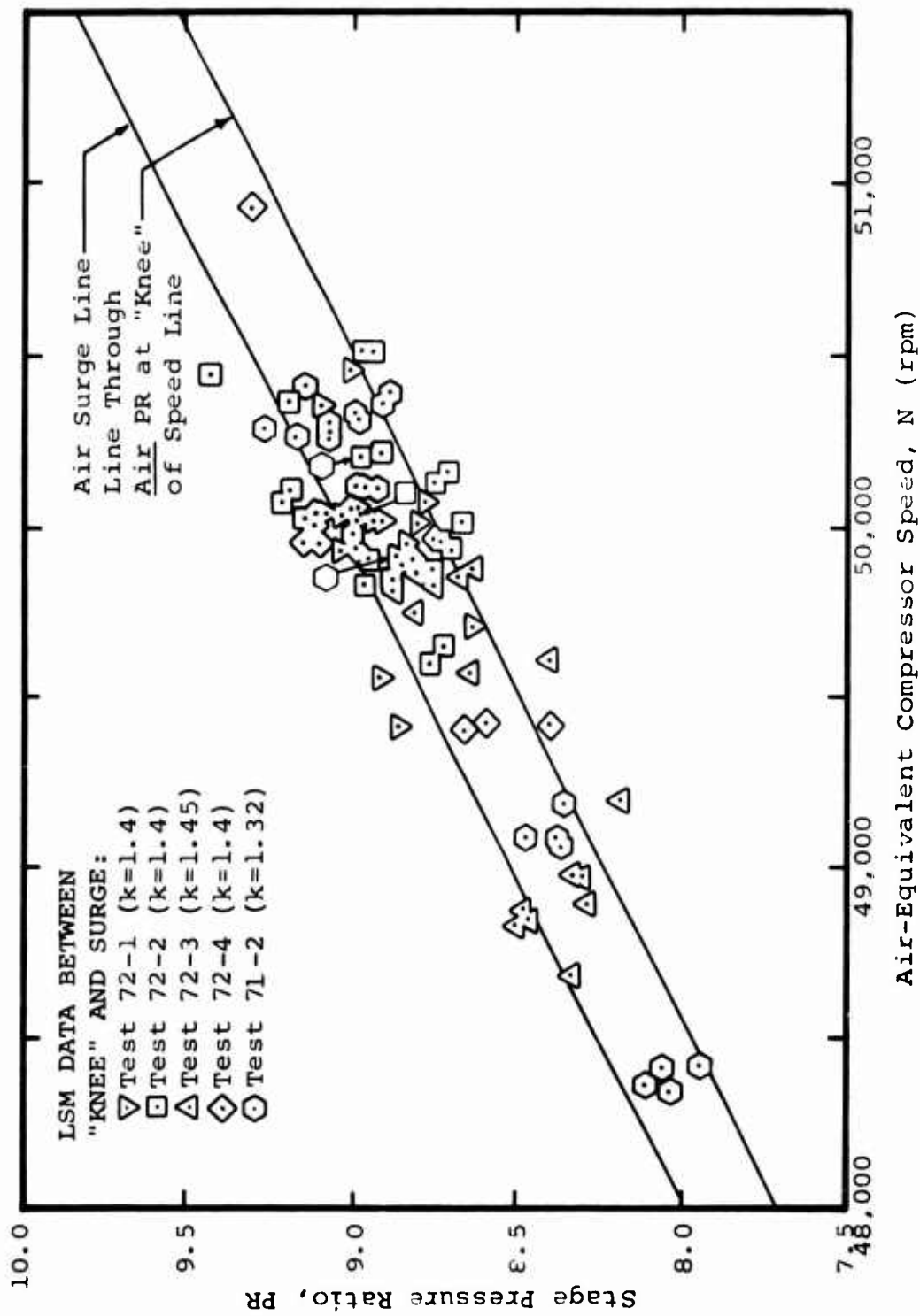


Figure 28. Stage Pressure Ratio for LSM Data Between "Knee" and Surge.

line and surge using LSM techniques is independent of (for the range of conditions tested):

- 1) The LSM gas inlet specific heat ratio
- 2) The impeller-to-shroud running clearance
- 3) The heat transfer from the compressor.

Mass Flow Rate at Choke Vs. Speed

Mass-flow-rate-at-choke data were obtained during test condition 72-1 over a wide speed range. These data are plotted on Figure 29 as inverted triangles. The Boeing air data at choke are also shown on Figure 29 plotted as circles. The solid line of this figure represents the best-fit curve through all of Boeing's choked flow rate air data. (Note that Boeing's choke flow rate at 50,000 rpm lies approximately 1% above this best-fit line.) This figure further demonstrates that the LSM flow modeling is excellent with an LSM gas mixture which duplicates the air inlet specific heat ratio.

The mass-flow-rate-at-choke data from a variety of LSM test conditions are plotted on Figure 30. The solid line of this figure represents the best-fit curve through all of Boeing's air data and is the same line shown on Figure 29. Boeing's 50,000-rpm point is shown by the circle. The LSM data are represented by various other symbols. The pair of dashed lines around the best-fit curve through the air data represents the approximate uncertainty band for LSM data.

These data show that:

- 1) Air mass-flow-rate-at-choke is well duplicated with an LSM gas which has an inlet specific heat ratio identical to air.
- 2) Based on inlet scaling, the mass-flow-rate-at-choke is higher than the corresponding air values when an LSM gas with a lower-than-air inlet specific heat ratio is used.
- 3) An LSM gas mixture with a slightly higher-than-air inlet specific heat ratio results in a slightly lower-than-air choke mass flow rate.

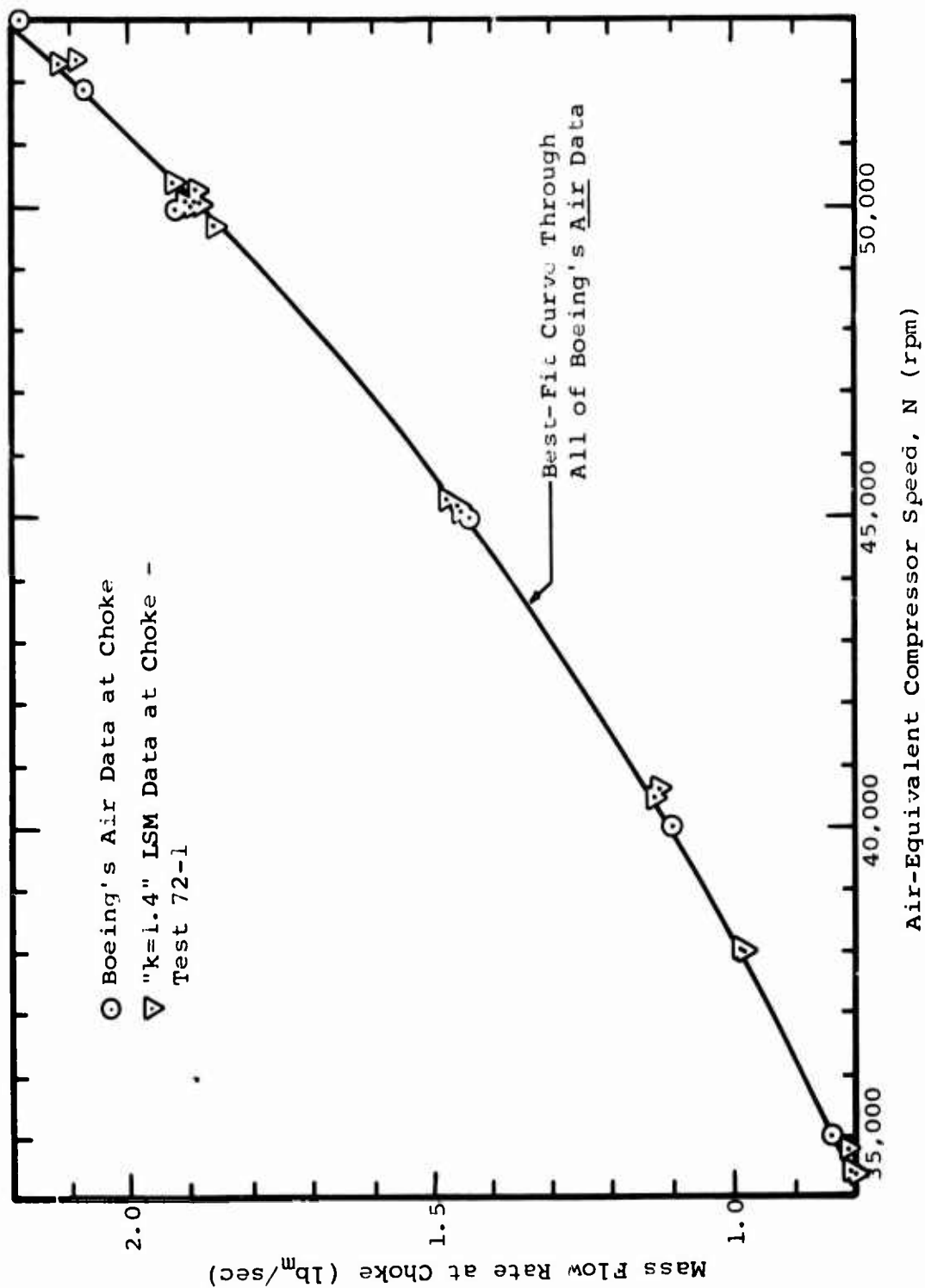


Figure 29. Mass Flow Rate at Choke.

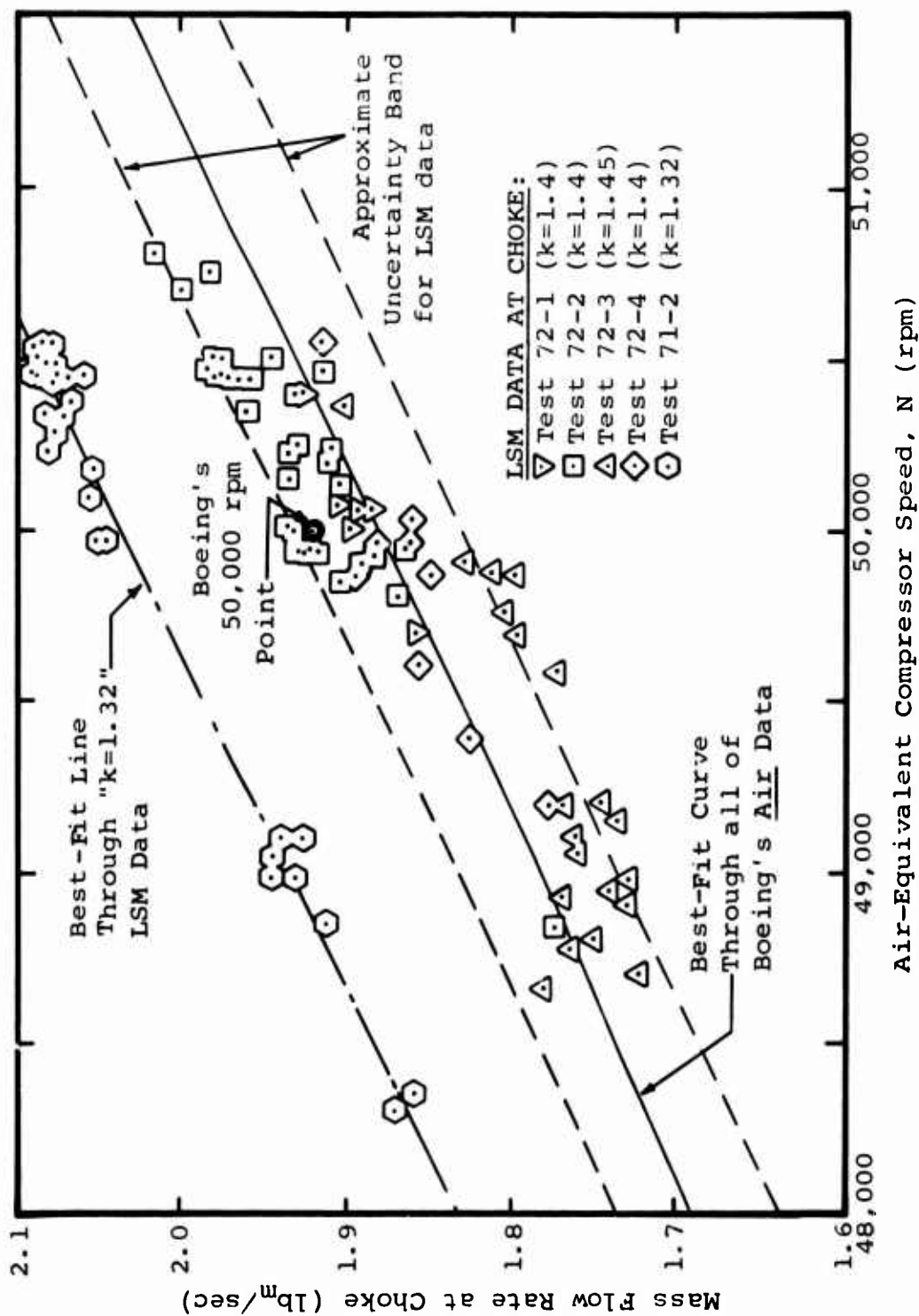


Figure 30. Mass Flow Rate at Choke.

Thus it can be seen that accurate modeling of the flow rate through high-pressure-ratio compressors based on a simple inlet scaling scheme requires the use of an LSM gas mixture whose inlet specific heat ratio closely duplicates that of air.

Isentropic Efficiency Data With LSM Gas

The first LSM data obtained during this program (Tests 71-1 and 71-2) showed excellent replication of the Boeing air map except for the magnitude of the isentropic stage efficiency. The LSM efficiency data fell about 1 to 2 percentage points lower than the air efficiency data. To determine why, a series of special tests was added to the program to study the effect of specific heat ratio, impeller tip running clearance, and heat transfer from the compressor on the measured stage efficiency.

These tests revealed that the original lack of correlation of efficiency between the LSM and air data was due to the larger-than-air impeller running clearances used during the 71-1 and 71-2 LSM test setups. These extra tests further showed that inlet specific heat ratio has no measurable effect on stage isentropic efficiency. However, heat transfer from the compressor does have a significant effect on the measured efficiency.

Replication of Boeing's Results

Test condition 72-1 closely replicates the test conditions used by Boeing for their air data: impeller-to-shroud running clearance of 0.005" to 0.010", no compressor insulation, and inlet specific heat ratio of 1.4. The LSM efficiency data from this test condition is shown in Figure 31. Although there is some scatter in these data, it is clear that the LSM data between the "knee" and surge points closely duplicate Boeing's measured efficiency in this same range. (Boeing's efficiency between "knee" and surge at 50,000 rpm was 71 to 72.5% maximum.) Some portion of the scatter in the LSM data results from the plotting of a large speed range on the same figure. The estimated uncertainty in the LSM efficiency data is about 1.2%. Although Boeing did not perform an uncertainty analysis on their air data, our best estimate of Boeing's air efficiency

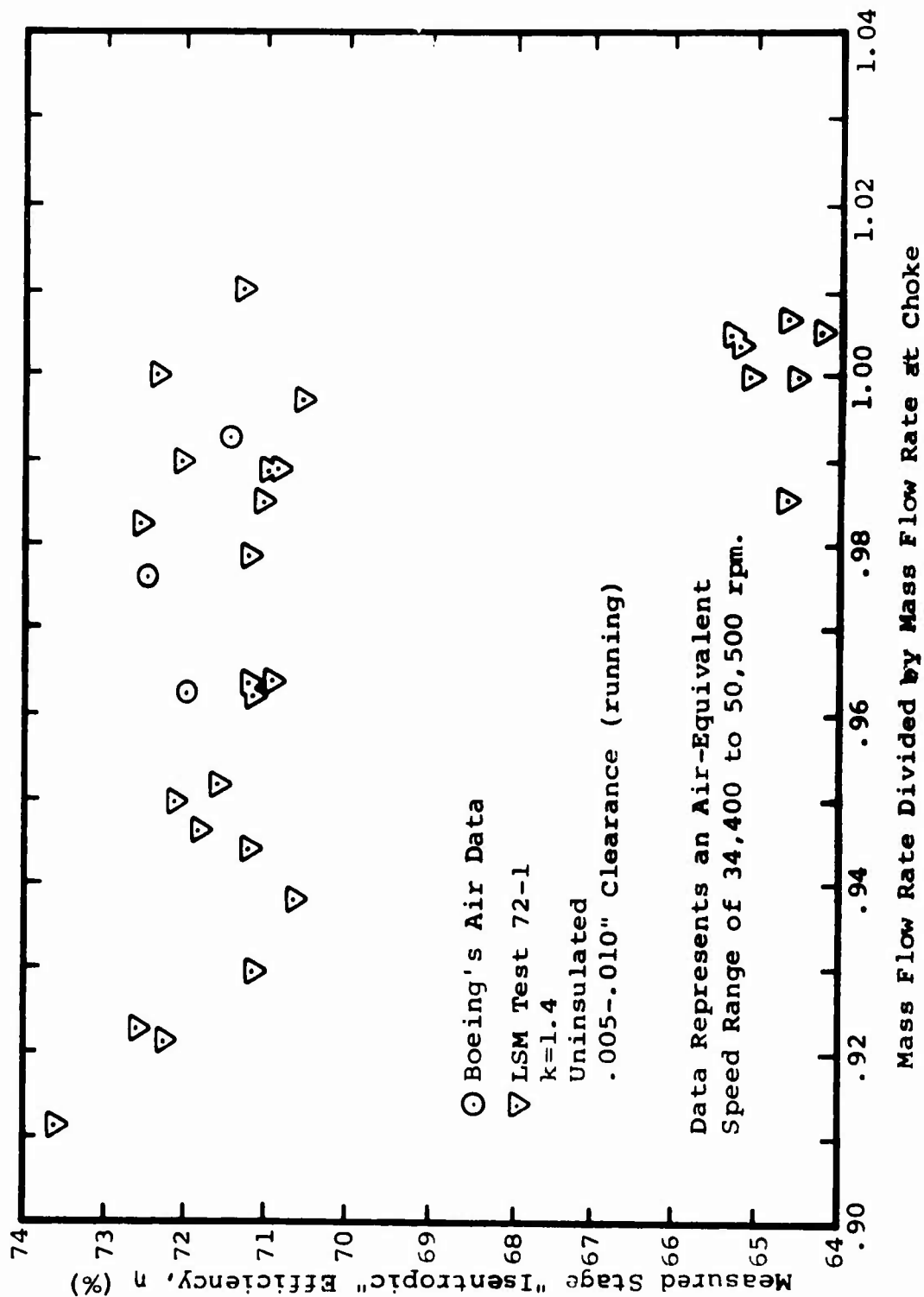


Figure 31. Measured Efficiency With Uninsulated Compressor and 0.005" to 0.010" Impeller Running Clearance.

uncertainty is about 1.1% (see Section 3.4).

Thus the data of Figure 31 shows that the air performance map including stage efficiency is well duplicated when the air conditions of no insulation, accurately modeled inlet specific heat ratio, and impeller running clearance are replicated.

Impeller-to-Shroud Running Clearance

The effect of impeller-to-shroud running clearance on measured efficiency can be seen by comparing Figure 32 (where the results from test condition 72-4 are plotted) with Figure 31. The data of Figure 32 show that when the impeller-to-shroud running clearance was increased from 0.005" - 0.010" up to 0.020" - 0.025", the efficiency is reduced by about 2 points.

Inlet Specific Heat Ratio

The data of Figure 33 (from test condition 72-3) show that the inlet specific heat ratio of the modeling gas has little or no effect on the measured efficiency. It is stressed that the data reduction computer program, which was used to calculate the efficiencies reported, calculated the actual and isentropic enthalpy rises based on the best available expressions for the enthalpy and entropy of the LSM gas as a function of pressure, temperature, and composition. Thus, the efficiency was always calculated from the basic definition of isentropic efficiency - not from any approximate expression of the form

$$\eta = \frac{P_r^{\frac{k-1}{k}} - 1}{TR - 1}$$

Heat Transfer

The effect of heat transfer from the compressor on measured efficiency is shown in Figure 34. These data were obtained with the compressor well insulated (test condition 72-2). (All other LSM data as well as the original air data were

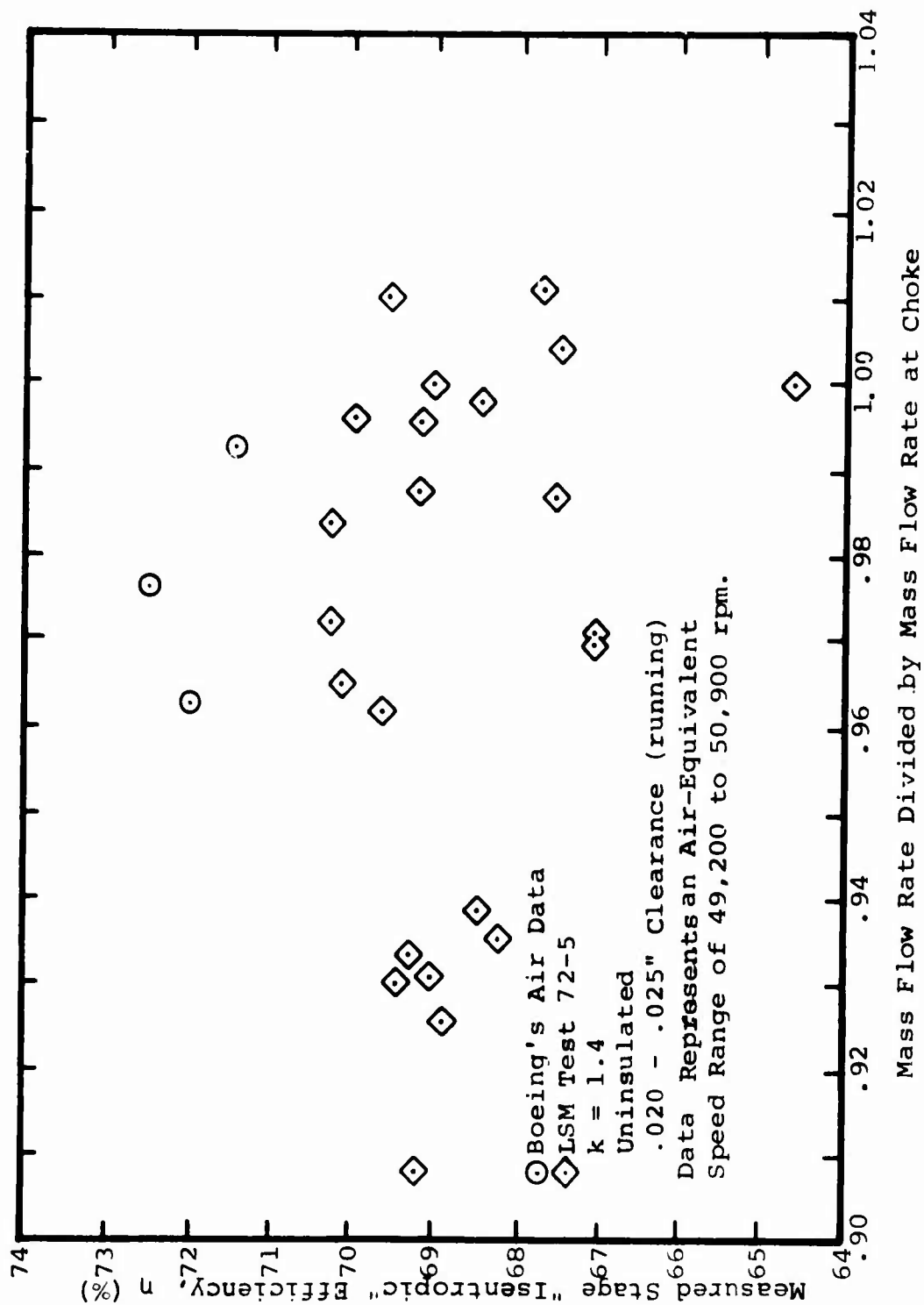


Figure 32. Measured Efficiency With Uninsulated Compressor and 0.020" to 0.025" Impeller Running Clearance.

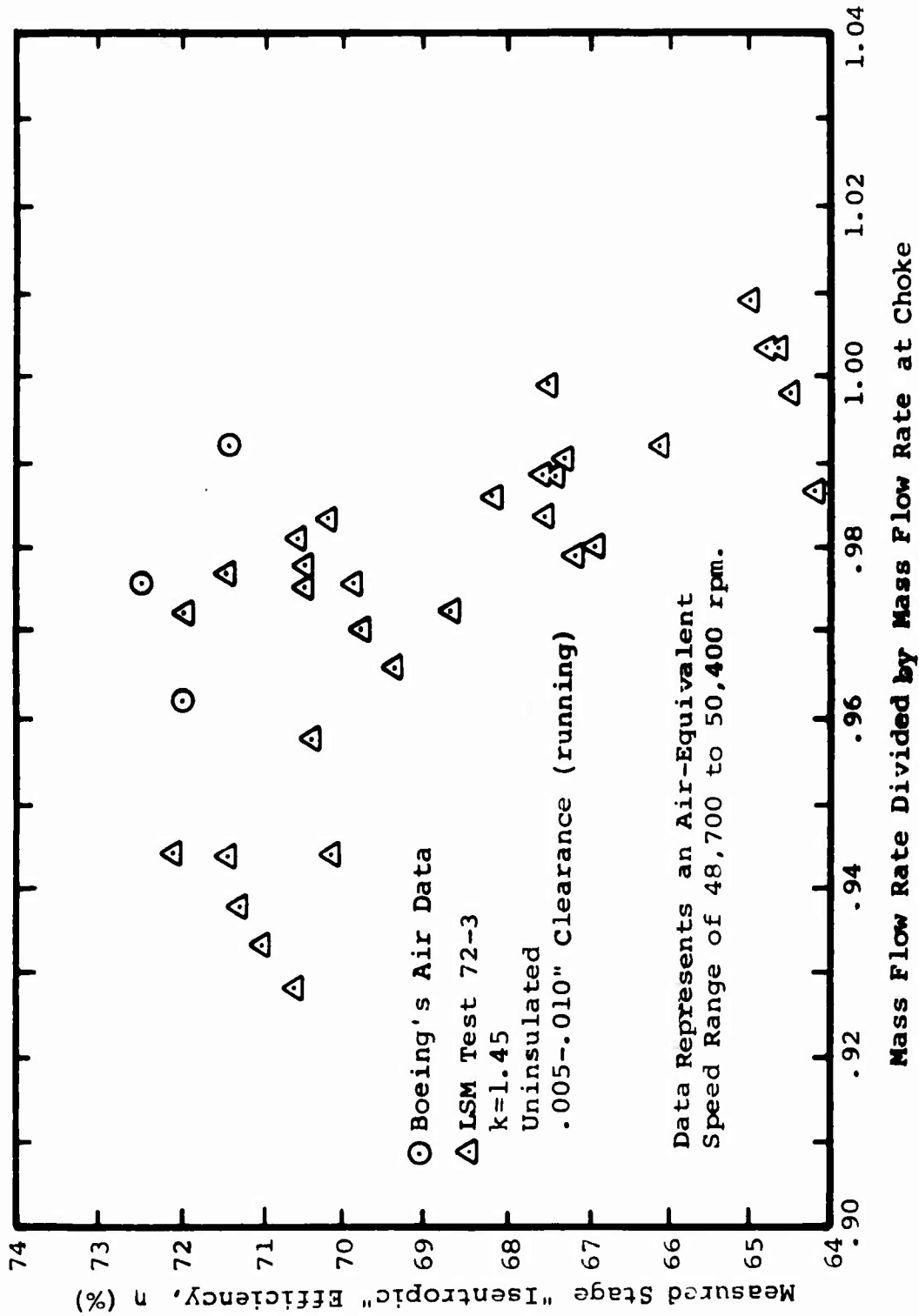


Figure 33. Measured Efficiency With Uninsulated Compressor, " $k=1.45$ " LSM, and 0.005" to 0.010" Impeller Running Clearance.

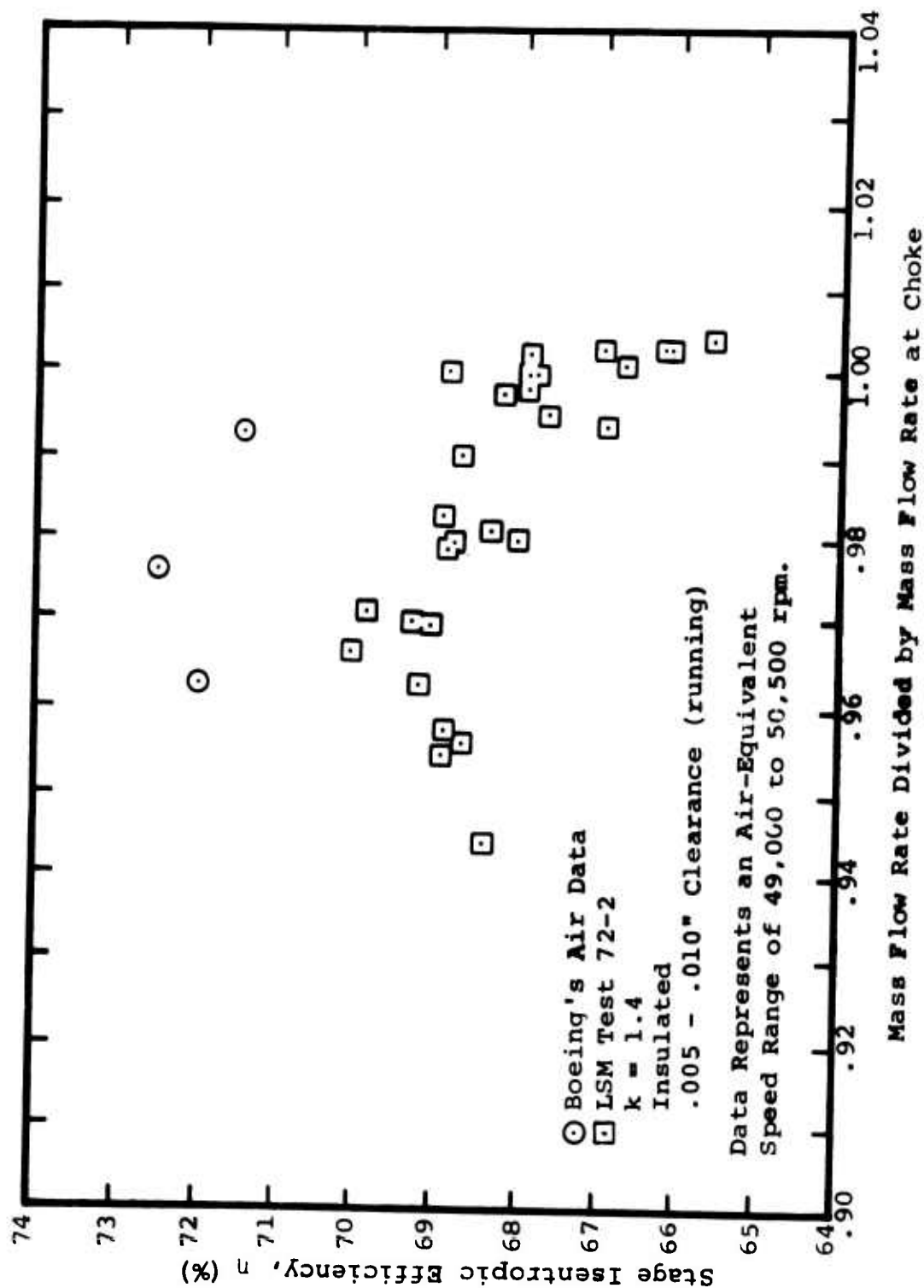


Figure 34. Isentropic Efficiency With Insulated Compressor and 0.005" to 0.010" Impeller Running Clearance.

obtained with no insulation on the compressor.) These results show a reduction of 2.0 to 2.5 percentage points in measured efficiency when heat transfer from the compressor is retarded. A heat transfer analysis (contained in Appendix III) shows that the effect of heat transfer on measured air efficiency is very nearly the same as the effect on measured LSM efficiency.* Thus the data shown in Figure 34 probably closely approximate the data which would have been obtained by Boeing in air had this compressor been tested with insulation.

The data of Figure 34 more closely represent the true isentropic efficiency for this compressor. All other efficiency data (obtained without compressor insulation) indicate a measured efficiency which is higher than the actual isentropic efficiency. Measuring the isentropic efficiency of a compressor without carefully insulating the compressor will produce an efficiency which will be higher than the true isentropic efficiency.

Although it is true that the efficiency of a machine does not have to be defined as (and consequently tested as) the isentropic (or adiabatic) efficiency, it is the isentropic efficiency that is the only practical true comparison of different machines, tested under different conditions. Since the measured efficiency of any compressor depends on the heat transfer from (or to) the compressor, only when all machines are tested under the same (insulated) conditions can their "isentropic" efficiencies be honestly compared.

Time-Average Static Pressures

In addition to closely replicating the Boeing air overall stage performance data, the modeling correlation portion of this LSM program demonstrated that the details of the fluid dynamics throughout the compressor, as reflected by static pressure distributions, are well replicated with the LSM testing scheme. Time-average static pressure measurements

* Basically, the driving temperature difference with LSM is lower, while the LSM gas heat capacity is also lower than air; these opposite effects very nearly balance out.

at numerous locations throughout the machine were obtained using the same static pressure taps used by Boeing. The locations of these static pressure taps are shown in Figures 10 and 11 and Table IV.

The comparison of the LSM and Boeing pressure distribution data throughout the compressor is discussed in this section. All data are presented as the ratio of the time-averaged static pressure (at each location) to the plenum pressure. Reference will occasionally be made to "line numbers". These "line numbers" were used by Boeing to designate (qualitatively) different mass flows. Line 3 is near surge, line 7 is near choke, and line 5 is about mid-range. No quantitative importance should be attached to a "line number" reference -- only the qualitative meaning suggested above.

Inducer/Impeller Shroud Static Pressure

Figure 10 shows the inlet, inducer, and impeller regions of the test compressor. Three static pressure taps are located circumferentially at each station. In interpreting the following plots, it is important to observe that Station 15 occurs at the approximate position where the bend-to-radial begins.

The inducer shroud pressure distribution obtained by Boeing in air is shown in Figure 35 for four tests in the flow rate range of 1.86 to 1.90 lbm/sec. Station 15 is located just short of 2.4" along the shroud from the inducer leading edge. A similar plot for three " $k = 1.4$ " LSM state points and one " $k = 1.3$ " LSM state point is shown in Figure 36. These curves represent best-fit curves through data from three circumferentially located pressure taps at each position along the shroud.

A portion of the original data used to generate these curves for both air and LSM is shown in Figure 37. The scatter in the data appears large because of the enlarged scale of the vertical axis used for this plot. The actual variation from tap to tap at any one circumferential location is only about 1 psia. This variation is caused by the influence of the diffuser vanes pressure field on the time-average circumferential static pressure distribution

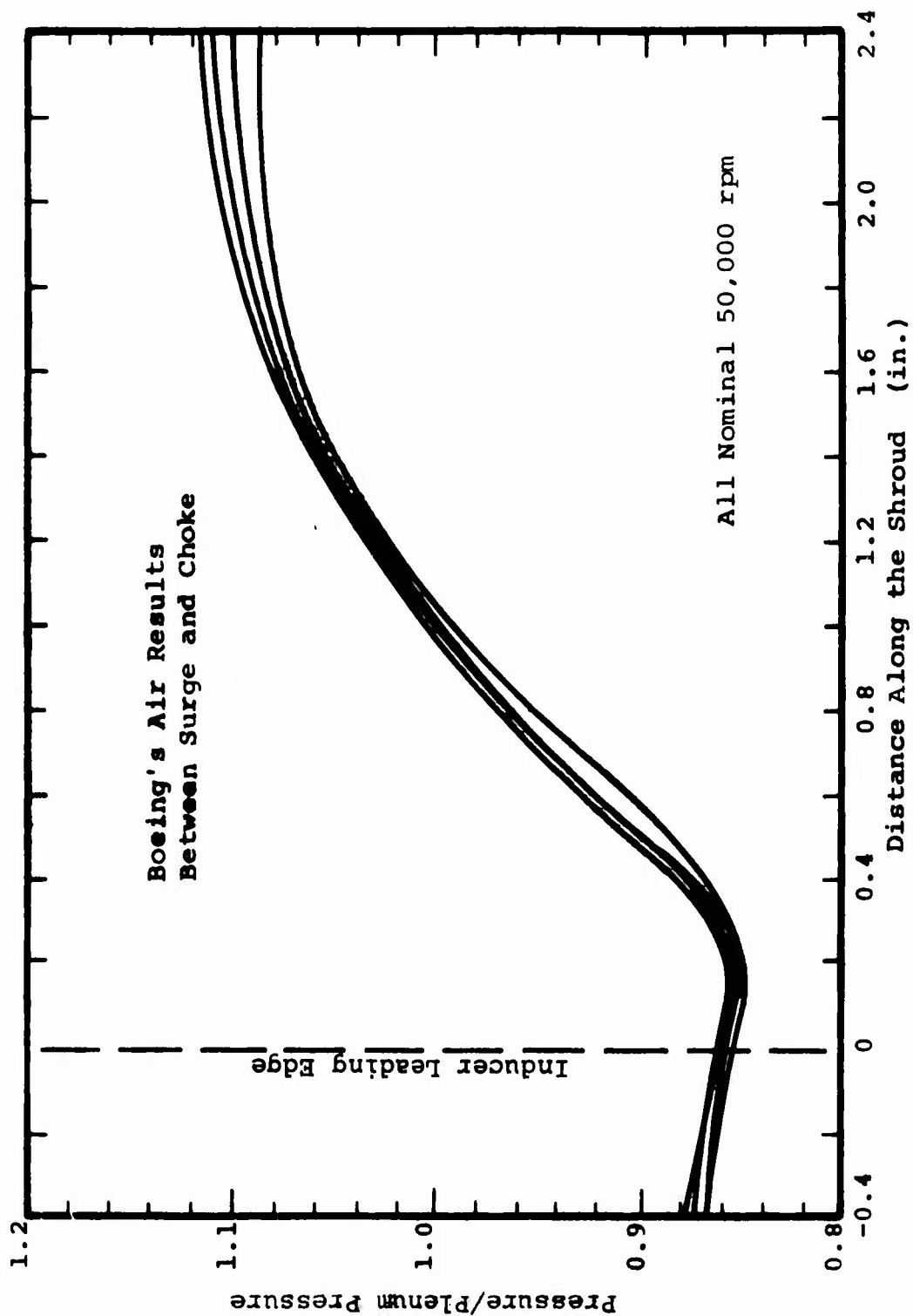


Figure 35. Inducer Shroud Static Pressure Distribution for Air.

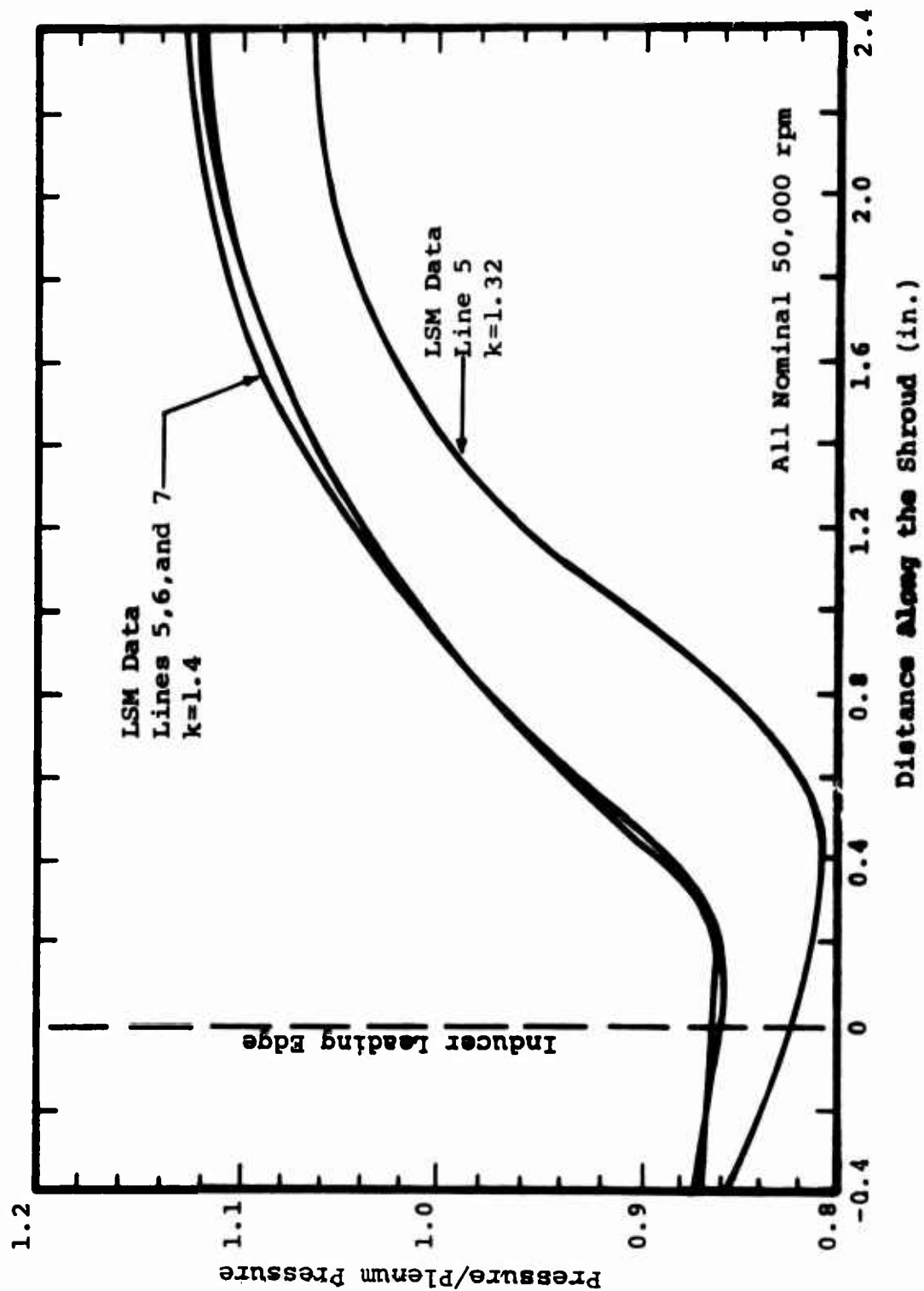


Figure 36. Inducer Shroud Static Pressure Distribution for LSM.

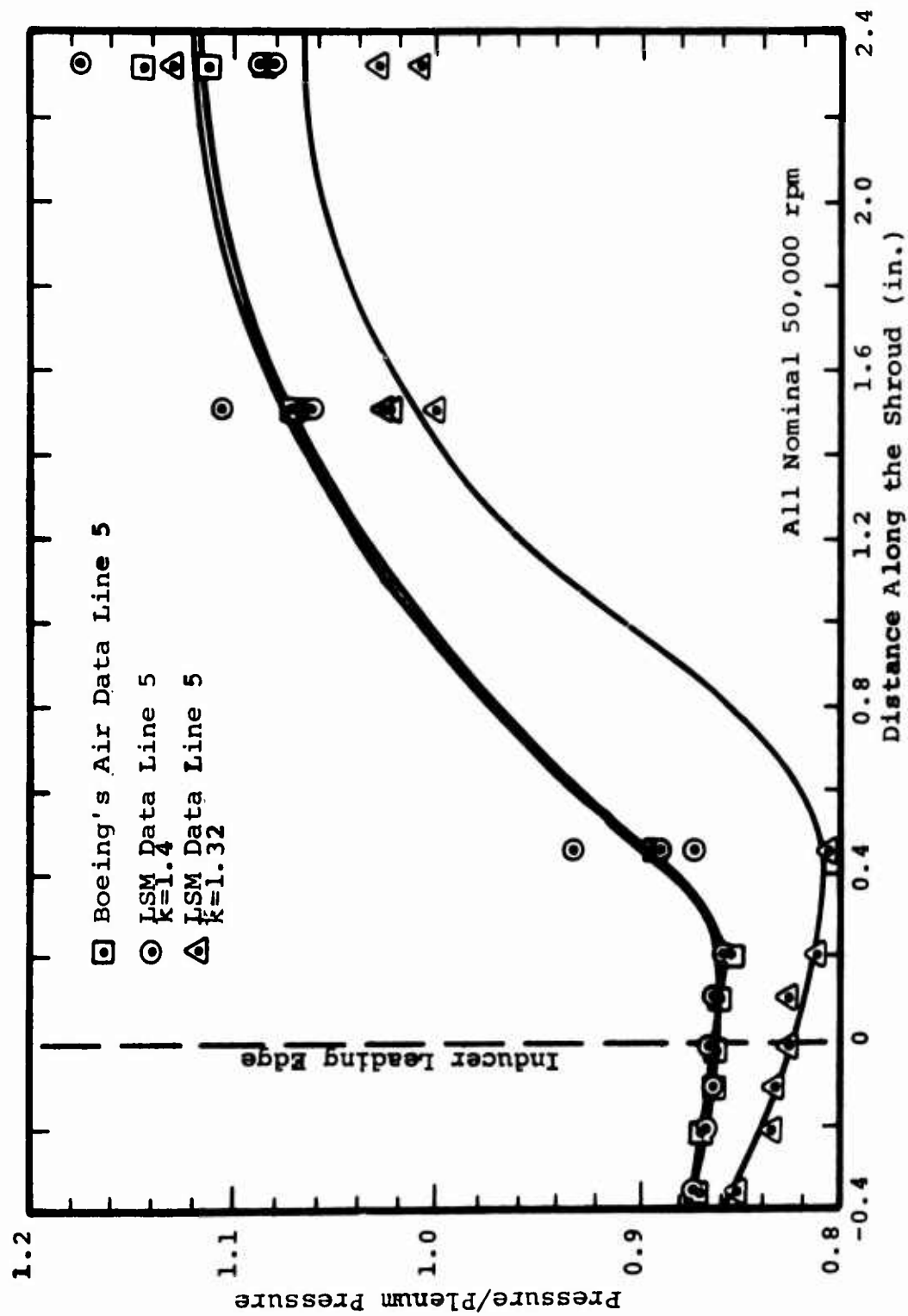


Figure 37. Inducer Shroud Static Pressure Distribution for LSM and Air.

in the inducer.

As can be seen, the pressure distribution with 1.4 LSM gas closely duplicates the pressure distribution obtained with air. The lower pressure along the inducer region with "k = 1.3" LSM gas is consistent with the higher air-equivalent flow rate of this gas. For both the air data and the LSM data, very little difference in the pressure distribution along the inducer was observed between surge and choke.

Figures 38, 39, 40 and 41 show the impeller shroud pressure distribution from the inducer leading edge to the impeller tip for four typical LSM tests. The data of these figures from upstream of the inducer to a distance along the shroud of about 2.4" are the same as shown on Figures 35, 36 and 37 (on a different scale). No air data are available for comparison with the LSM data between stations 16 and 19.

Impeller Exit Static Pressures

The impeller exit time-average static pressure data presented in this section are taken from the pressure taps shown in Figure 11 at the 1.03 radius ratio location. As will be seen, the measured static pressure at the impeller exit is a strong function of the circumferential location of the pressure taps with respect to the diffuser vane tips. The impeller exit pressures are plotted as a function of circumferential spacing relative to adjacent vane tips at the 1.03 radius ratio. In these figures, S is the circumferential distance measured from a vane tip, and S_0 is the circumferential distance between vane tips ($S_0 = 2.96"$); both S and S_0 are measured along the 1.03 radius ratio arc.

The impeller exit static pressure distribution as measured by Boeing and reported in Reference 6 is shown in Figure 42. Figure 42 is a corrected version of Figure 124 of Reference 6, which had the labels for the hub and shroud reversed. This figure shows the magnitude of the impeller exit static pressure in air with a plenum pressure of 14.7 psia.

Other air data, some of which are previously unpublished, are normalized by the plenum pressure and shown in Figures 43

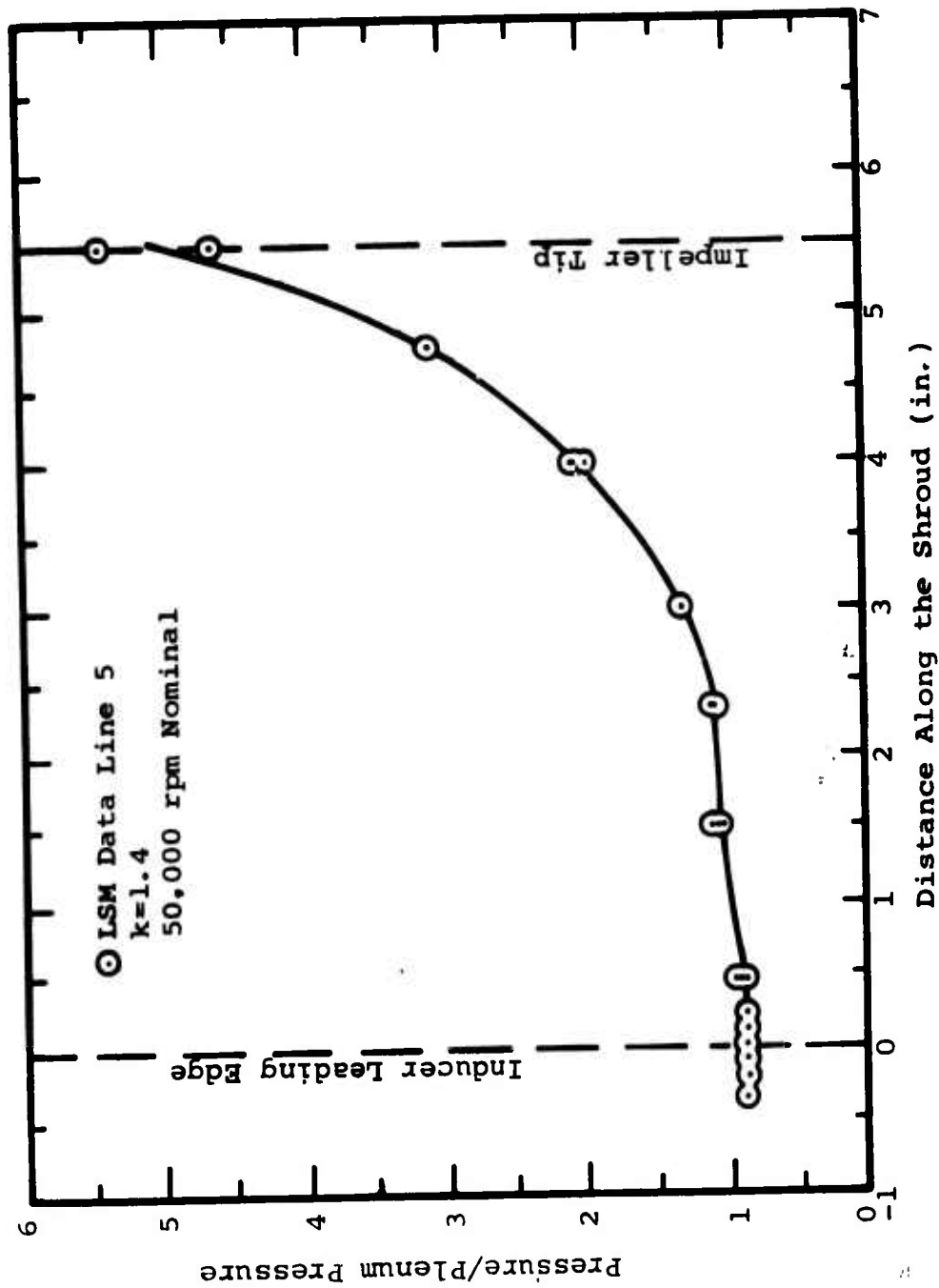


Figure 38. Impeller Shroud Static Pressure Distribution for LSM.

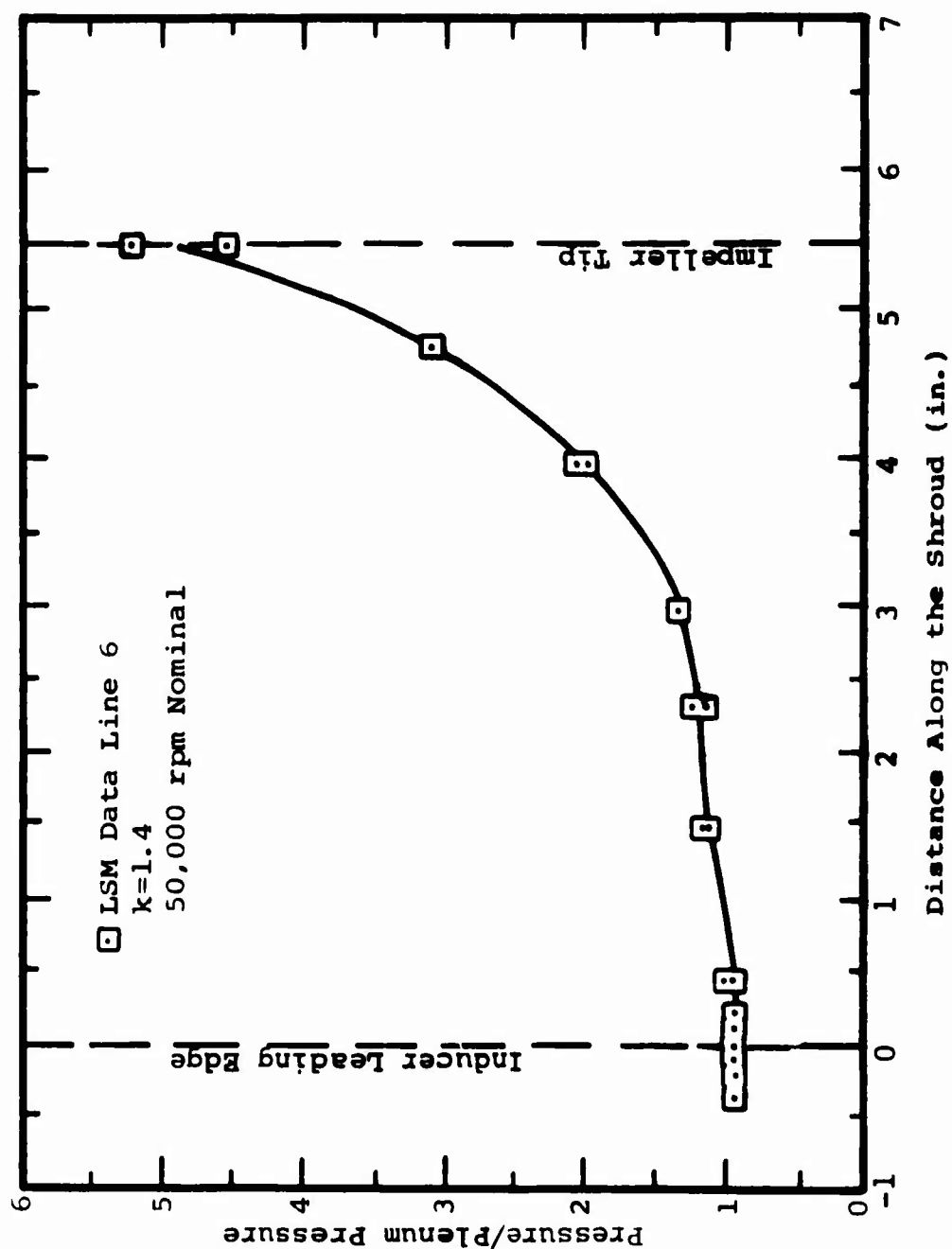


Figure 39. Impeller Shroud Static Pressure Distribution for LSM.

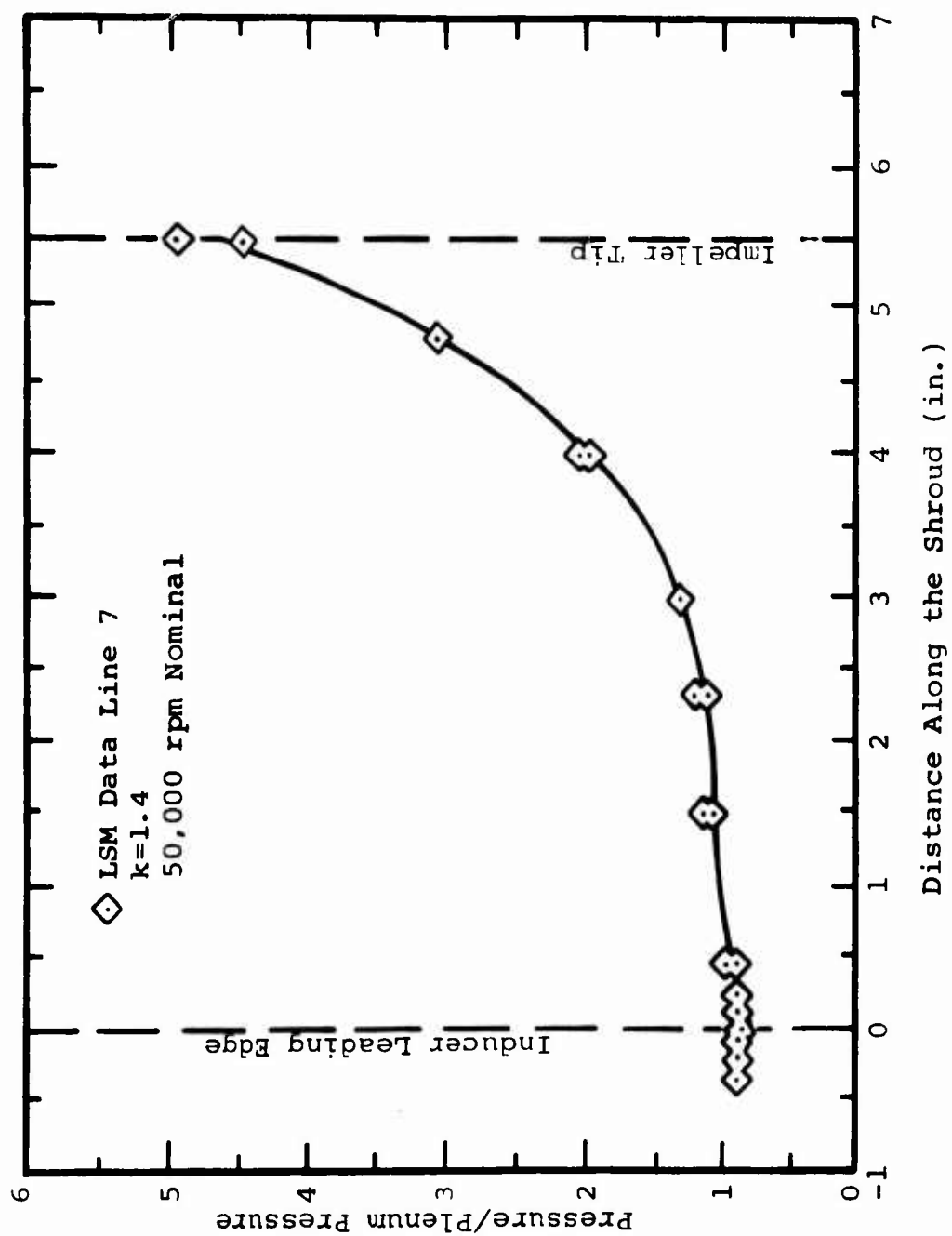


Figure 40. Impeller Shroud Static Pressure Distribution for LSM.

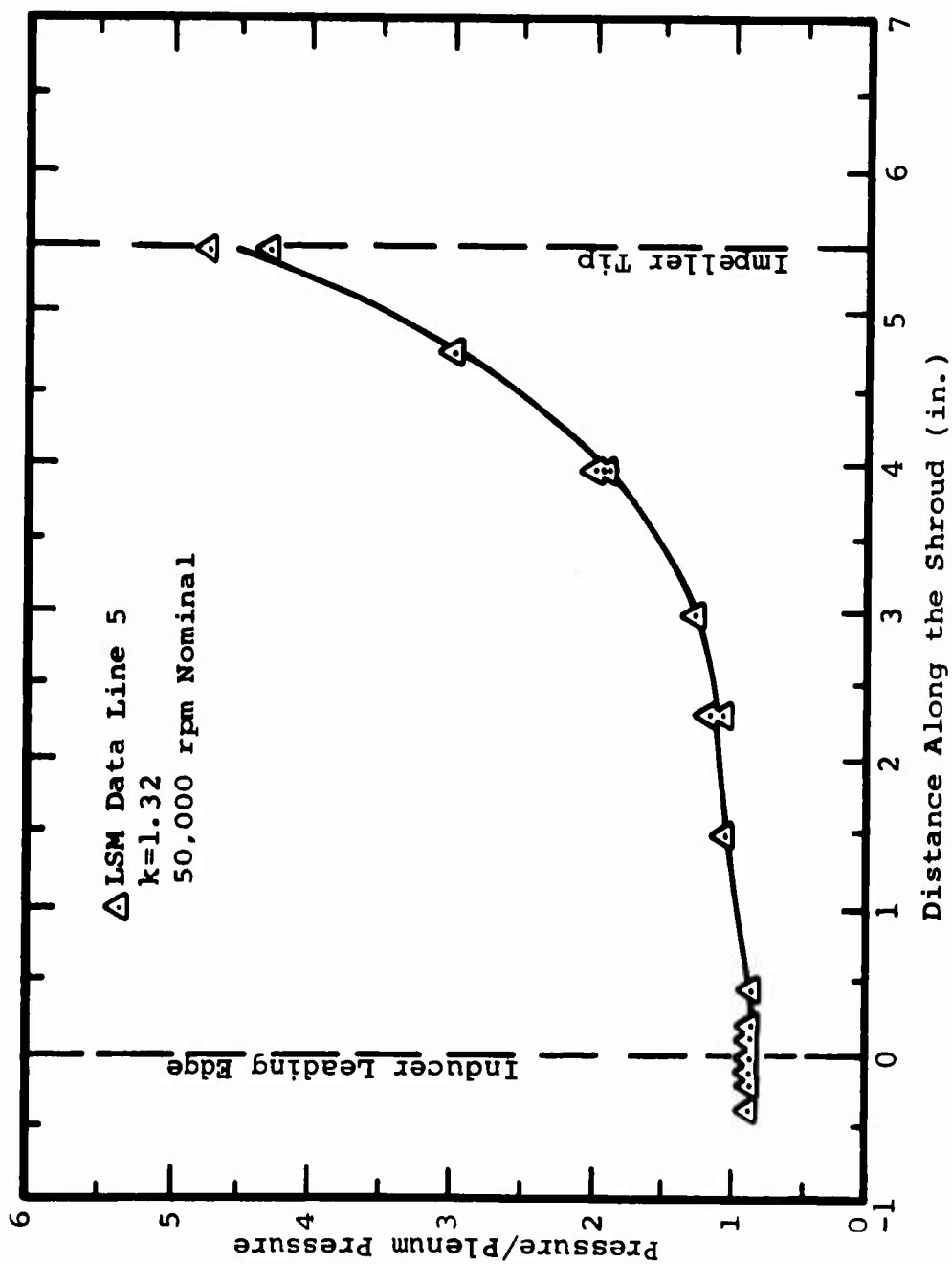


Figure 41. Impeller Shroud Static Pressure Distribution for LSM.

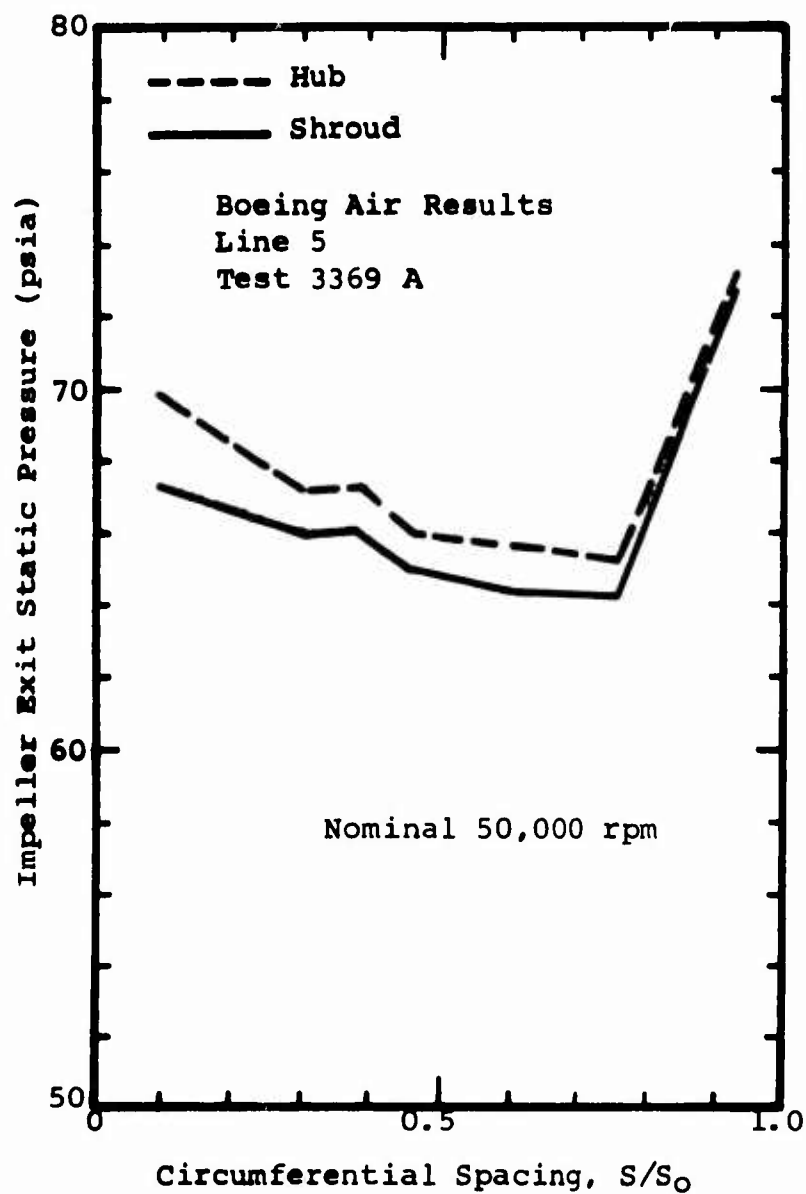


Figure 42. Circumferential Variation of Impeller Exit Static Pressure for Air.

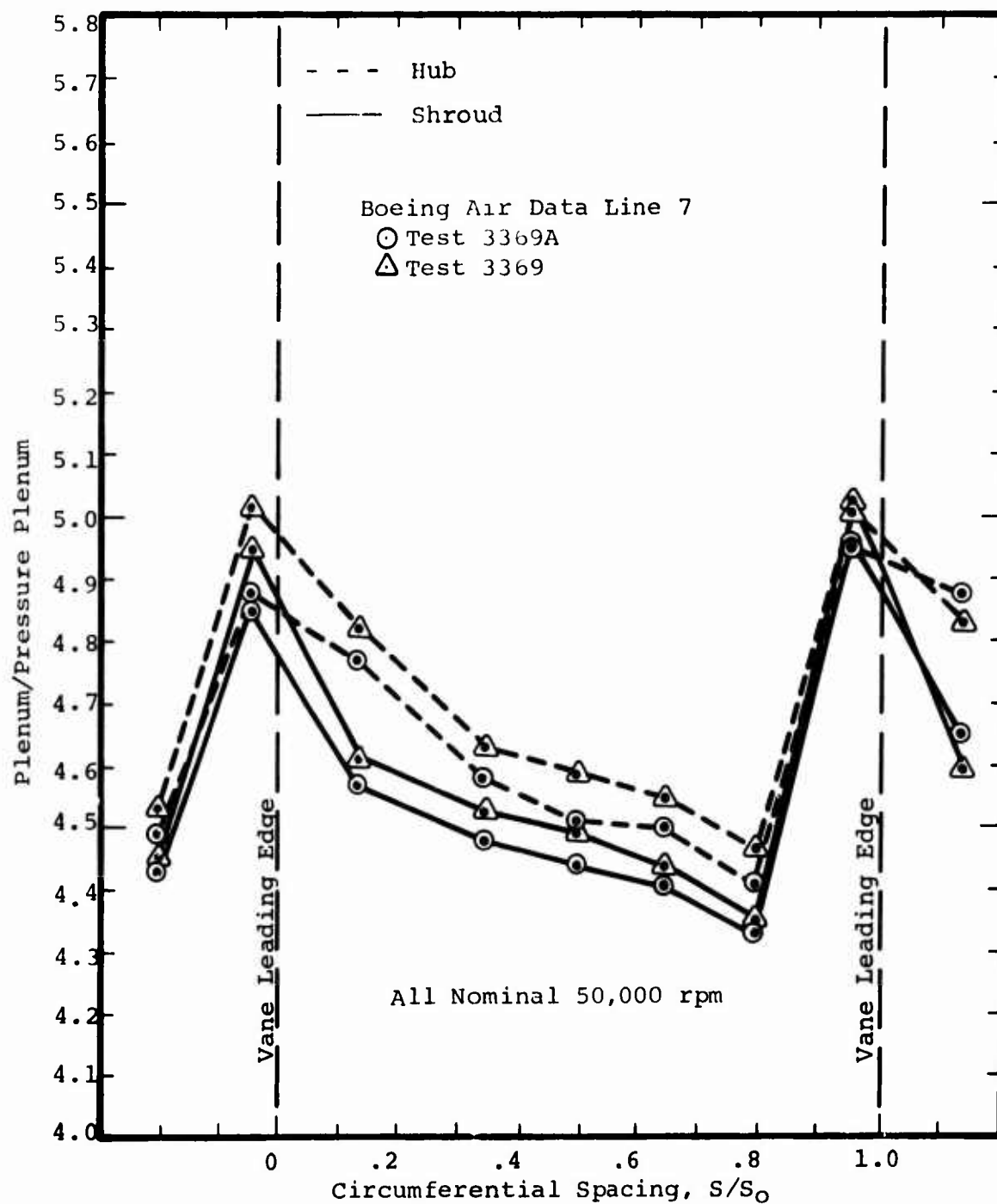


Figure 43. Circumferential Variation of Impeller Exit Static Pressure for Air.

and 44. These data are presented to show the variability of the impeller exit pressure data, especially in the regions of the vane leading edge.

Representative LSM impeller exit static pressure distributions are shown in Figures 45, 46, 47 and 48. Data for similar "line numbers" for LSM and air are compared in Figures 49 and 50. In the latter two figures, the static pressure distributions at the impeller exit are closely duplicated with LSM test gas. A detailed discussion of this pressure distribution is beyond the scope of this report. Some discussion can be found in Reference 7.

Diffuser Centerline Static Pressures

Following the convention established by Boeing, the time-average static pressures throughout the diffuser entry region as measured along a channel diffuser centerline are plotted as a function of path length. The vane leading-edge position is taken as an arbitrary zero.

Figure 51, extracted from Reference 6, shows some of the original air data obtained by Boeing. The line segments connecting the data points drawn by Boeing are reproduced in Figures 52, 53, 54, and 55 and show the comparison of the Boeing air data and the LSM data. As can be seen, the replication of the air static pressure distribution through the diffuser is very good except for the data in Figure 55. However, the type of pressure distribution shown in Figure 55 was observed by Boeing; Boeing air data for an unpublished test run are plotted in Figure 56 along with the LSM data from Figure 55.

These figures demonstrate the similarity of air and LSM static pressure data. They also demonstrate that more extensive data are required, probably using finer spaced pressure taps, before the subtle details of the effect of shocks, shock-boundary layer interactions, etc. on the static pressure distributions can be fully appreciated and related to the fundamental flow processes in this region.

The dynamic, static, and total pressure measurements are presented and discussed in Section 9.

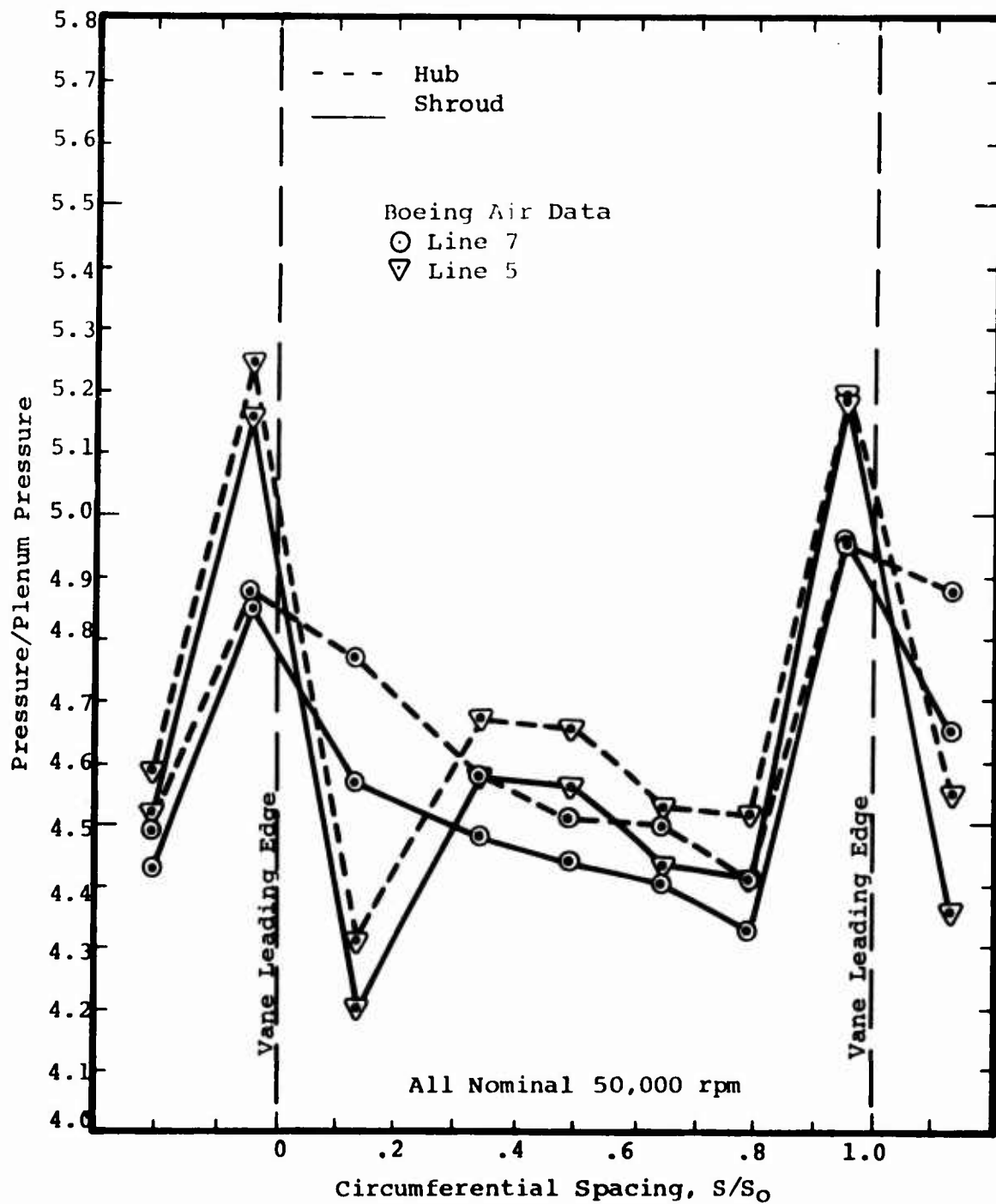


Figure 44. Circumferential Variation of Impeller Exit Static Pressure for Air.

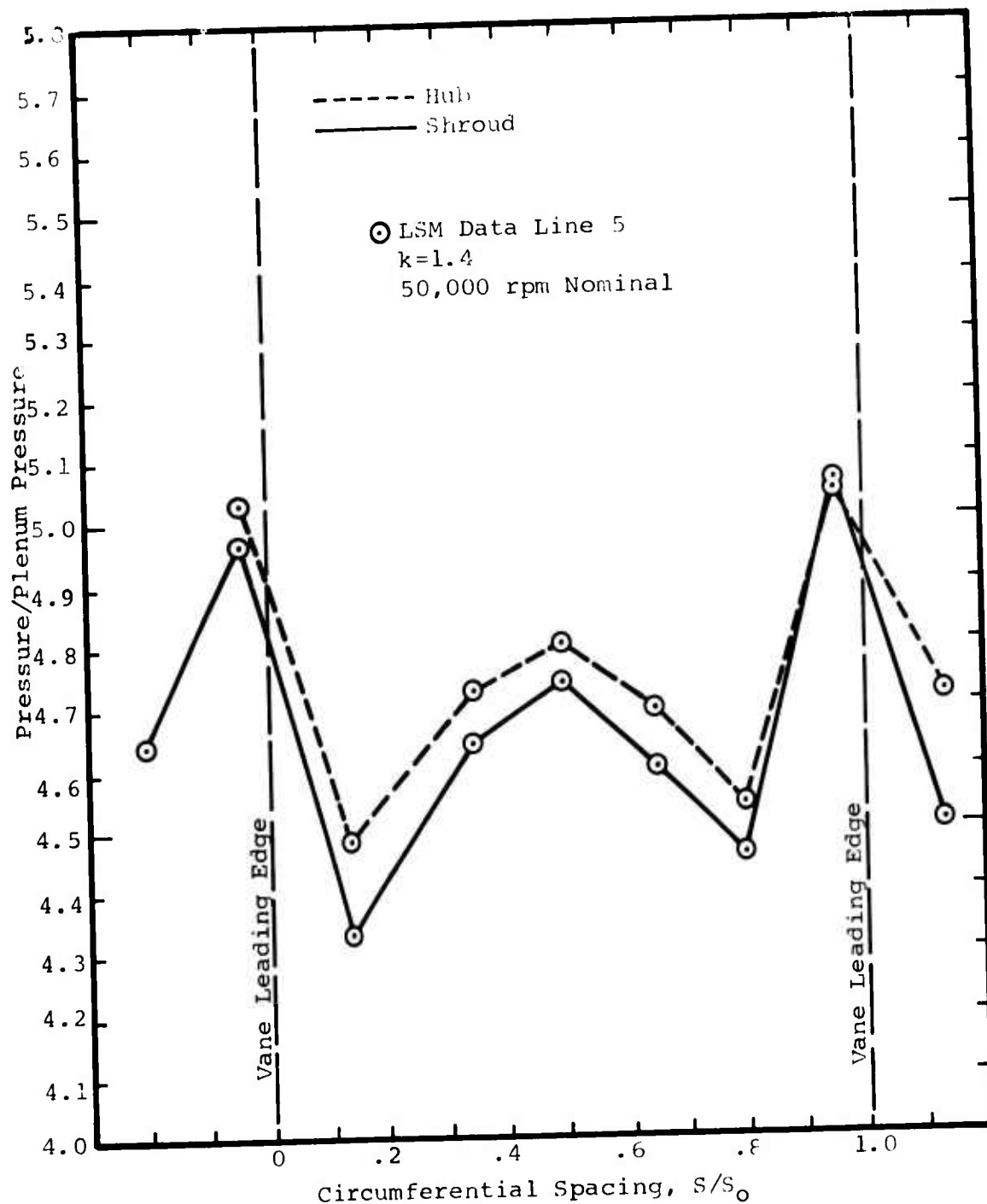


Figure 45. Circumferential Variation of Impeller Exit Static Pressure for LSM.

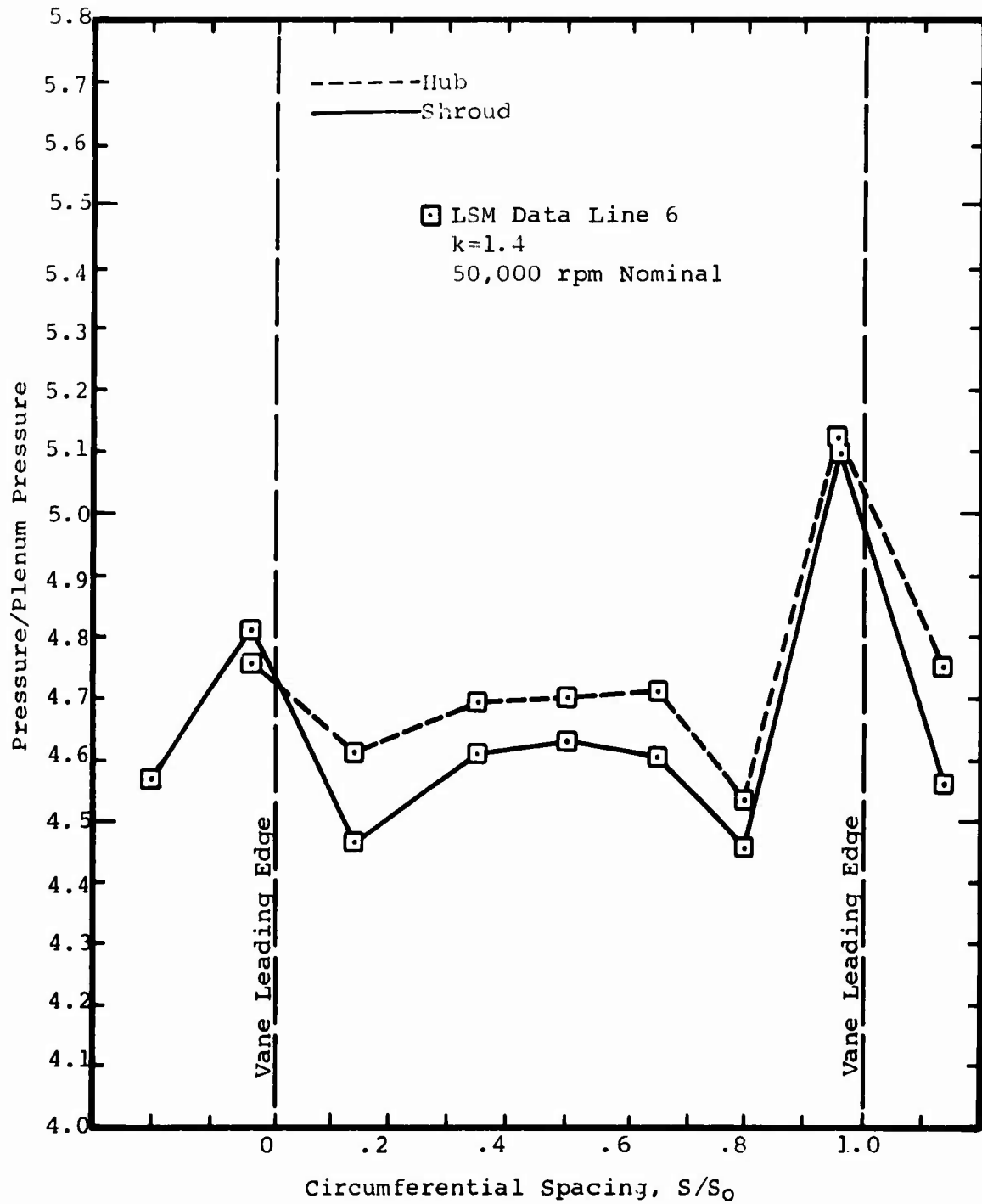


Figure 46. Circumferential Variation of Impeller Exit Static Pressure for LSM.

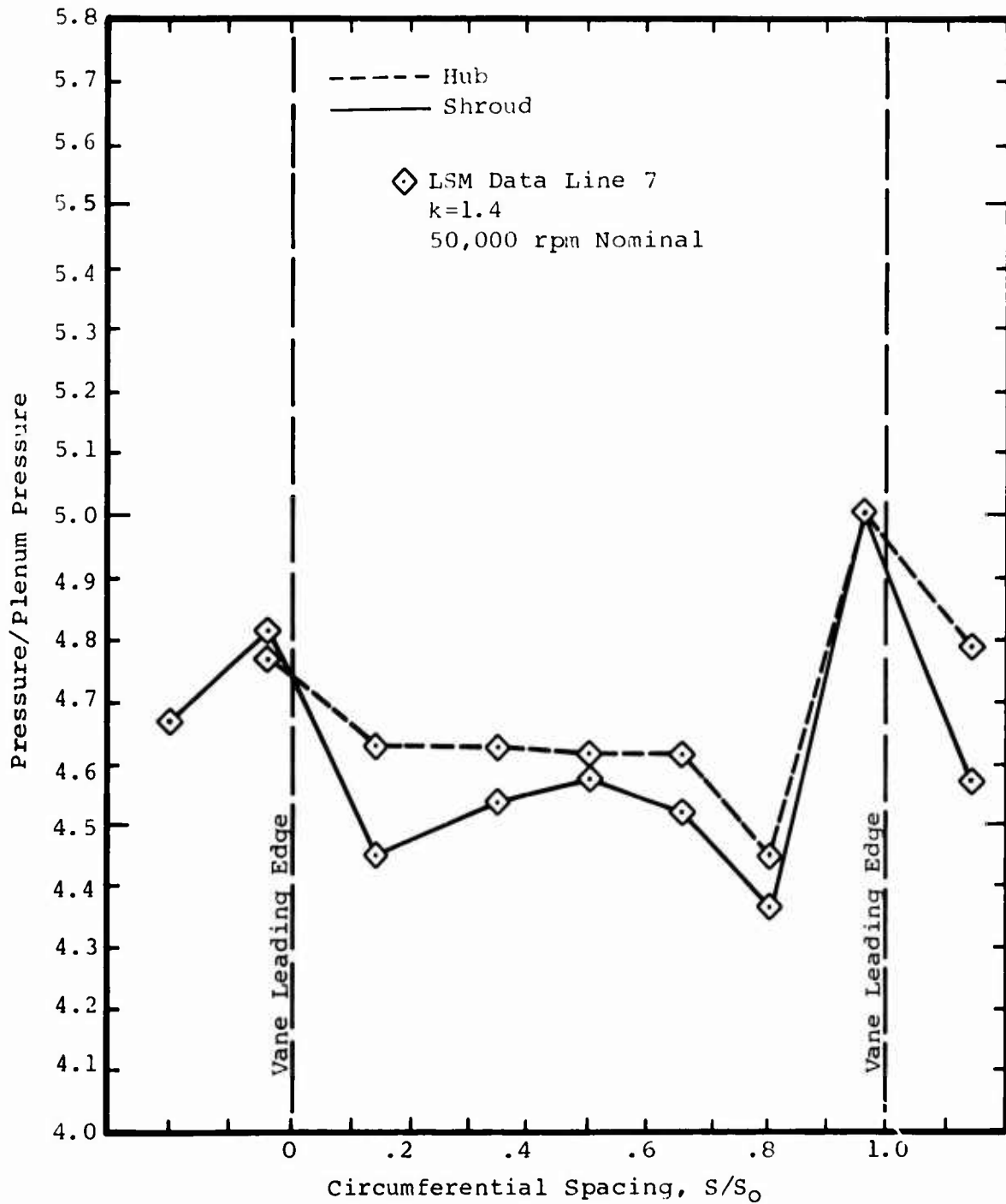


Figure 47. Circumferential Variation of Impeller Exit Static Pressure for LSM.

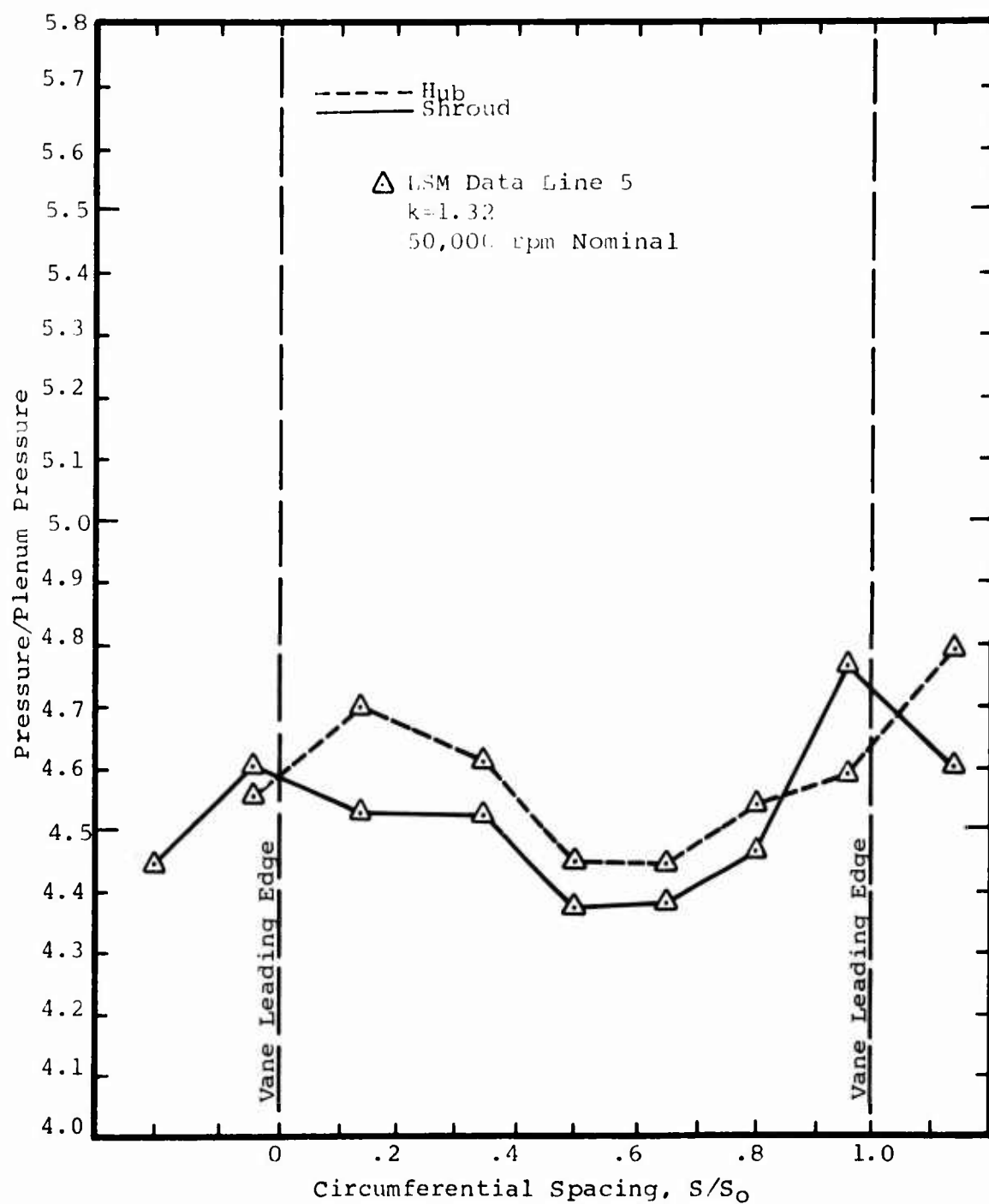


Figure 48. Circumferential Variation of Impeller Exit Static Pressure for LSM.

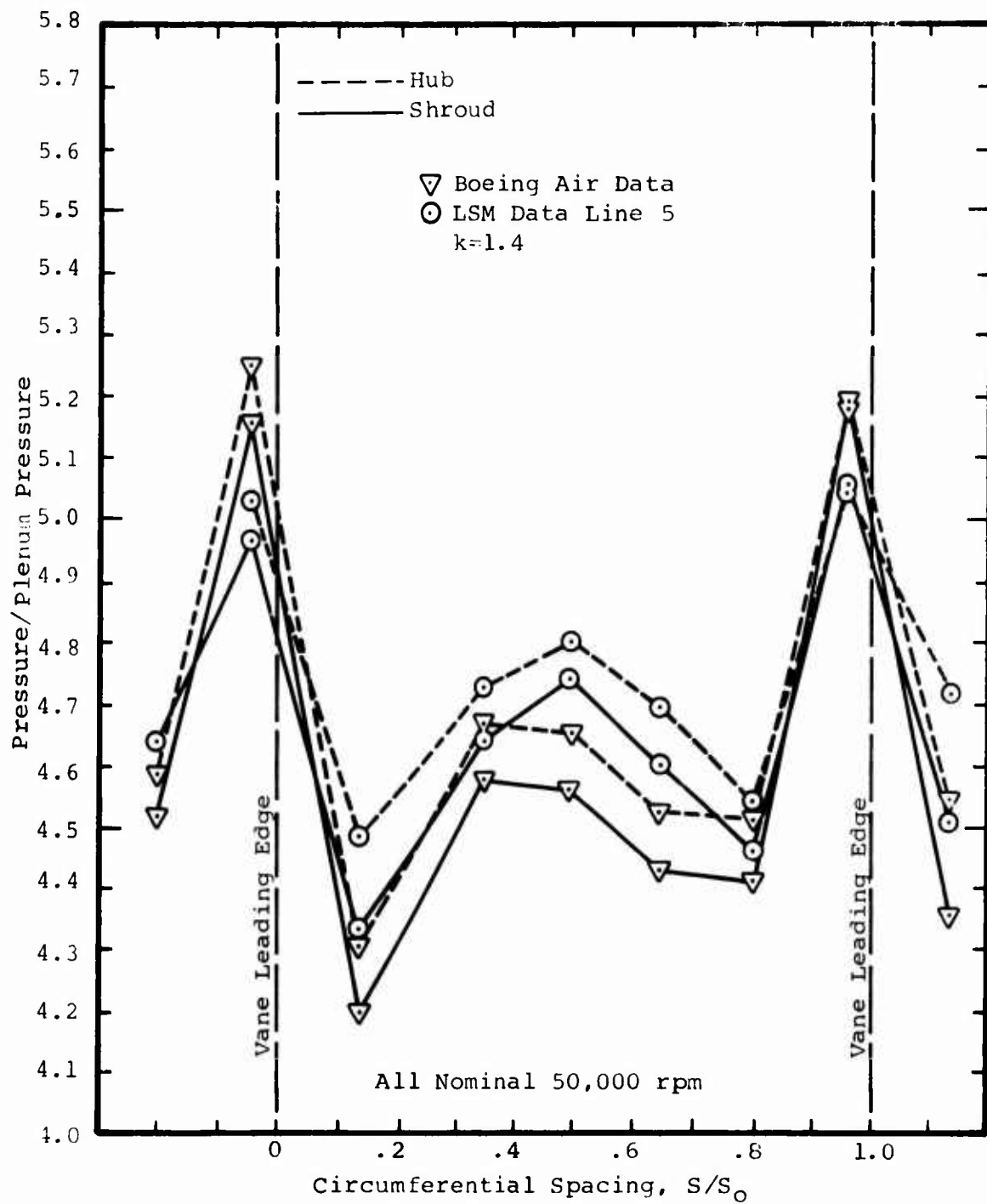


Figure 49. Circumferential Variation of Impeller Exit Static Pressure for LSM and Air.

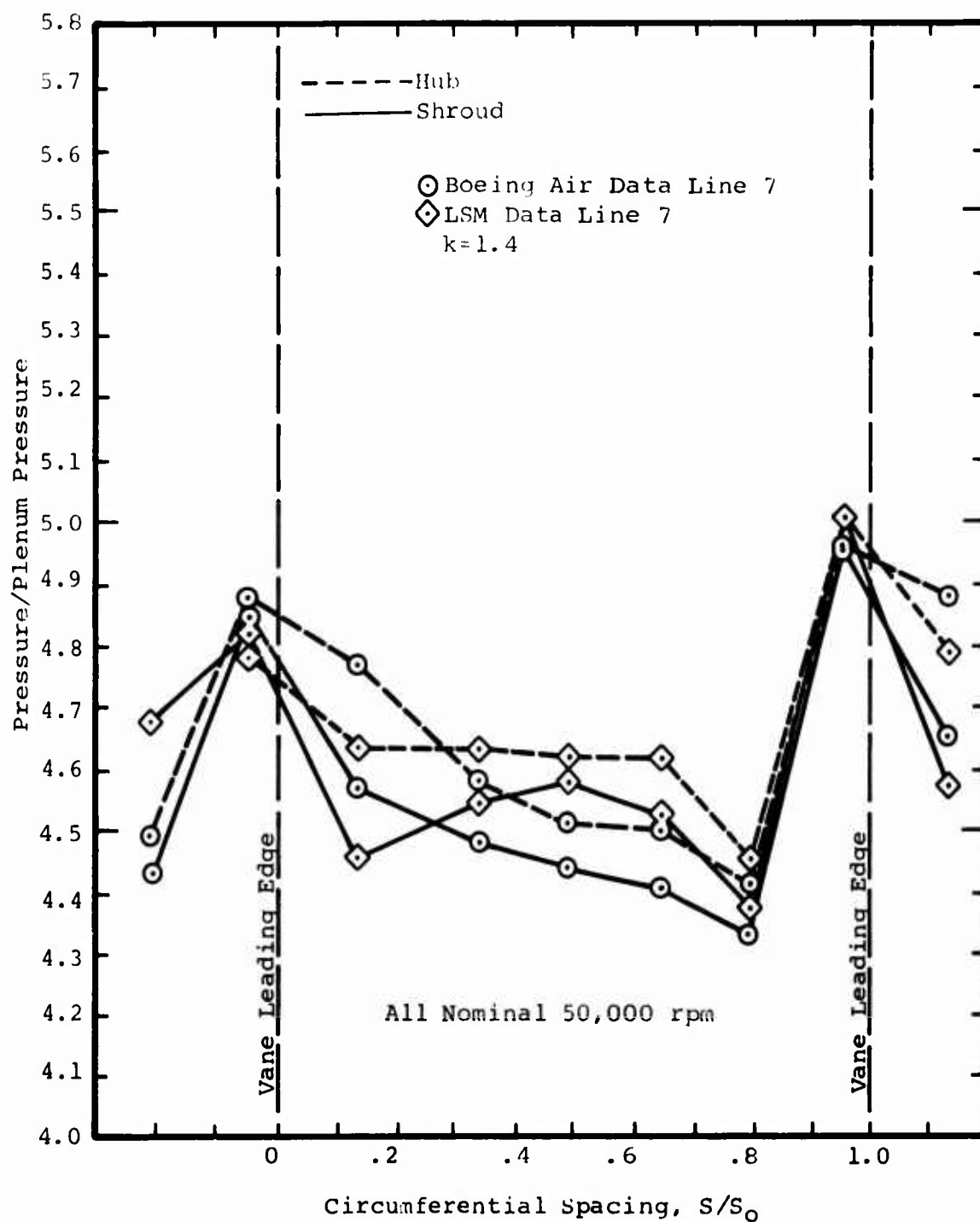


Figure 50. Circumferential Variation of Impeller Exit Static Pressure for LSM and Air.

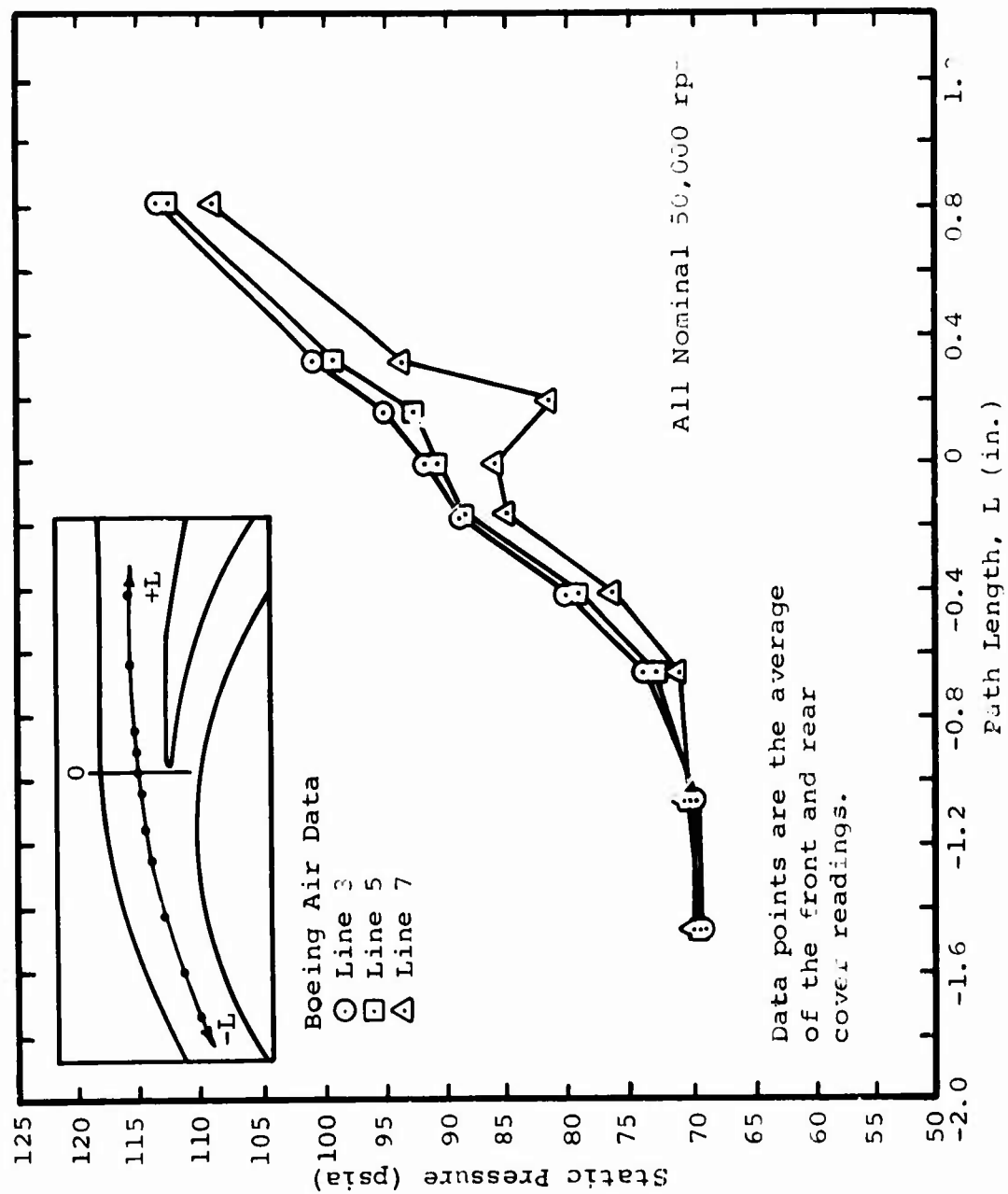


Figure 51. Static Pressure Variation Through the Diffuser.

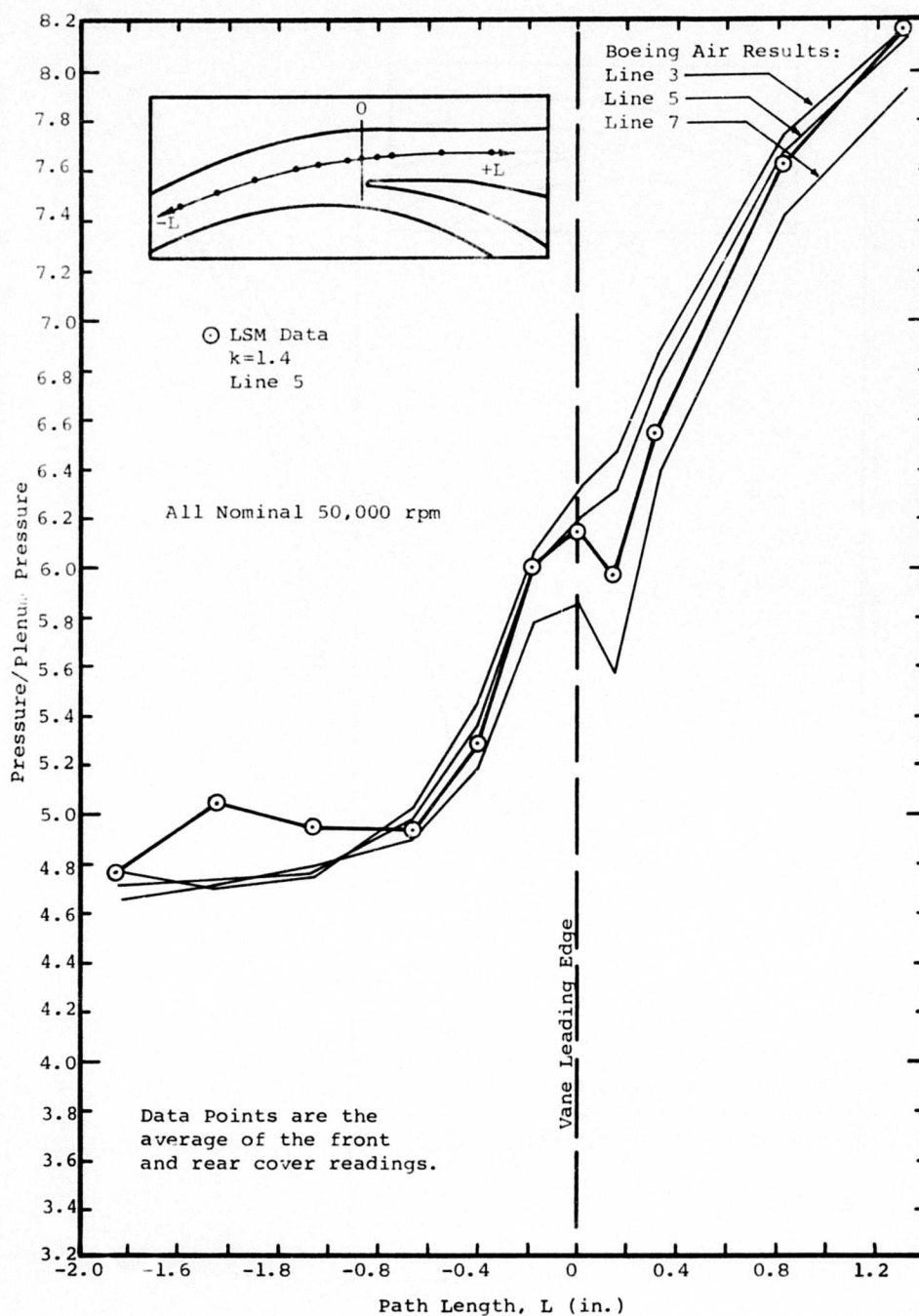


Figure 52. Static Pressure Variation Through the Diffuser.

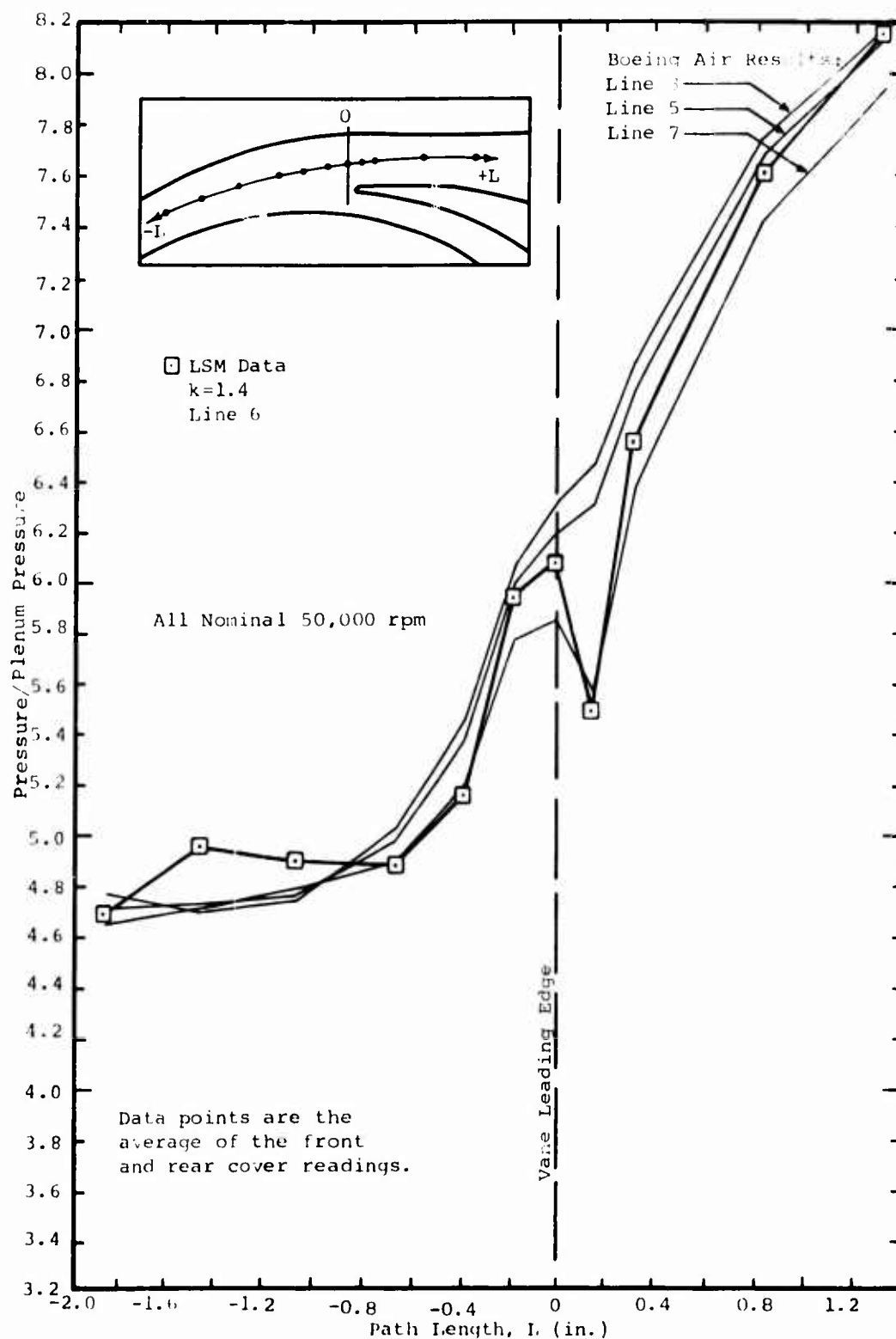


Figure 53. Static Pressure Variation Through the Diffuser.

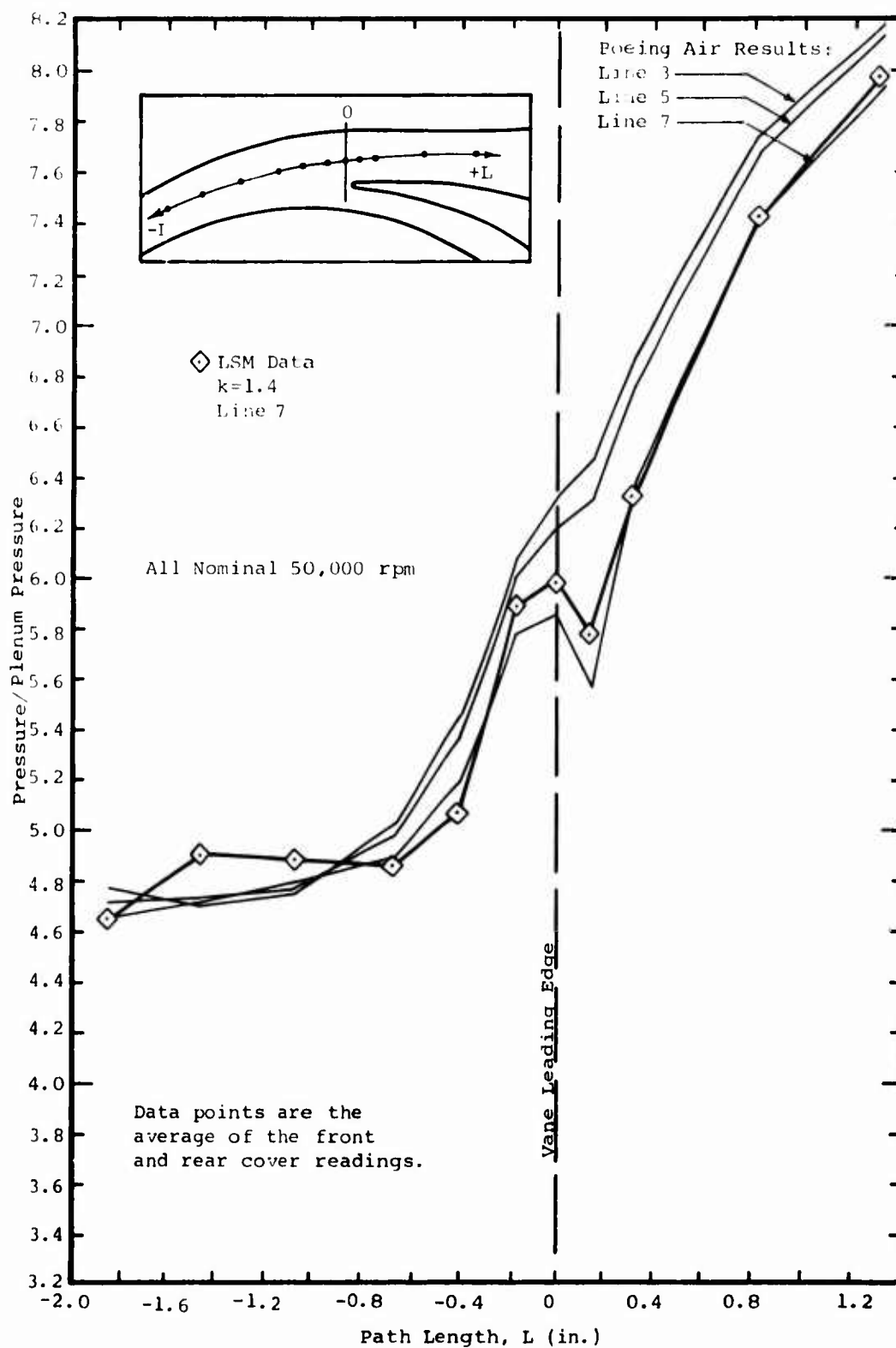


Figure 54. Static Pressure Variation Through the Diffuser.

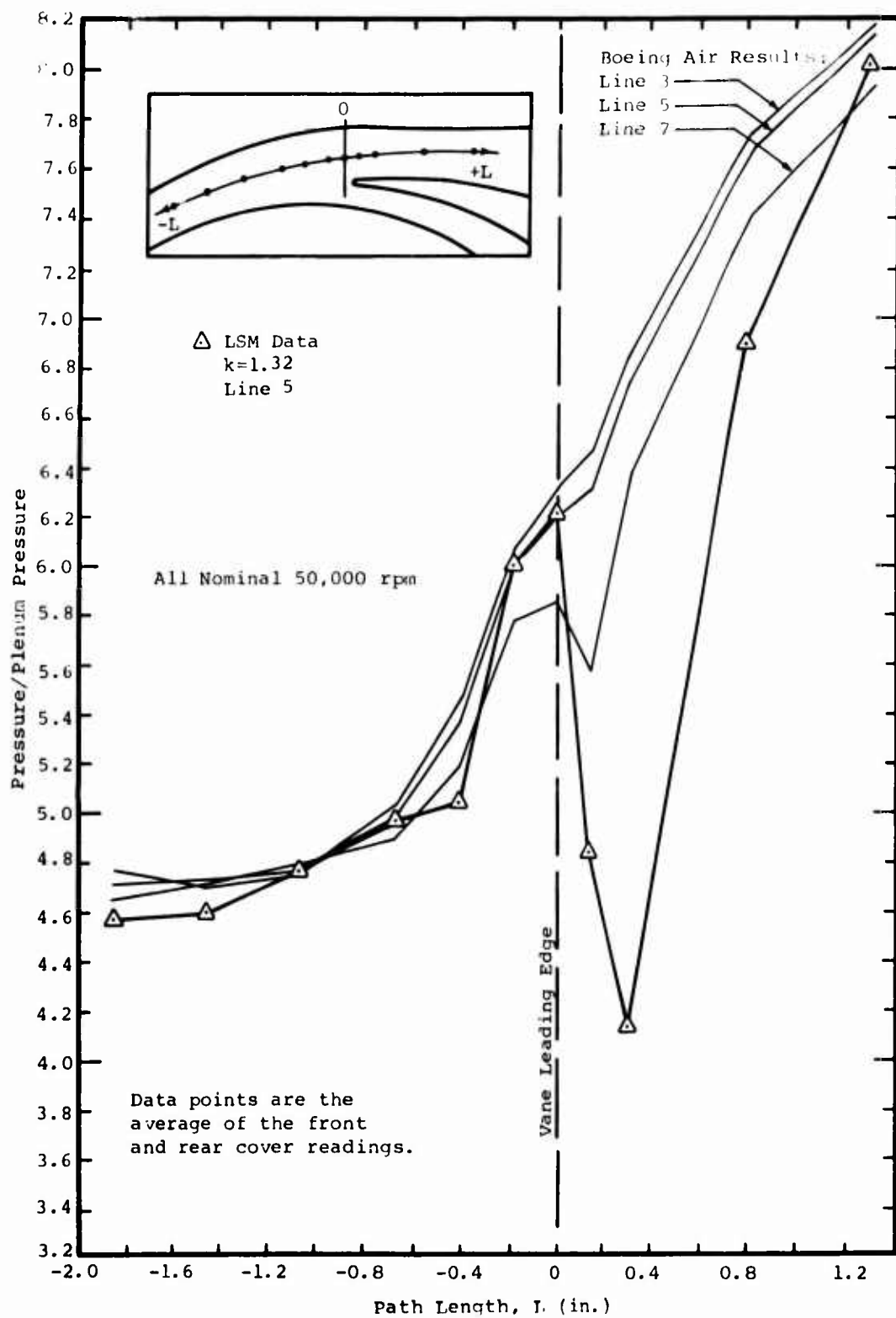


Figure 55. Static Pressure Variation Through the Diffuser.

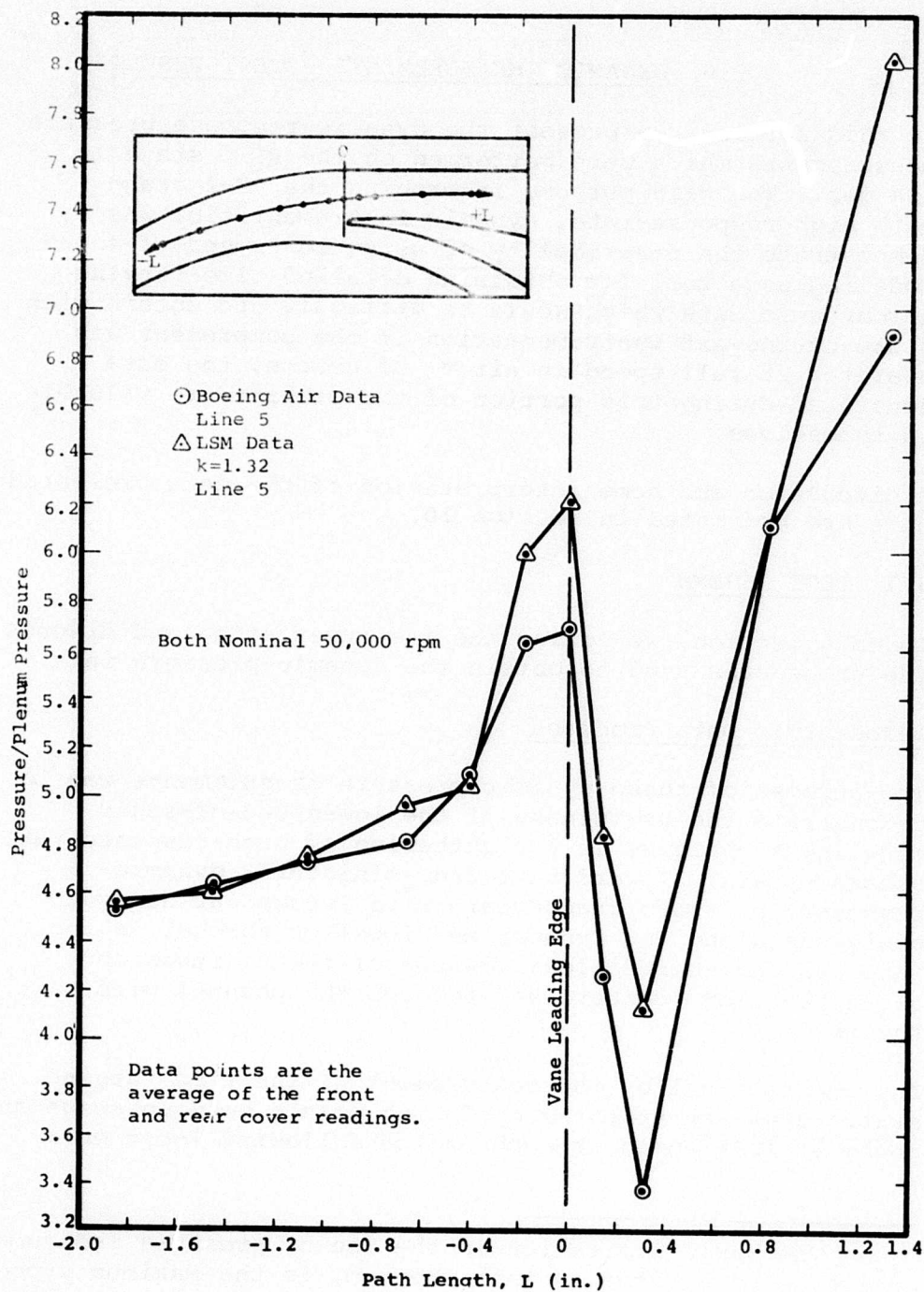


Figure 56. Static Pressure Variation Through the Diffuser.

9.0 DYNAMICS MEASUREMENTS - TEST RESULTS

In this section, we present the dynamic-response pressure measurements which were performed on the RF-2 stage in LSM gas. The main purpose in probing the RF-2 stage with high-response-rate, dynamic instrumentation was to demonstrate the practicality of using low-speed-of-sound modeling as a tool for obtaining detailed time-varying aerodynamic data which would be difficult to obtain with state-of-the-art instrumentation if the compressor was operated at full speed in air.* Of course, the data generated during this portion of the program are valuable in themselves.

A discussion and some interpretation of the data presented here are presented in Section 10.

9.1 TEST SCHEME

In this section, we review the instrumentation and discuss the procedures used to obtain the dynamic-pressure data.

Aerodynamic Data Produced

The purpose of these dynamic-pressure measurements was to demonstrate the usefulness of the low-speed-of-sound modeling techniques in the gathering of high-response-rate pressure data. Toward this end, miniature, dynamic-response, pressure transducers were located at numerous positions along the inducer and impeller shroud, in the vaneless and semivaneless regions of the diffuser, and along the flow "centerline" through the channel diffuser throat.

The contract called for measurement of the time-varying static pressure at three operating points between surge and choke at 100% speed at each of the following locations:

* The basic limitation in the use of pressure instrumentation, such as used in this program, is the maximum probe temperature.

- 1) Three locations between the impeller inlet and the impeller exit along the impeller cover.
- 2) Three locations on the front cover (shroud side) and three directly opposite locations on the rear cover (hub side) at the 1.03 radius ratio distributed circumferentially between a pair of diffuser vane tips.
- 3) Three locations on the front cover and three corresponding locations on the rear cover along the "centerline" of a single diffuser flow passage in the semivaneless space of the diffuser.
- 4) Three locations on the front cover and three locations on the rear cover along the channel "centerline" of a single diffuser passage in the region of the diffuser throat.

The contract also called for measurement of the time-varying total pressure at three operating points between surge and choke at 100% speed at each of the following locations:

- 1) Just downstream of the diffuser throat so that minimal flow blockage is produced by the probe.
- 2) Along the "centerline" of the diffuser passage in the vaneless space.
- 3) Along the "centerline" of the diffuser passage in the semivaneless space between the impeller tip and the throat of the diffuser.

Measurements of the dynamic* pressure were made at, typically, four or five different operating state points between choke and surge at each of the above specified locations and at several other selected locations as well. Selected samples of the time-varying pressure data are presented in this report.

* "dynamic" pressure \equiv "time-varying" or "instantaneous" pressure

Instrumentation

All aerodynamic instrumentation for these tests is described in Section 7. We briefly summarize the instrumentation relevant to the dynamic-pressure measurements here.

The locations of the static and total-pressure taps for the dynamic-pressure measurements are shown in Figures 12 and 13. These taps were located in the same positions (relative to the diffuser vanes) as some of the original Boeing time-averaged static-pressure taps but, of course, in a different diffuser passage. The exact location of these pressure taps is presented in Table V.

Table V, when used in conjunction with Figures 12 and 13, also gives the angular location of the impeller blading relative to these pressure taps when the impeller position signal reaches its minimum. (See Figure 17.) This impeller-position-indicator signal of Figure 17b will be shown, much compressed in time, in the data record photos to be presented later in this section.

Four strain-gauge-type pressure transducers with semiconductor sensing elements were utilized for this program. These transducers had a pressure-sensitive surface of 0.085" diameter. This diameter corresponds to an angular width of about 1.1° at the impeller tip and an angular width of about 2.7° in the inducer region.

The total-pressure probe is shown in Figure 15. The inside diameter of the total-pressure tube was 0.023", the outside diameter of the tube was 0.032", and the diameter of the total-pressure hole in the tube was 0.013". A transducer was threaded inside the total-pressure probe with the pressure-sensing surface of the transducer located 0.002" from the end of the tube. After completion of the program covered by this contract, the total-pressure probe was checked for frequency response on a bench-top setup. This check indicated that its response was less than 1,000 Hz. On the other hand, the dynamic pressure transducers are believed to have a basic frequency response in excess of 100,000 Hz.

When the first set of dynamic pressure data revealed the presence of low-frequency (60 Hz) electrical noise and high-frequency (250 kHz) "ringing" noise on the transducer

signals, a variable high- and low-pass filter was incorporated. This filter was utilized for about 50% of the data records. Tests were conducted which verified that the filtering did not affect the amplitude, phase, or frequency response of the pressure signals in the frequency range of interest.

Operating State Points

For the dynamic measurement portion of this program, a fine-adjustment valve was added in parallel to the larger, coarse-setting back-pressure valve in the LSM flow loop. This addition allowed for quite precise duplication of the operating "line" from test-to-test independent of small fluctuations in air-equivalent compressor speed. (Recall that the term "line" refers to a semiquantitative line between choke and surge located approximately parallel to the surge line and to the constant efficiency lines.)

This fine back-pressure-adjustment capability also allowed us to approach the surge limit more slowly. Doing this, we found that we could operate quite stably beyond Boeing's surge line. In addition, as this valve was closed further, we would hit a "surge" lasting only several seconds before the stage recovered; the frequency of these surges was governed by the amount of closure of the valve. That is, it appeared that, in the operating region between "completely stable" and "hard surge," the onset of a momentary "surge" was caused by "random" fluctuations in the system. Whether any one of these fluctuations put the stage into "surge" depended upon how close we were to the onset of "hard surge". By adjusting the position of the back-pressure valve, we could make "surge" occur at any frequency between several minutes and several seconds (averaged over a number of "surge" incidents). Thus, we discovered a "metastable" operating region beyond Boeing's surge line.

We have used the dynamic-pressure probes to study the onset and character of surge. The preliminary data indicates that with the RF-2 at 50,000 rpm, rotating stall does not exist. Surge appears to have a "one-dimensional" character.

The operating state point regions for the dynamic-pressure measurements are shown in Figure 57. Regions C, D and E are at or near choke, Regions A and B are between choke and surge, and Region S-A is just before surge. The length of the regions is due to variations in the air-equivalent speed from test to test. No change was observed in any of the fluctuating pressure signals in any one state point region with speed variations in this range. The data presented in Section 9.3 will be referred to the state points indicated on Figure 57.

9.2 DYNAMIC PRESSURE DATA

In this section we describe how to "read" the data photos, present selected samples of the dynamic pressure data photos, and discuss how the total-pressure probes affected the compressor aerodynamics.

How to "Read" the Data Photos

Two types of dynamic pressure data photos are contained in this report. An example of each type is shown in Figure 58. The particular examples shown in Figure 58 are from the rear cover (hub side), along the flow path "centerline" in the semivaneless region and at state point C. The map location of state point C is shown on Figure 57. The top photo of Figure 58 displays data from pressure tap 247; the bottom photo shows data from pressure taps 242, 245, 246, and 247 (reading from top to bottom). The physical location of these pressure taps is shown in Figure 12 and in Table V of Section 7.1.

The top (three-trace) photo of Figure 58 shows three signals, all triggered at the same instant and recorded simultaneously. The first and second traces (reading from the top) of this photo are at a sweep rate (horizontal scale) of 0.2 msec/div, and thus the entire length of trace shown corresponds to slightly more than one complete wheel rotation. The third trace is at a sweep rate of 0.05 msec/div, and the total length of this trace corresponds to approximately five impeller blades passing any fixed

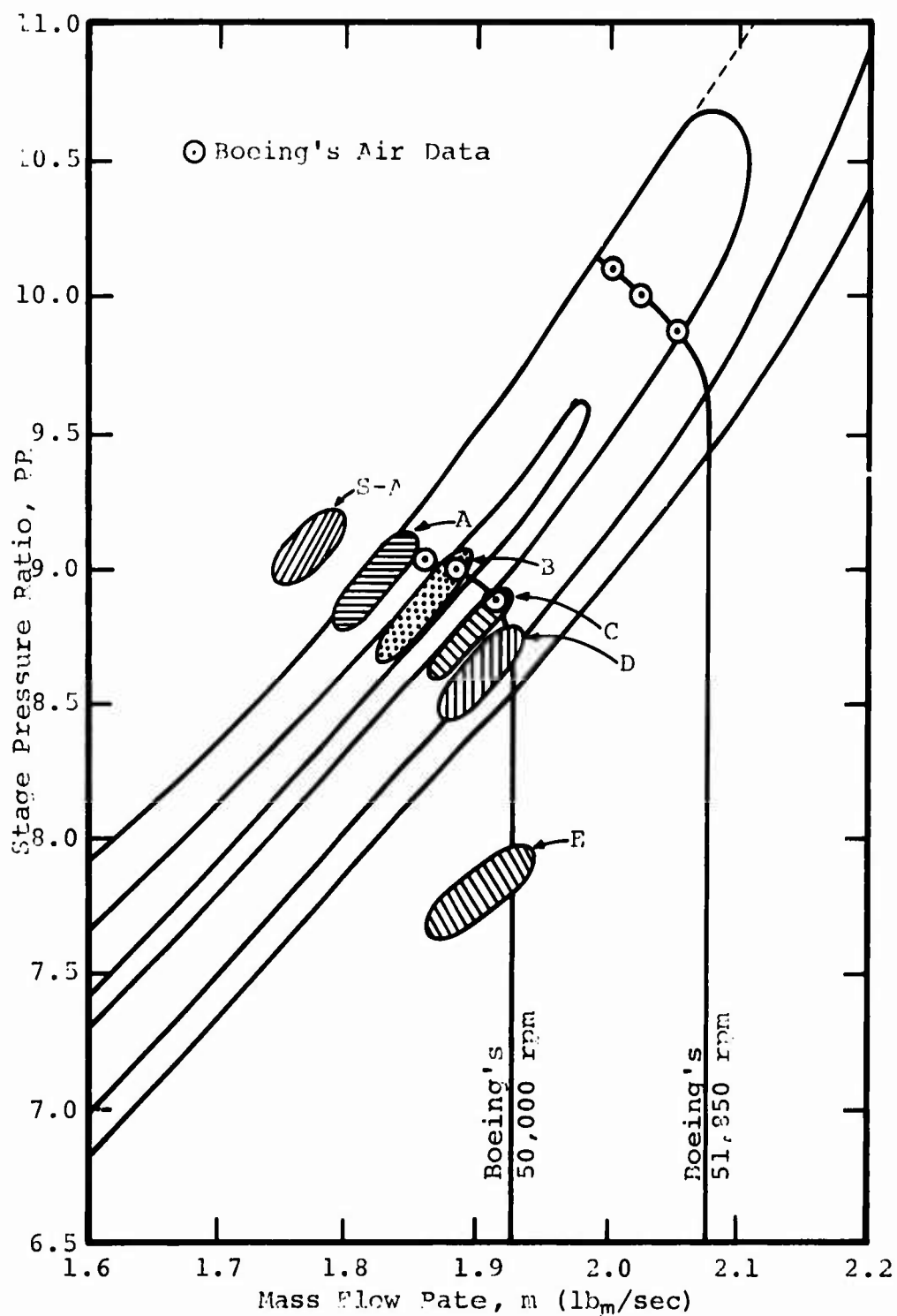
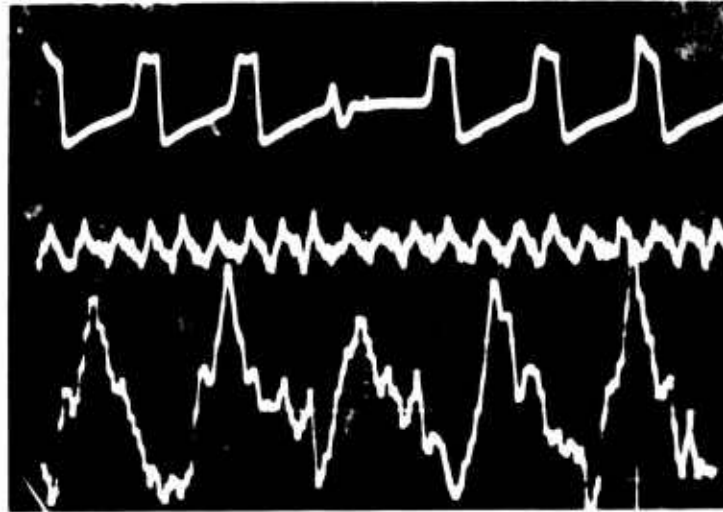
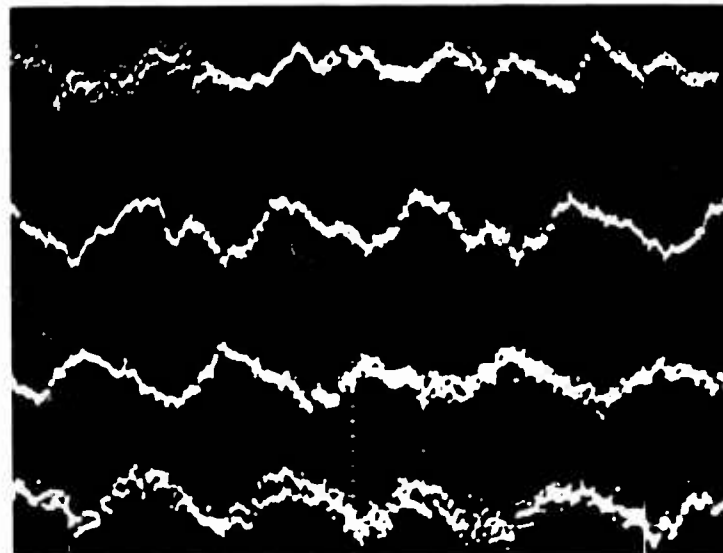


Figure 57. State Point Regions for the Dynamic Pressure Data.



- a. Three-trace photo showing (top-to bottom) impeller position indicator signal, pressure signal during slightly more than one wheel rotation, and pressure signal during five impeller blade passings.



- b. Four-trace photo showing unfiltered pressure signals recorded and triggered simultaneously from four pressure transducers.

Figure 58. Examples of Data Photos.

location. The first trace is the impeller position indicator signal. The small "cycle" in the center of this signal is a compressed version of the signal in Figure 17 of Section 7.1. The impeller blades are at the location indicated in Figure 12 (and Table V) at a time corresponding to the minimum signal of this small cycle. This instant can be interpreted relative to the second trace which is the pressure signal triggered at the same time as the first trace and recorded at the same sweep rate as the first trace.

The second and third traces of the top photo of Figure 58 are simultaneous pressure signals from the same transducer, each trace being triggered at the same time. The vertical scale of the second trace of this photo is 6.78 psi/div; the vertical scale of the third trace is 1.36 psi/div. Thus, the first five cycles of the pressure signal in the second trace are the same five cycles as displayed on the third trace.

The above statements apply to all three-trace photos displayed in this report with the exception that the vertical scales of the three traces may vary from photo to photo. All three traces were always triggered and recorded simultaneously and the sweep rate for the top two traces was always the same (0.2 msec/div).

In Figure 58 the pressure signals on this three-trace photo were filtered; some pressure signals on other three-trace photos were not.

The bottom photo of Figure 58 is an example of the data photos which show the pressure signals from four transducers (taps 242, 245, 246, and 247 in this example) triggered and recorded simultaneously and at the same sweep rate (0.05 msec/div). Thus the full length of the traces in these photos shows the passage of five impeller blades. The vertical scales of these four traces are, in all cases, approximately the same. (However, they may not be precisely identical; e.g., in Figure 58b the vertical scales are 6.58, 6.58, 6.58, and 6.78 psi/div respectively.) The exact vertical scales for all pressure traces of all the data photos presented have been tabulated for easy reference in the following data presentation.

The Dynamic Pressure Data

A selected set of the dynamic pressure data is shown in Figures 59 through 66. The pressure tap number (or numbers for four-trace photos) and the state point for each pressure trace are indicated below each photo. The numbers in parentheses refer to the vertical scale (psi/div) of the bottom trace of each three-trace photo. The vertical scales of all pressure signals of these figures are tabulated in Table IX.

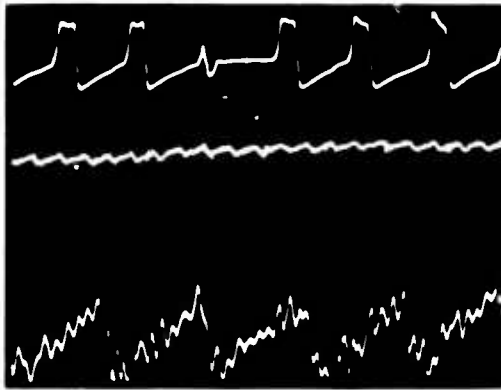
A fluid dynamic interpretation of these data using the compressor flow model discussed in USAAVLABS Technical Report 69-76⁷ is presented in Section 10.

Effect of the Total-Pressure Probes on the Compressor Aerodynamics

Except where indicated, all time-varying static pressure data were taken without a total-pressure probe in place. Furthermore, the total-pressure measurements were made with only one total-pressure probe in place at any one time.

No appreciable change in the compressor map data was observed when the total-pressure probe was located just downstream of the channel diffuser "throat" (pressure tap 303 of Figure 12). However, both the range and maximum pressure ratio were reduced when a total-pressure probe was located in either the vaneless region or the semivaneless region (pressure taps 301 and 302 respectively of Figure 12). The effect on the compressor map of placing the total-pressure probe in these regions is shown in Figures 67 and 68. In each of these figures the lowest mass flow rate shown was experienced just short of the surge limit with the total-pressure probe in locations 301 or 302.

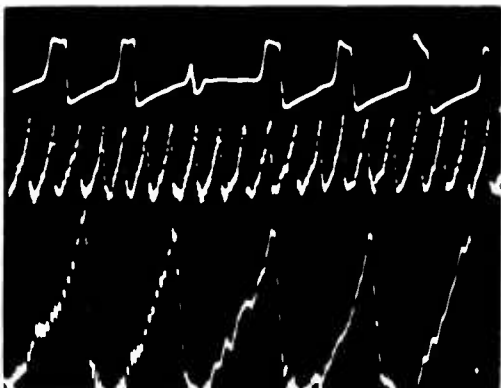
The effect of the total-pressure probes on the time-averaged static pressure variation along the flow path through several diffuser channels is shown in Figures 69, 70, and 71. These figures provide a comparison between the time-averaged static pressure distribution in an open diffuser channel (the data points indicated by circles and triangles) and the time-averaged static pressure distribution in the diffuser channel which contained the total-



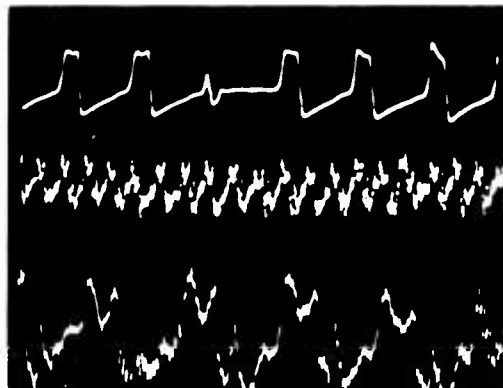
a. Tap 219 (0.69)
State Point A



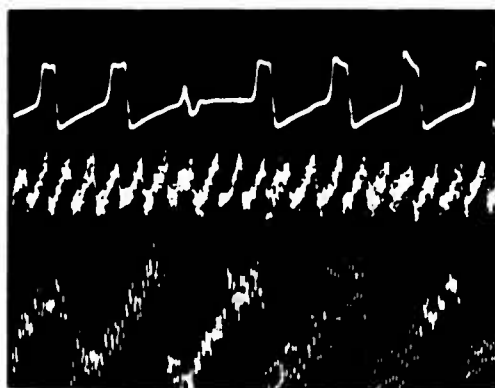
b. Tap 214 (0.68)
State Point A



c. Tap 213 (2.60)
State Point A



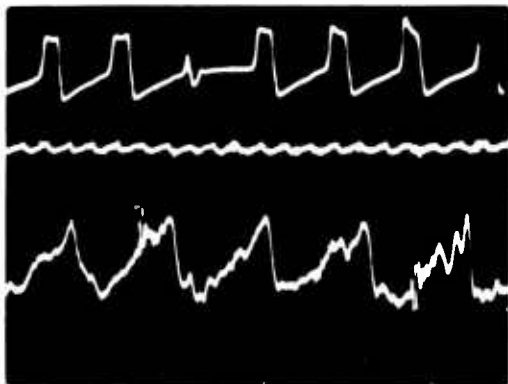
d. Tap 212 (2.60)
State Point A



e. Tap 211 (2.61)
State Point A

[Numbers in parentheses refer to the vertical scale (psi/div) of the bottom trace in each photo. See Table IX and Figure 58 for key to photos.]

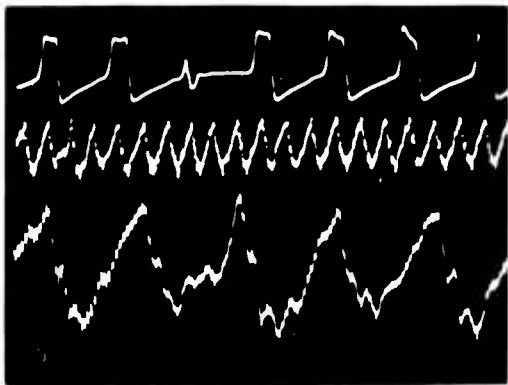
Figure 59. Impeller Shroud Pressure Fluctuations.



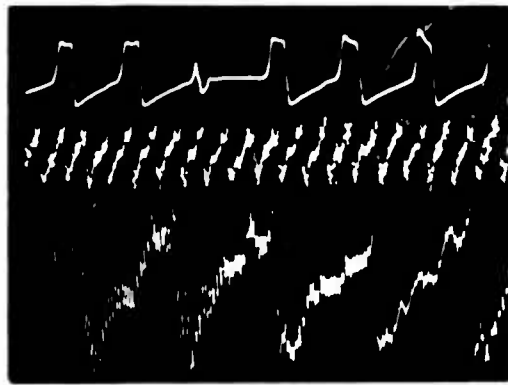
a. Tap 219 (0.69)
State Point D



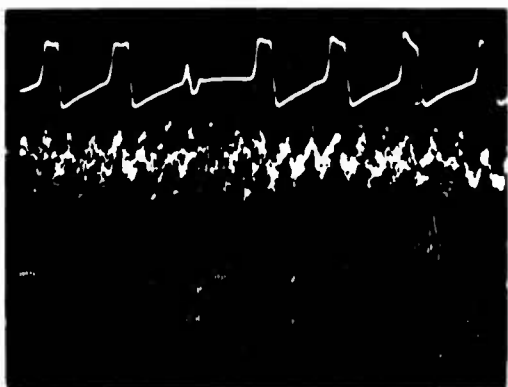
b. Tap 214 (0.68)
State Point D



c. Tap 213 (2.60)
State Point D



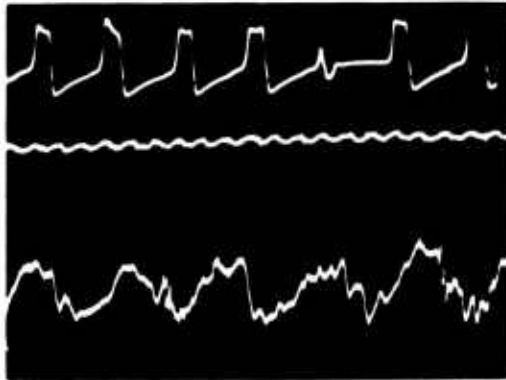
d. Tap 212 (2.60)
State Point D



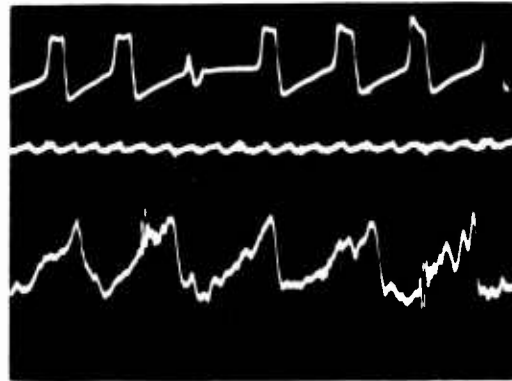
e. Tap 211 (2.61)
State Point D

[Numbers in parentheses refer to the vertical scale (psi/div) of the bottom trace in each photo. See Table IX and Figure 58 for key to photos.]

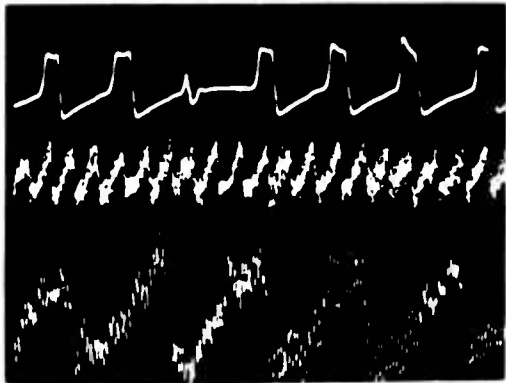
Figure 60. Impeller Shroud Pressure Fluctuations.



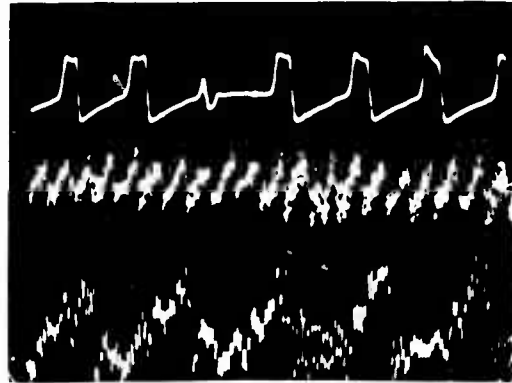
a. Tap 219 (0.69)
State Point D



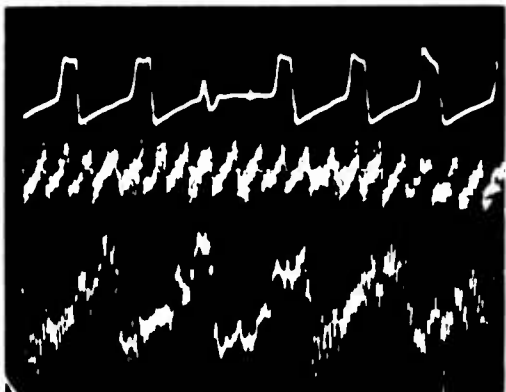
b. Tap 219 (0.69)
State Point D



c. Tap 211 (2.61)
State Point A



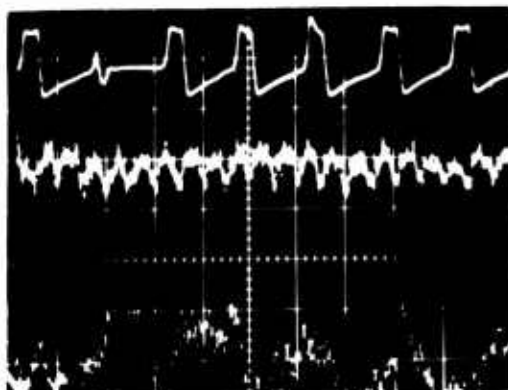
d. Tap 211 (2.60)
State Point A



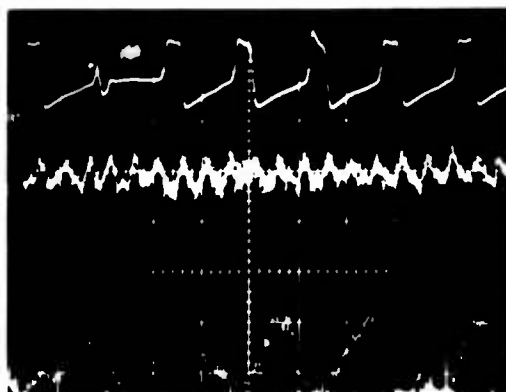
e. Tap 211 (2.60)
State Point A

[Numbers in parentheses refer to the vertical scale (psi/div) of the bottom trace in each photo. See Table IX and Figure 58 for key to photos.]

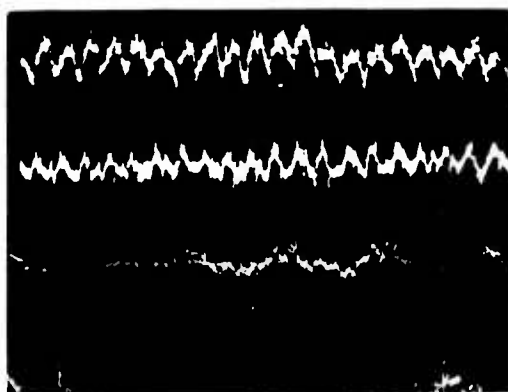
Figure 61. Impeller Shroud Pressure Fluctuations.



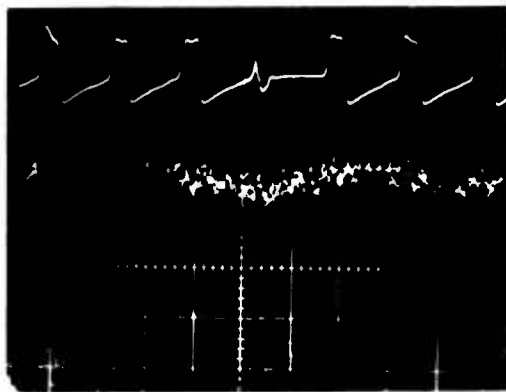
a. Tap 201 (2.60)
State Point A



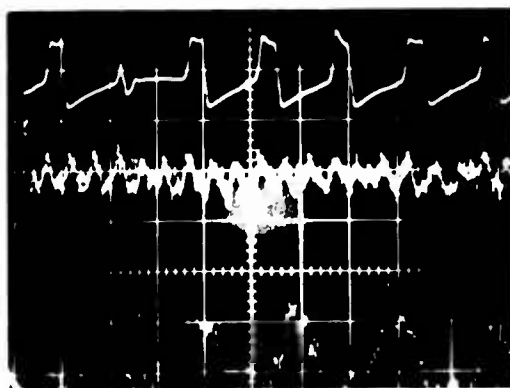
b. Tap 202 (2.60)
State Point A



c. Tap 203 (2.60)
State Point A



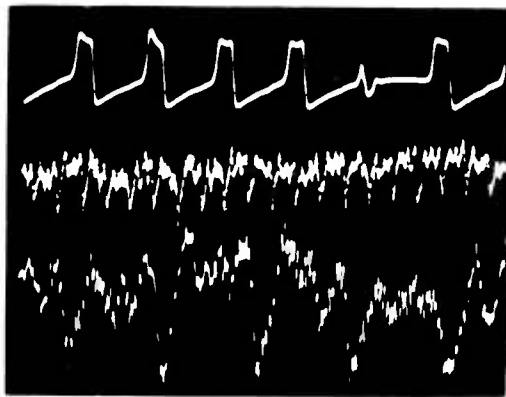
d. Tap 204 (2.70)
State Point A



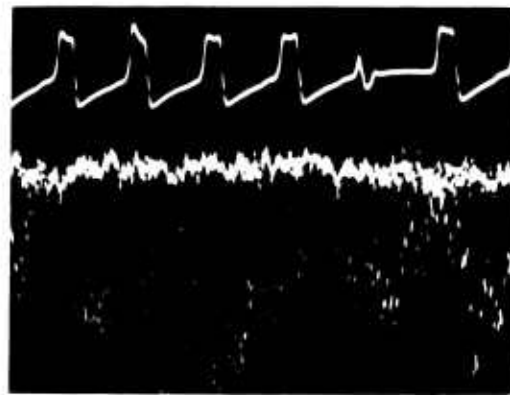
e. Taps 201, 202, 203, 204
State Point A

[Numbers in parentheses refer to the vertical scale (psi/div) of the bottom trace in each photo. See Table IX and Figure 58 for key to photos.]

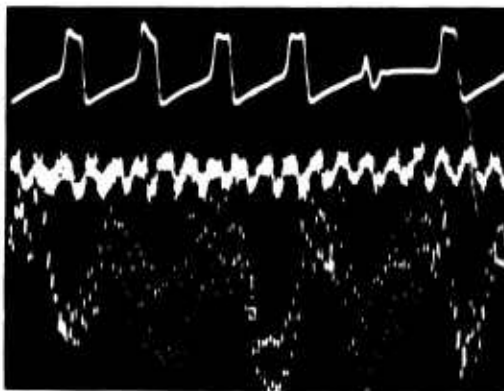
Figure 62. Impeller Exit Shroud Pressure Fluctuations.



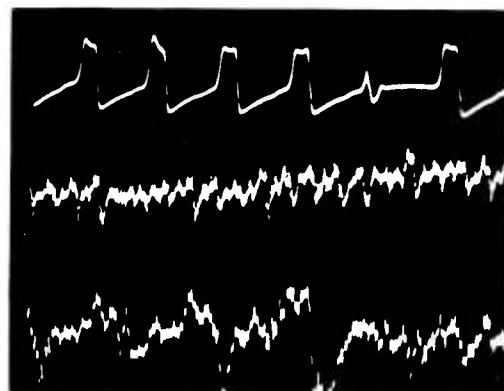
a. Tap 241 (2.60)
State Point A



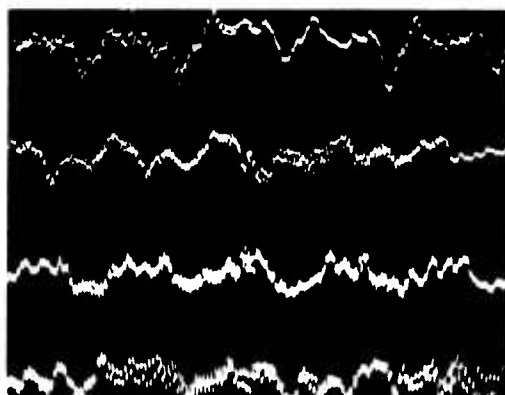
b. Tap 242 (2.60)
State Point A



c. Tap 243 (1.30)
State Point A



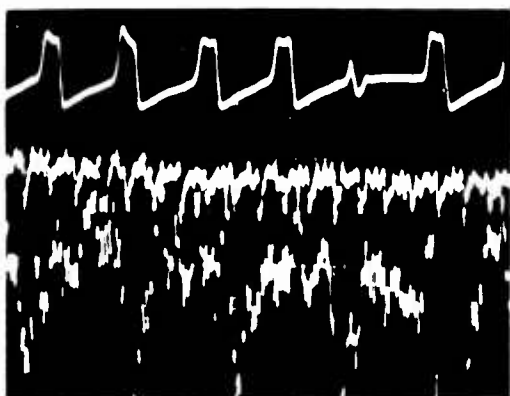
d. Tap 244 (1.35)
State Point A



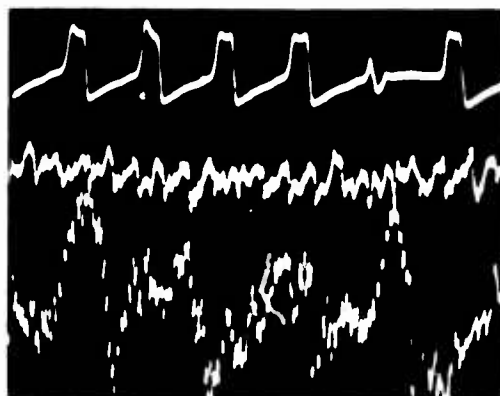
e. Taps 241, 242, 243, 244
State Point A

[Numbers in parentheses refer to the vertical scale (psi/div) of the bottom trace in each photo. See Table IX and Figure 58 for key to photos.]

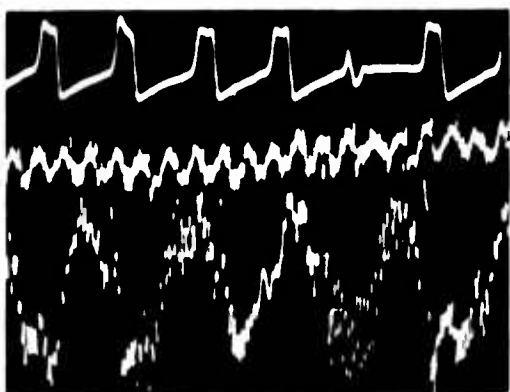
Figure 63. Impeller Exit Hub Pressure Fluctuations.



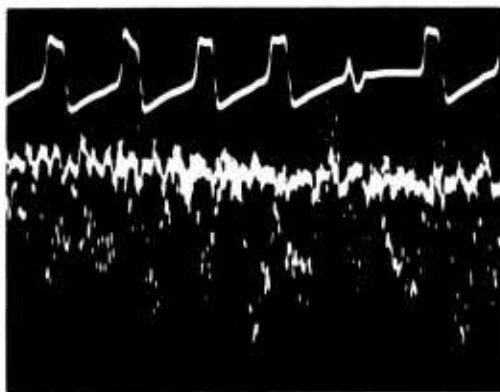
a. Tap 241 (1.30)
State Point D



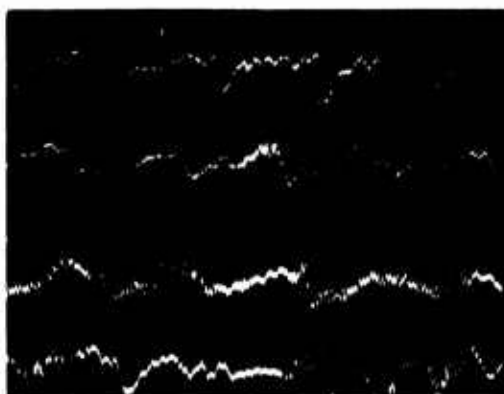
b. Tap 242 (1.30)
State Point D



c. Tap 243 (1.30)
State Point D



d. Tap 244 (1.35)
State Point D



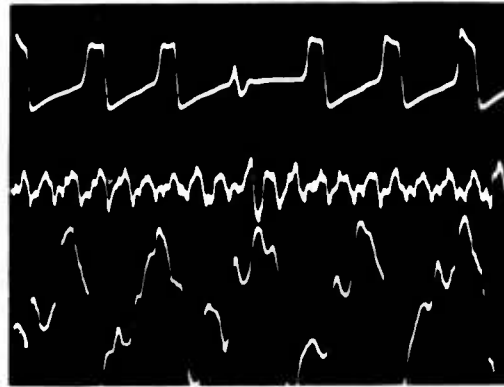
e. Taps 241, 242, 243, 244
State Point D

[Numbers in parentheses refer to the vertical scale (psi/div) of the bottom trace in each photo. See Table IX and Figure 58 for key to photos.]

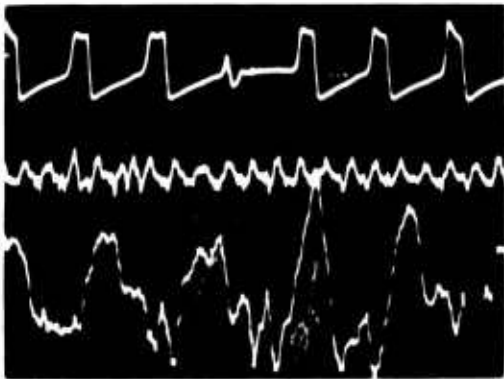
Figure 64. Impeller Exit Hub Pressure Fluctuations.



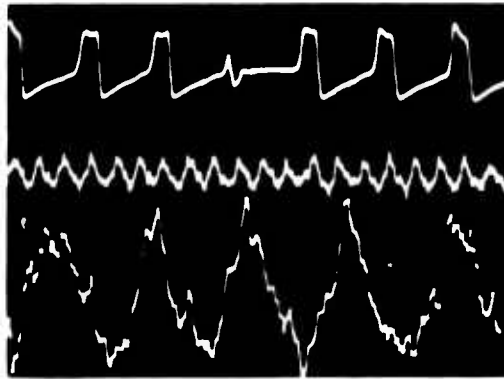
a. Tap 242 (1.32)
State Point D



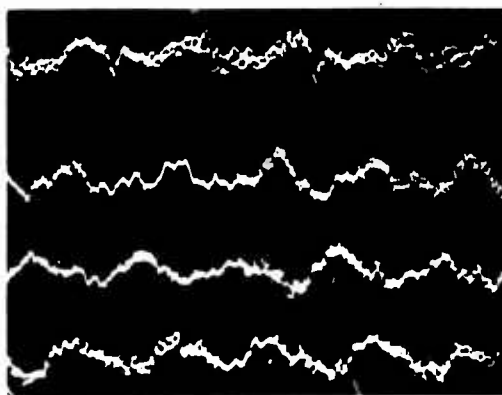
b. Tap 245 (1.32)
State Point D



c. Tap 246 (1.32)
State Point D



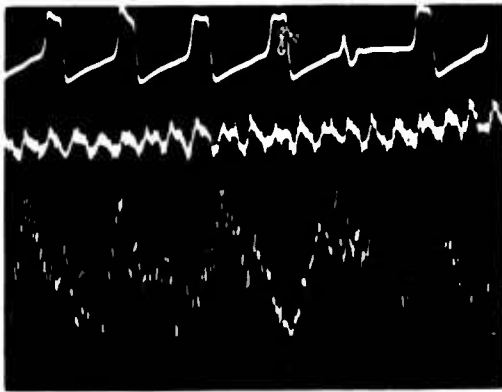
d. Tap 247 (1.36)
State Point D



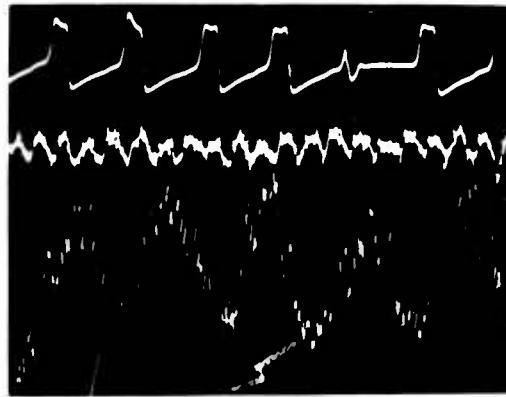
e. Taps 242, 245, 246, 247
State Point D

[Numbers in parentheses refer to the vertical scale (psi/div) of the bottom trace in each photo. See Table IX and Figure 58 for key to photos.]

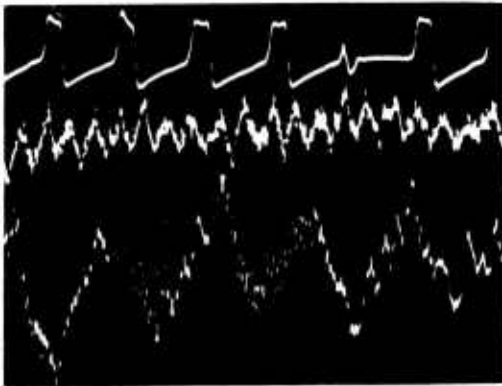
Figure 65. Semivaneless Hub Pressure Fluctuations.



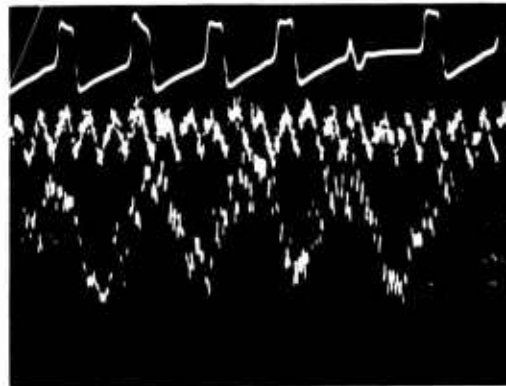
a. Tap 246 (1.32)
State Point A



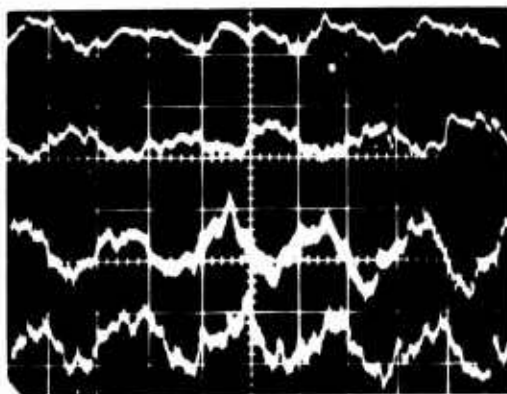
b. Tap 247 (1.32)
State Point A



c. Tap 248 (2.63)
State Point A



d. Tap 249 (2.74)
State Point A



e. Taps 246, 247, 248, 249
State Point A

[Numbers in parentheses refer to the vertical scale (psi/div) of the bottom trace in each photo. See Table IX and Figure 58 for key to photos.]

Figure 66. Diffuser Hub Pressure Fluctuations.

**TABLE IX. VERTICAL SCALES OF THE DYNAMIC
PRESSURE DATA PHOTOS**

| Figure Number | Tap Number (see Fig. 12) | State Point (see Fig. 57) | First Trace Vertical Scale* (psi/ div) | Second Trace Vertical Scale* (psi/ div) | Third Trace Vertical Scale* (psi/ div) | Fourth Trace Vertical Scale* (psi/ div) |
|------------------|-----------------------------------|------------------------------------|---|--|---|--|
| 59a | 219 | A | - | 6.90 | 0.69 | - |
| 59b | 214 | A | - | 6.80 | 0.68 | - |
| 59c | 213 | A | - | 6.50 | 2.60 | - |
| 59d | 212 | A | - | 6.50 | 2.60 | - |
| 59e | 211 | A | - | 6.53 | 2.61 | - |
| 60a | 219 | D | - | 6.90 | 0.69 | - |
| 60b | 214 | D | - | 6.80 | 0.68 | - |
| 60c | 213 | D | - | 6.50 | 2.60 | - |
| 60d | 212 | D | - | 6.50 | 2.60 | - |
| 60e | 211 | D | - | 6.53 | 2.61 | - |
| 61a | 219 | D | - | 6.90 | 0.69 | - |
| 61b | 219 | D | - | 6.90 | 0.69 | - |
| 61c | 211 | A | - | 6.53 | 2.61 | - |
| 61d | 211 | A | - | 6.50 | 2.60 | - |
| 61e | 211 | A | - | 6.50 | 2.60 | - |
| 62a | 201 | A | - | 6.50 | 2.60 | - |
| 62b | 202 | A | - | 6.50 | 2.60 | - |
| 62c | 203 | A | - | 6.50 | 2.60 | - |
| 62d | 204 | A | - | 6.75 | 2.70 | - |
| 62e | Comp. | A | 6.50 | 6.50 | 6.50 | 6.75 |
| 63a | 241 | A | - | 6.50 | 2.60 | - |
| 63b | 242 | A | - | 6.50 | 2.60 | - |
| 63c | 243 | A | - | 6.50 | 1.30 | - |
| 63d | 244 | A | - | 6.75 | 1.35 | - |
| 63e | Comp. | A | 6.50 | 6.50 | 6.50 | 6.75 |
| 64a | 241 | D | - | 6.50 | 1.30 | - |

* The horizontal scales for all three-trace photos are: first and second traces, 0.2 msec/div; third trace, 0.05 msec/div. The horizontal scales for the four-trace photos are 0.05 msec/div for all four traces.

TABLE IX - Continued

| Figure Number | Tap Number (see Fig. 12) | State Point (see Fig. 57) | First Trace Vertical Scale* (psi/div) | Second Trace Vertical Scale* (psi/div) | Third Trace Vertical Scale* (psi/div) | Fourth Trace Vertical Scale* (psi/div) |
|---------------|-----------------------------|------------------------------|--|---|--|---|
| 64b | 242 | D | - | 6.50 | 1.30 | - |
| 64c | 243 | D | - | 6.50 | 1.30 | - |
| 64d | 244 | D | - | 6.75 | 1.35 | - |
| 64e | Comp. | D | 6.50 | 6.50 | 6.50 | 6.75 |
| 65a | 242 | D | - | 6.58 | 1.32 | - |
| 65b | 245 | D | - | 6.58 | 1.32 | - |
| 65c | 246 | D | - | 6.58 | 1.32 | - |
| 65d | 247 | D | - | 6.78 | 1.36 | - |
| 65e | Comp. | D | 6.58 | 6.58 | 6.58 | 6.78 |
| 66a | 246 | A | - | 6.58 | 1.32 | - |
| 66b | 247 | A | - | 6.58 | 1.32 | - |
| 66c | 248 | A | - | 6.58 | 2.63 | - |
| 66d | 249 | A | - | 6.85 | 2.74 | - |
| 66e | Comp. | A | 6.58 | 6.58 | 6.58 | 6.85 |

*The horizontal scales for all three-trace photos are: first and second traces, 0.2 msec/div; third trace, 0.05 msec/div. The horizontal scales for the four-trace photos are 0.05 msec/div for all four traces.

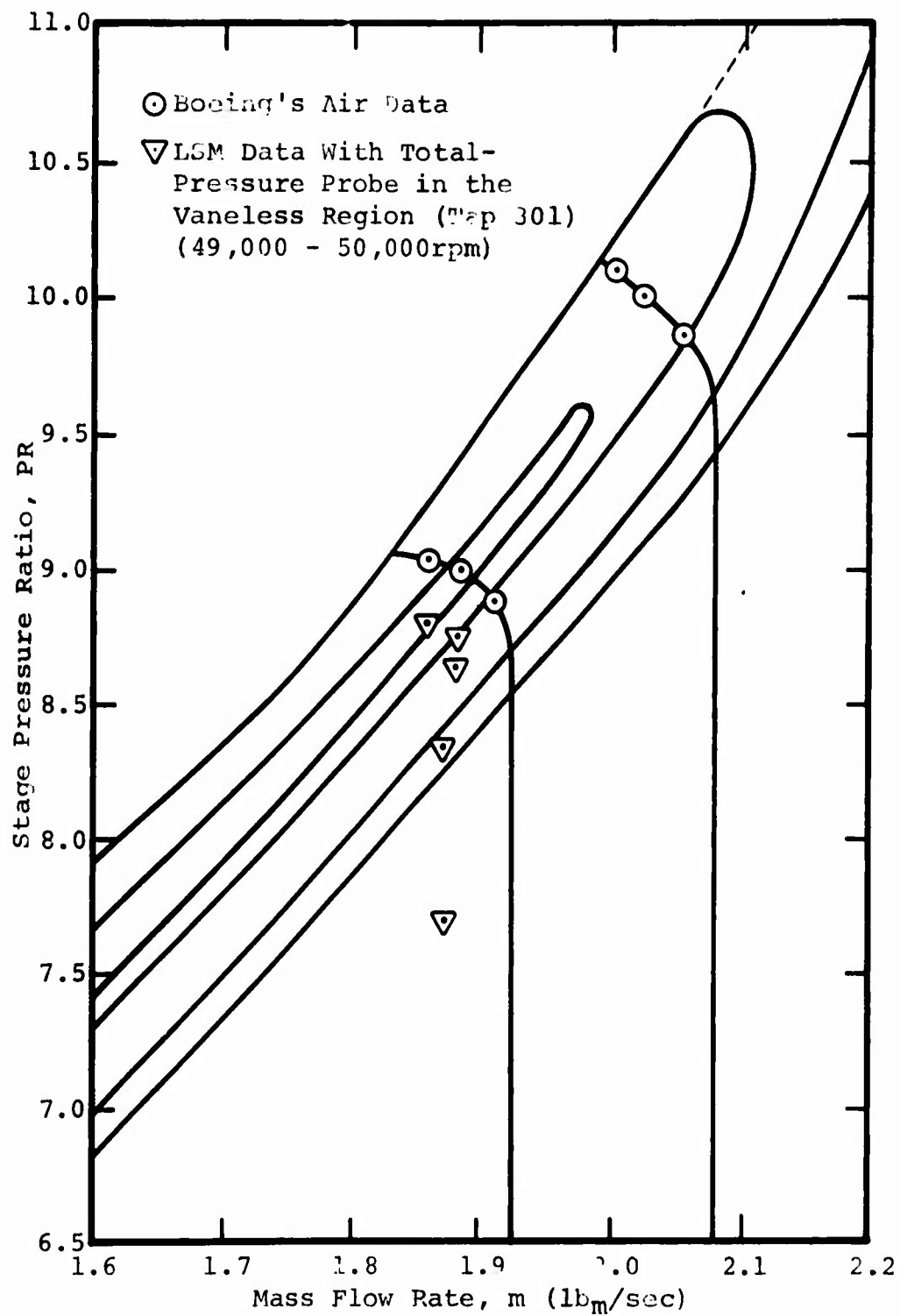


Figure 67. Effect of the Total-Pressure Probe at Tap 301 on the Compressor Map.

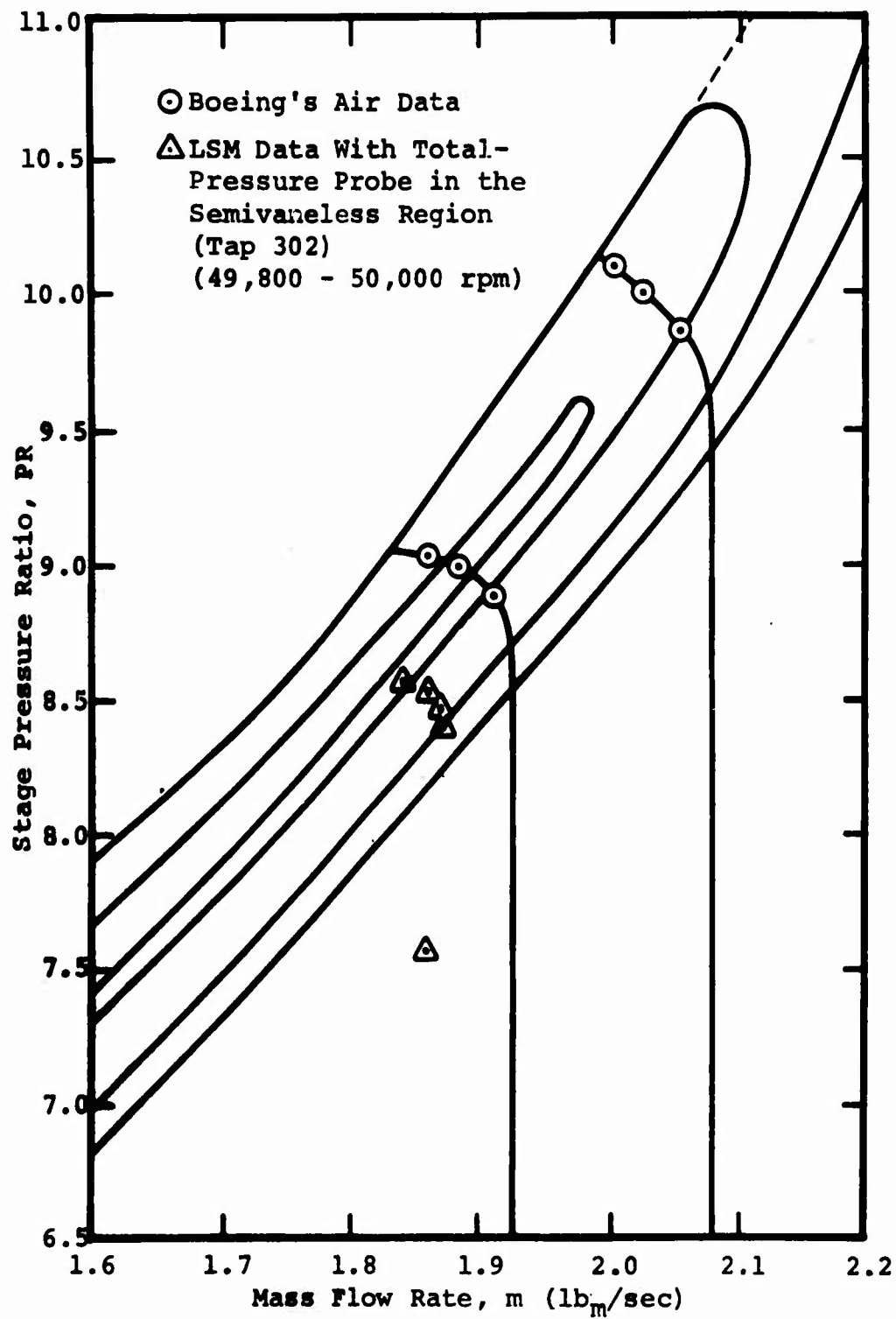


Figure 68. Effect of the Total-Pressure Probe at Tap 302 on the Compressor Map.

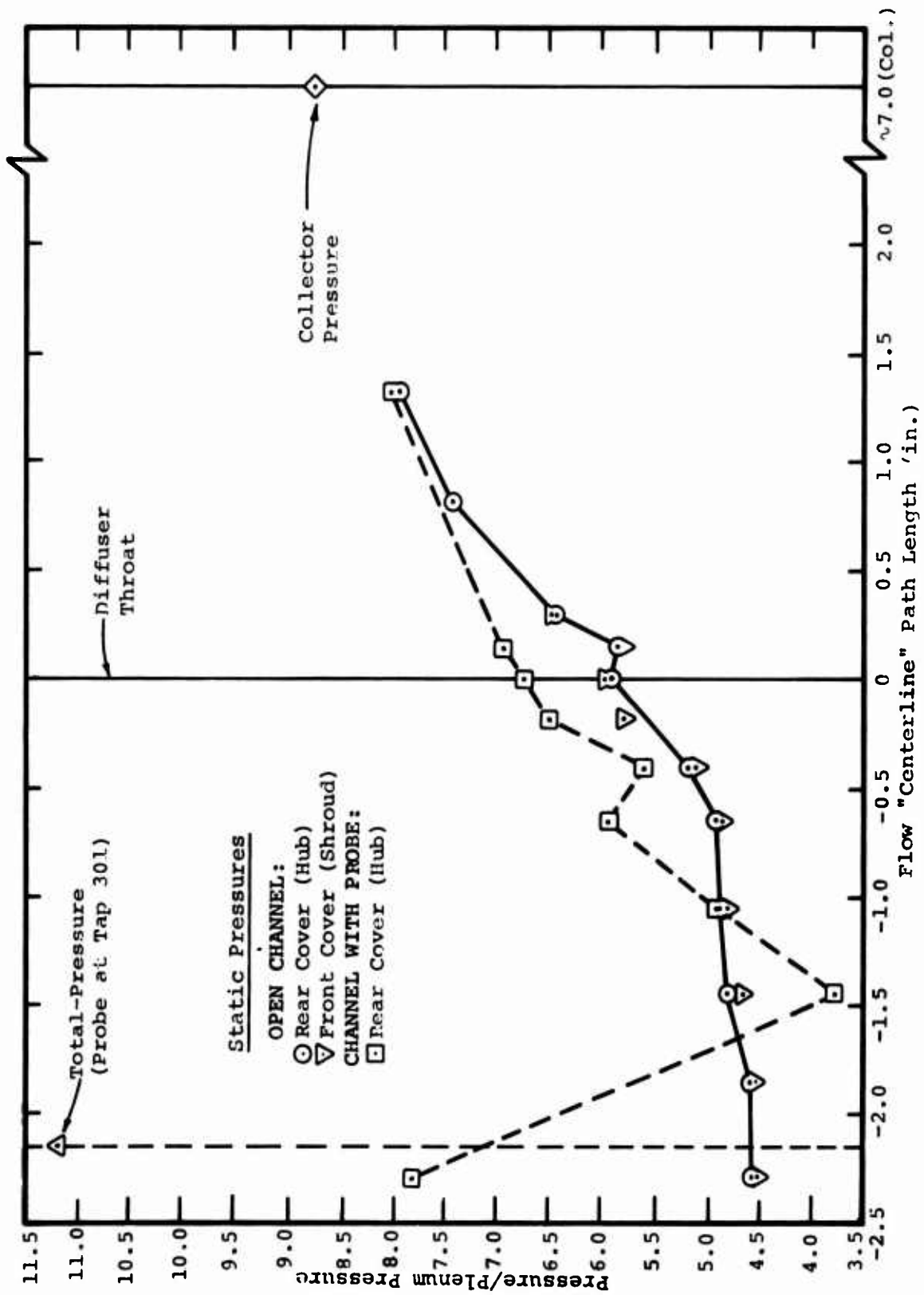


Figure 69. Effect of Total-Pressure Probe on Time-Average Static Pressures.

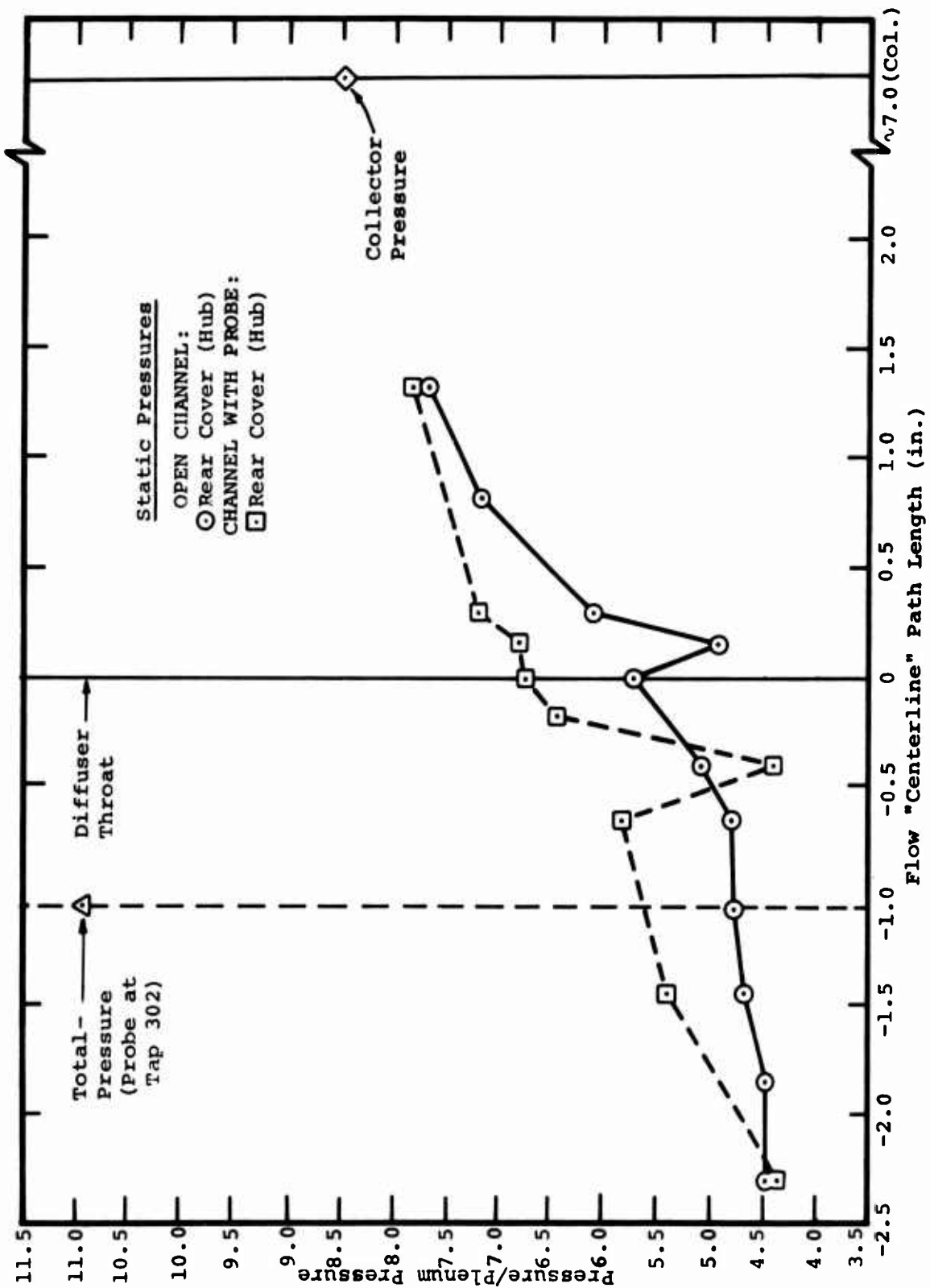


Figure 70. Effect of Total-Pressure Probe on Time-Average Static Pressures.

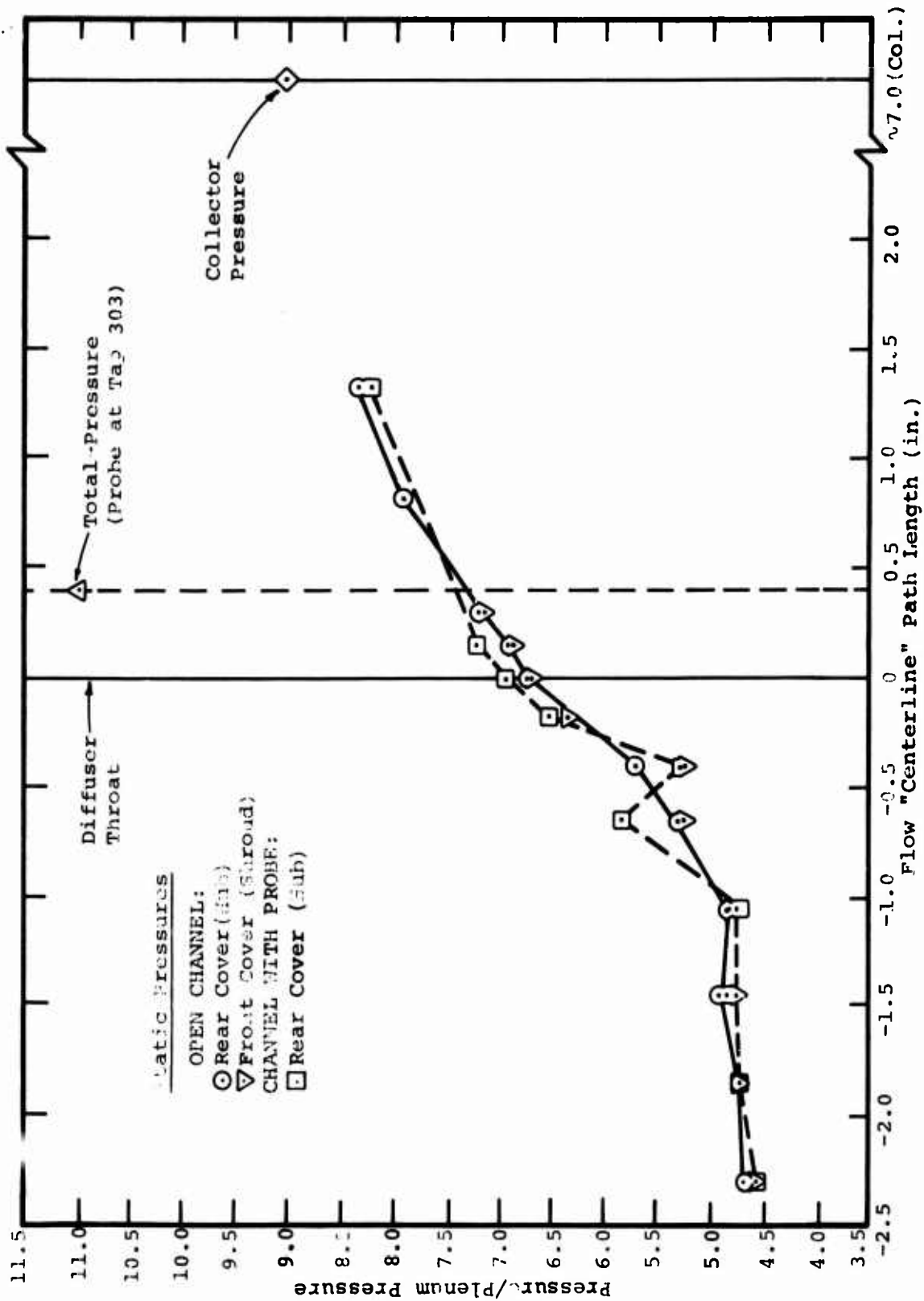


Figure 71. Effect of Total-Pressure Probe on Time-Average Static Pressures.

pressure probe (the data points indicated by squares). All data points in any one figure were obtained at the same time.

Also shown in Figures 69, 70, and 71 are the time-averaged total-pressure data measured using the total-pressure probes. These data are for the total pressure measured at tap locations 301, 302 and 303. The uncertainty of these total-pressure data is approximately 8%. The alignment of the probe (the alignment of the total-pressure probe hole to the diffuser geometry) was not changed during these tests. In all cases the "vector" through the total-pressure probe orifice was aligned with the tangent to the vane tip suction surface at each tap location. A calibration of the total-pressure probe at Mach number unity showed that the probe response is flat for this probe up to approximately $\pm 15^\circ$. Thus the total-pressure probe should have measured very closely the "time-average" total pressure of the flow at each tap location. These data are discussed in Section 10.

10.0 FLUID DYNAMIC INTERPRETATION OF LSM DATA

In this section we present some fluid dynamic interpretation of the pressure measurements performed on the RF-2 stage in LSM gas.

The data and its interpretation presented here follow the flow models and fluid dynamic analyses of the RF-2 stage which were presented in USAAVLABS Technical Report 69-76 (Reference 7). While the data interpretation given is not as extensive as could be developed under a program specifically directed towards probing the unknown fluid dynamic phenomenon of the centrifugal compressor, this interpretation does serve to illustrate the type of understanding that could be obtained with these and other types of instrumentation. Other types of flow data besides steady and time-varying pressure data are required to completely unravel the fluid dynamics of the flow through the RF-2 impeller and diffuser.

In Section 11, some recommendations are made on the type of dynamic response instrumentation that should be used to improve our understanding of, and ultimately our capability for vastly improving, our design methods for high-performance, high-pressure-ratio centrifugal stages.

10.1 SUMMARY OF RESULTS

The study of the LSM time-averaged and dynamic pressure data has shown the following main results:

- 1) Excellent agreement is obtained between the LSM time-averaged static pressure data throughout the stage and the original air data. This includes the pressure distributions on the impeller cover and the detailed static pressure distributions (including the influence of passage shocks) in the diffuser. Excellent agreement is also obtained with overall stage pressure ratio and efficiency. LSM testing, using a gas that closely replicates the air inlet specific heat ratio, produces detailed air-equivalent data for high-pressure-ratio centrifugal stages.

- 2) In measuring the dynamic pressure data, the use of the 200 kHz low-pass filter enhances the signal readability without distorting the information.
- 3) The impeller blade loading is "substantially" as expected even when the pressure traces are not corrected for probe size.
- 4) Blade leakage flow and rate of mass addition from jet to wake could explain the sharp negative pressure fluctuations near the impeller turn to radial (tap 214) and the loading characteristics in the suction surface/cover corner of the impeller passages in the radial portion of the impeller (taps 213 and 212).
- 5) Separation appears to occur at the end of the inducer as predicted in Reference 7. However, the pressure measurements in the inducer show that either intermittent separation or separation of some channels may occur in the vicinity of tap 219.
- 6) No explanation is offered for the high-frequency pressure fluctuations that appear in the center of the impeller passage in some pressure signals.
- 7) The apparent blade loading at the impeller exit where none is expected is explained by an induced jet/wake vortex motion established in the suction side of the blade.
- 8) Pressure fluctuations in the diffuser are caused by jet/wake mixing. There is probably a considerable influence of the diffuser vanes on the mixing process. Different pressure signatures between front and rear taps are caused by different degrees of mixing and/or a three-dimensional distortion of the jet/wake interface.
- 9) Taps 204 and 244 show a noisy pressure trace which nearly masks the blade frequency. This noise is caused by interference of the mixing process with the diffuser vane tip shock in this region.

- 10) The total-pressure probe used was not satisfactory for making dynamic total-pressure measurements but some time-average total-pressure data was produced.
- 11) Time-average total-pressure measurements show almost no stagnation pressure loss between the 1.03 radius ratio location and the channel diffuser throats. The indicated tip stagnation pressure measured was 165 psi (referenced to 29.92"Hg) compared to 175 psi measured by Boeing in the original air studies. Differences in probe design and location might account for this 10-psi difference. The measurements would indicate that the majority of impeller exit mixing stagnation pressure loss has occurred at a radius ratio less than 1.03.

10.2 TIME-AVERAGE MEASUREMENTS

The time-average measurements have been presented and discussed in Section 8. The summary of the LSM modeling correlation based on the test results was given in Section 8.2.

The fluid dynamic interpretation of this time-average data is the same as that presented in Reference 7 since the LSM data is in agreement with the original air data. Excellent reproduction of and agreement with the air-equivalent compressor stage performance data (pressure ratio, efficiency and range) and the detailed impeller cover and diffuser pressure distributions have been obtained.

10.3 DYNAMIC PRESSURE MEASUREMENTS

Impeller Shroud Pressure Measurements

Figures 59, 60, and 61 display the dynamic pressure transducer output data from transducers located along the shroud (cover) of the RF-2 impeller.

Table X shows the approximate angle subtended by the RF-2 impeller blade tip and by the pressure transducer at each of the five tap locations on the cover (see Figure 12). The ratio of the blade thickness to the diameter of the active element of the transducer is approximately 1/2.8. Thus, as the blade passes the transducer, there is a period of time

**TABLE X. ANGULAR SIZES OF IMPELLER BLADES
AND PRESSURE TRANSDUCERS**

| Tap Number (See Figs. 12 and 13) | Radius, r (in.) | $\frac{t^*}{2\pi r} \times 360^\circ$ (deg) | $\frac{D^*}{2\pi r} \times 360^\circ$ (deg) |
|---|--------------------|--|--|
| 219 | 1.82 | 1.0 | 2.65 |
| 214 | 2.25 | 0.77 | 2.18 |
| 213 | 3.00 | 0.57 | 1.61 |
| 212 | 3.80 | 0.45 | 1.28 |
| 211 | 4.54 | 0.38 | 1.08 |
| <p>* t = 0.030" = impeller blade thickness at cover. D = 0.085" = diameter of active area of pressure transducer.</p> | | | |

when the transducer senses the pressure from both the suction and the pressure sides of the blade. Furthermore, because of the averaging effect over the transducer surface (about 2.7° of effective arc in the inducer region (tap 219) and approximately 1° at the impeller exit (tap 211)), the transducer cannot resolve high-frequency (greater than about 100 kHz) pressure spikes.

Since the impeller has 18 blades, the angular separation between "blade pressure peaks" on the signal traces of the photos of Figures 59 to 66 represents 20° of impeller rotation. From Table X we see that the transducer active element occupies approximately one-tenth of the spacing between blades at tap 214 and about one-twentieth of the blade spacing at tap 211.

The pressure traces of Figures 59 to 61 show a fundamental frequency characterized by a large-amplitude, low-frequency "signature" which represents the fundamental blade passing frequency. For the LSM speed conditions shown, the fundamental blade frequency is approximately 10,000 Hz, which for the highest sweep rate on these photos (0.05 msec/div) produces about 5 cycles of pressure oscillation per trace.

Some of the traces of Figures 59 to 61 contain a high-frequency signal on top of the fundamental blade passing frequency. (See, for example, Figure 60e.) This high-frequency signal is approximately 250 kHz and this frequency was found to be the "ringing" frequency of the pressure transducers used. The photo of tap 214, in Figure 59b, illustrates the nature of the transducer signal when the 250-kHz signal was filtered from the output of the transducer. The 250-kHz signal should be ignored when analyzing the fluid dynamics of the flow.

Separation Point Location

Reference 7 showed that the flow in the RF-2 impeller did not separate in the inducer. This conclusion was based upon pressure measurements on the cover and boundary layer calculations. Figure 72 is reproduced from Reference 7 and shows the calculated blade loading along the impeller tip cover (together with measured data to be discussed later in this section). S is the streamline distance measured along the cover surface. Reference 7 concluded that separation in the impeller occurred approximately at a streamline

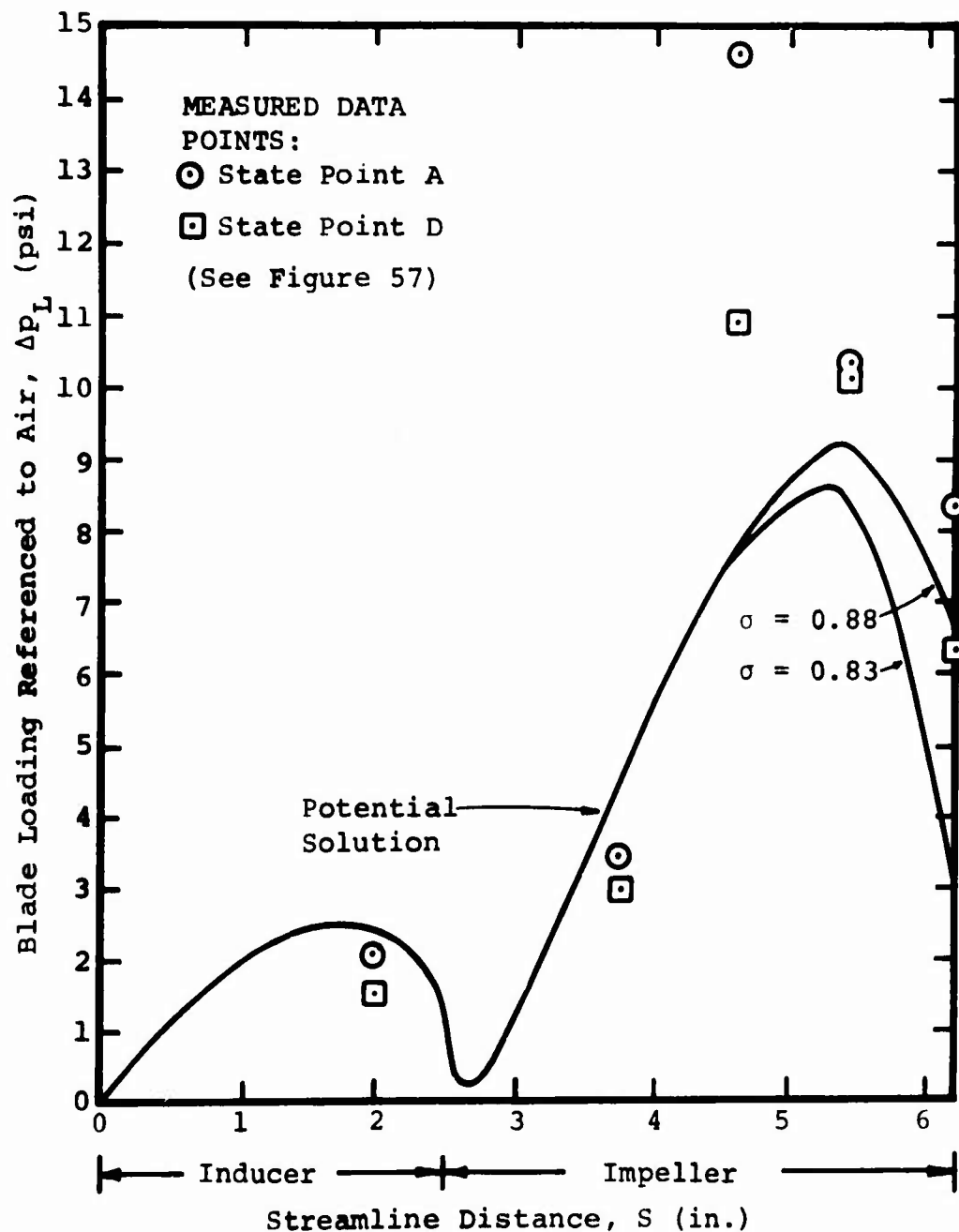


Figure 72. RF-2 Blade Loading at Cover From the Potential Solution and From Cover Dynamic Pressure Measurements.

distance $S = 3.4$ or slightly ahead of the location of tap 214. (See Figure 13.) The evidence available in Reference 7 could not clearly show where the separation occurs in the impeller passage. It could be on the suction surface of the blade, or another likely situation would be a meridional flow separation off the cover of the impeller as the flow turns rapidly to radial after leaving the inducer. In this latter case, the separated region could be expected to lie initially on the cover/suction corner of an impeller passage, at least in the initial stages of separation.

The tap 219 signal traces in Figures 59 through 61 basically show what would be expected from a potential flow pressure distribution in the inducer at this tap location. In these traces there is a sudden drop in the trace (pressure level) from the pressure side of the blade (corresponding to the peak of the signal trace) to the suction surface. This is followed by an almost linear rise in pressure across the flow passage back to the pressure side of the blade.

(Remember that the transducer sees the impeller blade rotate past it. Therefore, the transducer pressure signal displayed in time shows an increase in pressure as the blade approaches the transducer; this pressure reaches a maximum on the pressure side of the blade and then falls from pressure surface pressure to the suction side pressure as the blade passes under the transducer.)

Duplicate photos of the pressure signal from tap 219 (Figure 61) indicate, however, that this type of signal is not always observed. The pressure distribution sometimes shows a relatively flat spot near the suction side of the blade before the trace rises to the pressure side. Such a flat spot is indicative of the wake region of a barely-separated flow.

Because of the intermittent behavior of the trace of tap 219 (indicating at times a potential-flow-like pressure trace and at other times a wake/jet type trace), we could conclude that the flow at tap 219 is intermittently separated. Intermittent separation could be caused by a difference in geometry of individual inducer passages or the result of an unsteady separation point moving along the suction surface/cover corner.

There is no real evidence to indicate that separation in impeller geometries like the RF-2 is either steady or unsteady. Thus there is little we can say affirmatively about this possibility. We do know that the static pressure in the impeller is unsteady because of the influence of the diffuser vanes. It is also known that the pressure field induced by diffuser vanes has been observed, in some cases, to propagate all the way to the inlet of an impeller. Indeed, Reference 7 shows that this apparently is the case in the RF-2. Thus, an imposed unsteady diffuser vane pressure field in the impeller may couple with the separation fluid dynamics to produce an unsteady and moving separation point in the impeller.

We also know that the diffusing characteristics of high-Mach-number inducers are critically dependent upon the precise geometry of the leading-edge portions of the inducer blading. Small differences in inducer geometry could cause early or late separation of the flow in different passages, leading to intermittent-separation type pressure patterns such as observed in the inducer at tap 219.

It is interesting to note that the tap 219 traces of Figures 59 and 60 are of the same passages of the impeller (as can be determined by examining the blade position indicator trace). These traces seem to show an unseparated flow. However, the tap 219 trace in Figure 61a shows other impeller passages, and indicates that some passages are separated.

Impeller Blade Loading

The maximum pressure difference of the pressure signal traces* should be representative of the blade loading in the impeller cover region of the impeller flow passages. Interpreting the traces of taps 219, 214, 213, 212 and 211 in Figures 59 to 61 in this fashion, the blade loading is plotted

* The pressure transducer may be reading lower pressure differential Δp than exists across the blade because of the finite size of the probe.

in Figure 72 for state point A near surge and state point D near choke.

The blade loading Δp_L plotted in Figure 72 was the measured maximum pressure difference Δp taken from the dynamic traces and scaled to the equivalent air Δp_L :

$$\Delta p_L = \Delta p \frac{(\text{mN})_{\text{air}}}{(\text{mN})_{\text{LSM}}}$$

This is consistent with the blade loading analysis which follows.

The measured blade loading data "in general" follow the trend of the loading on the cover as calculated for the potential flow solution of Reference 7.

However, at taps 213, 212, and 211, the pressure loading Δp_L is appreciably higher than should exist according to the potential flow calculations. Why Δp_L does not follow the calculated curve in the radial portion of the impeller is not clear. We suspect that the separated jet/wake flow is significantly different from the assumed potential flow in this region of the flow and is the cause of the differences in Δp_L shown in Figure 72. Part of this difference could be caused by the dynamic twisting of the jet/wake in the radial portion of the impeller. Unfortunately, little is known quantitatively about this aspect of the impeller flow. Thus the blade loading near the cover cannot be quantitatively calculated. It is interesting to note, however, that an "overtwisting" jet/wake flow, with the wake largely on the hub of the impeller as postulated in Reference 7, would have an excess of mass flow on the cover. This would produce an excess in blade loading Δp_L over that shown by the calculated curve of Figure 72.*

* $\Delta p = 2m\Omega/g_o bZ$; and if m is larger than postulated in Reference 7, then Δp_L will be larger than calculated for Figure 72.

At the impeller exit, the slip of the flow is demonstrated by the data at taps 213, 212, and 211. Here there is observed a decrease in blade loading toward the impeller tip as predicted by the calculated curve of Figure 72.

Explanation of Pressure Trace Signatures

There does not exist today a good theory for predicting the velocity and pressure distribution from blade to blade in the impeller. Potential solutions usually assume a linear distribution of pressure or velocity from suction to pressure surface in order to match the blade loading. The model of Reference 7 used a constant pressure through the wake and a linear rise in pressure across the jet to the pressure surface. This produced a wake/jet pressure distribution and cover pressure as shown in Figure 73 (taken from Reference 7).

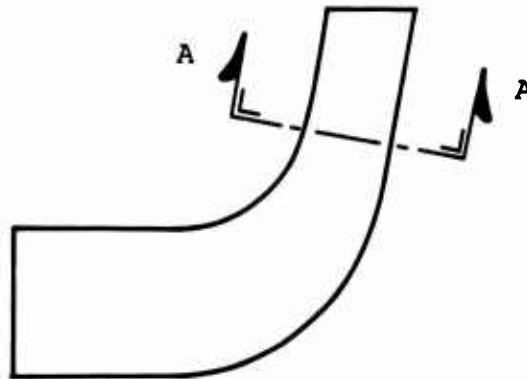
If the model of Reference 7 is correct, then the static pressure profile across a blade passage in Figures 59 and 60 should be the mirror image* of that shown in Figure 73. Some of the pressure fluctuation "signatures" displayed in Figures 59 and 60 do follow the type of trace expected from this model; in other cases they do not. In the following we discuss some possibilities for variations in the pressure profiles displayed.

If we apply the conservation of angular momentum to the total flow in the impeller passage at a given radius**, the blade loading, suction surface to pressure surface, is given by (see Appendix IV)

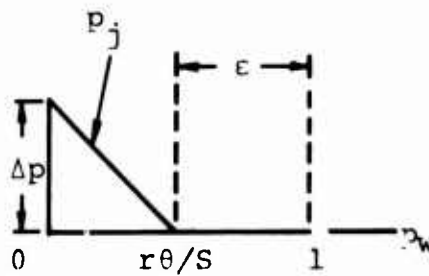
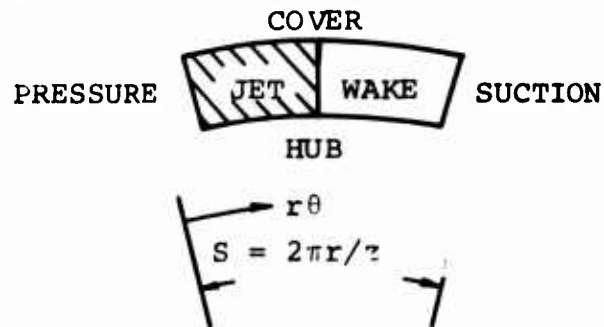
$$\Delta p = \frac{2m \Omega}{g_o bZ}$$

* The traces are the mirror image because time increases from left to right on the pressure signal photos; i.e. the transducer sees first the suction surface and then the pressure surface of the passage.

** Cover friction is neglected and a slip factor of unity is assumed.



SECTION A-A:



ASSUMPTION: $p_c = \epsilon p_w + (1-\epsilon)(p_w + \Delta p)$
 $= p_w + (1-\epsilon) \Delta p/2$

Figure 73. Model for Jet Pressure Variation.

where Δp = pressure-to-suction surface pressure difference
 m = total mass flow rate
 Ω = impeller rotational speed (rad/sec)
 b = passage depth in the axial direction
 Z = number of impeller blades

The blade loading Δp per passage as calculated by this equation will be the same regardless of how the flow within the passage distributes itself between jet and wake.

If conservation of angular momentum is applied to the jet and wake portions of the flow separately, assuming a slip factor of unity with the leakage flow as the sole contributor to mass addition to the wake*, the fractional pressure rise in jet and wake of the total blade loading is (see Appendix IV)

$$\frac{\Delta p_j}{\Delta p} = \frac{m_j}{m} + \left(\frac{r}{2m} + \frac{C_{\theta L}}{2m\Omega} \right) \frac{dm_j}{dr}$$

$$\frac{\Delta p_w}{\Delta p} = \frac{m_w}{m} + \left(\frac{r}{2m} + \frac{C_{\theta L}}{2m\Omega} \right) \frac{dm_w}{dr}$$

where Δp_j = pressure rise across the jet
 Δp_w = pressure rise across the wake

m_j/m = jet mass flow fraction

m_w/m = wake mass flow fraction

r = radius

$C_{\theta L}$ = leakage flow tangential velocity

$\frac{dm_w}{dr} = \text{radial rate of addition of wake mass flow} = - \frac{dm_j}{dr}$

m = total mass flow in channel

* Tip leakage is not the sole contributor to mass flow addition to the wake since secondary flow deposition of boundary layer fluid in the wake is also involved. In the present analysis we have neglected these effects compared to tip leakage.

If there is no tip leakage or radial rate of change of mass addition to the wake, these expressions show that the percentage of total passage pressure rise in the jet and wake is proportional to the mass flow in jet and wake respectively. For example, if 10% of the passage flow is in the wake, then 10% of the total-pressure rise between blades will occur in the wake and 90% in the jet. If there is tip leakage, these expressions show that an additional pressure rise can be imposed on the wake flow and hence less pressure rise occurs in the jet flow.

In Appendix IV, calculations are made of several wake flow mass fraction distributions between the separation position and the impeller exit, and it is shown how these distributions can affect the fractional pressure rise in wake and jet. These calculations show that a significant fraction of the total passage pressure rise can occur in the wake portion of the flow even near the separation point, if a significant amount of mass is transferred from the jet by leakage flow near the separation point radius.

Now, in Figures 59 and 60, the tap 214 traces show that a significant fraction of the total passage pressure rise (anywhere from 0.6 to 0.8 of the passage Δp) occurs on the suction side of the blade. Here a small wake flow is to be expected since separation was shown in Reference 7 to be slightly upstream of the location of tap 214. Following the arguments presented in Appendix IV, the traces at tap 214 could be caused by a large leakage flow or mass addition to the wake in the vicinity of tap 214. Such could occur if, for example, an exceptionally large clearance existed at this location. Unfortunately, no measurements of relative tip clearance along the impeller cover have been made.

Other Factors Affecting Passage Pressure Distribution

When blade loading is suddenly imposed upon the flow, for example, such as occurs at the bend to radial where the flow is unloaded after turning to axial and then is suddenly turned to radial (see Figure 72), the pressure distribution in the jet and wake portions of the passage flow will be concentrated near the blade surfaces. This is because the flow is turned most strongly near the blade surfaces. Thus, near the bend to radial, we should expect to see pressure distributions with peaks near the suction and pressure surfaces

of the blade and a smaller pressure gradient in the center part of the flow passage. This may also account in part for some of the pressure peakiness or spikes near the pressure surface and the concentrated dip on the suction surface in the traces on tap 214. However, the cause of spikes in the pressure distribution in the center of the passage, particularly near the region where the wake/jet interface should occur, is not readily explainable.

Blade Loading at Impeller Exit

The transducer outputs of tap 211 at the exit of the impeller (Figures 59 to 61) show a blade loading at the tip of the impeller where there should be none; the blades should unload at the tip of the wheel. We suspect that the "indicated" blade loading at the location of tap 211 is caused by a secondary-flow vortex motion induced at the impeller tip.

At the tip of the impeller, the high-relative-velocity jet flow emerges adjacent to the low-relative-velocity wake flow. The intense shear and mixing which result at this boundary (caused in large part by Coriolis forces which greatly enhance mixing) entrain the wake fluid into the jet in the immediate vicinity of the impeller blade tip. This mixing process establishes a circulatory vortex pattern in the radial plane relative to the blade. In the relative flow, a low-pressure center is thus formed in the vicinity of the impeller exit on the suction side of the blade. The hypothesized flow is indicated in Figure 74. The duplicate signal traces from tap 211 (for state point A given in Figure 61) in general illustrate this type of behavior. There is a sudden drop in pressure across the blade. This pressure drop corresponds to the static pressure depression at the center of the vortex created on the suction surface of the blade tip.

Why there are severe variations in trace signature at tap 211 is not clear. Some of the apparent nonrepetitiveness in pressure signature could be caused by the start of the wake/jet mixing process, as will be discussed next. Unless a vortex type flow such as hypothesized above exists at the exit, there appears to be no ready explanation for the rather significant pressure difference existing across the blade at tap 211.

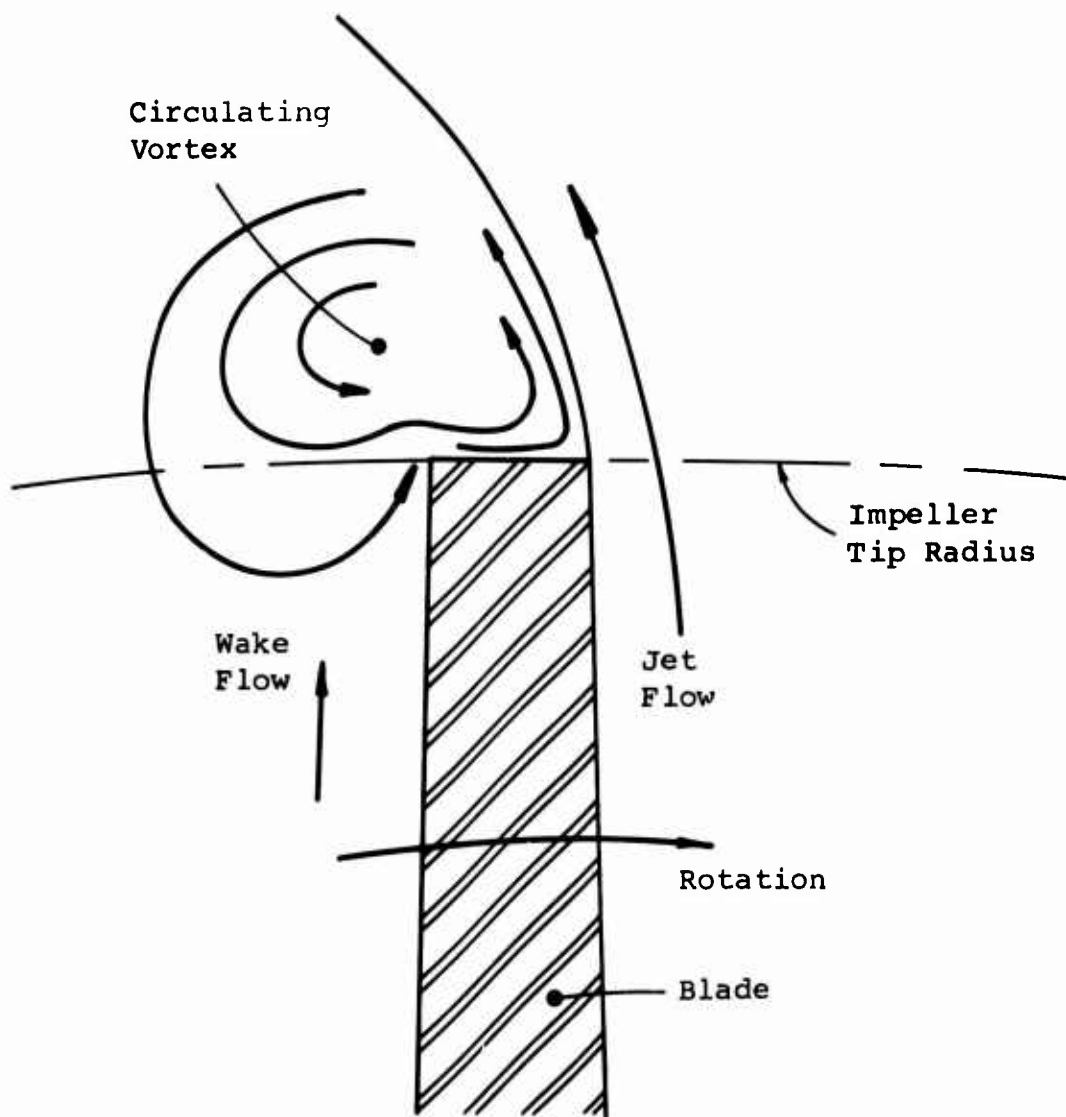


Figure 74. Vortex Pattern at Impeller Exit in Relative Flow.

Diffuser Static Pressure Measurements

Diffuser wall static pressure measurements are shown in Figures 62 through 66. Representative pressure traces are shown for either state point A (near surge) or state point D (near choke).

Except for some slight differences, as will be noted below, all of these pressure signals display pressure fluctuations caused by the mixing process in the diffuser entry region. The pressure fluctuation is a "sawtooth" of approximately constant amplitude where the "ramps" of the sawtooth are of approximately equal slope on the rising and falling portions of the pressure trace. This is the characteristic expected on the basis of the Dean and Senoo²⁹ wake/jet mixing process at the exit of a centrifugal compressor impeller.

As pointed out in Reference 29, the mixing process at the impeller exit between wake and jet flow leads to an increase in the angular momentum of the wake and a decrease in the angular momentum of the jet.

The force which causes these changes in angular momentum is a pressure force between wake and jet. This force rotates at impeller speed in absolute space and leads to a fluctuating pressure at each point in the diffuser and to a reversible work transfer between the jet and wake.

Immediately at the impeller exit this force will result in a pressure differential in the vicinity of the jet/wake boundary. Continual mixing and exchange of angular momentum as the flow proceeds outward in radius through the diffuser causes this pressure force to distribute throughout the jet and wake flows. This is a sawtooth oscillating pressure distribution rotating at impeller speed and of a primary frequency equal to the blade passing frequency. In Figures 62 through 66, the sawtooth pressure distribution exists in some form even into the throat of the channel diffusers. The implication is that the flow is not completely mixed-out well into the divergent portion of the channel diffusers. We also expect that there is a strong influence of diffuser vanes on the mixing.

Some Peculiarities of Diffuser Static Pressure Measurements

While there is a general pattern in the diffuser static tap traces, there are also some peculiarities which are worth noting.

Taps 204 and 244 are located immediately below a diffuser vane tip at the 1.03 radius ratio location. These taps are immediately adjacent to a relatively strong shock produced by the diffuser vane and channel flow. Flow at state point A, which is near surge, should produce a stronger shock system than the flow at state point D, which is near choke. The pressure signals at tap 204 and 244 in Figures 62 and 63 are "garbled" by the close proximity of this shock system, and the amount of distortion of the signal is worse for the state point A flow as might be expected. This is particularly true of the hub pressure signal for state point A as contrasted to that for state point D, for tap 244 (Figure 64).

The pressure signals from taps 241 through 244 located on the hub side of the diffuser display a distinct, periodic low-pressure peakiness which is not observed on the shroud taps at these locations. There is no rational explanation for this peakiness except that it could be the result of a distortion of the jet/wake flow pattern with the wake lying on the hub side. Reference 7 discusses how such a distorted jet/wake could result in a reduced rate of jet/wake mixing with radius on the hub side.

Total-Pressure Probe Measurements

The frequency response of the total-pressure probe used in these studies was not sufficient to resolve the fundamental blade passing frequency for the LSM tests (10 kHz). Thus, no useful information on the magnitude or characteristics of the fluctuating total-pressure between wake and jet in the entrance regions of the diffuser was obtained with these measurements. Insertion of a total-pressure probe upstream of the channel diffuser throat causes large flow disturbances and disruption of the entire stage flow even with the small dimensions of the probe used in this program. Stage pressure ratio was reduced and a much narrower range between

choke and surge was observed. (See Figures 67 and 68.)

Figures 69, 70, and 71 show the static pressure distribution in the vaneless, semivaneless and throat regions of the diffuser channel in which the probe has been placed (dashed line data) compared with the static pressure distributions in an unblocked channel (solid line data).

There was only a minor alteration in pressure distribution when the total-pressure probe was located in the diffuser channel and downstream of the throat. Further, there was no significant change in efficiency, pressure ratio, or range to surge when the total-pressure probe was in this position.

With the total-pressure probe located upstream of the throat (Figures 69 and 70), rather strong pressure gradients are produced in the static pressure distribution and higher throat static pressures and hence a lower throat Mach number occur. Undoubtedly a shock is formed on the total-pressure probe at least in the center of the channel. (Remember that the total-pressure probe is a tube passing straight across the channel from wall to wall.) This shock interacts with the wall boundary layers to alter the pressure distribution. Unfortunately, there is insufficient data in these figures to conclusively determine the nature of the shock/boundary layer interaction phenomena or to provide an explanation for the distribution of static pressures obtained.

The calibration of the total-pressure probe showed that it has a basically flat response for yaw angles up to $\pm 15^\circ$. The probe was used to obtain the time-averaged total pressure.

Figures 69 through 71 show that there is only a very slight reduction in indicated total pressure from the 1.03 radius ratio to the diffuser channel throat. This reduction is on the order of 2.5% or a 3.7 psi reduction at 50,000 rpm. The conclusion of Reference 7 was that the models discussed therein were essentially valid and that for the RF-2 there was little or no loss in stagnation pressure between the impeller tip and the throat of the diffuser channels. Further, Boeing's original air measurements using impeller tip stagnation pressure probes showed an indicated

stagnation pressure of 175 psi (referenced to a 29.92"Hg inlet). Reference 7 estimated that the mass flow average stagnation pressure should produce an indicated stagnation pressure in the range from 150 psi to 183 psi, assuming a 20% mass flow fraction in the wake. Thus, the present measurements agree with that analysis but are on the order of 10 psi lower than the indicated tip stagnation pressures measured by Boeing in the original RF-2 air studies.

In summary, then, the time-average stagnation pressure measurements suggest that Δp_o is approximately zero between the 1.03 radius ratio location and the diffuser channel throat and that all of the stagnation pressure loss caused by discharge mixing occurs very close to the impeller tip exit radius. Recent (unpublished) work at Stanford University on mixing processes in rotating flows indicates that exceptionally violent mixing can be expected to occur at the jet/wake interface at the blade location at the impeller exit*. Such strong mixing could account for a major portion of the jet/wake mixing stagnation pressure loss occurring close to the impeller tip.

The picture that emerges is one of very rapid mixing and a reduction in tip stagnation pressure very close to the impeller exit with continued mixing, but at a greatly reduced rate in the flow at least to the diffuser channel throat. The total-pressure probe measurements indicate that most of the stagnation pressure loss occurs by a radius ratio of 1.03.

* There are two jet/wake boundaries for each blade passage at the exit: one is the boundary coming off the blade tip and having the violent mixing as proposed here, and the other is the "quiescent" boundary that has come up through the impeller from the initial separation point. The violent jet/wake mixing is "turned on" only at the exit of the impeller where the first boundary originates. This is an hypothesis, and further research efforts are needed to clarify the fundamental phenomena occurring in this region.

11.0 SUMMARY AND CONCLUSIONS

11.1 SUMMARY OF PROGRAM RESULTS

Phase I of this program had the goal of establishing the accuracy and practicality of using low-speed modeling as a research and development tool for high-speed, high-pressure-ratio centrifugal compressors. Phase II examined the use of high-response-rate, pressure instrumentation as a tool to probe the aerodynamics of high-pressure centrifugal compressors. The results of these two phases are summarized separately.

Phase I - Modeling Correlation

A high-pressure-ratio, high-speed centrifugal compressor stage (developed under a separate program and fully tested with air under USAAVLABS support) was operated in a low-speed modeling gas (LSM gas) facility. The working fluid was a gas mixture which had both a low speed of sound and a specific heat ratio very close to that of air. The important dimensionless parameters duplicated to reproduce air compressor stage performance were geometry, Mach number, Reynolds number, and ratio of specific heats. The LSM gas test results were compared with the original air performance data.

A simple modeling scheme based on inlet modeling conditions has proven to be accurate and practical.

A portion of the air compressor map around 50,000 rpm was compared with the same portion of the compressor map developed from a series of LSM data. The data show excellent compressor performance modeling with simple inlet scaling when using an LSM gas which has an inlet specific heat ratio of about 1.4. LSM data fall in the correct location for their respective "air-equivalent" speeds.

LSM data taken with gases with inlet specific heat ratios sufficiently different from air did not produce acceptable modeling using simple inlet scaling. Therefore, duplication of the inlet specific heat ratio is required for accurate LSM modeling if simple scaling based on inlet conditions is to be used.

The details of the fluid dynamics through the inducer, impeller and diffuser, as reflected by the static pressure distribution in these components, were well replicated with the "k = 1.4" LSM gas. Inducer and impeller cover static pressure distribution and diffuser cover circumferential and "streamline" pressure distributions with "1.4" LSM gas agree with the 50,000-rpm air data quite well for three mass flows surveyed between surge and choke.

Accurate duplication of the impeller-to-cover air running clearance was necessary to reproduce air-equivalent stage efficiency.

A complete description of the Phase I results was presented in Section 8.

Phase II - Dynamic Measurements

Dynamic, high-response-rate measurements of static pressure were made on the impeller cover and the front and back walls of the vaned diffuser using LSM testing. An air-equivalent speed of approximately 50,000 rpm was used. Data were taken at at least three flow states between choke and surge conditions for this speed.

The analysis of the dynamic response rate data shows fundamental agreement with the aerodynamic models described in Reference 7, which was based upon the time-averaged air data replicated by LSM testing in Phase I.

Blade loading calculated from pressure-to-suction-surface pressure fluctuation amplitude is in essential agreement with the characteristic shape of the anticipated loading calculated from the potential flow/impeller separation model of Reference 7. Impeller cover separation point location agrees very well with that estimated.

A jet/wake type pressure distribution predicted for the impeller flow on the cover is observed in the dynamic response cover data. An analysis of the expected distribution of jet and wake pressure across the flow passage in the impeller explains in part some of the characteristics observed in the experimental data.

The pressure fluctuations observed in the diffuser flow agree qualitatively with the pressure characteristics expected in the wake and jet portions of the impeller exit flow as described by the impeller exit mixing theories of References 29 and 30.

The influence of the diffuser vanes upon the characteristics of the jet/wake mixing process is not resolvable with the limited data taken. The jet/wake mixing process appears to continue at least to the throat location of the channel diffusers.

Instantaneous stagnation pressure was not obtained from these tests because of insufficient frequency response of the total-pressure probe.

As hypothesized in Reference 7, time-averaged stagnation pressure measurements showed almost no stagnation pressure loss between the 1.03 radius ratio at the impeller exit and the channel diffuser throats.

The details of the results of the high-response-rate measurements are presented in Sections 9 and 10.

11.2 RECOMMENDATIONS FOR FUTURE WORK

A significant increase in the performance level of high-pressure-ratio, high-speed centrifugal compressors will ultimately depend upon improvement of the following factors:

- 1) Inducer/impeller pressure recovery
- 2) Diffuser pressure recovery
- 3) Range and stability.

In the inducer portion of the centrifugal rotor, the key question is the ability to establish good diffusion as a function of Mach number and inlet relative flow incidence.

In the impeller, the key fluid dynamic problems include:

- a better understanding of the jet/wake twisting dynamics of the impeller separated flow
- the influence of impeller flow on inducer behavior and flow separation location

- the influence of secondary flows on impeller jet/wake dynamic behavior
- the influence of tip leakage on impeller internal losses and flow dynamics
- the importance of secondary and tertiary (splitter) vane number and location on leakage, secondary flow, losses and jet/wake dynamics
- the calculation of impeller work input coefficient
- the proper calculation of impeller parasitic work
- an adequate confirmation of the impeller discharge mixing loss model.

The unresolved areas of the centrifugal diffuser include:

- the prediction of boundary layer backflow into the impeller
- the prediction of diffuser core flow stagnation pressure loss from impeller tip to channel diffuser throat
- the prediction of pressure recovery from impeller tip to channel diffuser throat
- the prediction of diffuser-throat boundary layer blockage
- the achievement of excellent channel diffuser recovery.

Surge, range, and stability are of vast practical concern in centrifugal compressor design. Despite this fact, there is no scientific understanding of the detailed phenomena involved. Over the past twenty-year period, there has been no fundamental research (in the open literature) which has addressed the problems of surge and stability. In fact the simplest questions cannot be answered today, including:

- Does the impeller importantly participate in surge?
- Does rotating stall in the diffuser and/or impeller precede surge?
- Is surge breakdown axisymmetric or significantly asymmetric?

- What is the progression of aerodynamic phenomena leading up to surge?

It should be obvious that the above unresolved fluid dynamic phenomena and design questions will ultimately depend upon a program of empirical measurements coupled to good fluid dynamic analysis and model building. Good empirical measurements will depend upon high-response-rate dynamic instruments which can resolve the highly time-dependent, unsteady fluid dynamics. For example, pressure dynamic measurements such as obtained on Phase II of this study will be essential to assist in resolving these questions.

But other instrumentation will be required also. Anemometer techniques must eventually be used to resolve the unsteady velocity flows. Hot-wire anemometry equipment and techniques are currently available for this purpose. However, the fragility of this instrumentation, particularly at high velocities and temperatures, and the dynamic response rate of hot-wire anemometers make it difficult to use this type of instrumentation in airflow testing of high-pressure centrifugals. LSM testing offers a significant advantage by reducing fundamental flow frequencies and velocity levels and makes appealing the use of LSM testing as a research and development tool.

The Phase II studies have shown that very small probes on the order of 0.032 inch diameter can greatly disrupt the fluid dynamics in the impeller-exit/diffuser-entry region and spoil overall performance. The use of hot-wire anemometry techniques may well suffer from this limitation unless small probes in larger-than-full-scale rigs are used.

The recent advent of laser anemometry is an appealing alternative to the study of these flows. However, the inability to use this technique close to boundary walls seems to negate the use of this technique for high-pressure-ratio centrifugal studies. A breakthrough on this problem will make the use of laser anemometry an attractive tool for the empirical study of these machines.

Other optical techniques, such as schlieren and holographic analysis, will also probably be required to unravel the

fundamental aerodynamic phenomena.

An important tool, as yet undeveloped, which would greatly assist in the understanding of these flows would be a good visualization technique (path line tracing) for use in high-Mach-number gas flows.

In the use of any of the above techniques, LSM testing offers two basic advantages over air testing: a reduction in fundamental rotative speed and absolute velocities coupled with reduced static temperatures throughout the stage hardware when reduced inlet temperature testing is performed. High-speed, high-pressure-ratio stages now produce fundamental blade passing frequencies and temperatures that are beginning to stress the available high-response-rate aerodynamic instrumentation. LSM testing can reduce the frequencies of the unsteady flow spectra by a factor of almost 2. Temperature levels, particularly at the exit of the impeller, can be reduced enough to make useful dynamic instrumentation such as the dynamic response pressure instrumentation used in this program.

Further, as centrifugal development advances, higher pressure ratios and higher speeds are a certainty. Even though response rate and maximum temperature levels of instrumentation can also be expected to be increased, LSM testing will continue to offer the advantage of reduced frequencies and temperatures and power, and the better utilization of commercial instrumentation in future centrifugal compressor development.

11.3 LSM TESTING - A PRACTICAL TOOL?

The principal objective of this research was to demonstrate the feasibility of low-speed-of-sound modeling as a practical tool in the research and development of advanced, high-pressure-ratio, high-speed centrifugal compressors. Both the practicality of this procedure and the correctness of the modeling have been established.

The testing of small, high-pressure-ratio, high-speed centrifugal turbomachinery presents difficult experimental conditions. High material stresses are developed, and the detailed material/stress analysis, design and development of

machinery to meet these conditions often impose a serious impediment to expedient development. When full-scale prototype machines are run on air, the final stress, vibration, and bearing designs must be carried out to make a successful test run. The aerodynamic test impeller is usually built nearly as ruggedly as the final production hardware, and it cannot be freely altered on the test stand. It is highly desirable to develop the aerodynamics first, using readily-modified hardware, without critical concern for stressing and vibration. The use of LSM testing at low rotational speeds reduces the fundamental frequencies of the unsteady aerodynamic phenomena and permits the use of instrumentation that might otherwise be difficult (if not impossible) to use.

The model testing of compressor aerodynamics using LSM techniques is therefore attractive. One of the principal reasons previous attempts have failed with this technique was a continual changing of the gas composition due to air intrusion. This work has proven that it is possible and practical to maintain an essentially constant gas composition throughout a test.

Another difficulty often posed as a problem with LSM testing is the lack of complete similarity modeling. No realistic modeling scheme can ever successfully duplicate all of the dimensionless parameters of the flow dynamics. However, successful modeling is achieved when the important dimensionless parameters which significantly influence the aerodynamics are correctly modeled. Previous workers have attempted to use low-speed-of-sound gas modeling for aerodynamic studies, but similarity of specific heat ratio was not achieved. This work has shown that duplication of the inlet specific heat ratio is critical to accurate modeling of high-pressure-ratio centrifugal compressors.

In summary, this program has shown that low-speed modeling (LSM) is simple, inexpensive, and practical. The results can be readily scaled on inlet conditions when the specific heat ratio of air is duplicated. Air compressor performance maps and detailed aerodynamics throughout high-speed turbomachinery hardware can be very well duplicated with LSM testing at about a 40% lower rotational speed than that required in air and about one-third the drive power. The test facility developed in this program has proved to be

both simple and inexpensive to use. This LSM testing technique should find wide usefulness in the design, development, and testing of many aerodynamic systems.

LITERATURE CITED

1. von Doenhoff, A. E., Braslow, A. L., and Schwartzberg, M. A., STUDIES OF THE USE OF FREON - 12 AS A WIND-TUNNEL TESTING MEDIUM, NACA TN-3000, August 1953.
2. Hartmann, M. J., and Wilcox, W. W., PROBLEMS ENCOUNTERED IN THE TRANSLATION OF COMPRESSOR PERFORMANCE FROM ONE GAS TO ANOTHER, Trans. ASME, May 1957, pp. 887-897.
3. Breugelmans, F., INVESTIGATION OF A ONE STAGE AXIAL FLOW SUPERSONIC COMPRESSOR, von Karman Institute, Internal Note 12, March 1965.
4. Wells, R. J., and McGrew, THE USE OF GASES OTHER THAN AIR IN THE ACOUSTICAL TESTING OF MODEL COMPRESSORS, ASME Paper No. 67-GT-27, 1967.
5. Welliver, A. D., and Acurio, J., ELEMENT DESIGN AND DEVELOPMENT OF SMALL CENTRIFUGAL COMPRESSORS, VOL. I & II, The Boeing Company; USAAVLABS Technical Report 67-30, U. S. Army Aviation Materiel Laboratories, Fort Eustis, Virginia, August 1967, AD384923-Vol. I, AD384924-Vol. II.
6. Welliver, A. D., and Acurio, J., DESIGN AND DEVELOPMENT OF SMALL, SINGLE-STAGE CENTRIFUGAL COMPRESSORS, The Boeing Company; USAAVLABS Technical Report 67-47, U. S. Army Aviation Materiel Laboratories, Fort Eustis, Virginia, September 1967, AD385595.
7. Dean, Robert C., Jr., Wright, David D., and Runstadler, Peter W., Jr., FLUID MECHANICS ANALYSIS OF HIGH-PRESSURE-RATIO CENTRIFUGAL COMPRESSOR DATA, Creare Incorporated; USAAVLABS Technical Report 69-76, U. S. Army Aviation Materiel Laboratories, Fort Eustis, Virginia, February 1970, AD872161.
8. Davis, H., EQUIVALENT PERFORMANCE PARAMETERS FOR TURBOBLOWERS AND COMPRESSORS, Trans. ASME, January 1958, pp. 108-116.
9. Ikui, T., and Inoue, M., PREDICTING EQUIVALENT PERFORMANCE OF BLOWERS AND COMPRESSORS FOR GASES FROM AIR TEST DATA,

LITERATURE CITED - Continued

Bulletin JSME, Vol. 12, No. 53, 1969, pp. 1072-1081.

10. Capon, R. S., and Brooke, G. V., THE APPLICATION OF DIMENSIONAL RELATIONSHIPS TO AIR COMPRESSORS, WITH SPECIAL REFERENCE TO THE VARIATION OF PERFORMANCE WITH INLET CONDITIONS, Aeronautical Research Committee (London), R & M No. 1336, June 1930.
11. Chapman, D. R., SOME POSSIBILITIES OF USING GAS MIXTURE OTHER THAN AIR IN AERODYNAMIC RESEARCH, NACA, TN3226, August 1954.
12. Martin, J. J., et. al., DATA AND EQUATIONS FOR SOME THERMODYNAMIC PROPERTIES OF "FREON-13B1" (CBrF_3), Engineering Research Institute, University of Michigan, Project M777, April 1953.
13. Downing, R. C., et. al., TRANSPORT PROPERTIES OF "FREON" FLUOROCARBONS AND OTHER RELATED FLUORINATED COMPOUNDS, Technical Bulletin C-30A, E. I. du Pont de Nemours & Co., 1966.
14. Messinger, C., and Downing, R. C., DERIVED EQUATIONS FOR "FREON-13B1" REFRIGERANT, Publication D-9B, E.
15. E. I. du Pont, THERMODYNAMIC PROPERTIES OF FREON-13B1 REFRIGERANT, Technical Bulletin T-13B1, E. I. du Pont de Nemours & Co., 1963.
16. E. I. du Pont, "FREON" FLUOROCARBONS, PROPERTIES AND APPLICATIONS, Product Information B-2, E. I. du Pont de Nemours & Co., 1969.
17. American Society of Mechanical Engineers, FLUID METERS - THEIR THEORY AND APPLICATION, ASME Research Committee on Fluid Meters, Fifth Edition, 1959.
18. Runstadler, P. W., Jr., PRESSURE RECOVERY PERFORMANCE OF STRAIGHT-CHANNEL, SINGLE-PLANE DIVERGENT DIFFUSERS AT HIGH MACH NUMBERS, Creare Incorporated; USAAVLABS Technical Report 69-56, U. S. Army Aviation Materiel Laboratories, Fort Eustis, Virginia, October 1969, AD865300.

LITERATURE CITED - Continued

19. El-Hakeem, A. S., A REFINED-TUBE METHOD FOR MEASURING THE SOUND WAVELENGTH IN GASES, American Journal of Physics, Vol. 33, 1965, pp. 263-265.
20. Romer, I. C., Gaggioli, R. A., and El-Hakeem, A. S., ANALYSIS OF QUADRIPOLE METHODS FOR THE VELOCITY OF SOUND, The Journal of the Acoustical Society of America, Vol. 40, No. 1, 1966, pp. 86-98.
21. El-Hakeem, A. S., Gaggioli, R. A., and Romer, I. C., REFINED TUBE METHOD FOR MEASURING THE SOUND WAVELENGTH IN GASES -- PRINCIPLES OF OPERATION, The Journal of the Acoustical Society of America, Vol. 40, No. 6, 1966, pp. 1485-1488.
22. Kline, S. J., and McClintock, F. A., DESCRIBING UNCERTAINTIES IN SINGLE SAMPLE EXPERIMENTS, Stanford University, Mechanical Engineering Department, January 1953.
23. Air Reduction, Inc., AIRCO RARE AND SPECIALTY GASES, Catalog, 1968.
24. Hodgman, C. D., et. al., HANDBOOK OF CHEMISTRY AND PHYSICS, 44th Edition, The Chemical Rubber Publishing Company, 1963.
25. Tribus, M., THERMOSTATICS AND THERMODYNAMICS, D. Van Nostrand Company, Inc., 1961.
26. Schwartz, F. L., GAS PROPERTY EQUATIONS FOR COMPUTERS, Gas Turbine International, Vol. 10, No. 3, May-June 1969.
27. Keenan, J. H., and Kaye, J., GAS TABLES, John Wiley & Sons, 1950.
28. Wilke, C. R., A VISCOSITY EQUATION FOR GAS MIXTURES, Journal of Chem. Phys.
29. Dean, R. C., Jr., and Senoo, Y., ROTATING WAKES IN VANELESS DIFFUSERS, Transactions ASME, Journal of Basic Engineering, September 1960, pp. 563-570.

LITERATURE CITED - Continued

- 30 Johnston, J. P., and Dean, R. C., Jr., LOSSES IN VANELESS DIFFUSER OF CENTRIFUGAL COMPRESSORS AND PUMPS, Transactions ASME, Journal of Engineering for Power, Vol. 88, No.1, January 1966.

APPENDIX I
LSM GAS PROPERTY EQUATIONS

The property equations for the individual components of the LSM gas mixture are tabulated in this appendix. The source, the accuracy, and the useful range of the equations are given.

The equations used to calculate the properties of the LSM mixture are also presented and discussed.

EQUATIONS FOR THE INDIVIDUAL COMPONENTS

Molecular Weight

Component: Freon-13B1
Source: Reference 16
Equation: $M_1^* = 148.93$
Units: [M] = [lbm/lb-mole]
Accuracy: Error negligible
Range: Entire range of interest

Component: Argon
Source: Reference 23
Equation: $M_2 = 39.948$
Units: [M] = [lbm/lb-mole]
Accuracy: Error negligible
Range: Entire range of interest

Component: Air
Source: (accepted value)
Equation: $M_3 = 28.96$
Units: [M] = [lbm/lb-mole]
Accuracy: Error negligible
Range: Entire range of interest

* In this appendix, subscript "1" denotes Freon-13B1, "2" denotes argon, and "3" denotes air values.

Discussion: Variable composition (i.e., air pollution, relative humidity, etc.) effects are neglected since all LSM mixtures used contained less than 5% air.

Viscosity

Component: Freon-13B1
Source: Reference 13 and curve fit
Equation: $g_{O\mu_1} = 8.897 \times 10^{-4} + 7.668 \times 10^{-5}T - 1.4 \times 10^{-8}T^2$
Units: $[g_{O\mu}] = [\text{lbm/ft hr}]$, $[T] = [^{\circ}\text{R}]$
Accuracy: $\pm 0.3\%$
Range: -50°F to 300°F (probably good also for higher temperatures)

Component: Argon
Source: Reference 24 and curve fit
Equation: $g_{O\mu_2} = 5.909 \times 10^{-3} + 9.954 \times 10^{-5}T - 1.7 \times 10^{-8}T^2$
Units: $[g_{O\mu}] = [\text{lbm/ft hr}]$, $[T] = [^{\circ}\text{R}]$
Accuracy: $\pm 0.2\%$
Range: 0°F to 500°F (probably good also for higher temperatures)

Component: Air

Discussion: The effect of air on the viscosity of the LSM gas mixture was not included since:

- 1) neglecting it greatly simplifies the programs,
- 2) the viscosity affects only the Reynolds number,
- 3) the viscosity of the pure (i.e., without air) LSM gas mixtures is very close to air and hence the addition of small amounts of air has little effect on it, and
- 4) all LSM mixtures used contained less than 5% air.

Specific Heats

Component: Freon-13B1
Source: References 12 and 14

Equation:
$$C_{v1} = 0.01750 + 1.940 \times 10^{-4}T - 8.35 \times 10^{-8}T^2$$

$$+ \frac{13.050678 \times 10^6}{T^4V} - \frac{1937.1348}{T^4V^3}$$

Units: $[C_v] = [\text{Btu/lbm } ^\circ\text{R}]$, $[T] = [^\circ\text{R}]$, $[V] = [\text{ft}^3/\text{lbm}]$

Accuracy: $\pm 0.5\%$ (or better)

Range: -100°F to 500°F (and probably beyond)

Discussion: This formula was checked using:

- 1) the equation given in Reference 11, which uses the spectroscopic wave numbers of CBrF_3 , and
- 2) the published calculated curves (Reference 13), which were based on enthalpy vs. temperature and pressure results.

The results of these methods were always within $\pm 0.5\%$ of each other.

Component: Argon

Source: Reference 23

Equation: $C_{p2} = 4.969/M_2$

$$C_{v2} = 4.969/[(1.6665)(M_2)]$$

Units: $[C_p] = [C_v] = [\text{Btu/lbm } ^\circ\text{R}]$, $[M] = [\text{lbm/lb-mole}]$

Accuracy: Error negligible (assumed)

Range: Entire range of interest

Discussion: Specific heat of Argon is assumed constant.

Component: Air

Source: Reference 25

Equation:
$$C_{v3} = [6.713 + 4.697 \times 10^{-4}T + 1.147 \times 10^{-6}T^2$$

$$- 4.696 \times 10^{-10}T^3 - 1.987]/M_3$$

Units: $[C_v] = [\text{Btu/lbm } ^\circ\text{R}]$, $[T] = [^\circ\text{K}]$, $[M] = [\text{lbm/lb-mole}]$

Accuracy: $\pm 0.72\%$ (and probably better)

Enthalpy

Component: Freon-13B1

Source: References 12 and 14

Equation: $H_1 = 0.0308325T + 9.7 \times 10^{-5} T^2 - 2.78333 \times 10^{-8} T^3$

$$- \left(\frac{0.923773 - 4.06408 \times 10^{-4} T}{V} \right)$$

$$+ \left(\frac{7.62117 - 4.58691 \times 10^{-6} T}{V^2} \right)$$

$$- \left(\frac{4.41512 \times 10^{-5} - 3.98789 \times 10^{-8} T}{V^3} \right)$$

$$- \left(\frac{5.43778 \times 10^6}{VT^3} \right) + \left(\frac{1130.00}{V^3 T^3} \right) + \text{constant}$$

Units: [H] = [Btu/lbm], [T] = [°R], [V] = [ft³/lbm]

Accuracy: $\pm 0.5\%$ (or better)

Range: - 100°F to 500°F (and probably beyond)

Discussion: The value of the constant is irrelevant.

This equation was checked against Reference 11. The difference in ΔH for any identical temperature change was less than 0.05%. This equation was also found to be within 0.1% of the values calculated using the spectroscopic wave numbers of Reference 11.

Component: Argon

Source: Reference 23 and the equation $H = C_p T$ for constant C_p

Equation: $H_2 = (4.969/M_2) (T - \text{constant})$

Units: [H] = [Btu/lbm], [T] = [°R]

Accuracy: Negligible error (assumed)

Range: Entire range of interest

Discussion: The value of the constant is irrelevant.

Component: Air

Source: Reference 26

Equation: $H_3 = 0.246427T - 1.96085 \times 10^{-5}T^2$
 $+ 1.93091 \times 10^{-8}T^3 - 4.12539 \times 10^{-12}T^4$
 $- 7.91904 \times 10^{-17}T^5 + 8.37535 \times 10^{-20}T^6$
 $+ \text{constant}$

Units: [H] = [Btu/lbm], [T] = [°R]

Accuracy: $\pm 0.1\%$

Range: 40 °F to 2400 °F (and probably beyond)

Discussion: The value of the constant is irrelevant.

Entropy

Component: Freon-13B1

Source: References 12 and 14

Equation: $S_1 = 0.0402952 \log T + 1.94 \times 10^{-4}T$
 $- 4.175 \times 10^{-8}T^2 + 0.0306992 \log V$
 $- \left(\frac{4.06408 \times 10^{-4}}{V} \right) + \left(\frac{2.29345 \times 10^{-6}}{V^2} \right)$
 $- \left(\frac{1.32930 \times 10^{-8}}{V^3} \right) - \left(\frac{3.26267 \times 10^{-6}}{VT^4} \right)$
 $+ \frac{484.284}{V^3 T^4} + \text{constant}$

Units: [S] = [Btu/lbm °R], [T] = [°R], [V] = [ft³/lbm]

Accuracy: $\pm 0.5\%$

Range: -100 °F to 460 °F (and probably beyond)

Discussion: The value of the constant is irrelevant.

This equation was compared with the tabulated data of Reference 15. For the range of T and p of interest, the difference in ΔS between this equation and the tables of Reference 15 was less than 0.3%.

Component: Argon

Source: Reference 23 and the equation

$$S = C_p \ln\left(\frac{T}{T_0}\right) - R \ln\left(\frac{p}{p_0}\right) \text{ for const. } C_p$$

Equation: $S_2 = 4.969 \ln (T/T_0)/M_2 - 1.987 \ln(p/p_0)/M_2$

Units: $[S] = [\text{Btu/lbm}^\circ\text{R}]$, $[T] = [^\circ\text{R}]$, $[p] = [\text{psia}]$

Accuracy: Error negligible (assumed)

Range: Entire range

Discussion: The value of T_0 and p_0 is irrelevant.

Component: Air

Source: Reference 25 and the equation

$$S = \int_{T_0}^T C_p(T) \frac{dT}{T} - R \ln \frac{p}{p_0}$$

Equation:
$$S_3 = [6.713 \ln \left(\frac{T}{T_0}\right) + 4.697 \times 10^{-4}(T-T_0) \\ + 1.147 \times 10^{-6}(T^2 - T_0^2)/2 - 4.696 \times 10^{-10} \\ (T^3 - T_0^3)/3 \\ - 1.987 \ln (p/p_0)]/M_3$$

Units*: $[S] = [\text{Btu/lbm}^\circ\text{R}]$, $[T] = [^\circ\text{K}]$, $[p] = [\text{psia}]$

Accuracy: $\pm 0.5\%$

Range: -50°F to 500°F (and probably beyond)

Discussion: The value of T_0 and p_0 is irrelevant.

The $\int C_p(T) \frac{dT}{T}$ part of this equation was checked against the gas tables of Reference 27 and found to agree within 0.4% in the temperature range of interest.

* Note mixed units here.

Equation of State

Component: Freon-13B1

Source: References 12 and 14.

Equation:

$$p_1 = \frac{-2.49597}{v^2} + \frac{0.0274558}{v^3} - \frac{0.00017894}{v^4} \\ + T \left[\frac{0.072047}{v} + \frac{0.00219617}{v^2} - \frac{0.000024787}{v^3} \right. \\ \left. + \frac{2.155 \times 10^{-7}}{v^4} \right] - \frac{1}{T^3} \left[\frac{5.877 \times 10^6}{v^2} - \frac{2.617 \times 10^3}{v^4} \right]$$

Units: [p] = [psia], [V] = [ft³/lb], and [T] = [°R].

Accuracy: $\pm 0.7\%$ in the range of interest to this LSM program. (See Reference 12 for a tabulation of accuracy over a wide range of pressures and temperatures.)

EQUATIONS FOR THE LSM GAS MIXTURE

This section displays and discusses the equations used to calculate the properties of the LSM gas mixtures. The LSM gas was treated as a three-component mixture: Freon, argon, and air. In the following discussion the gas composition is assumed to be precisely known. The effect of uncertainty in the LSM gas composition on gas properties is treated in Appendix II.

The Freons have a saturation curve which is closer to LSM "working conditions" than is the saturation curve for air. For pure Freon-13B1, the saturation temperature at 14.7 psia is -72°F and the saturation pressure at 70 °F is just over 200 psia. However, typical LSM gas mixtures have only 20% Freon by volume. And since saturation depends on the partial pressure of the Freon, the saturation of a typical LSM gas mixture when based on mixture pressure and temperature is -125°F at 14.7 psia and 1100 psia at 70°F. Therefore, with a "k = 1.4" LSM gas mixture, the gas state will always be quite far from saturation.

The basic assumption used here is that the LSM components mix like a perfect gas. While the individual components are not necessarily assumed to behave like perfect gases (for instance, the actual (non-ideal) equation of state of the Freon component is used in all calculations), the individual components are assumed to mix like perfect gases. Basically this means that the ratio of the partial pressure of each component to the mixture pressure is assumed to be equal to the volume (or mole) fraction of that component. This assumption greatly simplifies the calculation procedure while resulting in a negligible error.

Of course, the specific heats of the mixture are treated (correctly) as functions of temperature and pressure, as are the other thermodynamic and transport properties.

It should also be mentioned that the error bands listed with the property equations of the preceding section of this appendix are for the pure component. The largest uncertainty in component properties is for the Freon component. However, since the Freon component typically accounts for about 20% of the mixture by volume, the actual mixture uncertainties in each property (with known composition) are only about one-fifth of the uncertainties listed.

Gas Composition

The notation used to specify the composition of the LSM gas mixture is unconventional (though convenient). The words "pure" and "contaminated" refer to LSM without air and with air, respectively. They do not imply anything about the usable quality of the gas mixtures or the quality of the resulting compressor data.

y_1 is the volume fraction of Freon-13B1 in pure LSM.

y_2 is the volume fraction of Argon in pure LSM.

L is the volume fraction of Air in contaminated LSM.

$y_1(1-L)$ is the volume fraction of Freon-13B1 in contaminated LSM.

$y_2(1-L)$ is the volume fraction of Argon in contaminated LSM.

x_1 is the mass fraction of Freon-13B1 in pure LSM.

x_2 is the mass fraction of Argon in pure LSM.

Z is the mass fraction of Air in contaminated LSM.

$x_1(1-Z)$ is the mass fraction of Freon-13B1 in contaminated LSM.

$x_2(1-Z)$ is the mass fraction of Argon in contaminated LSM.

For an LSM mixture of the three components listed above, we can write the following equation:

$$L + [y_1(1-L)] + [y_2(1-L)] =$$

$$L + y_1 - y_1L + y_2 - y_2L =$$

$$L [1 - (y_1 + y_2)] + (y_1 + y_2) = 1$$

since, by definition, $y_1 + y_2 = 1$. A similar statement can be made about the mass fractions.

Molecular Weight

The molecular weight of any LSM gas mixture is given by

$$M_m = M_1 y_1 (1-L) + M_2 y_2 (1-L) + M_3 L$$

A useful relationship is

$$x_i = y_i \frac{M_i}{M_m}$$

Figure 75 shows y_1 vs. x_1 in a pure mixture of CB_rF_3 and Argon; Figure 76 shows M_m vs x_1 for pure LSM.

Gas Constant

The gas constant of any LSM gas mixture is given simply by

$$R_m = \frac{\tilde{R}}{M_m}$$

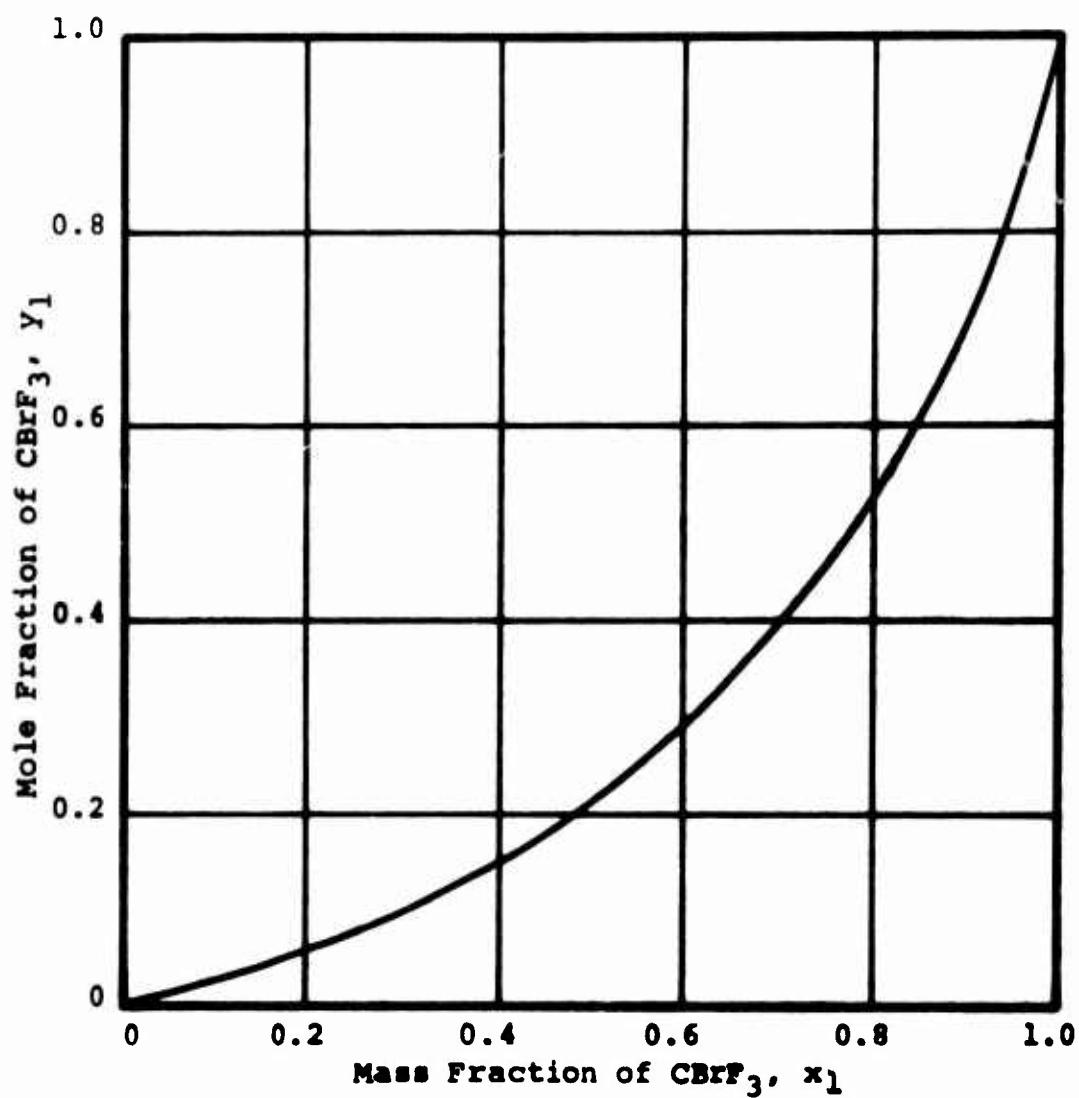


Figure 75. Relation Between Mole and Mass Fractions of CBrF_3 in a CBrF_3 /Argon Mixture.

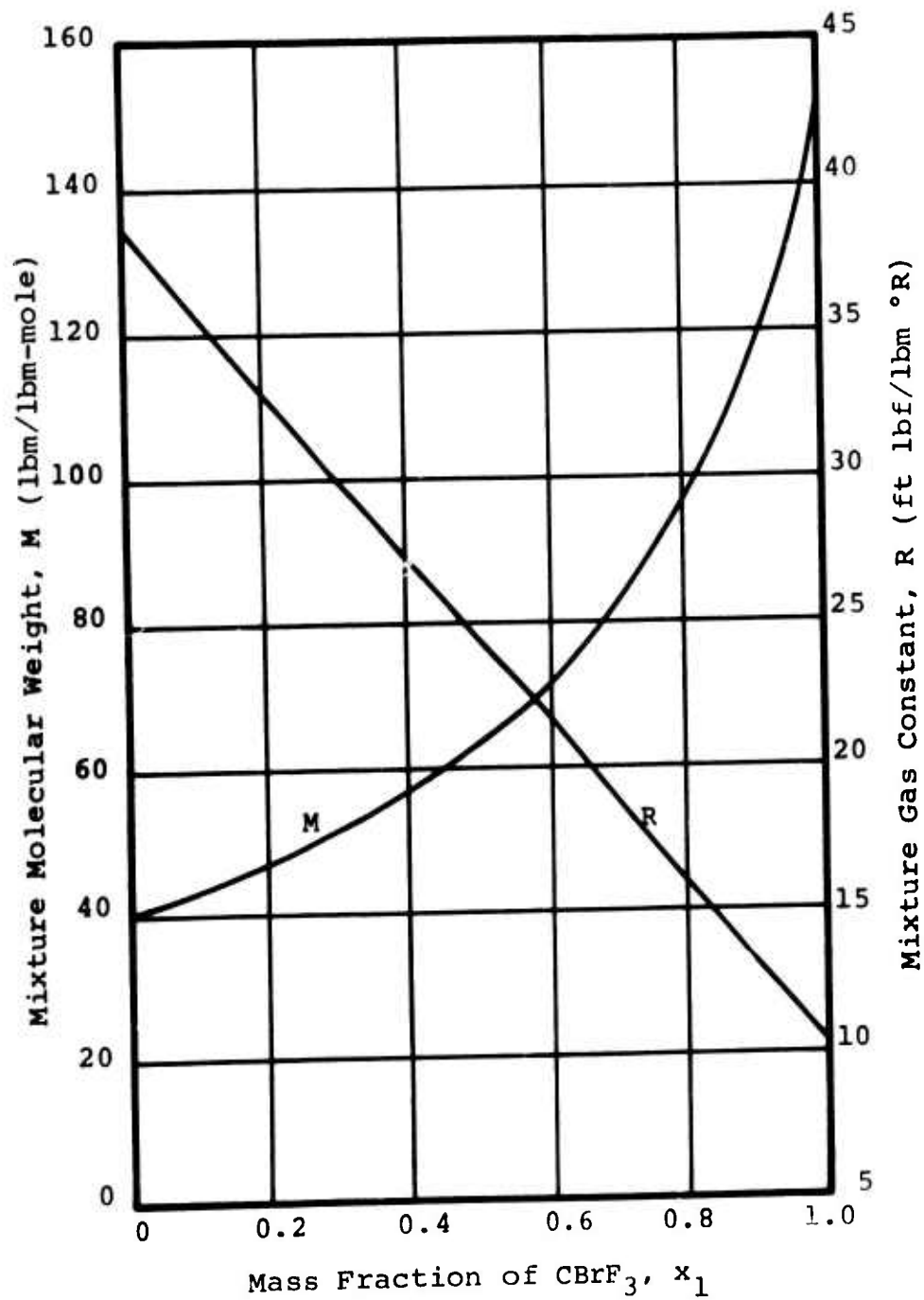


Figure 76 . Mixture Molecular Weight and Gas Constant for CBrF_3 /Argon Mixture.

where \tilde{R} is the universal gas constant.

Figure 76 shows R_m vs X_1 for pure LSM.

Viscosity

The viscosity of any LSM gas was calculated assuming pure LSM (see discussion in the previous section of this appendix) from the equation given in Reference 28:

$$\mu_m = \frac{\mu_1}{1 + \frac{(y_2/y_1) [1 + (\mu_1/\mu_2)^{1/2} (M_2/M_1)^{1/4}]^2}{(4/\sqrt{2}) [1 + (M_1/M_2)]^{1/2}}} + \frac{\mu_2}{1 + \frac{(y_1/y_2) [1 + (\mu_2/\mu_1)^{1/2} (M_1/M_2)^{1/4}]^2}{(4/\sqrt{2}) [1 + (M_2/M_1)]^{1/2}}}$$

The viscosity of several LSM gas mixtures is compared with the viscosity of air in Figure 77. The actual LSM viscosity at the inlet plenum temperature was used to assure close duplication of the air inlet Reynolds number under LSM test conditions.

Specific Heats

The specific heat at constant volume for any LSM gas mixture was calculated using

$$C_{vm} = x_1(1 - Z)C_{v1} + x_2(1 - Z)C_{v2} + ZC_{v3}$$

where the specific heats are per unit mass.

The specific heat at constant pressure for any LSM gas mixture was calculated using

$$C_{pm} = C_{vm} + R_m$$

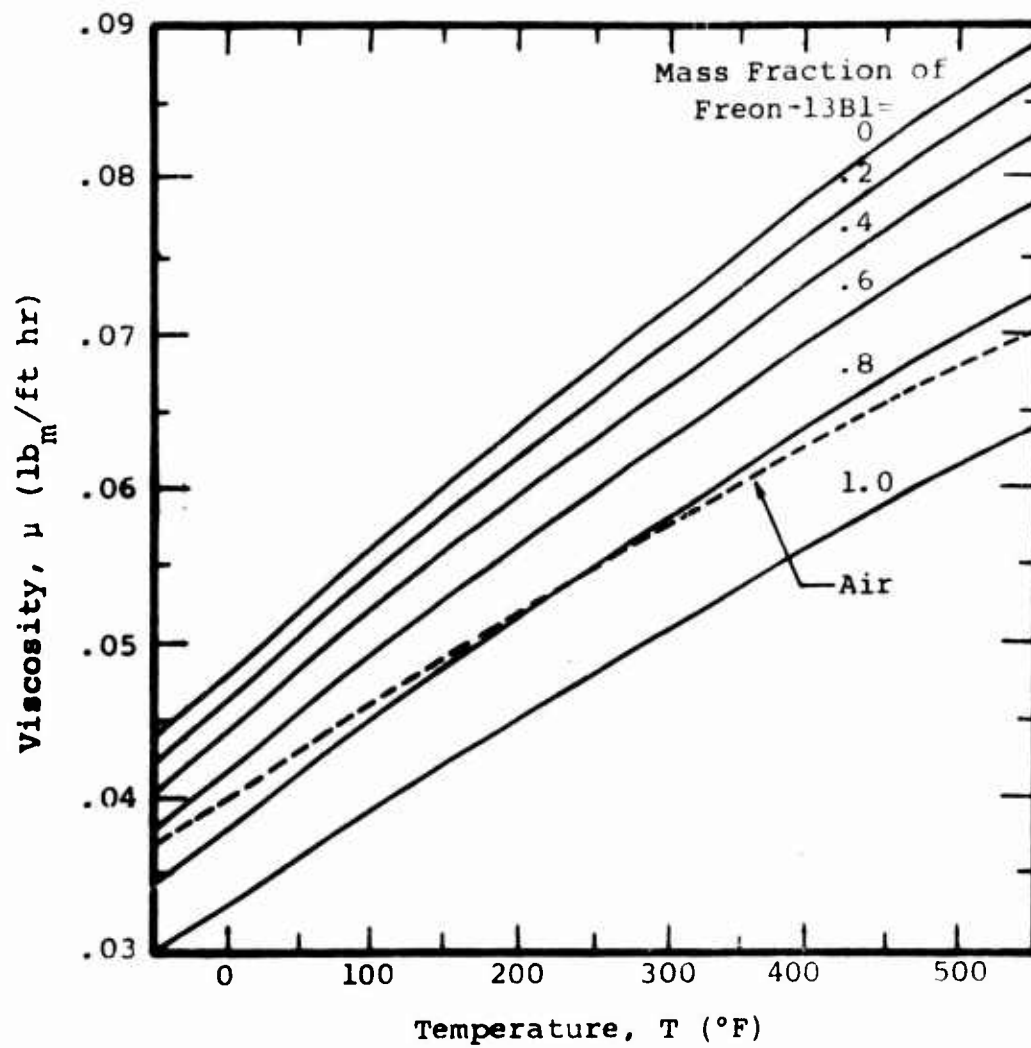


Figure 77. Viscosity of Various CBrF_3 /Argon Gas Mixtures.

The specific heats of the components are given in the preceding section of this appendix as functions of temperature and pressure. The partial pressures were used to evaluate the specific heats of each component at the desired state point.

Specific Heat Ratio

The specific heat ratio of any LSM gas mixture at any pressure and temperature was simply calculated by taking the ratio of the mixture specific heats. Thus

$$k_m = \frac{C_{pm}}{C_{vm}} \quad \text{or}$$

$$k_m = 1 + R_m/C_{vm}$$

Figure 1 shows the variation of the specific heat ratio with temperature for various LSM gas mixtures at a pressure of 14.7 psia. All of the data reduction calculations used the specific heat ratio at the actual temperature and pressure of the gas at the condition of interest. The mixture specific heat ratio was always evaluated using the combined specific heats of the individual components at the component partial pressure.

Enthalpy

The enthalpy of any LSM gas mixture at any temperature and pressure was calculated using

$$H_m = x_1(1 - Z)H_1 + x_2(1 - Z)H_2 + ZH_3$$

where the enthalpies of each component are per unit mass and are evaluated at the partial pressure of the component.

Entropy

The entropy of any LSM gas mixture at any temperature and pressure was calculated using

$$S_m = x_1(1 - Z)S_1 + x_2(1 - Z)S_2 + ZS_3$$

where the entropies of each component are per unit mass and are evaluated at the partial pressure of the component.

Speed of Sound

The speed of sound of any LSM gas mixture was calculated using

$$a_m = [k_m R_m T]^{1/2}$$

The variation of speed of sound with temperature for various LSM gas mixtures at a pressure of 14.7 psia is shown in Figure 78. All calculations were based on the temperature and component partial pressures (for k_m) as explained above.

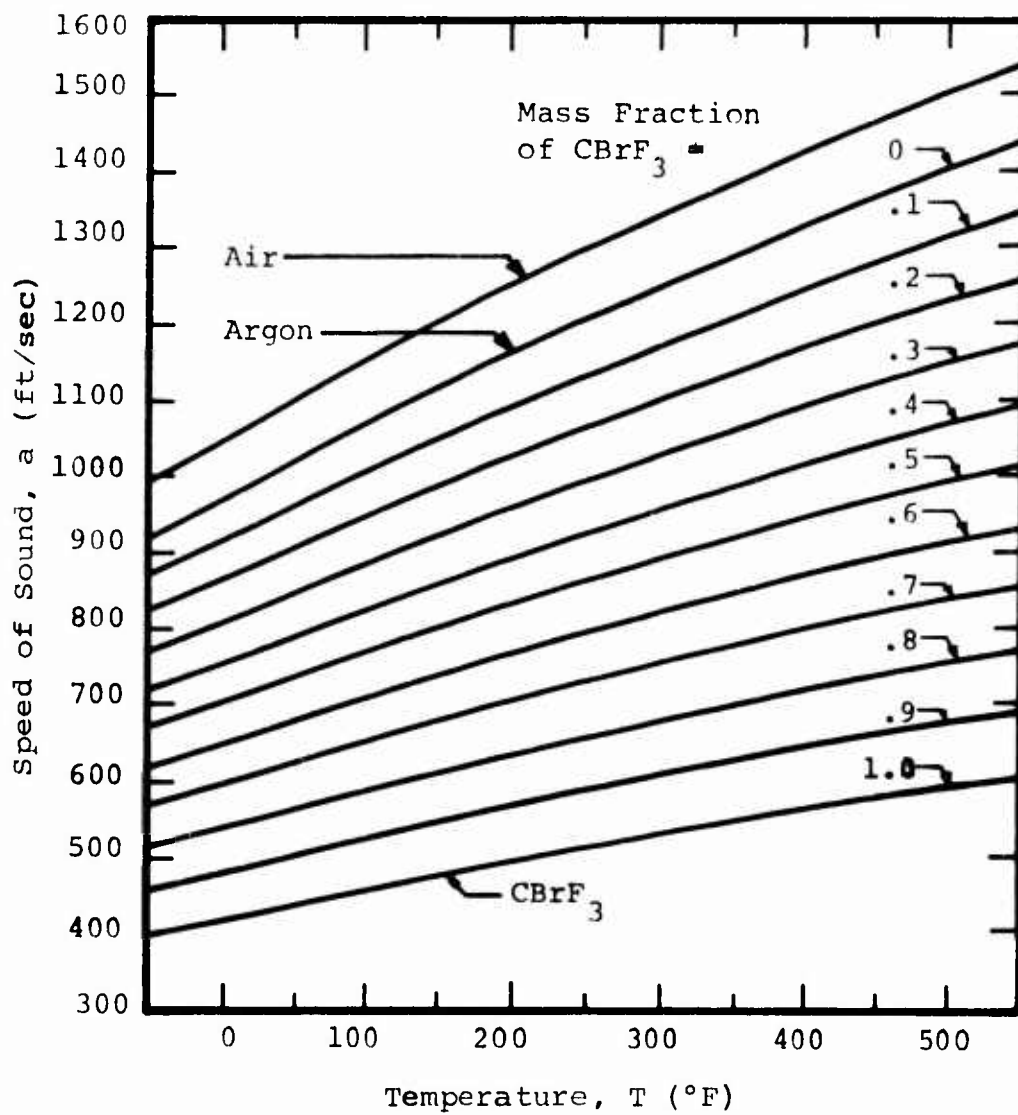


Figure 78. Speed-of-Sound Variation With Temperature for Various CBrF_3 /Argon LSM Gas Mixtures.

APPENDIX II

UNCERTAINTY ANALYSIS

The uncertainty in the primary quantities was estimated and discussed in Section 7.1. A summary is given in Table VI. This appendix contains the analysis which lead to the calculation of the level of uncertainty in the derived quantities as presented in Table VII.

DEFINITION OF UNCERTAINTY

Random errors represent "noise". The source of this "noise" is usually operator error or physical error due to thermal effects, friction, response time, etc. These errors appear in the final readout as scatter in the data. If these errors are truly randomly distributed, a twenty-to-one odds interval (the odds interval representing the experimenter's level of certainty that the uncertainty in the quantity under observation is as prescribed) is equal to twice the standard deviation. Kline and McClintock²² have shown that this same criterion is applicable when the form of the distribution of the errors is not known.

Let A represent a quantity to be calculated from a group of x_i primary quantities that are obtained as measurements.

It can be proven rigorously that if the quantity A is linear in each x_i and all the x_i 's are independent, the uncertainty in the result A is given precisely by the expression

$$\Delta A = \left[\left(\frac{\partial A}{\partial x_1} \Delta x_1 \right)^2 + \left(\frac{\partial A}{\partial x_2} \Delta x_2 \right)^2 + \dots \right]^{1/2} \quad (17)$$

if the x_i 's are normally distributed. Normalizing the above equation gives

$$\frac{\Delta A}{A} = \left[\left(\frac{x_1}{A} \frac{\partial A}{\partial x_1} \frac{\Delta x_1}{x_1} \right)^2 + \left(\frac{x_2}{A} \frac{\partial A}{\partial x_2} \frac{\Delta x_2}{x_2} \right)^2 + \dots \right]^{1/2} \quad (18)$$

Kline and McClintock²², in investigating distributions other than the normal distribution, concluded that the above expression gives very reasonable results when other than

normal distributions of random errors exist. Kline and McClintock concluded that the inaccuracies due to using this equation for other than a normal distribution are much smaller than the usual inaccuracies that occur in assigning uncertainty values to the primary physical quantities.

This discussion may seem to be sterile and irrelevant. If this is the case, one should reflect on the (deplorable) situation that exists in certain researches where uncertainty analyses are brushed under the carpet or ignored totally.

LSM UNCERTAINTY ANALYSIS

The uncertainty analysis for this LSM program was considerably complicated by the presence of a three-component gas mixture with (somewhat) variable composition. The uncertainties in the calculated parameters are generally dependent on both the imprecisions in knowing the LSM gas composition and the uncertainties in the properties of the LSM gas components.

In the following discussion, we have attempted to separate those quantities whose uncertainties are strongly influenced by the uncertainty in gas composition from those quantities which are essentially independent of the gas composition. The result of this attempt is that frequently in the discussion an uncertainty will be quoted as an uncertainty which would have resulted if the same instrumentation and measurement technique were utilized to measure the same parameters in pure air. These uncertainties will be compared to the additional uncertainties which result from the use of LSM.

Composition of the LSM Gas Mixture

The LSM gas used in this program was purchased commercially as a premixed gas. The composition of this pure* LSM was

* In this discussion, "pure" refers to a two-component LSM mixture with argon and Freon while "contaminated" refers to a three-component LSM mixture containing argon, Freon and air. The word contaminated in no sense indicates an unsuitable mixture but is used only as a reference term.

determined by a gas chromatograph "certified analysis" performed by the supplier. This analysis was checked by Creare by measuring the speed of sound of the delivered gas. [For one gas shipment, the measured speed of sound was inconsistent with the certified gas analysis supplied. A sample of this shipment was returned for re-analysis (after much hassling, as the supplier could not be convinced that he might have made a mistake). The re-analysis confirmed the gas composition fractions predicted by our speed-of-sound measurement. This incident increased our confidence in our technique for measuring the speed of sound.]

The amount of air contamination in the test loop at any time was determined by measurement of the speed of sound. By assuming that the ratio of Freon and argon concentrations remained unchanged from their original measured values, and that the only contaminant was air, the measurement of the LSM speed of sound gave the air fraction, the specific heat ratio, and the molecular weight of the gas mixture in the test loop. Thus the gas constant of the LSM mixture and the volume and mass fractions of each component, as well as the gas sound speed, could be determined at any time during (or after) a test.

Based on the uncertainties in the measured speed of sound and the temperature at which it is measured, the overall uncertainties for the LSM gas mixture as it exists in the test loop are summarized in Table XI. The uncertainties in knowing the amount of argon in the mixture are identical to those for Freon. Note that the absolute uncertainty in knowing the volume fraction of Freon is 2% of 0.196, or about 0.004. However, the absolute uncertainty in knowing the volume fraction of air is 0.01. The uncertainties the volume fraction of air cannot be reported as a relative uncertainty since the nominal fraction is 0. As will be seen below, these uncertainties in gas properties do NOT result in excessively large overall uncertainties in the important compressor parameters.

LSM Gas Component Property Equations

The LSM gas property equations for the individual components and an estimate of the uncertainties in these equations were

TABLE XI. OVERALL UNCERTAINTIES FOR A TYPICAL LSM GAS MIXTURE AS IT EXISTS IN THE TEST LOOP

| Item | Typical Value | Uncertainty |
|-------------------------------|--|---------------------------|
| Volume fraction of Freon-13B1 | $y_1 = .196$ | $\Delta y_1 / y_1 = 2\%$ |
| Mass fraction of Freon-13B1 | $x_1 = .476$ | $\Delta x_1 / x_1 = 13\%$ |
| Volume percent of air | - | $\Delta L = 1\%$ |
| Mass percent of air | - | $\Delta z = 2\%$ |
| Mixture molecular weight | $M = 61.3$ | $\Delta M / M = 0.75\%$ |
| Mixture gas constant | $R = 25.2 \text{ ft} \cdot \text{lb}_f / \text{lb}_m \cdot ^\circ\text{R}$ | $\Delta R / R = 0.75\%$ |

presented in Appendix I. That appendix also contained the basic equations needed to combine the individual property equations to calculate the properties of the gas mixture.

The uncertainties in the resulting equations for the LSM gas mixture properties at any given state point can be calculated using Equation 18 by combining:

- 1) the uncertainties in the basic equations for the individual components
- 2) the uncertainty in knowing the exact composition of the LSM gas mixture
- 3) the uncertainty in the measured temperature and pressure used to define the state point of interest.

The uncertainties in the mixture properties are displayed where needed throughout this analysis to calculate parameters of interest such as air-equivalent speed, air-equivalent flow rate, and compressor efficiency.

Air-Equivalent Compressor Speed

The LSM compressor speed N_m which must be set to model an air compressor speed N_a is obtained from the speed-of-sound ratio by Equation (1),

$$N_m = N_a \frac{a_{om}}{a_{oa}} = N_{eq} \frac{a_{om}}{a_{oa}} \quad (19)$$

Now a_{oa} is a predetermined value depending on the air conditions that are being modeled. The inlet sound speed in LSM a_{om} is related to the speed of sound measured at temperature T_{sos}^* and the plenum temperature by

* The subscript "sos" refers to conditions at the speed-of-sound device.

$$a_{om} = a_{sos} \sqrt{\frac{k_m(T_{om})}{k_m(T_{sos})}} \sqrt{\frac{T_{om}}{T_{sos}}} \quad (20)$$

It can be shown that the uncertainty in the ratio of k_m at the plenum temperature to k_m at the speed-of-sound measurement temperature is very small. Thus in this particular uncertainty calculation, this contribution can be neglected. However, it is important to point out that uncertainties in k_m and other properties have not been neglected "across-the-board" in this uncertainty analysis. Also, all LSM gas mixture properties are based on a three-component mixture and are always evaluated as functions of temperature and pressure. No "average values" are ever used in the data reduction program.

Thus, from Equation (20), we have

$$\frac{\Delta a_{om}}{a_{om}} = \left\{ \left[\frac{\Delta a_{sos}}{a_{sos}} \right]^2 + \left[\frac{1}{2} \left(\frac{\Delta T_{om}}{T_{om}} \right) \right]^2 + \left[\frac{1}{2} \left(\frac{\Delta T_{sos}}{T_{sos}} \right) \right]^2 \right\}^{1/2} \quad (21)$$

Inserting values from Table VI gives

$$\begin{aligned} \frac{\Delta a_{om}}{a_{om}} &= \left[(.005)^2 + (.0022)^2 + (.001)^2 \right]^{1/2} \\ &= 0.0055 \quad \text{or } 0.55\% \end{aligned} \quad (22)$$

Now, applying Equation (18) to Equation (19) gives

$$\frac{\Delta N_{eq}}{N_{eq}} = \left[\left(\frac{\Delta N_m}{N_m} \right)^2 + \left(\frac{\Delta a_{om}}{a_{om}} \right)^2 \right]^{1/2} \quad (23)$$

Since the uncertainty in actual speed was 0.2%, we have (upon performing the arithmetic indicated) the uncertainty in the air-equivalent compressor speed:

$$\frac{\Delta N_{eq}}{N_{eq}} = 0.0059 \quad \text{or } 0.59\% \quad (24)$$

Therefore, the total uncertainty in knowing the air-equivalent speed for any state point is about 0.6%. If the same instrumentation was used for air testing, only the terms $\Delta N_m/N_m$ and $\Delta T_{om}/T_{om}$ * would remain and the uncertainty would be $[(.002)^2 + (.0022)^2]^{1/2} = 0.3\%$. This is one of very few parameters which have more than a negligibly greater uncertainty associated with LSM model testing when compared to air testing using identical instrumentation.

Pressure Ratio

For typical operating conditions, the uncertainties in the plenum and collector pressure are 0.5% and 0.1% respectively, as discussed in Section 7.1. Thus the uncertainty in the pressure ratio, obtained from Equation (18), is

$$\begin{aligned} \frac{\Delta PR}{PR} &= \left[\left(\frac{\Delta p_{col}}{p_{col}} \right)^2 + \left(\frac{\Delta p_{pln}}{p_{pln}} \right)^2 \right]^{1/2} \\ &= (0.001)^2 + (0.005)^2 \quad (25) \\ &= 0.0051 \quad \text{or } 0.51\% \end{aligned}$$

This uncertainty is independent of both the type of gas used and any uncertainties in knowing the gas property equations or exact composition.

* It is important to note that an accurate measurement of inlet temperature is as important for air testing as it is for LSM.

Air-Equivalent Mass Flow Rate

The uncertainties associated with the actual and referred (air-equivalent) mass flow rates will be calculated below in some detail to demonstrate that uncertainties in LSM gas composition and property equations have a negligible influence on the uncertainty of the location of the mass flow (and of course pressure ratio) state point on the compressor map.* The results of this section are summarized on page 207.

In this mass flow rate uncertainty analysis, care must be taken to distinguish between the actual mass flow rate through the compressor M_m^{**} and the referred or air-equivalent mass flow rate M_{eq} . The flow rate uncertainties will be calculated for two cases:

- 1) The uncertainties with Creare's LSM instrumentation but assuming the gas is air (demonstrating the procedure that should be used in any mass flow rate uncertainty analyses with air).
- 2) The complete uncertainty analysis for M_m and M_{eq} with the LSM gas, including the effect of uncertainties in the gas composition and property equations.

* The uncertainties in gas composition do increase the uncertainty in N_{eq} and η over corresponding uncertainties in air testing.

** In this section, M_m refers to the actual flow of the "modeling" gas, whether it is LSM or air. The mass flow rate "referred" to standard pressure and temperature air conditions is M_{eq} .

It should be observed that the air-equivalent flow rate M_{eq} is a most important parameter of interest in compressor maps and scaling schemes obtained with either air or LSM.

The equation for the actual mass flow rate is *

$$M_m = Cd^2 YK \left[\frac{p_3}{T_3} \frac{M_m}{M_a} \Delta p \right]^{1/2} \quad (26)$$

$$\text{where } Y = 1 - \left[0.41 + 0.35 \left(\frac{d}{D} \right)^4 \right] \left[\frac{\Delta p}{p_3} \frac{(.03606)}{k_3} \right] \quad (27)$$

C = a constant depending on the units chosen and the local value of gravity

K = a function of Reynolds number

Δp = the pressure drop across the flowmeter

"3" = flowmeter conditions with LSM

"1" = plenum stagnation condition with LSM

"s" = standard or referred condition for air
(519.7°R, 29.92"Hg)

From the scaling relations presented in Section 4.2, the equation for air-equivalent or referred mass flow rate is

$$M_{eq} = M_m \frac{p_s}{p_1} \left[\frac{k_s}{k_1} \frac{M_a}{M_m} \frac{T_1}{T_s} \right]^{1/2} \frac{f(k_1)}{f(k_s)} \quad (28)$$

$$\text{where } f(k) = \left[\frac{k+1}{2} \right]^{\frac{k+1}{2(k-1)}} \quad (29)$$

* Equation appropriate for the orifice flowmeter technique used in these studies.

Now, if the gas is air, Equations (28) and (29) reduce to the standard compressor scaling relations if one assumes that $k(T_1) \approx k(T_s)$, which is justified if the actual inlet temperature is sufficiently close to the standard inlet temperature. In this case, $f(k_s) = f(k_1)$ and $M_a = M_m$ and (2) becomes

$$M_{eq} = M_m \left(\frac{p_s}{p_1} \right) \left(\frac{T_1}{T_s} \right)^{1/2} \quad (30)$$

or

$$M_{eq} = M_m \sqrt{\theta/\delta} \quad (31)$$

where $\delta = p_1/p_s$

$\theta = T_1/T_s$

It is important to observe that most uncertainty analyses estimate the uncertainty in M_m but neglect to calculate the uncertainty in M_{eq} . Since M_{eq} is often the value used on compressor maps, this latter step is essential for an accurate uncertainty analysis.

Applying Equations (18) to (26) gives, for the general case,

$$\frac{\Delta M_m}{M_m} = \left\{ \left[2 \frac{\Delta d}{d} \right]^2 + \left[\frac{\Delta Y}{Y} \right]^2 + \left[\frac{\Delta K}{K} \right]^2 + \left[\frac{1}{2} \frac{\Delta p_3}{p_3} \right]^2 + \left[\frac{1}{2} \frac{\Delta T_3}{T_3} \right]^2 + \left[\frac{1}{2} \frac{\Delta M_m}{M_m} \right]^2 + \left[\frac{1}{2} \frac{\Delta(\Delta p)}{\Delta p} \right]^2 \right\}^{1/2} \quad (32)$$

[Note that this is not completely correct since Y and K are not independent of p_3 , T_3 , k_3 and Δp . However, since these variables have only a weak effect on Y and K , a sufficiently accurate uncertainty calculation of M_m can be made using (32).]

However, the uncertainty in M_{eq} cannot be found by applying Equations (18) to (28) directly with $\Delta M_m / M_m$ inserted into the result. In the general case of a gas different from air, this procedure would result in an overestimate of the uncertainty in M_{eq} due to the "cancelling" effect of M and k . For the general case, Equations (26) and (28) must be combined before applying Equation (18). Before this is done for the general case, we will complete the analysis for the uncertainty when the test gas is air.

Uncertainty in the Flow Rate When the Test Gas Is Air

Combining (26) and (30) for air (where $M_m = M_{air}$) gives

$$M_{eq} = Cd^2 YK \left[\frac{p_s}{p_1} \left(\frac{T_1}{T_s} \right)^{1/2} \left[\frac{p_3}{T_3} \Delta p \right]^{1/2} \right]^{1/2} \quad (33)$$

Now, Equation (18) should not be applied blindly to (33) since, even though p_3 and p_1 and T_3 and T_1 are independent in a mathematical sense, they are not independent in an experimental-measurement-uncertainty sense. That is, since the two temperatures are measured with the same icebath and with thermocouples made in a similar manner from the same roll of thermocouple wire, and since the pressures were read on similar transducers calibrated in an identical manner, and since the same voltmeter was used to read all of these parameters, the errors in each pressure and temperature are not independent. If T_1 or p_1 were low, most probably T_3 or p_3 would also be low.

Thus, applying Equation (18) directly to (33) and treating the uncertainties in each quantity as independent would overestimate the uncertainty. The actual uncertainty in M_{eq} lies somewhere between that obtained by treating T_1 and T_3 and p_1 and p_3 as independent and that obtained by treating T_1 and T_3 and p_1 and p_3 as completely-coupled variables.

If T_1 and T_3 and p_1 and p_3 are considered completely independent, we have

$$\frac{\Delta M_{eq}}{M_{eq}} = \left\{ \left[2 \frac{\Delta d}{d} \right]^2 + \left[\frac{\Delta Y}{Y} \right]^2 + \left[\frac{\Delta K}{K} \right]^2 + \left[\frac{\Delta p_1}{p_1} \right]^2 + \left[\frac{1}{2} \frac{\Delta T_1}{T_1} \right]^2 + \left[\frac{1}{2} \frac{\Delta p_3}{p_3} \right]^2 + \left[\frac{1}{2} \frac{\Delta T_3}{T_3} \right]^2 + \left[\frac{1}{2} \frac{\Delta(\Delta p)}{\Delta p} \right]^2 \right\}^{1/2} \quad (34)$$

If T_1 and T_3 and p_1 and p_3 are completely coupled, we have

$$\frac{\Delta M_{eq}}{M_{eq}} = \left\{ \left[2 \frac{\Delta d}{d} \right]^2 + \left[\frac{\Delta Y}{Y} \right]^2 + \left[\frac{\Delta K}{K} \right]^2 + \left[\frac{1}{2} \left(\frac{\overline{\Delta p}}{p} \right) \right]^2 + \left[\frac{1}{2} \frac{\Delta(\Delta p)}{\Delta p} \right]^2 \right\}^{1/2} \quad (35)$$

where $\left(\frac{\overline{\Delta p}}{p} \right)$ is the maximum uncertainty in p_1 and p_3 measurements.

Now, Equation (32) with $\Delta M_m / M_m = 0$ and either Equation (34) or (35) are to be used to obtain $\Delta M_m / M_m$ and $\Delta M_{eq} / M_{eq}$ for the case where the gas is air.

Estimates of the uncertainties in the "independent" quantities follow:

| | | |
|-------------------------------|--|--|
| $\frac{\Delta d}{d} = 0.0003$ | $\frac{\Delta p_1}{p_1} = 0.005$ | $\frac{\Delta T_1}{T_1} = 0.0044$ |
| $\frac{\Delta Y}{Y} = 0.0002$ | $\frac{\Delta p_3}{p_3} = 0.001$ | $\frac{\Delta T_3}{T_3} = 0.003$ |
| $\frac{\Delta K}{K} = 0.006$ | $\left(\frac{\overline{\Delta p}}{p} \right) = 0.005$ | $\frac{\Delta(\Delta p)}{\Delta p} = 0.01$ |

Inserting these values into (32) gives

$$\frac{\Delta M_m}{M_m} = 0.008 \text{ or } 0.8\%$$

If T_1 and T_3 and p_1 and p_3 are assumed to be completely independent, we have from (34)

$$\frac{\Delta M_{eq}}{M_{eq}} = 0.010 \text{ or } 1.0\%$$

If T_1 and T_3 and p_1 and p_3 are completely coupled, we have from (35)

$$\frac{\Delta M_{eq}}{M_{eq}} = 0.0084 \text{ or } 0.84\%$$

Therefore, an uncertainty estimate for $\Delta M_{eq}/M_{eq}$ of 0.9% is reasonable.

Thus, we see that, if the test gas is air,

$$\frac{\Delta M_m}{M_m} = 0.8\% \text{ and } \frac{\Delta M_{eq}}{M_{eq}} = 0.9\%$$

Notice that the uncertainty in the referred mass flow rate for air is greater than the uncertainty in the actual mass flow rate. This statement is true in general for all air testing (including Boeing's), although the actual values of the two uncertainties depend on the measurement technique used.

Uncertainty in the Flow Rate for LSM Gas

Returning now to the general case, Equation (32) is valid for $\Delta M_m/M_m$, but Equations (26) and (28) must be combined before application of Equation (18) to obtain $\Delta M_{eq}/M_{eq}$. Combining gives

$$M_{eq} = Cd^2 YK \frac{p_s}{p_1} \left[\left(\frac{p_3}{T_3} \right) \left(\frac{T_1}{T_s} \right) \Delta p \right]^{1/2} \left[\frac{f(k_1)/k_1}{f(k_s)/k_2} \right] \text{ or } \quad (36)$$

$$M_{eq} = Cd^2 YK \frac{p_s}{p_1} \left[\left(\frac{p_s}{T_3} \right) \left(\frac{T_1}{T_s} \right) \Delta p \right]^{1/2} \frac{g(k_1)}{g(k_s)} \quad (37)$$

$$\text{where } g(k) = f(k)/k \quad (38)$$

Note that M_m has dropped out of Equation (37), indicating that although an uncertainty in M_m (caused by an uncertainty in the gas composition) does affect M_m , it does not result in any uncertainty in the main variable of interest M_{eq} .

Now we again have the lack of experimental independence of T_1 and T_3 and p_1 and p_3 . However, in addition we have the fact that k is a function of T (as well as gas composition and, to be correct, pressure also) and hence $g(k_1)$ and T_1 are not independent.

Consider for a moment the case of LSM where we assume complete certainty in the gas composition values. For this case $\Delta M_m / M_m = 0$ and, as before, Equation (32) gives

$$\frac{\Delta M_m}{M_m} = 0.8\%$$

Now, if T_1 and T_3 and p_1 and p_3 are treated as independent (and composition is precisely known), Equation (37) can be rewritten

$$M_{eq} = Cd^2 YK \frac{p_s}{p_1} \left[\frac{p_3}{T_3} \Delta p \right]^{1/2} \frac{h(T_1)}{h(T_s)} \quad (39)$$

$$\text{where } h(T) = \sqrt{T} g(k(T)) \quad (40)$$

Thus, using Equation (18), we have

$$\frac{\Delta M_{eq}}{M_{eq}} = \left\{ \left[\frac{2\Delta d}{d} \right]^2 + \left[\frac{\Delta Y}{Y} \right]^2 + \left[\frac{\Delta K}{K} \right]^2 + \left[\frac{\Delta p_1}{p_o} \right]^2 + \left[\frac{1}{2} \frac{\Delta p_3}{p_3} \right]^2 + \left[\frac{1}{2} \frac{\Delta T_3}{T_3} \right]^2 + \left[\frac{1}{2} \frac{\Delta(\Delta p)}{\Delta p} \right]^2 + \left[\left(\frac{\partial h_3}{\partial T_1} \frac{T_1}{h_3} \right) \frac{\Delta T_1}{T_1} \right]^2 \right\}^{1/2} \quad (41)$$

All terms in this equation are known except for the last. However, since the only effect of T_1 on M_{eq} is through $h(T)$, we can write

$$\frac{\partial h}{\partial T_1} \frac{T_1}{h} = \frac{\partial M_{eq}}{\partial T_1} \frac{T_1}{M_{eq}}$$

and by computer iteration we obtain

$$\frac{\partial M_{eq}}{\partial T_1} \frac{T_1}{M_{eq}} = 0.53$$

(Note: if the k was not a function of T , the value of $\partial M_{eq} / \partial T_1 T_1 / M_{eq}$ would be 0.50.)

Thus, from (41) we have $\Delta M_{eq} / M_{eq} = 0.010$ or 1.0%. Comparing this result with the result from the previous section, where the test gas was assumed to be air, shows that the variation of specific heat ratio with temperature contributes only a negligible amount to the uncertainty in M_{eq} . Said another way, the $k(T)$ variation must be (and is) taken into consideration in calculating M_{eq} , but it does not have to be taken into consideration in calculating the uncertainty in M_{eq} . Since similar statements can be made about the effect of $k(T)$ on the value of N_{eq} and the uncertainty in N_{eq} , the previous assumptions made in the calculation of the

uncertainty of N_{eq} are justified.

Thus the uncertainties in M_m and M_{eq} were, to a very good approximation, independent of the gas composition (at least for air and LSM), provided the gas composition is accurately known. The effects of uncertainty in gas composition will now be discussed.

For the general case with uncertainty in gas composition, Equations (32) and (37) apply. With $\Delta M_m / M_m = 0.0075$, we have $\Delta M_m / M_m = 0.0085$ or 0.85% (compared with 0.80% with composition known).

Now if T_1 and T_3 and p_1 and p_3 are treated as independent (and composition is not precisely known), Equation (37) becomes

$$M_{eq} = Cd^2 YK \frac{p_s}{p_1} \left[\frac{p_3}{T_3} \Delta p \right]^{1/2} \frac{h(T_1, \text{comp})}{H(T_s)} \quad (42)$$

$$\text{where } h(T, \text{comp}) = \sqrt{T} g(k(T, \text{comp})) \quad (43)$$

Thus, using Equation (18), we have

$$\begin{aligned} \frac{\Delta M_{eq}}{M_{eq}} = & \left\{ \left[\frac{2\Delta d}{d} \right]^2 + \left[\frac{\Delta Y}{Y} \right]^2 + \left[\frac{\Delta K}{K} \right]^2 + \left[\frac{\Delta p_1}{p_1} \right]^2 + \left[\frac{1}{2} \frac{\Delta p_3}{p_3} \right]^2 + \left[\frac{1}{2} \frac{\Delta T_3}{T_3} \right]^2 \right. \\ & \left. + \left[\frac{1}{2} \frac{\Delta(\Delta p)}{\Delta p} \right]^2 + \left[\left(\frac{\partial h}{\partial T_1} \frac{T_1}{h} \right) \frac{\Delta T_1}{T_1} \right]^2 + \left[\left(\frac{\partial h}{\partial y_i} \frac{y_i}{h} \right) \frac{\Delta y_i}{y_i} \right]^2 \right\}^{1/2} \quad (44) \end{aligned}$$

where y_i is a composition variable.

It has been assumed that the uncertainty in composition has a negligible effect on Y and K . (Composition errors affect Y through k , but the effect of any reasonable degree of uncertainty in composition on k is small and the effect of k variations on Y is very small, and so the effects of

uncertainties in gas composition on Y through k are very small indeed. Composition uncertainties also affect K through μ and Re . However, since the Re is large, and K is a weak function of Re , this uncertainty is also very small.

Now, as before, $\partial h / \partial T_1 T_1 / h = \partial M_{eq} / \partial T_1 T_1 / M_{eq} = 0.53$.

(It has been shown above that the effect of k on h is in general small. Furthermore, since the errors in composition have a small effect on k , it is expected that uncertainties in gas composition will have only a weak effect on h and hence also a weak effect on M_{eq} .)

Since the uncertainty in gas composition is related directly to the uncertainty in a_{sos} , we can write

$$\frac{\partial h}{\partial y_i} \frac{y_i}{h} \frac{\Delta y_i}{y_i} = \frac{\partial M_{eq}}{\partial a_{sos}} \frac{a_{sos}}{M_{eq}} \frac{\Delta a_{sos}}{a_{sos}} \quad (45)$$

From a computer iteration, we have

$$\frac{\partial h}{\partial y_i} \frac{y_i}{h} \frac{\Delta y_i}{y_i} = 1.6 \times 10^{-5}$$

which is very small, as expected. Inserting values into Equation (44) gives

$$\frac{\Delta M_{eq}}{M_{eq}} = 1.0\% \text{ for } T_1, T_3, p_1, p_3 \text{ independent}$$

and using similar logic,

$$\frac{\Delta M_{eq}}{M_{eq}} = 0.84\% \text{ for } T_1, T_3, p_1, p_3 \text{ coupled}$$

Summary of Mass Flow Rate Uncertainty Analysis

The results of this analysis for flow rate uncertainties are summarized in Table XII.

| TABLE XII. SUMMARY OF THE FLOW RATE UNCERTAINTY ANALYSIS | | |
|--|--------------------|--------------------------|
| Case | $\Delta M_m / M_m$ | $\Delta M_{eq} / M_{eq}$ |
| 1. If the test gas is air | 0.80% | 0.84 - 1.0% |
| 2. LSM with known composition | 0.80% | 0.84 - 1.0% |
| 3. LSM with "uncertain" composition | 0.85% | 0.84 - 1.0% |

We thus reach the important conclusion that:

Although uncertainties in the LSM gas composition result in a greater uncertainty in the actual gas flow rate (M_m) for LSM than for air, they do not result in any greater uncertainty in the referred flow rate (M_{eq}) for LSM than for air.

The reasons for this (stated somewhat imprecisely) are:

- 1) M_m drops out of the M_{eq} equation.
- 2) k has only a weak effect on M_{eq} .
- 3) μ has only a weak effect on M_{eq} .
- 4) Composition has only a weak effect on k and μ .

Further, we stress the fact that the effects of composition and temperature (and pressure where appropriate) on k and μ are retained when calculating results. For these they are important. However, they are unimportant in the calculation of the uncertainty bands in the final results.

Efficiency

The isentropic stage efficiency η for the LSM tests is a function of the plenum and collector pressure and temperature and the gas composition. The gas composition is determined

by knowing any two of the three parameters y_1 , y_2 and L .
In this analysis we will use

$$\eta = \eta(T_1, T_2, p_1, p_2, y_1 \text{ and } L) \quad (46)$$

Applying Equation (18) to this expression gives

$$\begin{aligned} \frac{\Delta\eta}{\eta} = & \left\{ \left[\left(\frac{\partial\eta}{\partial T_1} \frac{T_1}{\eta} \right) \left(\frac{\Delta T_1}{T_1} \right) \right]^2 + \left[\left(\frac{\partial\eta}{\partial T_2} \frac{T_2}{\eta} \right) \left(\frac{\Delta T_2}{T_2} \right) \right]^2 + \left[\left(\frac{\partial\eta}{\partial p_1} \frac{p_1}{\eta} \right) \left(\frac{\Delta p_1}{p_1} \right) \right]^2 \right. \\ & \left. + \left[\left(\frac{\partial\eta}{\partial p_2} \frac{p_2}{\eta} \right) \left(\frac{\Delta p_2}{p_2} \right) \right]^2 + \left[\left(\frac{\partial\eta}{\partial y_1} \frac{y_1}{\eta} \right) \left(\frac{\Delta y_1}{y_1} \right) \right]^2 + \left[\left(\frac{\partial\eta}{\partial L} \frac{L}{\eta} \right) \left(\frac{\Delta L}{L} \right) \right]^2 \right\}^{1/2} \end{aligned} \quad (47)$$

Since the equations for entropy and enthalpy are complicated functions of these independent variables, the terms in this equation are not easily evaluated analytically. Therefore, a computer iteration scheme was used to calculate the partial derivative terms in this equation for a typical LSM gas mixture ($k = 1.4$ at inlet conditions). This resulted in the following expressions:

$$\frac{\partial\eta}{\partial T_1} \frac{T_1}{\eta} = 1.74$$

$$\frac{\partial\eta}{\partial T_2} \frac{T_2}{\eta} = -2.07$$

$$\frac{\partial\eta}{\partial p_1} \frac{p_1}{\eta} = -0.58$$

$$\frac{\partial\eta}{\partial p_2} \frac{p_2}{\eta} = 0.58$$

$$\frac{\partial\eta}{\partial y_1} \frac{y_1}{\eta} = -0.36$$

$$\frac{\partial\eta}{\partial L} \frac{L}{\eta} = 0.0018$$

This list contains $\partial\eta/\partial L \Delta L/\eta$ rather than $\partial\eta/\partial L L/\eta$, since the term $(\partial\eta/\partial L L/\eta) (\Delta L/L)$ must be rewritten as $(\partial\eta/\partial L (\Delta L/\eta))$ before evaluation because the nominal value of L is zero.

Now, inserting these quantities and the quantities from Tables VI and XI into Equation (18) gives

$$\frac{\Delta\eta}{\eta} = [(.765)^2 + (.435)^2 + (.290)^2 + (.058)^2 + (.72)^2 + (.18)^2]^{1/2} \quad (48)$$

$\times 10^{-2}$

where the terms have been written in the same order as in Equation (47) to show which uncertainties are the largest contributors to the total uncertainty in efficiency. Notice that the largest uncertainties in efficiency result from the uncertainties in the plenum temperature measurement and the uncertainty of the fractions of Freon-13B1 and argon in the LSM gas mixture. Uncertainties in the amount of air contamination and the measured collector pressure contribute negligibly to the total uncertainty in efficiency.

The total uncertainty in LSM isentropic stage efficiency is

$$\frac{\Delta\eta}{\eta} = 0.012 \text{ or } 1.2\%$$

If the fractions of Freon-13B1 and argon in the LSM mixture were precisely known, the uncertainty in the efficiency would be 0.95%. (This, of course, does not mean that the uncertainty in Boeing's efficiencies is 0.95%. Boeing's actual uncertainty in efficiency can be determined only by a careful analysis of their original instrumentation and measurement techniques.

This discussion says nothing about errors in obtaining the true adiabatic efficiency when tests are conducted with an uninsulated compressor (as was done for all Boeing tests of interest to the present program). This will be discussed in Appendix III.

Table VII contains a listing of the uncertainty levels of the derived quantities for the LSM tests.

APPENDIX III

EFFECT OF HEAT TRANSFER ON MEASURED EFFICIENCY

Most compressor efficiency data is reported as isentropic (or adiabatic) efficiency. However, measured efficiencies on test stands approach isentropic (adiabatic) efficiencies only if care has been taken during testing to preclude significant heat transfer from the gas to the (machine and room) environment. If this is not done, heat transfer from the gas will reduce the collector gas temperature and hence will result in a measured efficiency which is higher than the actual isentropic efficiency of the stage being tested. As we shall see, this efficiency error can be several points or more under conditions typical of centrifugal test rigs.

One might argue that a compressor should be tested in an environment similar to that in which it is to be used. However, since environmental conditions can have a strong influence on measured efficiency, the only valid comparison that can be made between stages tested under different environmental conditions is a comparison of the true isentropic efficiencies obtained with sufficient insulation around the compressor to preclude significant heat transfer.

All Boeing air data referenced in this report were obtained without compressor insulation. Because of this, the LSM tests were also performed without collector insulation. This raises an immediate question of whether the difference in the heat transfer effects in the two cases (LSM and air) might result in a significant difference in measured efficiency in these two cases. This question is addressed theoretically in this appendix. In addition, several LSM tests were performed with the compressor well insulated to study the effect of heat transfer on measured efficiency. These tests revealed that when the compressor was well insulated, the measured efficiency decreased by 2 to 3 percentage points. The lower efficiency (that is, that obtained with an insulated collector) is more closely representative of the true isentropic efficiency for this machine.

Because of the complex external geometry of the compressor, a precise heat transfer calculation is difficult. Rather

than attempt a detailed calculation, we instead performed an approximate calculation which was sufficiently accurate to estimate:

- 1) the fractional increase in measured efficiency due to heat transfer
- 2) the relative effect of heat transfer on measured efficiency for both air vs LSM testing.

As will be shown in the analysis below:

- 1) A 2 to 3 percent increase in efficiency (over the true isentropic value) is to be expected when 50,000-rpm (air-equivalent speed) testing is performed on the RF-2 compressor without insulation.
- 2) The change in heat transfer that occurs with no insulation on the compressor with either LSM or with air has very nearly the same effect on the measured efficiency in both cases. (Of course, the problem of a different effect of heat transfer on measured efficiency with air and LSM does not enter if both experiments are performed with an insulated compressor.)

Heat transfer from the compressor reduces the measured gas temperature in the collector and thus results in a measured efficiency which is higher than the actual isentropic efficiency. Letting $\Delta\eta$ refer to the increase in measured efficiency due to heat transfer from the gas to the environment, an approximate expression for the fractional change in efficiency is

$$\frac{\Delta\eta}{\eta} = \frac{\Delta T_{col}}{T_{col} - T_{oi}}$$

where ΔT_{col} is the difference between the collector gas temperature with insulation and the collector gas temperature without insulation (that is, ΔT_{col}

is the reduction in the collector gas temperature due to heat transfer)

T_{col} is the temperature of the gas in the collector and

T_{oi} is the stagnation temperature of the gas in the plenum.

In the following analysis we assume that the compressor has been operating sufficiently long so that a steady state has been established (relative to heat transfer and property changes throughout the compressor). It is important to remember that if compressor test data is obtained too early in a test run so that thermal steady state has not yet been established, the measured efficiency will be higher than the true isentropic efficiency by an additional amount due to transient heat transfer from the gas to the compressor material which acts as a thermal sink.

Under steady-state conditions, the decrease in the internal energy of the gas in the collector caused by heat transfer is

$$mC_p \Delta T_{col}$$

where ΔT_{col} is the collector gas temperature reduction due to heat transfer.

The heat transfer from this collector gas to the environment is the sum of the convective and radiative components and is given approximately by

$$UA(T_{col} - T_{\infty}) + \sigma \epsilon A(T_w^4 - T_{\infty}^4)$$

where m = mass flow rate of the gas (lbm/sec)
 C_p = specific heat capacity of the gas (Btu/lbm $^{\circ}$ R)
 U = overall heat transfer coefficient gas-wall-air (Btu/hr ft 2 $^{\circ}$ R)
 A = surface area for heat transfer (ft 2)
 T_{∞} = temperature of the environment ($^{\circ}$ R)
 T_w = temperature of the compressor surface ($^{\circ}$ R)

σ = Stefan-Boltzmann constant = 0.1713×10^{-8}
 Btu/hr ft²(°R)⁴
 ϵ = emissivity of the surface

In writing this expression, we have replaced complex integrals involving surface geometry, spatial surface temperature variations, and view factors by an approximate term for the radiative heat transfer. The convective heat transfer from the gas to the inside compressor wall, the conduction through the wall, and the convection to the environment are represented by an overall heat transfer coefficient, U , given by

$$U = \frac{1}{\frac{1}{h_i} + \frac{d}{k} + \frac{1}{h_o}}$$

where h_i = inside (gas to wall) heat transfer coefficient
 d = wall thickness
 k = wall conductivity
 h_o = outside (wall to room air) heat transfer coefficient.

We expect that the overall convective heat transfer will be limited by the heat transfer rate from the wall to the room air. That is, we expect $h_o \ll k/d$ and $h_o \ll h_i$. This expectation was confirmed by experimental measurements which showed that T_w (of the collector) was always within 10°-15°F of T_{col} . Thus, to an accuracy sufficient for the analysis here, we have taken $U \approx h_o$.

Equating the change in the internal energy of the gas to the heat transfer from the gas and solving for ΔT_{col} gives

$$\Delta T_{col} = \frac{1}{MC_p} [h_o A(T_w - T_\infty) + \sigma \epsilon A(T_w^4 - T_\infty^4)]$$

The heat transfer coefficient, h_o , can be evaluated from empirical expressions involving the Nusselt number and the geometry. For free convection, the Nusselt number is a

function of the Grashof number and the Prandtl number of the room air evaluated at a mean air temperature. For forced convection, the Nusselt number is a function of the Reynolds number.

We will assume:

- 1) Heat transfer is from the collector surface only, and the surface is at the collector gas temperature.
- 2) The collector can be approximated by a 4.5-inch-diameter horizontal cylinder to estimate h_o .

We will consider four cases:

- I: LSM with external natural convection
- II: LSM with external forced convection at 10 ft/sec
- III: Air with external natural convection
- IV: Air with external forced convection at 10 ft/sec

We will use the values contained in Table XIII which are typical of operation near the point of maximum efficiency at 50,000 rpm (air-equivalent speed).

| TABLE XIII. VALUES USED FOR HEAT TRANSFER CALCULATION | | |
|---|------|------|
| PARAMETER | AIR | LSM |
| m (lbm/sec) | 1.9 | 1.9 |
| C_p (Btu/lbm $^{\circ}$ R) | 0.25 | 0.13 |
| h_o (free conv.) (Btu/hr ft 2 $^{\circ}$ R) | 1.55 | 1.53 |
| h_o (10 ft/sec conv.) (Btu/hr ft 2 $^{\circ}$ R) | 2.9 | 3.0 |
| A (ft 2) | 8.8 | 8.8 |
| T_w ($^{\circ}$ R) | 1135 | 960 |
| T_{∞} ($^{\circ}$ R) | 520 | 520 |
| T_{oi} ($^{\circ}$ R) | 520 | 460 |
| ϵ | 0.65 | 0.65 |

Using these values for the four cases gives the results listed in Table XIV and Table XV .

| TABLE XIV. HEAT TRANSFER - FOUR CASES | | | |
|---------------------------------------|-------------------------------------|---|------------------------------------|
| Case | $h_o A(T_w - T_\infty)$ (Btu/hr) | $\sigma \epsilon A(T_w^4 - T_\infty^4)$ (Btu/hr) | $\Delta T_{col} m C_p$ (Btu/hr) |
| I (LSM/free) | 5,900 | 7,600 | 13,500 |
| II (LSM/forced) | 11,600 | 7,600 | 19,200 |
| III (Air/free) | 8,400 | 15,600 | 24,000 |
| IV (Air/forced) | 15,700 | 15,600 | 31,300 |

| TABLE XV. EFFECT OF HEAT TRANSFER ON EFFICIENCY | | | |
|---|--------------------------|----------------------------|----------------------|
| Case | ΔT_{col} (°R) | $T_{col} - T_{oi}$ (°R) | $\Delta \eta / \eta$ |
| I (LSM/free) | 15 | 500 | 0.03 |
| II (LSM/forced) | 22 | 500 | 0.04 |
| III (Air/free) | 14 | 615 | 0.02 |
| IV (Air/forced) | 19 | 615 | 0.03 |

The heat transfer rates for the four cases considered are displayed in Table XIV to demonstrate the relative magnitude of convective and radiative heat transfer. Also, note that although the total amount of heat transfer from the compressor gas is greater for air than for LSM, the effect of this heat transfer on ΔT_{col} is slightly greater for LSM (due to the lower stage temperature rise for LSM).

Case I we believe most closely represents the heat transfer condition during the LSM testing at Creare for the uninsulated compressor cases. The results given in Table XV show that the calculated fractional increase in measured efficiency for the LSM tests when the compressor was not insulated is about 0.03. This means that at a state point with a measured efficiency of 72%, the expected isentropic efficiency (with an insulated collector) for LSM testing would be about 70%. This calculated 2% difference in measured efficiency (between insulated and noninsulated cases) agrees quite well with the data reported in Section 8.

Although the exact heat transfer environment during Boeing's air tests is not known, Table XV shows (for Case III) that if the heat transfer was by free convection along with radiation, the actual adiabatic efficiency for the air data would be expected to be about 2% lower than the efficiency measured in the uninsulated case tested by Boeing.

These calculations, coupled with the experimental LSM data, show the importance of heat transfer on measured vs. true isentropic efficiency. Note that the effect of heat transfer on measured efficiency is about the same for the uninsulated cases of air and LSM. Of course, if the air tests and the LSM tests were both performed with a well-insulated compressor, $\Delta\eta/\eta$ would be 0 for both cases. That is, the measured LSM and air efficiencies in the case of an insulated collector would both represent the true adiabatic efficiency, and the measured efficiency values should be identical, within the experimental uncertainty for this type of testing.

APPENDIX IV
CALCULATION OF JET/WAKE FRACTIONAL PRESSURE RISE

In Section 9 we presented a selected sample of the dynamic pressure data; in Section 10 we discussed this data. In this appendix we supplement the brief analysis of Section 10 by examining the details of the wake/jet fluid dynamics relative to the pressure traces.

It is important to recognize both tip leakage (between impeller blades and cover) and mass addition to the wake flow in adjusting the proportion of total passage pressure rise distributed in the wake and jet portions of the flow.

If the conservation of angular momentum is applied to the total flow in the impeller passage at a given radius, the blade loading Δp , i.e., the suction surface to pressure surface pressure difference, is

$$\Delta p = \frac{2m\Omega}{g_o bZ} \quad (49)$$

where m = total mass flow rate
 Ω = impeller rotational speed
 b = passage depth in axial direction
 Z = blade number

The derivation of Equation 49 is for radial blades and assumes that Δp is the average blade loading at radius r . Cover friction is neglected and a slip factor of unity is assumed. In deriving this equation, it is immaterial how the flow within the control volume distributes itself between wake and jet.

In applying the conservation of angular momentum to a single passage, tip leakage flow cancels on each side of the control volume and thus does not affect the final passage blade loading. (Note that this is based upon the assumption that the leakage flow does not change the condition of slip factor unity for the passage flow, which is a basic assumption in the derivations. In reality, leakage over the blades will affect the slip factor and hence the blade loading.) However, if we now want to deduce the pressure distribution across the flow passage, and in particular the relative distribution in pressure between the wake and jet portions of the passage

flow, then tip leakage flow and resultant mass addition to the wake must be considered.

We will look at several cases of increasing complexity to see how mass flow distribution between wake and jet and tip leakage can influence blade loading distribution.

First consider the case of no tip leakage and no mass transfer between wake and jet, but with a certain percentage of the mass flow in the wake. Assuming no slip in either the wake or jet (slip factor of unity), Equation 49 can be applied to both the wake and jet flows, giving

$$\Delta p_w = \frac{2m_w \Omega}{g_o b z} \quad (50)$$

$$\Delta p_j = \frac{2m_j \Omega}{g_o b z} \quad (51)$$

and
$$\Delta p = \Delta p_w + \Delta p_j = \frac{2m \Omega}{g_o b z} \quad (49)$$

The percentage of total passage Δp which is split between jet and wake is proportional to the mass flow in the jet and wake respectively. For example, if 20% of the passage flow is in the wake, then the loading across the wake region of flow will be 20% of the total loading, while 80% of the total loading will appear across the jet portion of flow.

Next we consider mass addition to the wake by tip clearance leakage flow over the blades from pressure surface to suction surface. Applying the conservation of angular momentum to the jet and wake, we arrive at the pressure rise across the jet and wake

$$\Delta p_j = \frac{2m_j \Omega}{g_o b z} + \left(\frac{r \Omega}{b g_o z} + \frac{C_{\theta L}}{b g_o} \right) \frac{dm_j}{dr} \quad (52)$$

$$\Delta p_w = \frac{2m_w \Omega}{g_o b z} + \left(\frac{r \Omega}{b g_o z} + \frac{C_{\theta L}}{b g_o} \right) \frac{dm_w}{dr} \quad (53)$$

and
$$\Delta p = \Delta p_w + \Delta p_j = \frac{2m\Omega}{g_o bZ} \quad (49)$$

Because the leakage flow leaving the jet is exactly the same as the leakage flow entering the wake, the total passage Δp remains the same as given by Equation 49 (again remembering that our assumptions preclude leakage changing the passage flow slip factor). Recasting these equations in the form of fractional pressure loading of the jet and wake respectively to the total passage loading gives

$$\frac{\Delta p_j}{\Delta p} = \frac{m_j}{m} + \left(\frac{r}{2m} + \frac{C_{\theta L}}{2m\Omega} \right) \frac{dm_j}{dr} \quad (54)$$

$$\frac{\Delta p_w}{\Delta p} = \frac{m_w}{m} + \left(\frac{r}{2m} + \frac{C_{\theta L}}{2m\Omega} \right) \frac{dm_w}{dr} \quad (55)$$

If there is no leakage flow, the terms dm_j/dr and dm_w/dr are identically zero and Equations 52 and 53 reduce to Equations 50 and 51 derived earlier for no leakage flow.

We see from Equations 52 and 53 that additional pressure rise across the wake and hence less rise across the jet can result from tip leakage into the wake. Again, these equations have been derived assuming a slip factor of unity for both the wake and jet flows. The first term in parentheses on the right-hand side of these equations represents the additional pressure rise across the wake (decrease in pressure rise across the jet) caused by mass flow addition to the wake (from the jet). The second term in the parentheses results from the tip leakage angular momentum, and this also can result in the increase to wake pressure rise (and a decrease in jet pressure rise).*

The term dm_w/dr represents the rate of change with radius of mass flow in the wake, and, for the case under consideration, this can be evaluated from the distribution of mass flow

* In reality, tip leakage is not the sole contributor to mass flow addition in the wake since other factors such as secondary flow and the deposition of boundary layer fluid in the wake by Coriolis forces are also involved. We are neglecting these effects compared to tip leakage.

fraction in the wake with radius. Now we do not really know how the wake mass flow fraction varies with radius in the RF-2 wheel. For purposes of estimating the influence of tip leakage on jet/wake pressure distribution, two cases of assumed wake flow mass fraction distribution between separation point radius and impeller exit radius have been assumed, and calculations based on these distributions are shown in Figure 79. In these cases, separation is assumed to occur at $r/r_2 = 0.4$ (separation at the end of the inducer where the RF-2 turns to radial). At the separation point, the wake mass flow fraction is assumed to be zero and a value of $m_w/m = 0.2$ is assumed at the impeller exit. The RF-2 impeller operating in air at 50,000 rpm is assumed. One distribution is linear with radius and the other is a parabolic distribution with radius. In both calculations, a constant leakage tangential velocity $C_{\theta L}$ with radius has been used, even though this is basically an incorrect assumption. (Leakage velocity $C_{\theta L}$ will decrease with radius as the blade loading pressure difference Δp increases with radius.)

These calculations show that a significant difference in loading distribution can result from the continual mass addition to the wake. The results also clearly display that a large portion of the passage loading Δp can appear across the wake portion of the flow near the separation point if the rate of mass addition to the wake is large at this location.

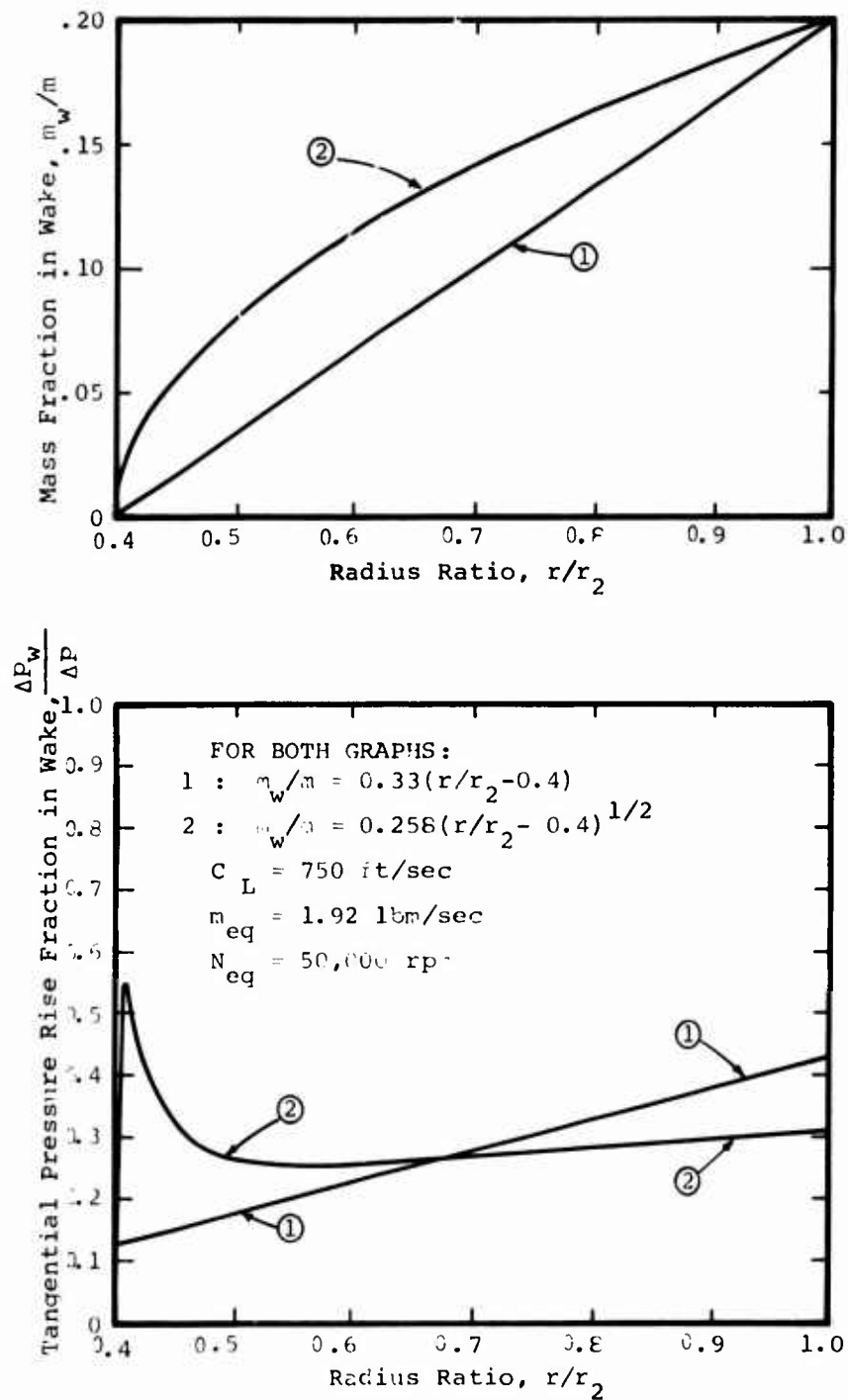


Figure 79. Influence of Wake Mass Flow Fraction Distribution on Wake and Jet Tangential Pressure Rise.